

Multiphase Interactions

G.F. Oweis
S.L. Ceccio
University of Michigan

Y. Matsumoto
University of Tokyo

C. Tropea
I.V. Roisman
Technical University of Darmstadt

Y. Tsuji
Osaka University

R. Lyczkowski
Argonne National Laboratory

T.R. Troutt
Washington State University

J.K. Eaton
Stanford University

F. Mashayek
University of Illinois

12.1	Cavitation	12-1
	Cavitation Nuclei and Bubble Growth • Collapse of Cavitation Bubbles and Erosion • Acoustic Cavitation • Hydrodynamic Bubble Cavitation • Sheet Cavitation • Vortex Cavitation • Cavitation in Hydraulic Machinery • Cavitation in Biomedical Applications • Other Occurrences and Applications of Cavitation	
12.2	Bubble Physics	12-17
	Single Spherical Bubble Dynamics • Bubble Deformation and Fragmentation Due to the Collapse • Bubbles Cloud Dynamics	
12.3	Droplet Breakup, Coalescence, and Wall Impact	12-35
	Droplet Breakup Mechanisms • Binary Drop Collisions • Drop-Wall Impact	
12.4	Particle Interactions	12-51
	Particle-Particle Collision • Particle-Wall Interaction • Erosion	
12.5	Particle and Droplet Dispersion in Turbulent Flows	12-81
	Introduction • Time Scales • Particle Dispersion in Turbulent Shear Flows • Body Force Effects on Particle Dispersion • Two-Way Coupling Effects on Particle Dispersion	
12.6	Turbulence Modulation by Particles	12-86
	Introduction • Mechanisms of Turbulence Modification • Analytical Approaches • Methods for Studying Turbulence Modulation • Observations of Turbulence Modulation • Summary	
12.7	Combustion	12-98
	Introduction • Overview of Single-Phase (Gaseous) Combustion • Isolated Drop • Groups of Drops • Spray Modeling	

12.1 Cavitation

G.F. Oweis and S.L. Ceccio

Cavitation is the physical phenomenon associated with the inception, growth, and implosion of cavities (vapor-filled voids or bubbles) in the body of a flowing or a quiescent liquid due to changes in the fluid pressure. Cavitation may occur entirely in the bulk of the liquid or close to solid boundaries of the flow. Cavitation is similar to boiling in the inception and growth of bubbles, except that in the latter bubble formation is due to a rise in liquid temperature, while in the former bubble formation is driven by a drop

in the liquid static pressure. Pressure variations in the fluid can be achieved hydrodynamically or acoustically. During vaporous (inertial) cavitation, the cavities are filled mostly with fluid vapor. Vaporous cavitation bubbles are often short-lived and produce a high-intensity acoustic pressure upon collapse. Gaseous cavitation bubbles are filled mostly with noncondensable gases, and these gaseous bubbles may persist for longer periods, collapse much less violently, and produce much less noise and damage compared to vaporous bubbles. Pockets of gas and vapor can form and persist on flowing surfaces, and this is referred to as *partial* or *attached* cavitation. Cavitation *inception* occurs when cavitation is first detected in the flow as the mean pressure in the flow is reduced, and *developed* cavitation describes an advanced stage of cavitation, where the size of the cavity is of comparable magnitude to a characteristic flow dimension. *Desinence* occurs when cavitation is eliminated through an increase in the mean pressure. Cavitation is undesirable in liquid handling machinery because it may cause damage to solid surfaces, induce noise and vibrations, and lead to reduction in the mechanical efficiency. Conversely, there are useful scientific and engineering applications that employ cavitation. Comprehensive reviews of this subject can be found in Brennen (1995), Young (1989), and Franc et al. (1995).

12.1.1 Cavitation Nuclei and Bubble Growth

Liquid water can be brought to evaporation at a constant pressure by raising its temperature. This phase change can also be achieved at a constant temperature by reducing the pressure to the corresponding vapor pressure (e.g., water at 1 atm and room temperature, 25°C, can be brought to boiling by heating to 100°C while keeping the pressure fixed, or by reducing the pressure to vapor pressure, 0.03 atm, while keeping the temperature fixed at 25°C). The process of phase change takes place at a phase boundary in the liquid. If such an interface is not present, the bulk of the liquid can sustain pressures below vapor pressure (or remain liquid at temperatures above the saturation temperature) (Carey, 1992). (see Chapter 3 for a discussion on nucleation and boiling.)

Theoretical predictions based on the van der Waals intermolecular forces of attraction indicate that *pure* water (no dissolved gas or impurities) can withstand high levels of tension corresponding to pressures much less than the vapor pressure (several hundred atmospheres of tension). The fracture of the liquid due to the failure of intermolecular forces is called *homogeneous nucleation*. In most practical applications, these high levels of tension are not approached. Instead, voids or bubbles (cavitation) appear in the liquid as the liquid evaporates at the interface of small gas inclusions, or *nuclei*. This process is called *heterogeneous nucleation*, and it is the most common form of cavitation initiation. It is often sufficient to bring the operational pressure to or slightly below the evaporation pressure for these bubbles or voids to appear.

Cavitation nuclei can be present in the body of the liquid, or on the surfaces of suspended particles or boundaries that come in contact with it as described in Section 3.1. Cavitation nuclei often exist as small bubbles of gas (a few microns to a few hundred microns) that are in equilibrium with the liquid, or as gas-filled miniature pockets on the surfaces of solid particles or solid flow boundaries. Nuclei can also form when dissolved gas in the liquid comes out of solution. The amount and properties of nuclei in the fluid can strongly influence the pressure at which inception occurs. The growth of nuclei can often be approximated by the growth of small spherical bubbles in an unbounded liquid.

The Rayleigh–Plesset equation (Brennen, 1995) describes the dynamics of growth and collapse of a spherical bubble nucleus in an otherwise quiescent, infinite fluid medium. It couples the forces acting on the bubble with the motion of the surrounding fluid:

$$\rho_l \left[a_b \frac{d^2 a_b}{dt^2} + \frac{3}{2} \left(\frac{da_b}{dt} \right)^2 \right] + \frac{4\mu}{a_b} \frac{da_b}{dt} = \left(p_{\infty,0} - p_v + \frac{2\sigma}{a_{b,0}} \right) \left(\frac{a_{b,0}}{a_b} \right)^{3k} - p_{\infty} + p_v - \frac{2\sigma}{a_b} \quad (12.1)$$

where the subscript 0 refers to the initial conditions of the bubble. The liquid pressure far away from the bubble is p_{∞} . The bubble contains both vapor and noncondensable gas of partial pressures, p_v and p_g , respectively. The gas obeys the polytropic gas law. The exponent k is the polytropic gas constant, and $k = 1$ for isothermal processes and $k = c_p/c_v$ for adiabatic processes. p_g is equal to the first term on the right-hand side

(RHS) of the equation. In this formulation the liquid compressibility is neglected (see Section 12.2 for further discussion of bubble physics.)

With the left-hand side (LHS) set to zero, Eq. (12.1) describes the quasi-static equilibrium of a bubble (temporal dependence of the bubble radius is negligible). Consider a small bubble (cavitation nucleus) that exists in a quasi-static equilibrium in the body of a liquid. The pressure inside the bubble, p_b , is counteracted by the liquid pressure on the bubble surface, p_l , and by the surface tension forces, or

$$p_g + p_v = \frac{2\sigma}{a_b} + p_l \tag{12.2}$$

where $p_b = p_g + p_v$. When this nucleus experiences a drop in the liquid pressure, such as when it passes through a venturi throat, it may grow quasi-statically from its initial equilibrium radius, $a_{b,0}$, to a larger equilibrium radius, provided that the bubble radius does not exceed the *Blake critical radius*. A bubble exposed to tension will grow unboundedly when its radius is above this critical value given by

$$a_{b,c} = \left[\frac{9km_G T_b K_G}{8\pi\sigma} \right]^{1/2} = \left[\frac{3}{2} \frac{ka_{b,e}^3 p_{g,e}}{\sigma} \right]^{1/2} \tag{12.3}$$

The subscript e refers to the equilibrium state of the bubble. Here, m_G and K_G are the gas mass and gas constant, respectively, and T_b the bubble temperature. An equivalent critical liquid pressure is given by

$$p_{l,c} = p_v - \frac{4}{3}\sigma \left[\frac{8\pi\sigma}{9km_G T_b K_G} \right]^{1/2} = p_v - \frac{4}{3}\sigma a_{b,c} \tag{12.4}$$

In the venturi example, if the liquid pressure drops to or below the critical pressure, the bubble radius will grow explosively to a maximum radius that can be of the order of hundred times its initial size, and the nucleus would then be considered to have cavitated. Figures 12.1a and b show the response of a nucleus,

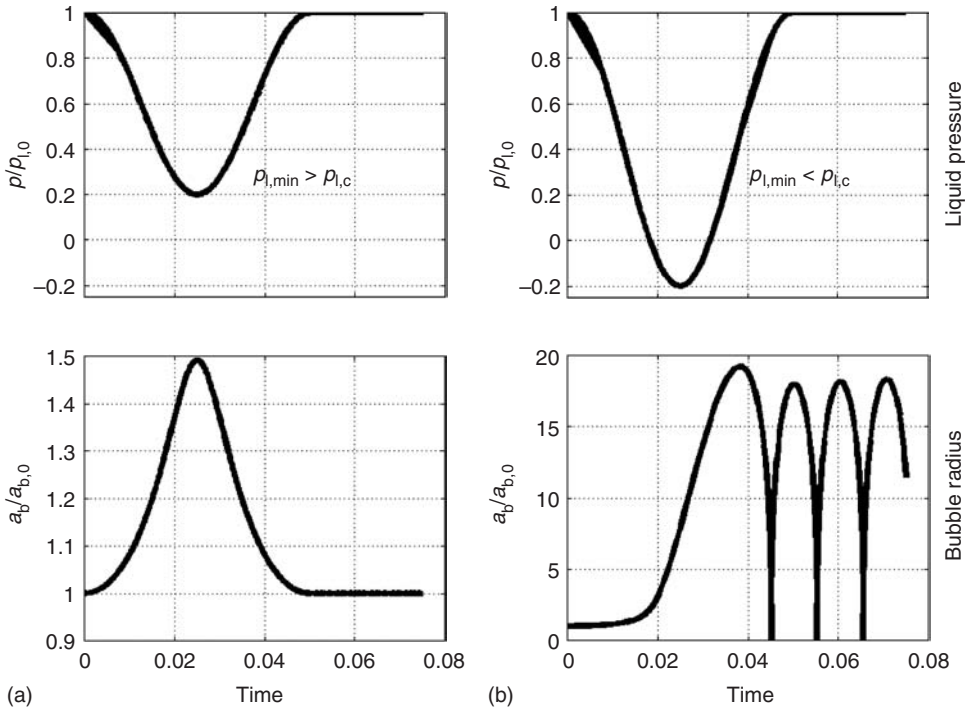


FIGURE 12.1 Changes in the radius of a bubble as it is exposed to a sinusoidal variation in the surrounding pressure: the minimum pressure is above the critical pressure (a) and below the critical pressure (b).

initially in equilibrium, to a sinusoidal variation in the liquid pressure. Figure 12.1a shows the change in bubble radius when the minimum liquid pressure is above the critical pressure: the bubble radius responds quasi-statically. Next, Figure (12.1(b)), the tension exceeds the critical pressure. Notice the growth rate of the cavitating nucleus, its violent collapse, and the multiple rebounds. Not all nuclei will lead to cavitation (explosive bubble growth). Only the nuclei that reach the critical radius will cavitate, and these are considered the *active nuclei*.

When a bubble cavitates, its radius will grow asymptotically. Thus, the maximum bubble radius, $a_{b,m}$, is related to the total time that the bubble remains in the region of tension, Δt :

$$a_{b,m} \approx \frac{2}{3} \left(\frac{-p_\infty + p_v}{\rho_l} \right)^{1/2} \Delta t \quad (12.5)$$

The nuclei distribution in a flow can be quite variable, depending on the source of the liquid and the upstream flow conditions. Consequently, the characterization of cavitation inception must be accompanied by a measurement of the nuclei content.

Measurement methods for cavitation nuclei can be hydrodynamic, acoustic, or optical (Gindroz and Billet, 1993). Holography and light scattering have been used to detect the presence of cavitation nuclei (Ran and Katz, 1993). In these methods, the optically measured size of detected bubbles is used to infer the critical pressure. The absorption and scattering of acoustic signals is also used to detect and count nuclei (Chahine and Kalumuk, 2003). A direct measurement of the presence of nuclei is achieved when a liquid sample is passed through a region of known low pressure. Nuclei with radii that exceed the critical radius will cavitate. The Blake critical radius is computed from this pressure and presented as the nuclei radius. The event rate of these cavitating bubbles can then be counted by visual observation. Moreover, when a cavitating bubble is convected to a region of higher pressure downstream, it will collapse producing an acoustic emission. The noise pulses can be detected and counted, giving another independent measurement of the nuclei. Devices that measure nuclei through inducing cavitation events are called *cavitation susceptibility meters* (d'Agostino and Acosta, 1991; Ceccio et al., 1991). The amount of dissolved gas in the liquid will also influence the number of free nuclei and the inception process. Measurements of the total dissolved gas (or of one gas component, such as oxygen) are often reported, but this quantity only indirectly relates to the free gas content.

12.1.2 Collapse of Cavitation Bubbles and Erosion

The collapse of cavitation bubbles is of practical importance, because of the associated high potential for damage and noise production. Once a cavitating bubble has reached its maximum radius and encountered a region of higher pressure (either through convection to a high-pressure region or via a change in the mean pressure field), the bubble will start its collapse. During the final stages of bubble implosion, the bubble wall velocity can reach or exceed the liquid speed of sound, and shock waves are produced in the liquid. Liquid compressibility in the vicinity of the bubble cannot be neglected in this instance, and the Rayleigh–Plesset equation (Eq. [12.1]) should be modified to include this effect. One of the existing modifications is the Gilmore equation (Franc et al., 1995; Leighton, 1994) and is given by

$$a_b U \frac{dU}{da_b} \left(1 - \frac{U}{c_l} \right) + \frac{3}{2} U^2 \left(1 - \frac{U}{3c_l} \right) = h \left(1 - \frac{U}{c_l} \right) + \frac{a_b U}{c_l} \left(1 - \frac{U}{c_l} \right) \frac{dh}{da_b} \quad (12.6)$$

where $U = da_b/dt$, c_l is the liquid speed of sound, and h the enthalpy of the liquid at the bubble wall, with $h = 0$ for the liquid very far away. Whether the bubble wall speed will reach the liquid speed of sound depends on the noncondensable gas mass inside the bubble, which determines the amount of damping of the bubble mechanical energy.

Higher noncondensable gas contents lead to increased damping, and result in less violent collapse and reduced possibility for shock pressure production. Experimentally measured values of the pressure levels in the immediate vicinity of spherically collapsing bubbles in water are of the order of hundreds of atmospheres. The intense pressure waves created in the liquid can cause damage to nearby solid surfaces.

A time scale for the bubble collapse is the Rayleigh collapse time, which depicts the time it takes for a vapor-filled spherical bubble to implode from its maximum to its minimum radius, and is given by

$$t_c = 0.915a_{b,m} \left(\frac{\rho_l}{\Delta p} \right)^{1/2} \tag{12.7}$$

where $a_{b,m}$ is the maximum bubble radius, Δp the difference between the liquid static pressure and the vapor pressure. The acoustic emission produced by the collapse of a cavitation bubble is proportional to the mechanical potential energy of the bubble:

$$E_M = \frac{4}{3} \pi a_{b,m}^3 \Delta p \tag{12.8}$$

The collapsing bubble is largely a monopole sound source, with the largest emissions taking place during the rapid volume deceleration and acceleration at the point of minimum bubble volume. The amount of this energy converted into acoustic energy during bubble collapse is strongly related to the amount of deformation that the bubble undergoes during collapse.

The collapse of the bubble can be influenced by gravity and the presence of free and solid surfaces (Blake and Gibson, 1987). The quantity

$$\gamma = \left(\frac{\rho_l g a_{b,m}}{\Delta p} \right)^{1/2} \tag{12.9}$$

scales the buoyancy force with the force due to the pressure difference across the bubble interface. When $\gamma > 1$, the bubble collapse becomes nonspherical and is characterized by the formation of a jet, where the lower side of the bubble caves inward and upward, and penetrates the upper wall of the bubble. A similar jet formation occurs when the bubble collapses near a solid boundary as shown in Figure 12.2 reproduced from Tomita and Shima (1990). Note that the jet is directed toward the solid surface. Measurements of jet speeds of upto 150 m/sec have been observed (Philipp and Lauterborn, 1998; Brujan et al., 2002). The water hammer effect of this jet can induce instantaneous pressures on the surface given by $P_{jet} = \rho_l c_l u_{jet}$, where c_l is the liquid speed of sound and u_{jet} the jet velocity. Jet impact on a nearby solid boundary can lead to very high surface stresses and produce instantaneous pressures on the solid surface exceeding hundreds of bars. These high pressures are capable of inducing surface damage.

Cavitation erosion is caused by the *repetitive* impingement of cavitation-induced pressure pulses on a solid flow boundary and often results from material fatigue. Erosion predictions on metal surfaces have

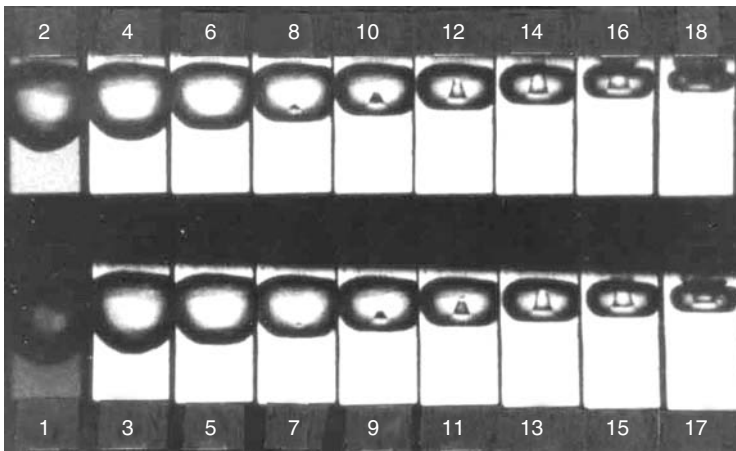


FIGURE 12.2 A series of images that shows the collapse of a cavitation bubble near a solid boundary. The images are with 2 μ sec time intervals, and each is 1.4 mm wide. Note the formation of the reentrant jet directed toward the wall. (Reproduced from Tomita, Y. and Shima, A., *Acustica*, 71, 161, 1990.)

been mostly based on combining the concept of cavitation intensity (frequency of occurrence and levels of peak pressures from collapsing cavities) with one or more representative material properties. Such properties can be the hardness, elastic modulus, tensile strength, or their combinations. An example of such combination is the ultimate resilience, defined as

$$UR = \frac{(\text{tensile strength})^2}{2(\text{Young's modulus})} \quad (12.10)$$

(Hammit, 1980). Cavitation intensity depends on the flow conditions, and the form of cavitation. Studies on cavitation erosion in metals and alloys often produce scattered results. Erosion measures include mass loss measurements and mean depth of penetration rate (MDPR):

$$MDPR \sim \rho_1 \frac{\eta}{\varepsilon} u^n \quad (12.11)$$

where η is an energy-transfer efficiency term, ε related to the material properties, u the impact speed, and n an exponent. Care should be taken to determine how specific MDPR formulations are derived.

Despite the scatter in cavitation erosion data, a general trend in erosion behavior can be described as depicted in Figure 12.3 for a ductile metal. There is an *incubation period* (I) before a damage to the surface can be noticed, followed by an *acceleration* of the rate of erosion (II). As the specimen is exposed further to cavitation, the erosion rate will *plateau* (III) for quite some time before it drops, in what is known as the *attenuation phase* (IV). The rate of erosion and the damage properties depend also on the microscopic material structure. For ductile materials that have the potential to store elastically and respond to the cavitation hammering energy, damage is often due to fragmentation and is in the form of craters. In fragile alloys, erosion often causes cracks and occurs along crystal lines, and thus causes more material loss than in ductile metals.

12.1.3 Acoustic Cavitation

Sometimes referred to as vibratory cavitation (low driving frequencies) or ultrasonic cavitation (high driving frequencies), acoustic cavitation describes the growth and collapse of cavitation nuclei due to their exposure to acoustic pressure waves in a liquid (Leighton, 1994). As in many forms of cavitation, the presence of cavitation nuclei is usually required to initiate and sustain the cavitation process. Once the cavitation process is initiated, the collapse of the bubbles and their fragmentation can act as nuclei for new cavitation bubbles. Consider an underwater acoustic horn emitting a sinusoidal pressure signal fluctuating about a mean amplitude. The water will experience compression (high pressure) and rarefaction (low-pressure) patterns due to the passage of the wave. If the rarefaction amplitude of the wave drops below the vapor pressure, cavitation can occur. The principle behind the control of acoustic cavitation is the ability to synchronize the acoustic forcing with the dynamics of the bubble in order to achieve the desired effect such as timely bubble growth or collapse. Production of acoustic waves in the liquid can be achieved by magnetostriction type devices, or by the more widely used piezoelectric crystal transducers. The electrical input to a piezoelectric element is transformed into displacement of the piezoelectric crystal surface that is then transferred to the liquid in the form of acoustic waves. To achieve acoustic signals of sufficient amplitude for cavitation, acoustic mirrors or acoustic lenses can be used to focus the acoustic energy into a miniature volume. Focusing can also be achieved by using curved emission transducers. The focusing volume is proportional to the emitted acoustic wavelength and inversely proportional to the transducer size.

Pulsed ultrasound refers to the emission of a train of wave packets of fundamental frequency (f_0), and pulse repetition frequency (f). The pulse duration divided by the pulse repetition period ($1/f$) gives the portion of the time that the transducer is actually emitting or the *duty cycle*. Passive acoustic cavitation describes cavitation events induced by the acoustic emissions from other cavitation bubbles.

It can be shown from the Rayleigh–Plesset equation that a bubble acts as spring–damper system. Consider a cavitation nucleus of initial radius (a_0) that is at the focal point of an ultrasonic transducer emitting at a single frequency (f_0) and with peak amplitude P_0 . The bubble wall will oscillate under the

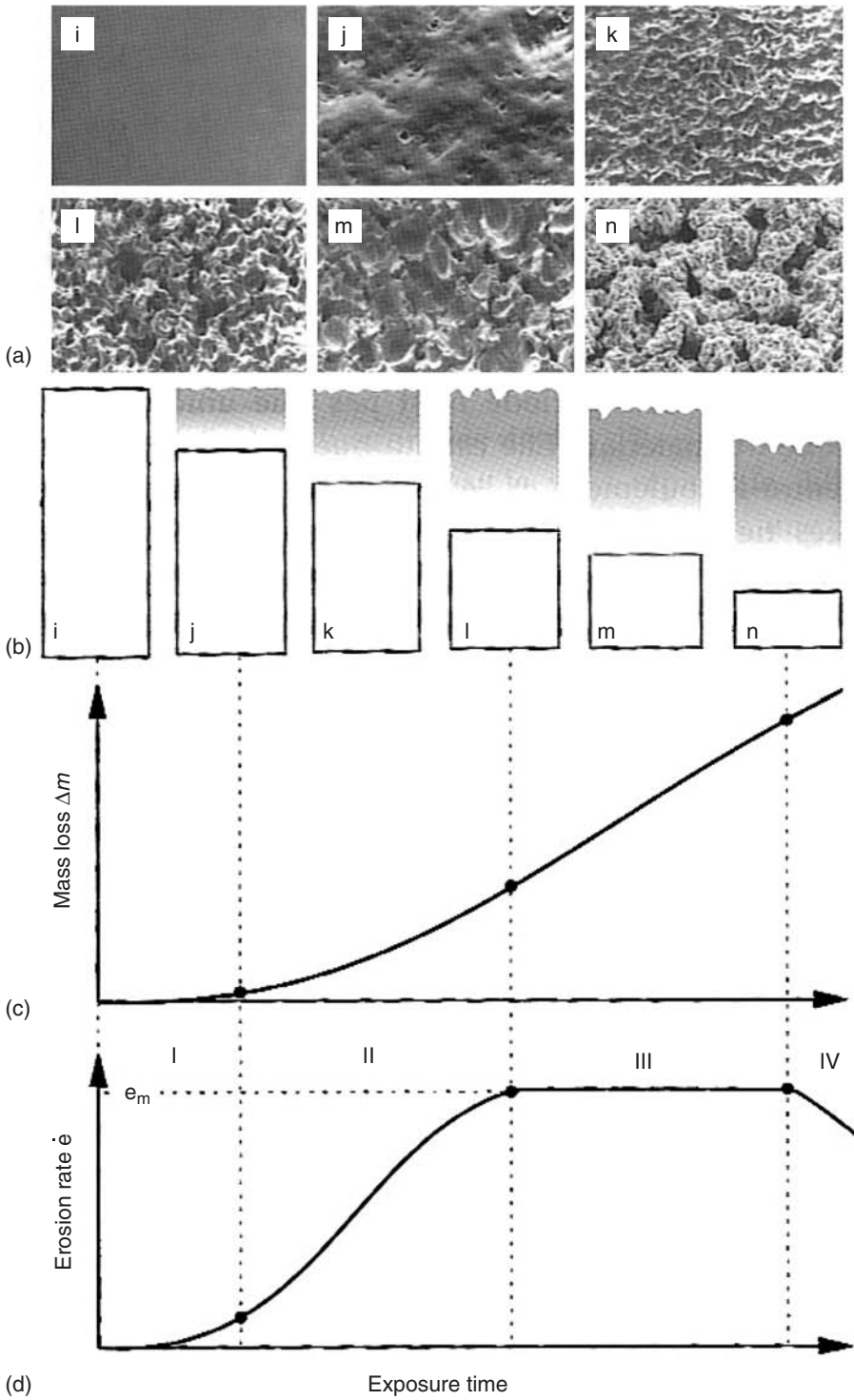


FIGURE 12.3 Erosion behavior of a ductile alloy with cavitation exposure time: (a) scanning electron microscope images showing the surface appearance; (b) cross-sectional schematics of the pitting behavior; (c) accumulative mass loss; (d) erosion rate showing the four stages of erosion. (From Franc et al., *La Cavitation Mecanismes Physiques et Aspects Industriels*, Presses Universitaires de Grenoble, Grenoble, 1995. Copyright EDP Sciences, with permission.)

effect of the forcing acoustic wave, similar to a forced damped oscillator, for *small* bubble oscillation amplitudes. The undamped natural frequency of bubble oscillation in (rad/sec) is given by

$$\omega_n = \left[\frac{1}{\rho_l a_{b,c}^2} \left\{ 3k(p_\infty - p_v + 2(3k - 1) \frac{\sigma}{a_{b,c}}) \right\} \right]^{1/2} \quad (12.12)$$

The bubble wall motion will be in phase with the forcing pressure if the forcing frequency is less than the bubble natural frequency (resonance). Increasing the forcing frequency above resonance will cause the bubble oscillations to be out of phase with the forcing pressure by 180°. Increasing the driving pressure amplitudes causes the bubble wall motion amplitude to become nonlinear, and undergo large volume oscillations, i.e., cavitation. The oscillations can be stable (*stable cavitation*) or unstable (*transient cavitation*).

During the growth part of bubble oscillation, the increasing bubble size translates into a drop in the non-condensable gas concentration in the bubble interior below the gas concentration in the liquid. This leads to mass diffusion of the gas from the liquid into the bubble. During the contraction phase of the bubble, the opposite occurs, and gas is diffused from the bubble into the liquid. Due to the larger surface area and thinner concentration boundary layer during the growth phase compared with the contraction phase, there would be a net mass diffusion into the bubble. The overall increase in the gas mass in the bubble interior is called '*rectified diffusion*' (Blake, 1949; Hsieh and Plesset, 1961). Since the diffusion time scales are usually much larger than the bubble characteristic time scale (Rayleigh time for instance), diffusion can often be neglected. In transient or unstable cavitation, the driving pressure is increased beyond the linear oscillation until the bubble growth becomes unbounded, followed by violent implosion. The bubble may rebound after collapse or it may fragment into multiple fragments. Brennen (2002) suggests that the bubble fission may be due to an instability forming on the bubble wall or due to jet formation. A number of conditions are required for unstable cavitation to occur; one of them satisfies the Blake critical pressure (or radius) threshold.

When the bubble reaches its minimum radius during implosion, the interior pressure and temperature can momentarily reach extremely high levels. Emission of shock waves in the liquid that travel at liquid Mach numbers greater than 1 has been observed (Pecha and Gompf, 2000). Light emission has also been observed from cavitation bubbles collapsing under an ultrasonic pressure field (Holzfuss et al., 1998; Matula et al., 1998; Hilgenfeldt et al., 1999). This phenomena is known as *sonoluminescence*. Putterman and Weninger (2000) discuss how the high pressures and small minimum bubble volumes during the last stages of collapse result in dramatic increases in the bubble energy density, which is essential for the production of light. The detailed physics of sonoluminescence is still a subject of investigation.

The collapse of cavitation bubbles may cause jet formation and pressure shock waves that have useful noninvasive surgical and lithotriptic effects (Vakil and Everbach, 1993; Coleman et al., 1995; Tran et al., 2003). Ultrasonic cavitation is now commonly used in industrial and electronic component cleaning operations (Niemczewski, 1999; Ferrel and Crum, 2002).

12.1.4 Hydrodynamic Bubble Cavitation

Hydrodynamic cavitation occurs when the flow of a liquid leads to reduction in pressure and cavitation. In these flows the cavitation number, which is a measure of the level of pressure in the flow, is defined as

$$\sigma = \frac{p_\infty - p_v}{1/2\rho U^2} \quad (12.13)$$

Hydrodynamic bubble cavitation (traveling bubble cavitation) and sheet cavitation (Section 12.1.5) are the two major forms of cavitation that take place on the surface of a hydrofoil or the face of a propeller blade. The operational parameters that give rise to one type or the other can be difficult to predict, and subtle changes in flow conditions (e.g., nuclei content, incident flow angle, boundary layer tripping, or Reynolds number) can lead to the inception or desinence of one or both forms. This underlines the complexity involved in predicting and scaling hydrodynamic cavitation behavior on full size prototypes from small models tests. The formation of traveling bubble cavitation can lead to significant noise, vibration, and damage if the bubbles collapse on the blade surface.

In traveling bubble cavitation, singly identifiable bubbles can be seen to move in the flow direction while attached to the surface of the blade or hydrofoil. They often have the form of hemispherical caps during the growth phase (Figure 12.4). A closeup examination of traveling bubbles indicates that there is a thin film of liquid separating a bubble from the surface. The dynamics of the boundary layer and its interaction with the bubble have significant impact on cavitation inception, bubble growth, and the consequent cavity collapse (Kuhn de Chizelle et al., 1995).

The growth and collapse of traveling bubbles can be scaled with spherical bubble dynamics for many applications (Ceccio and Brennen, 1991). However, if the bubbles interact with the boundary layer flow, they can be deformed, which reduces the level of noise they emit upon collapse. If many bubbles are present, interaction between the bubbles can become important. These interactions are discussed in Brennen (1995).

12.1.5 Sheet Cavitation

Sheet cavitation occurs when a pocket of gas or vapor forms on a solid surface due to the flow of the liquid (Figure 12.5). Sheet cavitation is often formed when there is wall-flow reversal or boundary layer separation due to an adverse pressure gradient (rising pressure in the flow direction) on the surface. If the

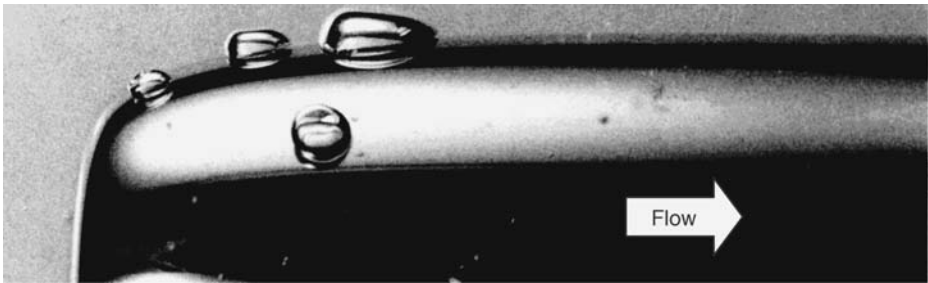


FIGURE 12.4 Traveling cavitation bubbles over an axisymmetric body of revolution.

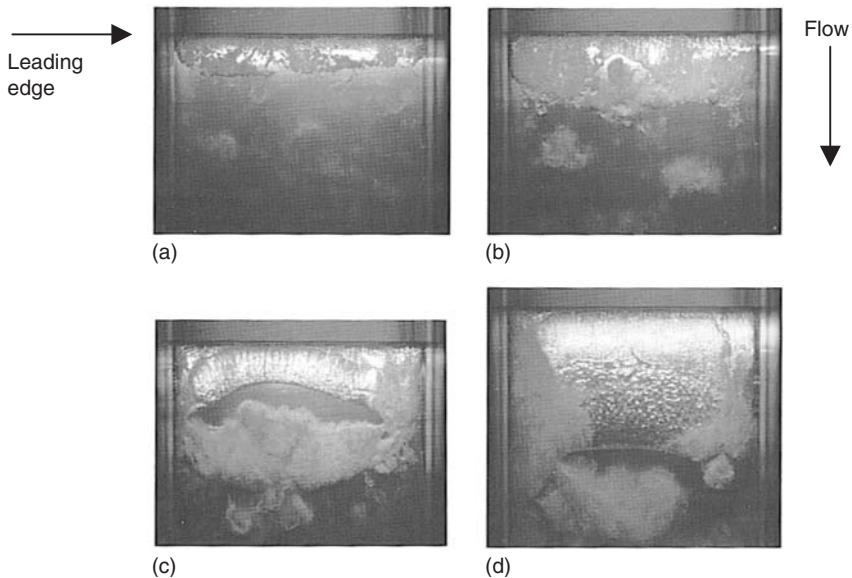


FIGURE 12.5 Sheet cavitation on a two-dimensional NACA009 hydrofoil: (a) incipient cavitation; (b) developing cavitation; (c) cloud shedding; and (d) cavity refilling.

cavity terminates on the cavitating surface, it is called a *partial cavity*. If the cavity extends beyond the cavitating object into the wake of the flow, it is called a *supercavity*. The shape of the cavity in the detachment region is affected by the type of surface material depending on whether it is hydrophilic or hydrophobic (Leger and Ceccio, 1998). For hydrophilic surfaces, the cavity interface curves downstream forming a forward facing step, with a recirculation region just upstream. The forward-facing step and the recirculation region are not present on hydrophobic surfaces, and the cavity detachment is close to the boundary layer separation point. Prediction of the cavity detachment point over a given surface can be performed with very good accuracy by invoking the potential flow theory to provide the pressure distribution in the liquid flow. This can then be combined with boundary layer calculations to predict the separation point. Laberteaux and Ceccio (2001a) present such an example.

When a laminar boundary layer separates from the surface, it can become turbulent and reattach to the surface just downstream of the separation point. In this case, the detachment of the sheet cavity is expected to occur in the narrow region between the laminar separation and turbulent reattachment of the boundary layer, or the ‘separation bubble.’ Turbulent boundary layers are more resistant to adverse pressure gradients and separation and can resist the formation of partial cavities. Increased background flow turbulence levels, surface roughness, and surface trips can induce laminar to turbulent boundary layer transition. By artificially tripping the laminar boundary layer on a hydrofoil into turbulence, Arakeri and Acosta (1973) showed that the occurrence of attached cavities could be delayed. Also, if the underlying boundary layer is transitional or turbulent, complex bubble–boundary layer interactions can occur, as shown in Figure 12.6 (Li and Ceccio, 1996).

Franc et al. (1995) map the σ – α space of a NACA 16-012 hydrofoil at $Re = 1 \times 10^6$ with relation to the shapes of sheet cavitation occurring on the foil, where α is the angle of attack. For low angles of attack, the laminar boundary layer separation is toward the rear end of the foil, and an attached cavity is formed

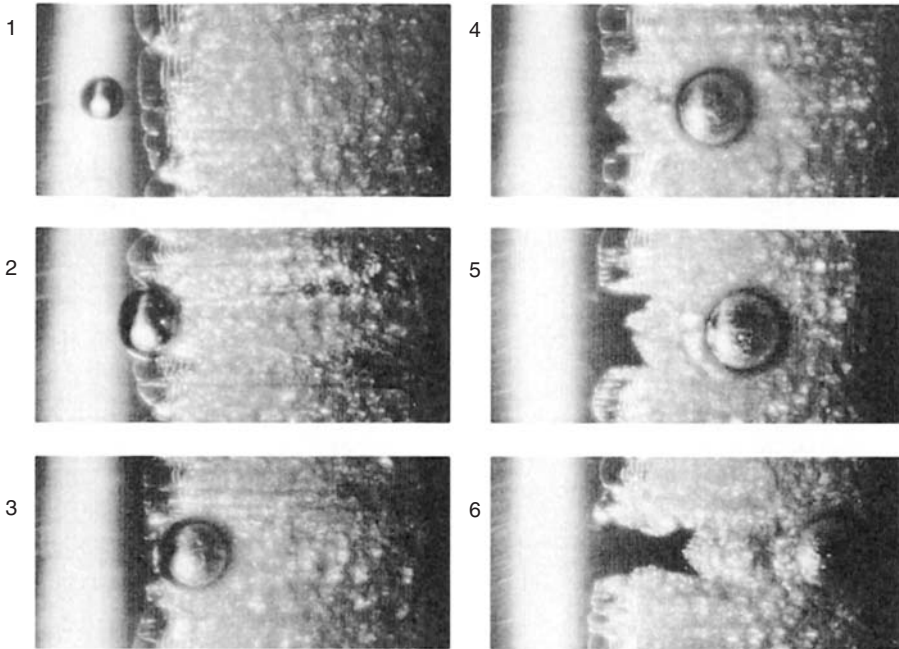


FIGURE 12.6 Images of several bubbles over a two-dimensional NACA 63,A012 hydrofoil. The process of sheet cavitation sweeping by the traveling bubble is shown. The bubble does not disturb the cavity, until it has passed downstream, when the sweeping action takes place.

near the separation point and it extends into the blade wake. Increasing α to a moderate angle of attack leads to the formation of a band of a single hemispherical bubbles on the blade surface, which transform with reduction of the cavitation number, σ , into an attached partial cavity terminating on the blade surface. A further reduction in σ forms a supercavity. The interior of partial and super-cavities is single-phase vapor (or single-phase gas–vapor mixture). Further increase in the angle of attack α combined with an increase in the cavitation number can cause the attached cavity to become “frothy” or filled with a liquid–vapor mixture, also known as *open* partial cavity. At extreme angles of attack corresponding to stall, the open cavity is not attached to the blade surface anymore except for the leading edge, and cavitation can be noticed in the wake vortices shed in the liquid.

Under certain conditions of Re , σ , and free-stream turbulence levels, a partial cavity can undergo stable or an unstable pulsation. Wade and Acosta (1966) predict that cavities of length, l_c , on a hydrofoil of cord length, c , become unsteady and pulsatile when $\frac{3}{4}c < l_c < \frac{4}{3}c$. In this pulsatile phenomena, part of the liquid flow that reattaches to the blade surface in the cavity closure region will form a jet that reenters underneath the cavity (jet directed upstream toward the cavity detachment point). When the partial cavity is at its maximum size, the reentrant jet can cause a large portion of the cavity to pinch off and be swept downstream. The bubble cloud will collapse downstream, producing substantial acoustic noise, and possible material damage. The small remaining portion of the cavity left attached to the surface will grow smoothly through evaporation and gas diffusion from the liquid to a maximum size, and the cycle repeats. Thick cavities are often unstable and associated with unsteady pulsation. The pulsation phenomena is associated with periodic, strong structural loading, which is undesirable. In stable quasi-steady pulsatile cavities, a Strouhal number (St) can be defined to describe the pulsation:

$$St = \frac{f_p l_c}{U_\infty} \tag{12.14}$$

where f_p is the pulsation frequency and l_c a characteristic length.

The Strouhal number for strongly shedding partial cavities is often between 0.2 and 0.4 when l_c is the mean cavity length (George et al., 2000). Laberteaux and Ceccio (2001a, 2001b) studied open partial cavities in detail. They showed that the liquid flow behind the cavity resembled the flow aft of a backward facing step. The cavities terminated near the point of maximum cavity thickness, and cavitating vortices were shed in the turbulent cavity wake. The collapse of these cavitating vortices is believed to contribute to cavitation damage. The formation of reentrant flow is strongly related to the shape of the cavitating object. Figure 12.7 shows the difference between two cavitating hydrofoils. The first has no spanwise variation and the second has a swept profile. In the unswept case, the reentrant flow leads to an unstable partial cavity. But, the reentrant flow in the swept geometry is deflected in the spanwise direction, producing a stable, closed cavity.

12.1.6 Vortex Cavitation

The swirling motion of a vortex requires the presence of a pressure gradient directed away from the center of rotation to counterbalance the centrifugal force. Thus, the pressure in the center of the vortex is lower than the surrounding fluid, and it is possible for the pressure in the core of a liquid vortex to drop below vapor pressure. If nuclei are present in this low-pressure region, they may explosively grow, resulting in *vortex cavitation*. The axial flow inside the vortex core can be slower or faster than the fluid outside the core, which may cause an additional pressure difference. Line vortices often occur near the termination of lifting surfaces, and Figure 12.8 shows developed cavitation occurring in a tip vortex.

The Gaussian vortex, which is a widely used model for concentrated line vortices, is characterized by a zero radial velocity profile and a tangential (azimuthal) velocity profile as a function of radial distance from the vortex center, r , given by

$$u_\theta(r) = \frac{\Gamma_o}{2\pi r} (1 - e^{-\eta_r(r/R)^2}) \tag{12.15}$$

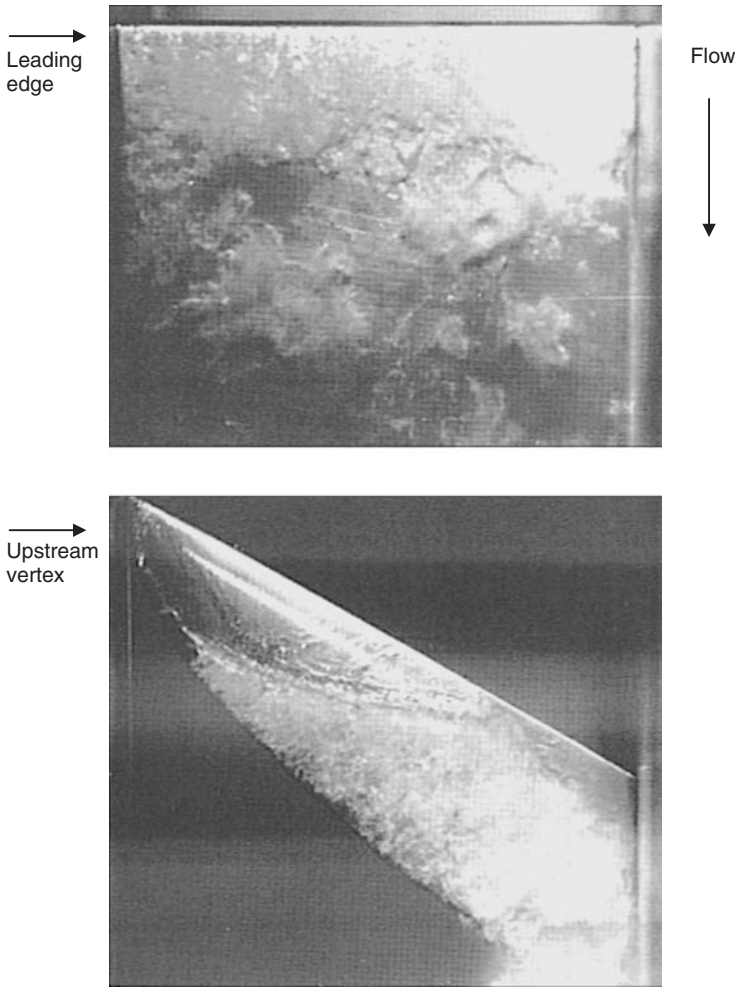


FIGURE 12.7 Partial cavities on a two-dimensional hydrofoil and on a three-dimensional hydrofoil (swept at 30°). Both hydrofoils have the same section shape.

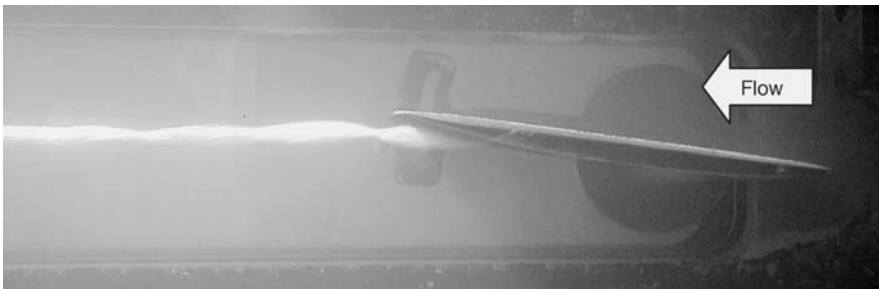


FIGURE 12.8 Developed tip vortex cavitation from a stationary hydrofoil.

Two parameters are needed to characterize the vortex: its core radius, R , which gives the location of maximum tangential velocity, and its total circulation, Γ_0 . The circulation distribution is given by

$$\Gamma(r) = \Gamma_0(1 - e^{-\eta(r/R)^2}) \quad (12.16)$$

where $\eta_1 = 1.257$ is a constant. The pressure drop at the vortex center is given by

$$p_c = p_\infty - 0.870\rho_1\left(\frac{\Gamma_0}{2\pi R}\right)^2 \tag{12.17}$$

Vortex cavitation is often the first type to appear in hydrodynamic applications. When inception occurs, individual nuclei are captured by the vortex and cavitate. With a further reduction in pressure, the core is filled with a vapor and gas mixture. Based on momentum conservation argument in a Rankine vortex (which has a uniform ‘top hat’ vorticity distribution), Arndt and Keller (1992) predicted the diameter of the vapor-filled region to be 71% of the original liquid vortex core diameter. The inception number is usually *not* equal to the desinence number. This hysteresis pattern is due to the nonlinear bubble dynamics. Vortex cavitation predictions are sensitive to the flow nuclei and dissolved gas content.

The formation of tip vortices results from the pressure difference between the suction side and pressure side near the tip of a finite-span lifting surface. Prediction of tip vortex cavitation follows the viscous scaling of McCormick (1962). He showed that the tip vortex core radius is scaled with the boundary layer thickness on the blade pressure surface, and this is Reynolds number-dependent. In addition, the circulation strength of the tip vortex is related to the lift generated on the lifting surface, or the lift coefficient, C_L . Then, the inception cavitation number has the form

$$\sigma_i = KC_L^2 Re^m \tag{12.18}$$

where K is a scale factor and m a constant depending on the boundary layer regime ($m = 2/5$ for a turbulent boundary layer). In axial pumps and ducted propellers, there is an additional effect due to the confinement gap between the blade tip and the shroud. Other forms of cavitation in concentrated vortices include hub vortex cavitation, which forms on the hub of a propeller or a hydraulic turbine.

Regions of free turbulent shear flow can contain many regions of concentrated vorticity (coherent structures). Shear flow cavitation can form in the high-speed regions of jets, wakes, and separated shear layers. Figure 12.9 shows the cavitating turbulent shear flow associated with a free shear layer. The inception of these flows is often difficult to predict, as it is strongly related to the details of the turbulent flow and nuclei distribution. A recent review of this type of cavitation is found in Arndt (2002).

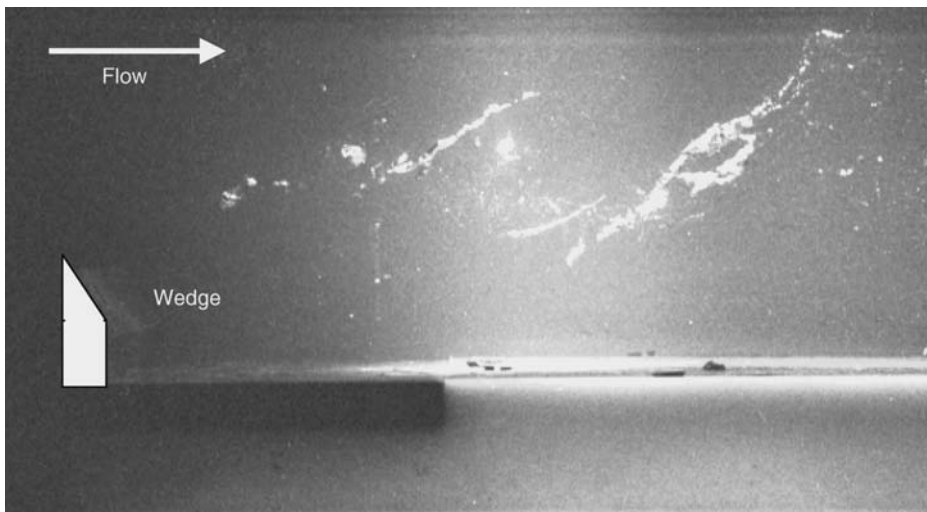


FIGURE 12.9 Cavitation inception in a turbulent shear flow formed downstream of a wedge.

12.1.7 Cavitation in Hydraulic Machinery

Cavitation can occur in both pumps and turbines. Bubble, sheet, and vortex cavitation have all been observed within these devices, and persistent cavitation can lead to reduction in efficiency, vibration, and erosion damage. The cavitation parameter in hydraulic machinery is usually referred to as the *Sigma Thoma number* and is given by

$$\sigma_T = \frac{H_{sv}}{H} \quad (12.19)$$

where H_{sv} is the net positive suction head (NPSH) and is given by

$$H_{sv} = \frac{1}{g} [P_0 - P_v + \frac{1}{2} \rho V_0^2] \quad (12.20)$$

with H being the *total head* under which the turbomachinery is operating. If the nondimensional flow rate $Q/2\pi\Omega D^3$ is held constant (analogous to the angle of attack in stationary hydrofoils), then one can write the Thoma number as

$$\sigma_T = \left(\frac{n_s}{S} \right)^{4/3} \quad (12.21)$$

where

$$n_s = \frac{\Omega Q^{1/2}}{(gH)^{3/4}} \quad (12.22)$$

and

$$S = \frac{\Omega Q^{1/2}}{(gH_{sv})^{3/4}} \quad (12.23)$$

Here n_s is the specific speed, while S is the suction specific speed; D is the impeller eye diameter (in m), Ω the rotational speed (in rad/sec), Q the flow rate (in m³/sec), and H and H_{sv} are (in m). The inlet of a pump or the exit of a turbine are regions of reduced pressure and increased potential for cavitation. Radial flow machines have relatively low specific speeds (high heads and low throughput) and axial machines usually possess high specific speeds (low heads and high throughputs). Knapp et al. (1970) suggest that the flow in radial machines be treated as flow in passages for cavitation studies, while axial flow machines can be geometrically developed, such that the flow is treated as that over cascade of hydrofoils. They also point out common factors and regions of increased cavitation potential in turbomachinery such as surface discontinuities, junctions between surfaces, gaps, unsteady flows and recirculating regions, and surface roughness effects.

The cavitation performance of turbomachinery is often presented as a plot of specific performance (e.g., specific head rise or specific power output) vs. Thoma number. As the Thoma number is decreased to the *inception Thoma number*, cavitation appears, but the performance of the turbomachinery may be only slightly affected. With decreasing Thoma number, cavitation becomes more developed, and the performance of the device will degrade. The *critical Thoma number* is reached when the performance is reduced by a defined fraction from the noncavitating case (e.g., 3%). Further reductions will lead to significant degradation of performance as the *breakdown Thoma number* is reached. Figure 12.10 shows the trends of typical pump performance curves vs. the Thoma number.

For marine propellers, the related cavitation number, σ , depends on the advance coefficient $J = U_\infty/(2\pi\Omega D)$ (analogous to the angle of attack in stationary hydrofoils), the thrust coefficient $K_T = T/\rho_l(2\pi\Omega)^2 D^4$, and the torque coefficient $K_T = Q/\rho_l(2\pi\Omega)^2 D^5$, where T is the thrust and Q the torque.

The degree to which cavitation is developed in turbomachinery can affect various parameters of the device. Incipient cavitation has the possibility of intermittent noise production. In partially developed cavitation, noise, structural vibrations, and damage to surfaces can occur. For fully developed cavitation, where

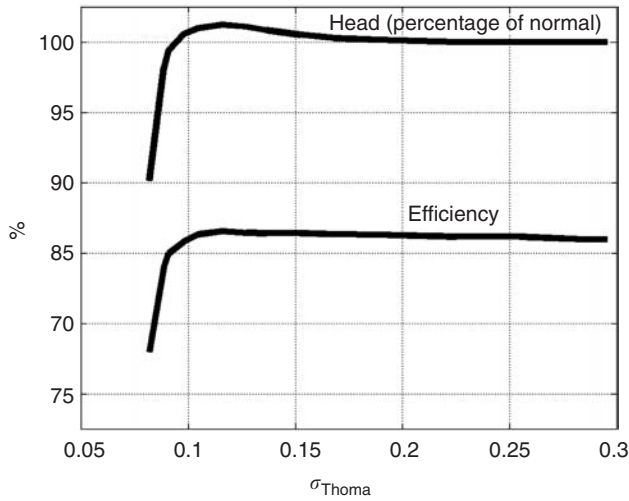


FIGURE 12.10 Typical pump performance curves at a constant flow rate as a function of the Thoma cavitation number.

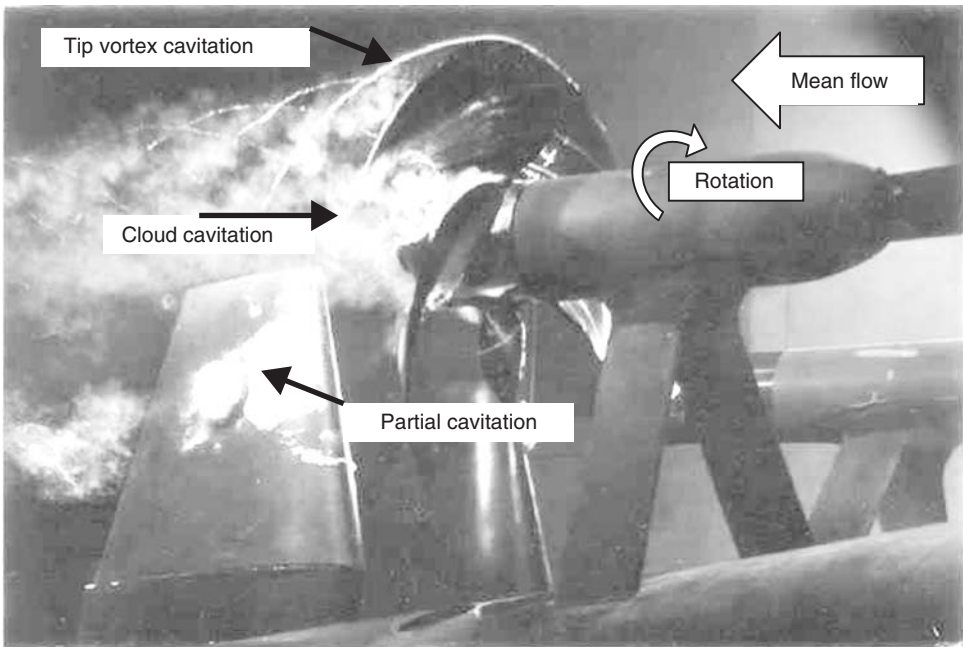


FIGURE 12.11 (Color insert follows page 13-40) Tip vortex cavitation, cloud cavitation, and partial attached cavitation on a model of a marine propeller. (Courtesy of Dr. Y.T. Shen, Naval Surface Warfare Center-Carderock Division.)

the volume of the cavities becomes significant, mechanical efficiency degradation, head loss, and damage are expected. Figure 12.11 shows vortex, sheet, and cloud cavitation on a model of a marine propeller.

Cavitation is a serious problem in hydraulic systems such as valves because of the potential for damage and vibration (Johnston et al., 1991; Jozsa et al., 1994; Porteiro et al., 1997; Carlson, 2001). Cavitation damage (pitting) has been observed in the liners of diesel engines, due to vibratory excitation of nuclei in the liquid (Zhou et al., 1982).

Cavitation can also occur in injector nozzles and fuel pumps in automotive applications. In fuel injection systems, as in diesel engines where the fuel speed is in excess of a 100 m/sec, cavitation can occur and cause flow disturbances that can improve atomization of the injected fuel (Badock et al., 1999; Einfeld, 2002; Yuan and Schnerr, 2003).

12.1.8 Cavitation in Biomedical Applications

In contrast with industrial and naval applications where cavitation is most often undesirable because of its erosion potential, the same damaging effects of collapsing bubbles have been implemented as a tool in biomedical applications, namely, surgery and lithotripsy. For example, pulsed ultrasound can be focused with precision on kidney or gall stones. An initial high-intensity pulse is often applied to generate cavitation nuclei, and then followed by less intense pulses to drive the bubble nuclei into transient cavitation, i.e., explosive bubble growth and violent implosion that lead to stone damage. The *in vivo* bubble dynamics are often quite complex. Clouds of bubbles are often created, and the bubble dynamics in these clouds are harder to predict than single bubble dynamics. For instance, the speed of sound in the cloud can be lower than the speed of sound in the liquid alone, and thus shock wave formation is more likely to occur. The shock can focus in the center of the cloud, leading to an improved lithotriptic effect over single bubble collapse (Brennen, 2003). Ultrasonic focusing can be also used in noninvasive surgery for pulverizing cancer tumors (*necrosis*). Bubble clouds often occur at the focal point. The cloud can backscatter the incoming acoustic pulses, causing increased absorption in the region upstream of the focal point, thus leading to the growth of the lesion (incised tissue) in a direction opposite to the incoming ultrasonic wave. This unintended effect and the resulting pulverization of blood and tissue into a paste have been observed to arrest bleeding in internal organs (*hemostasis*). Jet formation due to cavitation collapse is believed to puncture cell walls and improve drug delivery or allow targeted drug delivery to certain areas such as tumors. Bailey et al. (2003) provide a review of ultrasound in therapy.

Analogous to ultrasound focusing, very short pulses (pico- to nanoseconds) of infrared laser beams from Q-switched YAG (*Yttrium Aluminum Garnet*) or Ruby lasers are focused in laser-eye-surgery procedures into the intended area of the cornea to induce noninvasive, precise surgical effect. A vaporous cavitation bubble grows explosively at the laser focal volume, collapses violently, and generates a shock wave in what is known as optical cavitation, thus producing the surgical effect (Vogel et al., 1986). Additionally, microbubbles are used as contrast agents in ultrasonic imaging. Microbubbles existing in the area under investigation are excited by ultrasonic emissions from an emitting transducer. In response, the bubble volume will oscillate, and the acoustic emissions from the oscillatory motion of the bubble can then be picked by a receiving transducer.

12.1.9 Other Occurrences and Applications of Cavitation

The high pressures and temperatures associated with the collapse of cavitation bubbles have been used to initiate chemical reactions in a process known as *sonochemistry* (Riesz et al., 1990; Suslick, 1997; Beckett and Hua, 2001). These same extreme pressures and temperatures have also been exploited for environmental water purification (*aquasonolysis*) (Madge and Jensen, 2002; Lifka et al., 2003). The formation of radicals upon bubble collapse accelerates the degradation of contaminants through oxidization. Additionally, the shearing effect due to bubble oscillations can break up long-chain molecules. The production of cavitation bubbles near a metal surface can be used to mechanically work the surface in a process known as 'shot-less peening.' Cavitating jets can be used for this purpose (Soyma and Asahara, 1999).

Lastly, cavitation can occur in natural processes, for example, when the knuckles are cracked with a popping sound. Head trauma has been associated with cavitation when there is a sudden impact of the cranium (Goldsmith, 2001). *Alpheus heterochaelis* (the "snapping shrimp") uses sound produced by a cavitating jet to stun nearby prey (Versluis et al., 2000). Also, the maximum height of trees may be limited by cavitation during the transpiration of water (Koch et al., 2004).

12.2 Bubble Physics

Y. Matsumoto

12.2.1 Single Spherical Bubble Dynamics

Bubble motion from a surrounding pressure variation is one of the most fundamental gas–liquid two-phase flow problems and is closely related to the macroscale behavior of two-phase flows, the performance of cavitating fluid machinery, and medical ultrasound applications. Of great significance to the analysis of such problems is the prediction of the radial motion of a bubble, namely, its growth and collapse. The bubble motion can be solved exactly by the integration of the conservation equations for mass, momentum, and energy for the gas phase inside the bubble and the liquid phase outside the bubble. Since it is not easy to solve the complete equations in many cases, a polytropic change (isothermal or adiabatic) is assumed for the gas inside the bubble. However, it is well known that the thermal phenomena inside the bubble can have a significant influence on the bubble motion (Chapman and Plesset, 1971; Nigmatulin, 1981; Prosperetti et al., 1988; Kamath and Prosperetti, 1989; Prosperetti, 1991; Takemura and Matsumoto, 1994; Kameda and Matsumoto, 1999). To account for thermal effects, a reduced-order model has been introduced using ordinary differential equations (ODEs), instead of the full conservation equations for mass, momentum, and energy.

12.2.1.1 Direct Numerical Simulation (DNS) of a Single Bubble

In a single-phase flow, the conservation equations of mass, momentum, and energy are described by partial differential equations (PDEs) if the flow is treated as a continuum. In multiphase flow, these conservation equations are not described by the same set of PDEs, because there are discontinuities between the phases. However, it is possible to describe the governing equations by PDEs in each phase and connect the two phases at the interfaces. The governing equations and boundary conditions at a bubble interface were described by Hsieh (1965). Matsumoto and Takemura (1994) simulated the collapsing bubble motion numerically by using the full equations for mass, momentum, and energy in the gas and liquid phases. Takemura and Matsumoto (1994) calculated the bubble growth caused by an external pressure reduction by taking into account internal phenomena such as thermal and mass diffusion with mist formation due to homogeneous condensation.

12.2.1.1.1 Governing Equations

12.2.1.1.1.1 Gas Phase

1. The mass conservation equations:

- For the gas mixture inside the bubble,

$$\frac{\partial \rho_m}{\partial t} + \frac{1}{r^2} \frac{\partial}{\partial r} (r^2 \rho_m u_{mg}) = 0 \tag{12.24}$$

where $\rho_m = \rho_n + \rho_v + \rho_{lg}$, $\rho_m u_{mg} = \rho_n u_n + \rho_v u_v + \rho_{lg} u_{mg}$, (subscript g denotes the gas phase, l the liquid phase, n the noncondensable gas, v the vapor in the gas phase, and m the mixture condition; also, the subscript lg denotes the mist inside the bubble and gl the noncondensable gas in the liquid phase), ρ is the density, r the coordinate in the radial direction and u the radial velocity.

- For the vapor

$$\frac{\partial \rho_v}{\partial t} + \frac{1}{r^2} \frac{\partial}{\partial r} \left\{ r^2 \left(\rho_v u_{mg} - \rho_{mg} D_{mg} \frac{\partial c_v}{\partial r} \right) \right\} = -\Gamma \tag{12.25}$$

where $\rho_{mg} = \rho_n + \rho_v$, $c_v = \rho_v / \rho_{mg}$. D is the diffusion coefficient, c the concentration, and Γ the mass of vapor which changes to mist per unit volume per unit time.

- For the number density distribution function of droplets (Frenkel, 1946),

$$\frac{\partial n(a)}{\partial t} + \frac{1}{r^2} \frac{\partial}{\partial r} (r^2 n(a) u_{mg}) + \frac{\partial (n(a) I_a)}{\partial a} = 0 \tag{12.26}$$

where $n(a)$ is number density distribution function vs. radius of the droplet. I_a is the growth rate of the droplet radius and is given by

$$I_a = \alpha(p_v - p_s) / (\rho_l \sqrt{2\pi \mathfrak{R}_v T}) \quad (12.27)$$

where α is the accommodation factor whose value is estimated to be 0.4 (Hatamiya and Tanaka, 1986), p the pressure, subscript s denotes the saturated condition, \mathfrak{R} the gas constant and T the temperature. Critical radius r^* and the nucleation rate J are given as

$$r^* = 2\sigma / \rho_l \mathfrak{R}_v T \ln(p_v / p_s) \quad (12.28)$$

$$J = \left(\frac{2\sigma m}{\pi} \right)^{1/2} \frac{1}{\rho_l} \left(\frac{p_v}{kT} \right)^2 \exp\left(-\frac{4\pi r^{*2} \sigma}{3kT} \right) \quad (12.29)$$

where σ is the surface tension, m the molecular unit mass, and k the Boltzmann constant. The parameter Γ in Eq. (12.25) is defined as

$$\Gamma = \frac{d}{dt} \int \frac{4}{3} \pi \rho_l a^3 n(a) da \quad (12.30)$$

2. The momentum conservation equation for the mass inside of the bubble is

$$\begin{aligned} & \frac{\partial}{\partial t} (\rho_m u_{mg}) + \frac{1}{r^2} \frac{\partial}{\partial r} (r^2 \rho_m u_{mg} u_{mg}) \\ &= -\frac{\partial p_{mg}}{\partial r} + \frac{4}{3} \frac{\mu_{mg}}{r} \left(\frac{\partial u_{mg}}{\partial r} - \frac{u_{mg}}{r} \right) + \frac{4}{3} \frac{1}{r^2} \frac{\partial}{\partial r} \left[r^2 \mu_{mg} \left(\frac{\partial u_{mg}}{\partial r} - \frac{u_{mg}}{r} \right) \right] \end{aligned} \quad (12.31)$$

where μ is the viscosity.

3. The energy conservation equation for the mass inside of the bubble is

$$\begin{aligned} & \frac{\partial}{\partial t} (\rho_n e_n + \rho_v e_v + \rho_{lg} e_{lg}) + \frac{1}{r^2} \frac{\partial}{\partial r} \{ r^2 (\rho_n e_n u_n + \rho_v e_v u_v + \rho_{lg} e_{lg} u_{mg}) \} \\ &= -\frac{P_{mg}}{r^2} \frac{\partial}{\partial r} (r^2 u_{mg}) + \frac{1}{r^2} \frac{\partial}{\partial r} \left(r^2 \lambda_{mg} \frac{\partial T}{\partial r} \right) + \frac{4}{3} \mu_{mg} \left(\frac{\partial u_{mg}}{\partial r} - \frac{u_{mg}}{r} \right)^2 \end{aligned} \quad (12.32)$$

where e is the specific internal energy and λ is the thermal conductivity.

4. The equation of state is

$$p_n = \rho_n \mathfrak{R}_n T \quad (12.33)$$

and

$$p_v = \rho_v \mathfrak{R}_v T \quad (12.34)$$

12.2.1.1.1.2 Liquid Phase

1. The mass conservation equations:

- For mixture of the liquid,

$$\frac{\partial \rho_{ml}}{\partial t} + \frac{1}{r^2} \frac{\partial}{\partial r} (r^2 \rho_{ml} u_{ml}) = 0 \quad (12.35)$$

where $\rho_{ml} = \rho_l + \rho_{gl}$, $\rho_{ml} u_{ml} = \rho_l u_l + \rho_{gl} u_{gl}$.

- For the noncondensable gas in the liquid,

$$\frac{\partial \rho_{gl}}{\partial t} + \frac{1}{r^2} \frac{\partial}{\partial r} \left\{ r^2 \left(\rho_{gl} u_{ml} - \rho_{ml} D_{gl} \frac{\partial c_{gl}}{\partial r} \right) \right\} = 0 \quad (12.36)$$

where $c_{gl} = \rho_{gl}/\rho_{ml}$

- The momentum conservation equation for the liquid phase is

$$\begin{aligned} & \frac{\partial}{\partial t} (\rho_{ml} u_{ml}) + \frac{1}{r^2} \frac{\partial}{\partial r} (r^2 \rho_{ml} u_{ml} u_{ml}) \\ &= -\frac{\partial p_1}{\partial r} + \frac{4}{3} \frac{\mu_{ml}}{r} \left(\frac{\partial u_{ml}}{\partial r} - \frac{u_{ml}}{r} \right) + \frac{4}{3} \frac{1}{r^2} \frac{\partial}{\partial r} \left\{ r^2 \mu_{ml} \left(\frac{\partial u_{ml}}{\partial r} - \frac{u_{ml}}{r} \right) \right\} \end{aligned} \quad (12.37)$$

- The conservation equation of energy for the liquid is

$$\begin{aligned} & \frac{\partial}{\partial t} (\rho_1 e_1) + \frac{1}{r^2} \frac{\partial}{\partial r} \{ r^2 \rho_1 e_1 u_1 \} \\ &= -\frac{p_1}{r^2} \frac{\partial}{\partial r} (r^2 u_1) + \frac{1}{r^2} \frac{\partial}{\partial r} \left(r^2 \lambda_1 \frac{\partial T}{\partial r} \right) + \frac{4}{3} \mu_1 \left(\frac{\partial u_1}{\partial r} - \frac{u_1}{r} \right)^2 \end{aligned} \quad (12.38)$$

- The Tait equation is applied for the equations of state in the following form:

$$\frac{p + B}{p_\infty + B} = \left(\frac{\rho}{\rho_\infty} \right)^n \quad (12.39)$$

where $B = 304.9$ MPa and $n = 7.15$ in the case where the liquid is water.

12.2.1.1.2 Boundary Conditions at the Gas-Liquid Interface

- The boundary conditions for mass conservation follow

The mass flux due to phase change \dot{M}_v is expressed by the following equation:

$$\dot{M}_v = \alpha (p_s - p_v) / (\sqrt{2\pi} \dot{\lambda}_v T_w) \quad (12.40)$$

where the subscript w denotes the bubble wall. The concentrations and gradients of vapor and noncondensable gas in the liquid at the interface are related to \dot{M}_v and \dot{M}_n by the following equations:

$$\dot{M}_v = \frac{D_{mg} \rho_{mgw} (\partial c_v / \partial r)_w}{1 - c_{vw}} + \frac{c_{vw}}{1 - c_{vw}} \dot{M}_n \quad (12.41)$$

$$\dot{M}_n = \frac{D_{gl} \rho_{mlw} (\partial c_{gl} / \partial r)_w}{1 - c_{glw}} + \frac{c_{glw}}{1 - c_{glw}} (\dot{M}_v + \dot{M}_{lg}) \quad (12.42)$$

\dot{M}_{lg} is

$$\dot{M}_{lg} = \begin{cases} 0, & \dot{R} - u_{mg} \geq 0 \\ \rho_{lg} (\dot{R} - u_{mg}), & \dot{R} - u_{mg} < 0 \end{cases} \quad (12.43)$$

where R is the bubble radius and the dot denotes the derivative with respect to time.

- The boundary condition for momentum conservation is

$$-p_{1w} + \frac{4}{3} \mu_1 \left(\frac{\partial u_1}{\partial r} - \frac{u_1}{r} \right)_w + \{ \rho_{mg} (u_{mg} - \dot{R}) (u_{mg} - u_1) \}_w \quad (12.44)$$

$$= -p_{mgw} + \frac{2\sigma}{R} + \frac{4}{3} \mu_{mg} \left(\frac{\partial u_{mg}}{\partial r} - \frac{u_{mg}}{r} \right)_w$$

3. The boundary condition for energy conservation is

$$\begin{aligned} & \lambda_{ml} \left(\frac{\partial T}{\partial r} \right)_w - \lambda_{mg} \left(\frac{\partial T}{\partial r} \right)_w + \frac{5}{2} (\mathfrak{R}_v - \mathfrak{R}_n) T_w \{ (1 - c_{vw}) M_v - c_{vw} M_n \} \\ & = M_v \left\{ L + \frac{4}{3} \frac{\mu_l}{\rho_{lw}} \left(\frac{\partial u_l}{\partial r} - \frac{u_l}{r} \right)_w - \frac{4}{3} \frac{\mu_{mg}}{\rho_{mg}} \left(\frac{\partial u_{mg}}{\partial r} - \frac{u_{mg}}{r} \right)_w \right\} \\ & + \frac{1}{2} M_v \{ (\dot{R} - u_{lw})^2 - (\dot{R} - u_{mgw})^2 \} \end{aligned} \quad (12.45)$$

where L is the latent heat.

The temperature and concentration at the wall of the noncondensable gas in the liquid are

$$T_{lw} = T_{gw} \quad (12.46)$$

$$c_{glw} = H_n p_{nw} \quad (12.47)$$

where H_n is Henry's constant.

12.2.1.1.3 Pressure and Temperature Distribution Inside and Outside a Bubble

Figure 12.12 and Figure 12.13 show the time histories of the pressure and temperature distribution inside and outside a bubble and Table 12.1 lists the computational conditions. The pressure surrounding the bubble increases from 10 to 100 kPa in a stepwise manner. When the bubble motion starts, the expansion wave propagates outside and the pressure distribution is formed in the liquid phase according to the motion of the bubble interface. At the rebound of the bubble, the pressure peak appears at some distance from the interface and the pressure propagates outward. The pressure inside the bubble is uniform because the speed of sound is much higher than the velocity of the interface. In Figure 12.13, the temperature distribution is uniform in the liquid phase because of the large heat capacity of the liquid. On the other hand, a nonuniform distribution appears in the gas phase, because the temperature rises during the collapse phase as the heat transfers to the liquid at the interface. After rebounding, the temperature inside the bubble decreases to a value less than its initial value. The internal energy of the gas is reduced by thermal diffusion the heat is deposited and diffuses around the bubble when the gradient of the temperature is negative.

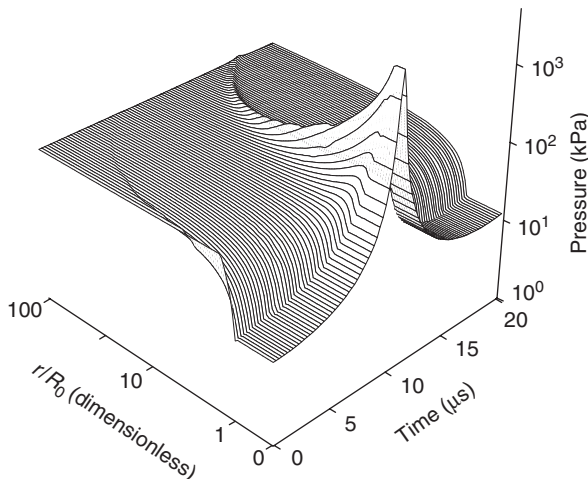


FIGURE 12.12 Time history of the pressure distribution inside and outside a nitrogen bubble.

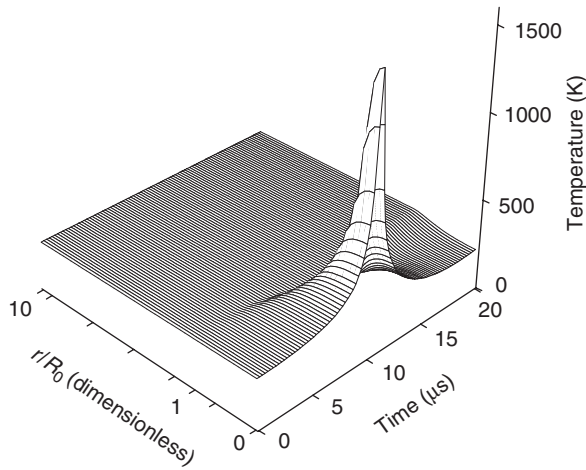


FIGURE 12.13 Time history of the temperature distribution inside and outside a nitrogen bubble.

TABLE 12.1 Computational Conditions

Gas Phase	Nitrogen
Liquid phase	Water
Initial bubble radius, R_{b0}	100 μm
Initial ambient pressure, p_0	10 kPa
Step increase of ambient pressure	10–100 kPa
Initial temperature	293 K

12.2.1.1.4 Effect of Thermal Diffusion on the Bubble Motion

Figure 12.14 shows the behavior of the bubbles with different gases inside them under the same conditions as Table 12.1, except for the gas species. Table 12.2 shows the properties of the internal gas. The Peclet number Pe is defined as $Pe = \rho_0 c_{p0} R_0^2 \omega_N / \lambda$, where c_{p0} is the isobaric specific heat and ω_N denotes the natural angular frequency of a bubble, assuming adiabatic changes. Nondimensional scales R^* and t^* are defined as $R^* = R/R_0$ and $t^* = t/R_0 \sqrt{\rho_{l\infty}/p_{l0}}$, respectively. When the bubble radius reaches a maximum or minimum value, the pressure has a minimum or maximum value, respectively. The mean temperature (defined as $T_{\text{mean}} = \int_0^R r^2 \rho_g T_g dr / \int_0^R r^2 \rho_g dr$) has a maximum at almost the same time as the bubble radius reaches a minimum. However, it does not have a minimum when the bubble radius reaches a maximum. This is because the heat input has positive or negative values despite the work received from the liquid phase, and has a time lag. Therefore, the sum of the work that the bubble receives per unit time from the liquid phase and the heat input becomes zero before the radius takes the minimum or the maximum value. This is the minimum or the maximum point of the temperature. Upon collapse, the work received from the liquid per unit time decreases so rapidly that the temperature takes the maximum at almost the same time as the radius reaches the minimum value. On the other hand, upon expansion, the bubble supplies work to the liquid phase and the heat flows outward from the gas phase due to the temperature distribution developed during the collapse phase. Therefore, the temperature decreases rapidly and the gradient of the temperature at the gas–liquid interface becomes positive. Subsequently, the heat flows inward from the liquid phase and the mean temperature takes the minimum value when the sum of the work received from the liquid per unit time and the heat input becomes equal to zero.

In the case of a helium bubble (when Pe is relatively small), the heat transfers outward through the bubble wall quickly and the bubble shrinks to a smaller size during the collapse period. The temperature inside the bubble does not become so high. In the case of xenon (where Pe is large), the heat input and

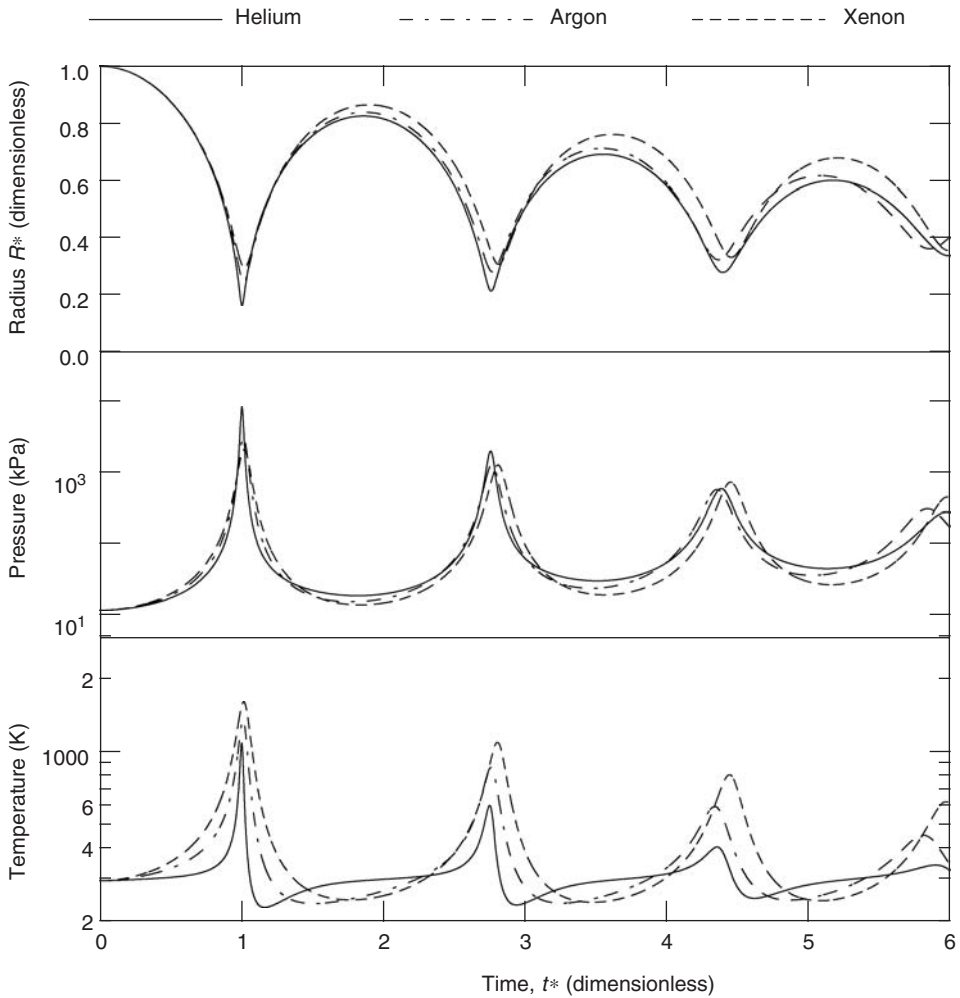


FIGURE 12.14 Time histories of the bubble radius, pressure at the bubble center and mean temperature inside the bubble with different gases.

TABLE 12.2 Properties of the Internal Gas (100 kPa, 293 K)

Gas	Helium	Argon	Xenon
Thermal conductivity (mW/m/K)	153.5	17.4	5.4
Peclet number, Pe	12.3	109.1	347.7

output are not large, so the bubble cannot shrink as much and the temperature inside the bubble reaches higher values.

12.2.1.1.5 Bubble Motion and Mist Formation Inside a Bubble

Figure 12.15 shows the time histories of the radius, mean temperature, and mean density of mist (upper panel) and the distributions of the temperature, concentration of vapor, and density of mist inside the bubble at several points (lower panel) in the case when the surrounding pressure has a stepwise decrease from 100 to 5 kPa. The other computational conditions are the same as listed in Table 12.1. The lower panel shows the distributions at the times from A to H indicated in the upper panel. In the figure, A to E show the growth period and those from F to H show the collapse period. The abscissa is the

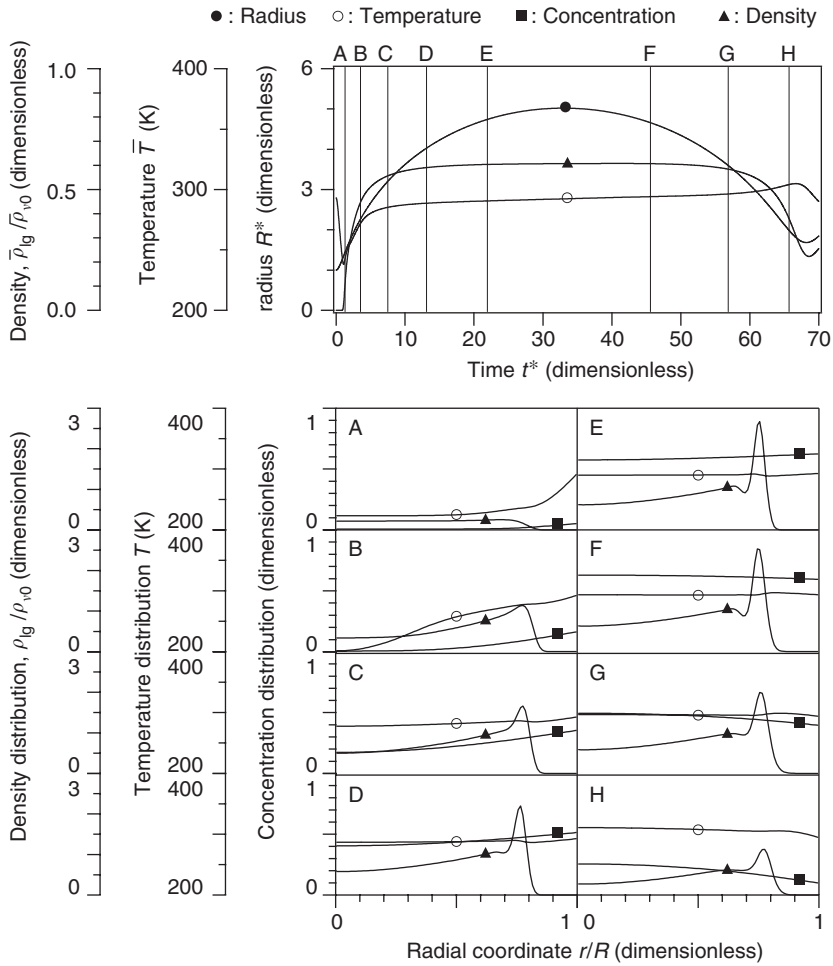


FIGURE 12.15 Time histories of the bubble radius, mean temperature and mean density of the mist inside the bubble (upper panel), and the distributions of the temperature, concentration of the vapor and density of the mist inside the bubble at several points (lower panel) in the case of a nitrogen bubble.

nondimensional distance, in which 0 identifies the bubble center and 1 corresponds to the bubble wall. As the bubble expands, the temperature inside the bubble decreases at the initial stage and then recovers to the surrounding temperature due to the latent heat released by the formation and growth of mist and the heat penetration from the bubble wall. After that, the temperature remains almost constant except during the rebounds. The mean density of the mist increases at the beginning of the expansion, and the formation and growth of the mist exerts an effect on the bubble motion at that time. After the temperature inside the bubble has become almost constant, the mean density of the mist is also nearly constant and the total mass of the mist increases in proportion to the volume of the bubble. The temperature inside the bubble does not become so high at the end of the collapse, because energy from the outside is consumed by the evaporation of the mist. It is evident that distributions of temperature, vapor concentration and density of the mist do occur and the spatial distribution of the mist density is rather complicated due to the slow diffusion process.

12.2.1.2 Reduced-Order Modeling of a Single Bubble

The single bubble motion can be simulated in detail, solving the full equations for the mass, momentum, and energy as outlined in the previous section. However, it is computationally expensive to calculate all

equations when many bubbles are treated, such as in bubbly flows. Many researchers have developed reduced-order models for the liquid and gas phase phenomena.

12.2.1.2.1 Effect of Compressibility in the Liquid Phase

If the liquid is assumed to be incompressible, the momentum conservation equation can be easily integrated from the bubble wall to infinity and the boundary condition for the pressure can be taken into account. Rayleigh (1917) first considered bubble collapse in a liquid, assuming a vacuum cavity. The effect of the surface tension and viscosity in the liquid was taken into account later, and the Rayleigh–Plesset equation (1949) was defined as:

$$R\ddot{R} + \frac{3}{2}\dot{R}^2 = \frac{1}{\rho_l} \left\{ p_b - p_\infty - 4\mu_l \frac{\dot{R}}{R} - \frac{2\sigma}{R} \right\} \quad (12.48)$$

where p_b is the pressure inside the bubble, p_∞ the ambient pressure, and σ the surface tension of the liquid. When the velocity of the bubble wall becomes comparable to the speed of sound of the liquid, the compressibility of the liquid has to be considered (Keller and Kolodner, 1956). The model with a first-order correction for compressibility is often used

$$\left(1 - \frac{\dot{R}}{c}\right)R\ddot{R} + \frac{3}{2}\left(1 - \frac{\dot{R}}{3c}\right)\dot{R}^2 = \left(1 + \frac{\dot{R}}{c}\right)\frac{1}{\rho_l} \{p_b - p_\infty - p_c(t + R/c)\} + \frac{R}{\rho_l c} \dot{p}_b \quad (12.49)$$

where c is the speed of sound and $p_c(t)$ the variable part of the pressure in the liquid at the location of the bubble center in the absence of the bubble.

A nonequilibrium phase change, such as evaporation and condensation during the collapse phase, is discussed next (Tomita and Shima, 1979; Fujikawa and Akamatsu, 1980). Fujikawa and Akamatsu (1980) derived the equations, which take into account the effects of nonequilibrium behavior at the bubble wall on the bubble motion:

$$R\ddot{R} \left(1 - 2\frac{\dot{R}}{c} + \frac{\dot{m}}{\rho_l c}\right) + \frac{3}{2}\dot{R}^2 \left(1 + \frac{4}{3}\frac{\dot{m}}{\rho_l c} - \frac{4}{3}\frac{\dot{R}}{c}\right) - \frac{\dot{m}R}{\rho_l} \left(1 - 2\frac{\dot{R}}{c} + \frac{\dot{m}}{\rho_l c}\right) \quad (12.50)$$

$$- \frac{\dot{m}}{\rho_l} \left(\dot{R} + \frac{\dot{m}}{2\rho_l}\right) + \frac{p_\infty - p_{l,r=R}}{\rho_l} - \frac{R\dot{p}_{l,r=R}}{\rho_l c} = 0$$

and

$$p_{l,r=R_b} = p_v + p_g - \frac{\dot{m}^2(\rho_{vi} + \rho_{gi} - \rho_l)}{\rho_l(\rho_{vi} + \rho_{gi})} - 2\frac{\sigma}{R} - 4\frac{\mu_l}{R} \left(\dot{R} - \frac{\dot{m}}{\rho_l}\right) \quad (12.51)$$

where \dot{m} is the mass flux caused by the phase change, and ρ_{vi} and ρ_{gi} the density of the vapor and non-condensable gas at the bubble interface, respectively. The nonequilibrium behavior may result in additional cushioning of the bubble collapse.

12.2.1.2.2 Effect of Thermal Phenomena on the Gas Phase

The temperature gradient at the bubble wall is used by some researchers instead of calculating the entire temperature distribution inside a bubble. Prosperetti (1991) investigated the thermal diffusive effects and Storey and Szeri (2001) suggested a model in which the bubble interior is assumed to be isothermal when the bubble radius is larger than the equilibrium value, and to be adiabatic when the radius is smaller. Shimada et al. (2000) investigated the model which assumes a homogeneous heat distribution inside a bubble. Toegel et al. (2000) estimated the penetration depth of mass and heat diffusion, and calculated an approximate energy flux at the bubble wall. Preston et al. (2003) considered a temperature gradient based on a linear analysis (Prosperetti et al., 1988).

Figure 12.16 shows a comparison of the time history of bubble radii between the isothermal model, the adiabatic model, the model, and DNS (Direct Numerical Simulation). In this case, the model of Matsumoto and Beylich (1985) is applied to the governing equations and boundary conditions for the bubble motion, and that developed by Preston et al. (2003) is employed for the temperature gradient at the bubble wall. The gas inside the bubble is air and the initial bubble radius is 10 μm . The other calculation conditions are the

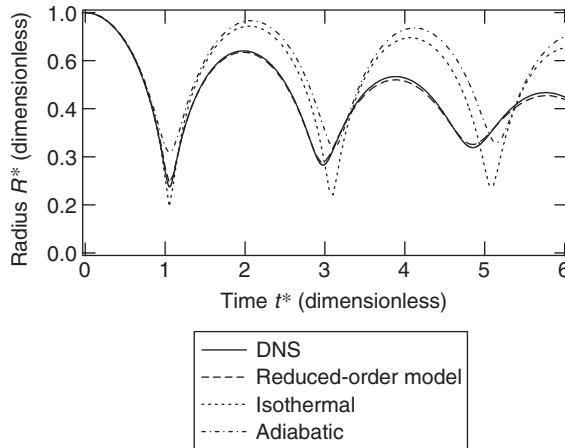


FIGURE 12.16 Comparison of time histories of radii between DNS and reduced-order model.

same as in Table 12.1. Compared with the DNS, the amplitudes of the bubble motions in the case of isothermal and adiabatic model are too large. In the collapse phase, the bubble radius in the case of the isothermal model is too small because the temperature inside the bubble is assumed to be isothermal and the internal energy of the gas phase does not become high. The bubble in the case of the adiabatic model cannot shrink as much as that of DNS, because the heat inside the bubble does not transfer to the liquid phase. On the other hand, the reduced-order model can capture the DNS-predicted bubble motion well. It is reasonable and efficient to apply such a reduced-order model for the computation of a multiple bubble system.

12.2.1.3 Nonlinear Behavior and Acoustic Turbulence

12.2.1.3.1 Nonlinear Oscillation of a Microbubble

To model the dynamics of the bubble in an oscillating field, it is important to take into account the nonlinear phenomena. Many researchers have investigated this topic. Recently, the nonlinear behavior of a microbubble in an ultrasound field has been used for medical ultrasound imaging with microbubble contrast agents. The nonlinear effect was investigated by many researchers (Esche, 1952; Noltingk and Neppiras, 1950; Neppiras and Noltingk, 1951; Flynn, 1964; Borotnikova and Soloukin, 1964; Neppiras, 1969). Lauterborn (1976) simulated the frequency response curve of a bubble (Figure 12.17). This curve shows the amplitudes of the radial oscillation of a bubble of radius 1.0 μm in water at a mean ambient pressure of 1 bar (100 kPa) plotted as a function of f/f_N for various amplitudes of oscillation where f is a driving frequency, f_N is the natural frequency of the bubble, R_n is the radius at rest, and R_{max} is the maximum radius. The numbers above the peaks indicate the order of the resonance, n/m , and the case $m = 1$ with $n = 2, 3, 4$ denoting the higher harmonics and the case $m = 2$ with $n = 1$ denoting the subharmonics. The equations that account for the compressibility of the liquid were employed in this calculation. As the amplitude of the ambient pressure grows larger, the superharmonic and subharmonic peak responses become greater. As the pressure amplitude increases, these peaks shift to lower frequencies. The influence of the internal phenomena on this nonlinear behavior has also been investigated (Matsumoto and Watanabe, 1989).

12.2.1.3.2 Acoustic Turbulence from a Microbubble

The bubble motion in an ultrasound field shows chaotic behavior due to the nonlinearity of the oscillation when the sound amplitude is increased. This phenomenon is called “acoustic turbulence” (Lauterborn, 1989). The bifurcation and chaotic behaviors of bubble oscillation have been calculated by assuming that the interior gas obeys a polytropic relationship, which neglects the thermal dissipation (Lauterborn, 1987).

Figure 12.18 shows the time history of the power spectrum of acoustic pressure from an air microbubble. The bubble motion is simulated when the ambient ultrasound pressure increases linearly from 0 to 1 MPa in 5000 cycles. The initial bubble radius is 2.0 μm and the ultrasound frequency is 1 MHz. When the ultrasound

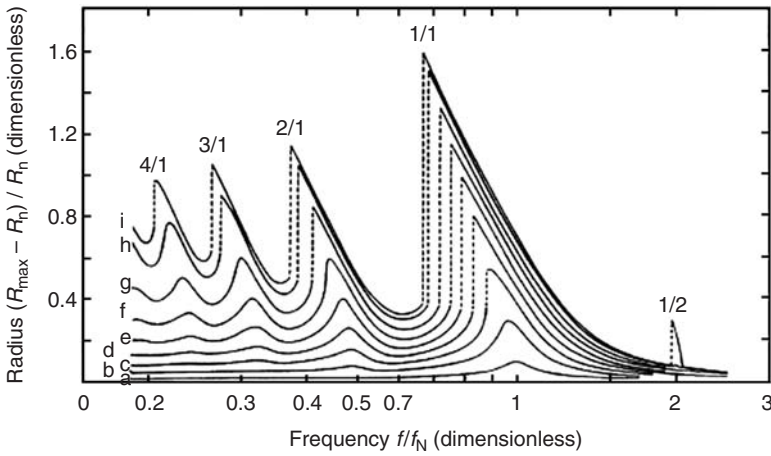


FIGURE 12.17 Numerically computed amplitudes of radial oscillation of a bubble (a) 0.1 (b) 0.3 (c) 0.5 (d) 0.7 (e) 0.9 (f) 1.1 (g) 1.3 (h) 1.5 (i) 1.6 bar. (Adapted from Lauterborn, W., *J. Acoust. Soc. Am.*, 59, 283–293, 1976. With permission.)

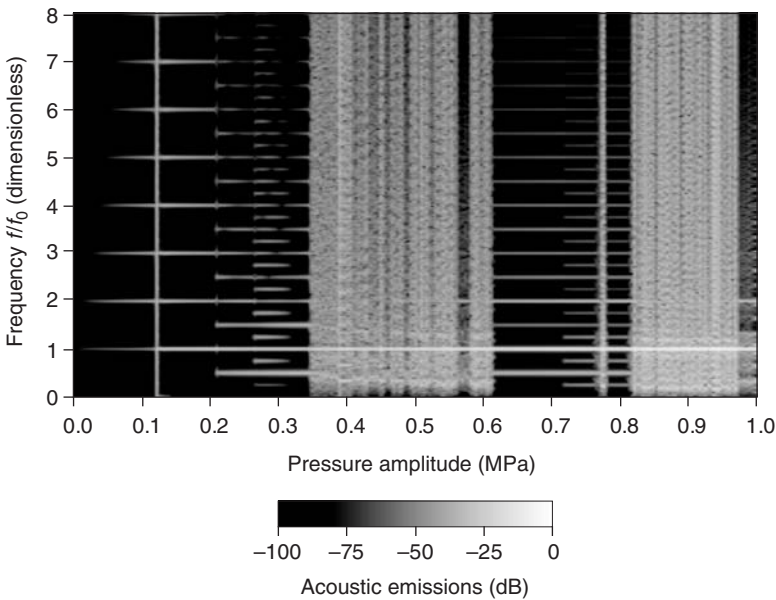


FIGURE 12.18 Power spectrum of the acoustic pressure from an air microbubble.

driving starts, the bubble begins to oscillate in the fundamental mode. As ultrasound amplitude increases, the emitted acoustic pressure increases and it gradually involves the nonlinearity associated with the higher harmonic modes. Bifurcation occurs and the 1/2 harmonic modes begin to appear in each higher harmonic mode, when the pressure amplitude approaches 200 kPa. A further bifurcation appears and the 1/4 harmonic modes emerge at 250 kPa. Thereafter the bubble oscillation becomes chaotic. When the ambient ultrasound pressure reaches about 600 kPa, nonchaotic oscillations occur for a short time, and then the bubble motion returns to chaotic behavior. In this case, the subharmonic modes are barely visible at this relatively low forcing amplitude.

12.2.2 Bubble Deformation and Fragmentation Due to the Collapse

It is well known that the spherical shape of a collapsing bubble is unstable and the shape assume the form of a microjet, which may induce bubble fission. The spherical shape of the bubble is maintained by the surface tension and the viscous force acting on the bubble surface. Deformation will occur when the characteristic anisotropy in the fluid forces overcomes the surface tension and the viscous force. The stability with regard to nonspherical disturbances has been investigated from a hydrodynamic point of view by Birkhoff (1954), Plesset and Mitchell (1956), Brennen (1995, 2002), and Hao and Prosperetti (1999), among others. These analyses essentially examine the spherical equivalent of the Rayleigh–Taylor instability. If the inertia of the gas in the bubble is assumed to be negligible and the viscosity is small enough, then the amplitude, $a_n(t)$, of a spherical harmonic distortion of order n ($n > 1$) will be governed by the equation

$$\ddot{a}_n + \left[3 \frac{\dot{R}}{R} + 2(n+2)(2n+1) \frac{\nu}{R^2} \right] \dot{a}_n + (n-1) \left[- \frac{\ddot{R}}{R} + (n+1)(n+2) \frac{\sigma}{\rho R^3} + 2(n+2) \frac{\nu \dot{R}}{R^3} \right] a_n = 0 \tag{12.52}$$

where ν is the kinetic viscosity. The coefficients are determined by the dynamic behavior of the bubble radius, $R(t)$. It can be seen from this equation that the most unstable conditions occur when $\dot{R} < 0$ and $\ddot{R} \geq 0$. These conditions will be reached just before the rebound of a collapsing bubble. The most stable conditions take place when $\dot{R} > 0$ and $\ddot{R} < 0$, which is the case for growing bubbles as they approach their maximum size.

The fact that the coefficients in Eq. (12.52) are not constant in time results in differences from the Rayleigh–Taylor instability for a plane boundary. The coefficient of a is not very different from the case of the plane boundary in the sense that instability is promoted when $\ddot{R} > 0$, while surface tension and viscosity have stabilizing effects. The primary difference is caused by the \dot{a} term. As the bubble grows, the wavelength on the surface increases, and hence the growth of the wave amplitude is lessened. The reverse occurs during collapse. It is easily found from Eq. (12.52) that the initial acceleration phase of bubble growth, in which $\ddot{R} \geq 0$ is unstable with respect to spherical harmonic perturbations of fairly high order, n . However, the remainder of the growth phase during which $\dot{R} > 0$, $\ddot{R} < 0$ is stable with regard to all spherical harmonic perturbations. So, the bubble in the acceleration phase is usually considered to be stable in cavitation experiments. This could be caused either by the brief acceleration phase or the greater stabilizing effect of surface tension in smaller bubbles. On the other hand, it is clear from the theory that the bubble may become highly unstable with respect to nonspherical disturbances during the rebound phase because \ddot{R} reaches very large positive values. The instability appears in several different ways depending on the violence of the collapse and the presence of other boundaries. The instability of the collapsing bubble has been investigated by many researchers (Blake and Gibson, 1987; Tomita and Shima, 1990; Lindau and Lauterborn, 2003). Cavitation bubbles that collapse to a size an order of magnitude smaller than their maximum size inevitably emerge from that collapse as a cloud of smaller bubbles rather than as a single vapor bubble. This fragmentation could be caused by a single micro jet as shown in Figure 12.19, or it could be due to a spherical harmonic disturbance of higher order. The behavior of collapsing bubbles that are filled with a noncondensable gas corresponding with the lower values of \ddot{R} and the instability could be weaker resulting in spherical stability. Thus, acoustically excited cavitation bubbles that contain a substantial amount of gas often remain spherical during their rebound phase. In other instances, the instability is sufficient to cause fragmentation. Several examples of fragmented and highly distorted bubbles emerging from the rebound phase are shown in Figure 12.20. It shows the dynamic behavior of bubble growth and collapse with the sequential decrease and increase of the surrounding pressure. The first pressure reduction creates cavitation bubbles from a heated thin wire at 2.44 msec, and the bubbles grow under the ambient pressure whose value is almost the same as that of the saturated vapor pressure of the bulk temperature. At 4.27 msec the pressure increases and the bubbles begin to shrink. Large fluctuations of the pressure are observed due to

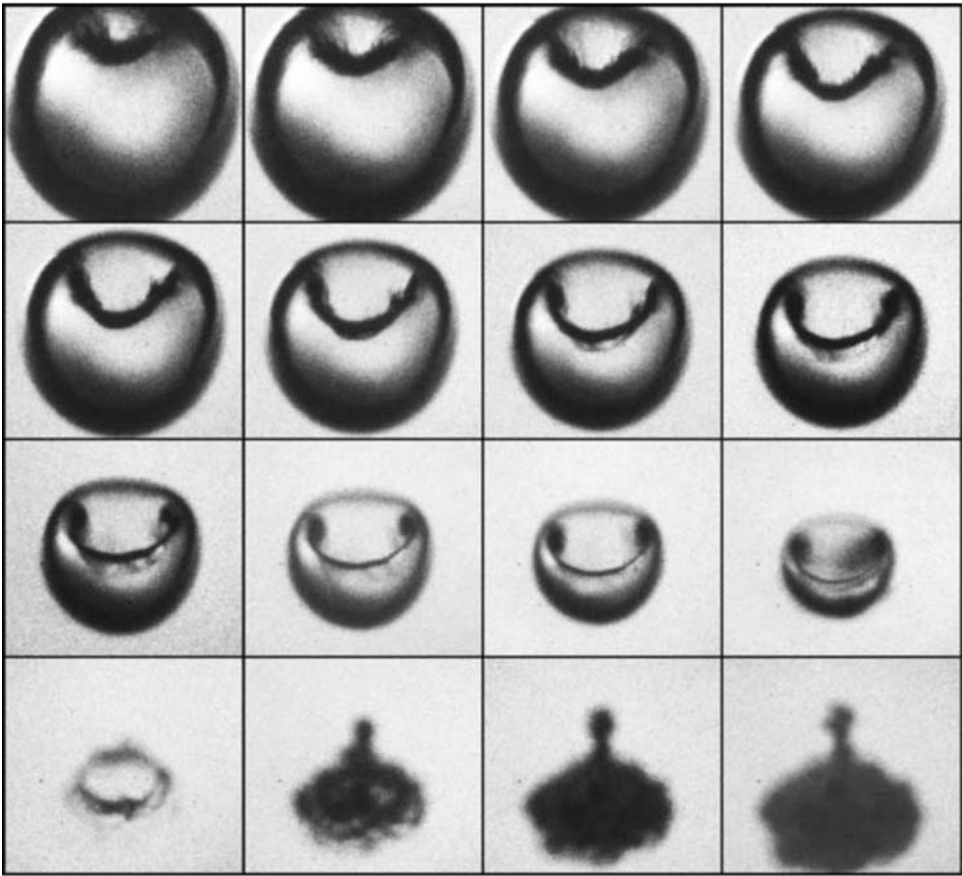


FIGURE 12.19 Jet and counterjet development at an angle of 45° from above the wall; $\gamma = 2.6$ ($\gamma = d/R_{\max}$, the distance of the bubble center from the wall at the moment of formation d and the maximum bubble radius R_{\max}). Interframe time 1 s, exposure time 200 nsec, $R_{\max} = 1.5$ mm, frame size 1.2 mm \times 1.1 mm. (From Lindau O. and Lauterborn, W., *J. Fluid Mech.*, 479, 327–348, 2003. With permission.)

the interference with the reflected pressure waves from the bubbles and the bottom. Because of non-spherical instability, the bubbles collapse in an irregular fashion into tiny fragments. This creates many small bubbles, and they grow to cavitation bubbles when the ambient pressure decreases at 9.26 msec. With the next intense expansion wave at 10.50 msec, many cavitation bubbles grow from the remaining bubble nuclei, and at 11.11 msec, they are unified into a single bubble with an irregular shape.

12.2.3 Bubbles Cloud Dynamics

The cavitating collapse of a bubble cloud generates very high pressures and temperatures. The pressure can reach 100 MPa to 1 GPa in a very short period, which causes severe erosion, noise, and vibration in hydraulic machines. However, this high concentration of energy has been utilized recently for biomedical, environmental, and other industrial applications.

Many researchers have investigated the dynamics of a bubble cloud. Omta (1987) investigated the oscillation and sound emission of a bubble cloud analytically and numerically. In his study, the averaged equations derived by Bishevel and van Wijngaarden (1984) were used. d'Agostino and Brennen (1989) linearized the governing equations for a bubbly mixture together with the Rayleigh–Plesset equation to

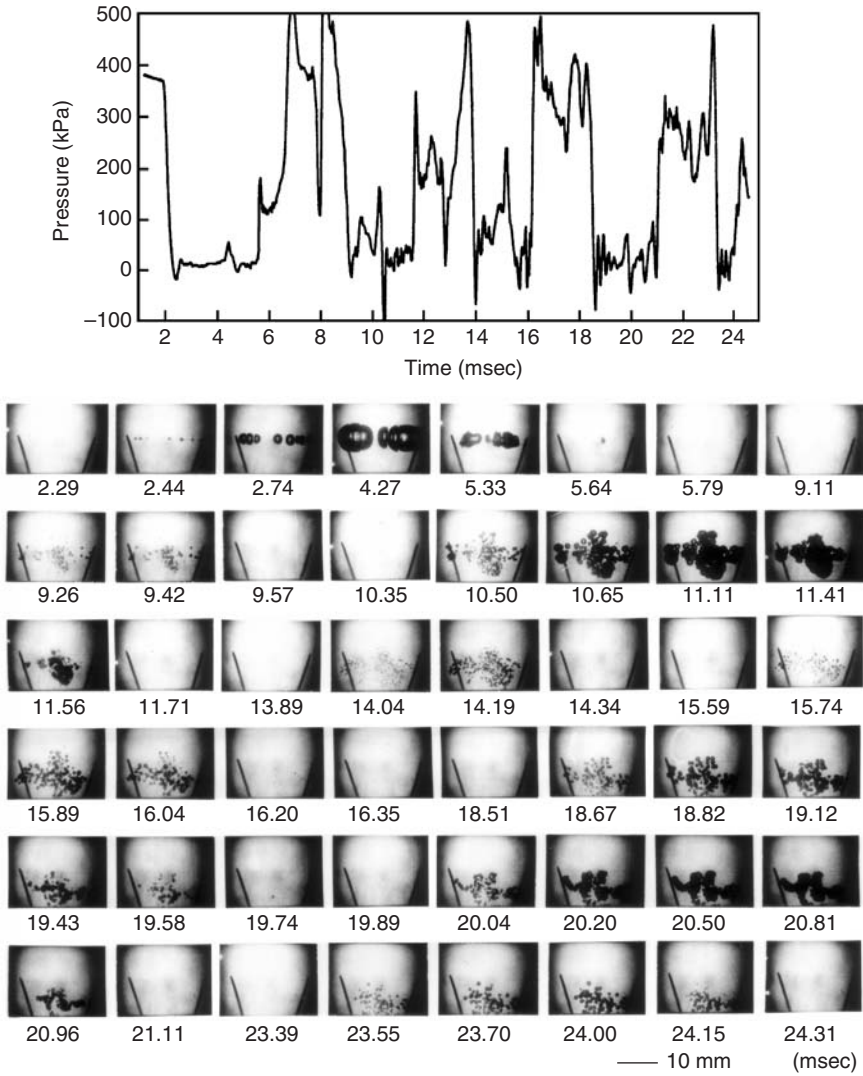


FIGURE 12.20 Growth and collapse of cavitation bubbles due to decrease and increase in the ambient pressure. The gas content is 2.7 ppm. (From Matsumoto, Y. and Aoki, M., *Bull. JSME* 27, 1352–1357, 1984. With permission.)

investigate the analytical solutions for a spherically symmetric bubble cloud. Chahine and Duraiswami (1992) numerically investigated the dynamics of a multibubble cloud consisting of several bubbles and compared their results with analytical results obtained by asymptotic expansions. Shimada et al. (2000) investigated the behavior of cloud cavitation in connection with the cavitation damage using the set of governing equations for the spherical bubble cloud, where the internal phenomena of each bubble and the compressibility of the liquid are taken into account. They concluded that when the bubble cloud collapses, a very high pressure with a high frequency is emitted from each of the bubbles near the center of the cloud.

12.2.3.1 Spherical Bubble Cloud

In this section, the analytical solutions for a spherical bubble cloud are introduced (d’Agostino and Brennen, 1989). The geometry of the spherical cloud is depicted in [Figure 12.21](#).

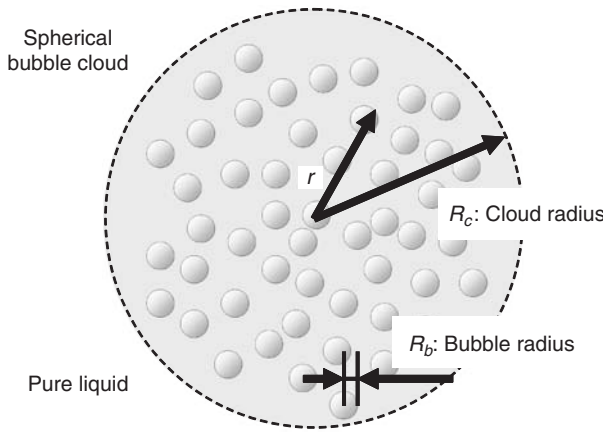


FIGURE 12.21 Spherical bubble cloud.

The relative motion of the two phases, the mass of the dispersed phase and all the damping mechanisms for the bubble dynamics are neglected, and the liquid is assumed to be inviscid and incompressible. The mass and momentum conservation equations are

$$\nabla \cdot \mathbf{u} = \frac{\beta}{1 + \beta\tau} \frac{D\tau}{Dt} \tag{12.53}$$

$$\rho \frac{D\mathbf{u}}{Dt} = -(1 + \beta\tau)\nabla p \tag{12.54}$$

where β is the number density of bubbles per unit liquid volume, τ the individual bubble volume, and D/Dt indicates the Lagrangian derivative. The bubble radius, R_b , is determined by the Rayleigh–Plesset equation.

$$R_b \frac{D^2 R_b}{Dt^2} + \frac{3}{2} \left(\frac{DR_b}{Dt} \right)^2 = \frac{1}{\rho} \left(p_g + p_v - p - \frac{2\sigma}{R_b} \right) \tag{12.55}$$

where p_g is the partial pressure of noncondensable gas, p_v the partial pressure of the vapor, and σ the surface tension.

For simplicity, the following assumptions are employed: (1) The bubble cloud is spherical. (2) The mean-flow velocity is purely radial and small. (3) The void fraction is uniform and relatively low inside the cloud. (4) All the bubbles have the same equilibrium radius, R_{b0} (the subscript 0 indicates the unperturbed value). (5) The vapor pressure inside the bubble is constant. (6) The pressure of the noncondensable gas in the bubbles changes isothermally. Let the perturbation of the far-field pressure be defined in the complex plane by the equation $p_\infty = p_0[1 + \varepsilon \exp(i\omega t)]$ with $\varepsilon \ll 1$. After applying the assumptions and linearizing eqs. (12.53) – (12.55) with the equation $R_b(r, t) = R_{b0}[1 + \varphi(r, t)]$ with $[\varphi(r, t)] \ll 1$, the normalized variation of the bubble radius φ and the natural frequencies ω_n are

$$\varphi(r, t) = -\varepsilon \frac{p_0(1 - \alpha_0)/\rho R_{b0}^2}{\omega_b^2 - \omega^2} \left(\frac{1}{\cos kR_{c0} - \alpha_0 \sin(kR_{c0})/kR_{c0}} \right) \frac{\sin kr}{kr} e^{i\omega t} \tag{12.56}$$

$$\omega_n^2 = \omega_b^2 / \left(1 + \frac{3\alpha_0(1 - \alpha_0)R_{c0}^2}{(n - 1/2)^2 \pi^2 R_{b0}^2} \right) \tag{12.57}$$

$$\omega_b^2 = \frac{3p_{g0}}{\rho R_{b0}^2} - \frac{2\sigma}{\rho R_{b0}^3} \tag{12.58}$$

Here, ω is the frequency of the far-field pressure, ω_b the natural frequency of a single bubble at isothermal conditions, α the void fraction, R_c the cloud radius, and k the wave number in the bubbly flow.

The natural frequencies of the spherical bubble cloud will extend to much lower frequencies than that of a single bubble if the initial void fraction, a_0 , is much larger than the square of the ratio of bubble size to cloud size ($\alpha_0 \gg R_{b0}^2/R_{c0}^2$). Figure 12.22 shows the natural mode shapes of the normalized bubble radius, the pressure and the bubble concentration per unit liquid volume in the cloud ($n = 1 - 4$). The first mode consists of the same phase. Higher modes have n antinodes and $n - 1$ node(s) within the cloud. The envelope is proportional to $1/r$, and the amplitudes at the bubble cloud interface become much smaller at the higher modes.

When the damping effects are included, the attenuation is much greater at the higher frequencies, so that the dominant feature of the response is the first mode natural frequency of the cloud. On the other hand, the response at the bubble natural frequency ($n = \infty$) becomes much less significant.

12.2.3.2 Spherical Bubble Cloud Model

In the previous section, a theoretical analysis for a spherical bubble cloud was introduced; however, the results are limited to the case in which the volumetric change of the bubbles is very small. In this section, the volumetric change of a spherical bubble cloud is simulated by using the model proposed by Shimada et al. (2000), to illustrate nonlinear response.

12.2.3.2.1 Concept and Assumptions of a Spherical Bubble Cloud

Shock waves propagate inside a bubble cloud. Kameda et al. (1996, 1998) clarified that internal phenomena can have a significant influence on shock wave propagation and in certain cases the compressibility of the liquid cannot be ignored, depending on the amount of bubble motion. It has been determined that a very high pressure of $O(10^8)$ – $O(10^9)$ Pa emerges near the center of the cloud cavitation when it collapses violently. In such a case, the compressibility of the liquid should be taken into account. Therefore, to analyze collapsing phenomena of a bubble cloud rigorously, internal phenomena of the individual bubbles and liquid compressibility should be included. Bubbles in the cloud shrink violently, so that gases in a bubble cannot be treated as ideal. For simplicity, the ambient temperature rise of the liquid and the mass transformation of noncondensable gases through the bubble wall are not considered. In the numerical simulation, the following assumptions are employed: (1) The bubble cloud and each bubble maintain spherical symmetry as they oscillate. (2) The bubbly liquid inside the cloud is treated as a continuum fluid,

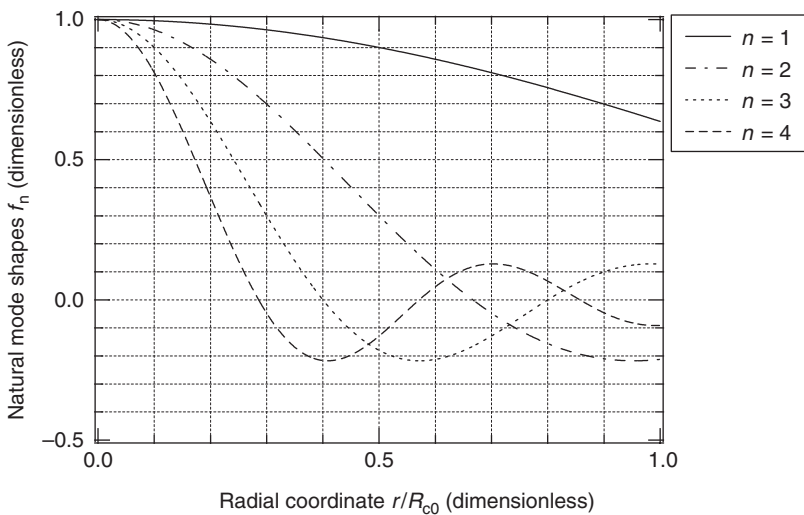


FIGURE 12.22 Natural mode shapes of the normalized bubble radius, the pressure and the bubble concentration per unit liquid volume in the cloud ($n = 1 - 4$).

whose mass and momentum are assumed to be equal to those of the liquid phase, because the mass in a unit volume of the gas phase is much smaller than that of the liquid phase. (3) Bubbles move with the surrounding liquid, and are small enough to ignore the slippage between the bubble and the liquid. (4) Coalescence and fragmentation of bubbles in the cloud are ignored. (5) Viscosity of the bubbly mixture is ignored in the cloud because it has little influence on the wave phenomena. (6) The temperature of the liquid in the cloud is constant. (7) The pressure and temperature inside each bubble are uniform except for the thin boundary layer near the bubble wall, compared with the bubble radius. (8) Temperature at the bubble wall is equal to that of the liquid. (9) Mass of the noncondensable gas inside a bubble is constant. (10) Gases inside a bubble obey the van der Waals gas law. (11) Coalescence and fragmentation of mist inside a bubble are ignored. The thermal behavior inside the bubble and the pressure wave phenomena in the bubble cloud, namely, the evaporation and condensation of liquid at the bubble wall, heat transfer through the bubble wall and the compressibility of the liquid are included.

The geometry of a spherical bubble cloud is the same as in [Figure 12.21](#) A bubble is located at the center of the cloud to avoid a singularity.

12.2.3.2.2 Governing Equations

The Keller equation (Keller and Kolodner, 1956) is applied to the equation of motion of the spherical bubble cloud interface (Eq. [12.59]) to take the compressibility of the surrounding liquid into account.

$$R_c(1 - \frac{\dot{R}_c}{c})\ddot{R}_c + \frac{3}{2}\left(1 - \frac{\dot{R}_c}{3c}\right)\dot{R}_c^2 = \frac{1}{\rho_l}\left(1 + \frac{\dot{R}_c}{c} + \frac{R_c}{c}\frac{d}{dt}\right)\left(p_w - p_\infty - 4\frac{\mu_l}{R_c}\dot{R}_c\right) \quad (12.59)$$

where R_c is the radius of the bubble cloud, c the speed of sound in the surrounding liquid, ρ_l the density of the liquid, p_w the pressure at the surface of the cloud, p_∞ the ambient pressure, and μ_l the viscosity of the liquid. In a bubble cloud, the mass and momentum conservation equations for bubbly flow (Eqs. [12.60] and [12.61]) and the conservation equation for the number density of bubbles (Eq. [12.62]) are also solved. The Tait equation (12.63) is employed as the equation in liquid phase.

$$\frac{\partial(1 - \alpha)\rho_l}{\partial t} + \frac{1}{r^2}\frac{\partial}{\partial r}\{r^2(1 - \alpha)\rho_l u_l\} = 0 \quad (12.60)$$

$$\frac{\partial(1 - \alpha)\rho_l u_l}{\partial t} + \frac{1}{r^2}\frac{\partial}{\partial r}\{r^2(1 - \alpha)\rho_l u_l^2\} + \frac{\partial \rho}{\partial r} = 0 \quad (12.61)$$

$$\frac{\partial n_b}{\partial t} + \frac{1}{r^2}\frac{\partial}{\partial r}\{r^2 n_b u_b\} = 0 \quad (12.62)$$

$$\frac{p + B}{p_\infty + B} = \left(\frac{\rho_l}{\rho_{l\infty}}\right)^n \quad (12.63)$$

where α is the void fraction, u_l the velocity of the liquid, and n_b the number density of the bubbles. The velocity of a bubble, u_b , is assumed to be equal to u_l (assumption [3] above). In the Tait equation, $B = 304.9$ MPa and $n = 7.15$ for water.

For each bubble motion, the following phenomena are taken into consideration: the compressibility of the surrounding liquid, the mass and heat transfer through the bubble wall, the evaporation and condensation of the vapor, and the mist generation from the vapor inside the bubble (Matsumoto and Beylich, 1985), Equations (12.50) and (12.51) are applied as the dynamic equations for the bubble radius. The energy conservation equation in the gas phase with mist and the nucleation rate equation of mist are also solved.

12.2.3.3 Computational Conditions

In this simulation, the behavior of a spherical bubble cloud, which consists of many microbubbles is investigated. Such a microbubble cluster may be generated in high (HIFU) applications, which have attracted much attention recently, because they are less invasive than conventional medical treatments. [Table 12.3](#) lists the computational conditions. Acoustic cavitation induced by ultrasound is highly

TABLE 12.3 Computational Conditions

Gas Phase	Air
Liquid phase	Water
Initial cloud radius, R_{c0}	0.5 mm
Initial bubble radius, R_{b0}	1 μm
Initial ambient pressure, p_0	101.3 kPa
Initial temperature	293 K
Initial void fraction	0.1%
Amplitude of ambient pressure	10–100 kPa
Frequency of ambient pressure	10 kHz–4 MHz

dependent on the ultrasound frequency. In medical applications, a typical frequency of ultrasound is around 0.5 to 5 MHz. When the ultrasound frequency is 4 MHz, the wavelength is about 0.4 mm in water or tissue. The focal region is considered to be around 2 to 4 times the wavelength. In this simulation, it is assumed that the region of the bubble cloud is 0.5 mm in radius and each bubble radius is 1 μm (the natural frequency is about 4 MHz). The ambient pressure fluctuation is assumed to be a pulse wave and the frequency of the wave extends from 10 kHz to 4 MHz for amplitudes of 10, 25, 50, 75, and 100 kPa.

12.2.3.4 Frequency Response of a Spherical Bubble Cloud

The bubbles which are located near the center of the bubble cloud violently collapse when the bubble cloud oscillates at its resonance frequency. The maximum pressures inside the bubbles and maximum cloud radii are calculated for various conditions. Figure 12.23 shows the results. The horizontal axis corresponds to the frequency of the ultrasound. The vertical axis corresponds to the maximum pressure inside the bubbles normalized by the amplitude, and the maximum cloud radius normalized by the initial radius.

When the frequency is sufficiently low, around 10 kHz, the normalized maximum pressure is nearly equal to 1. This means that the ultrasound does not focus in the cloud and the attenuation of the bubbly liquid is negligible corresponding to the long wavelength of the ultrasound. The reason for the normalized maximum pressure inside the bubbles to exceed unity is the effect of the surface tension. In fact, the normalized maximum pressure in the liquid phase converges to unity for the same computational conditions. On the other hand, the normalized maximum pressure converges to 0 due to the large attenuation of the bubbly liquid when the frequency is near the natural frequency of a single bubble, which is about 4 MHz. When the frequency range is from approximately 180 to 200 kHz, the bubble cloud resonates and the normalized maximum pressure becomes very high. Furthermore, the normalized pressure becomes higher as the pressure amplitude of the ultrasound becomes greater. The normalized pressure exceeds 2000, which corresponds to 200 MPa, in the case of 100 kPa pressure amplitude at a frequency of 180 kHz. Additionally, in the case of 100 kPa pressure amplitudes, the high pressures appear even for a lower frequency. The cloud radius hardly changes in each case. This is because the changes of the cloud radius are mainly caused by the volumetric changes of the bubbles in the cloud and the initial void fraction is only 0.1% as shown in Table 12.3.

12.2.3.4.1 Low-Pressure-Amplitude Cases ($\Delta p = 10 \text{ kPa}, 25 \text{ kPa}$)

The response curves of the maximum pressure in the case of 10 and 25 kPa pressure amplitude are almost the same as those shown in Figure 12.23. The ultrasound propagation in these cases are shown since the cloud, at first, shows nearly linear oscillation for these conditions. Two different peaks are observed in the response curves of the maximum pressure: one at 200 kHz and the other at 600 kHz. Figure 12.24 shows the pressure distributions of the liquid phase over about 0.5 T (T is the cycle of the ultrasound), at each 0.01 T. The amplitude of the ambient pressure is 10 kPa at a frequency of 200 kHz (left panel) and 600 kHz (right panel). The pressure inside the cloud changes at almost the same phase as the cloud in the 200 kHz case. This is the first resonance mode of a spherical bubble cloud (see Figure 12.22). The first mode frequency is slightly lower than the natural frequency calculated by Eq. (12.57) since the damping effects are not considered in that formula. In fact, d'Agostino and Brennen (1989) showed

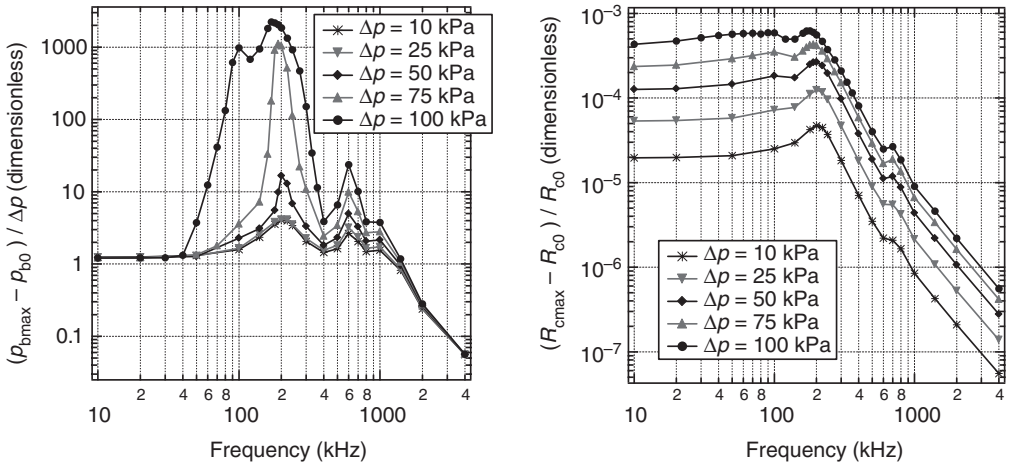


FIGURE 12.23 Frequency response curves at various amplitudes of the ambient pressure. Left panel: maximum pressure inside the bubbles; right panel: maximum bubble cloud radius.

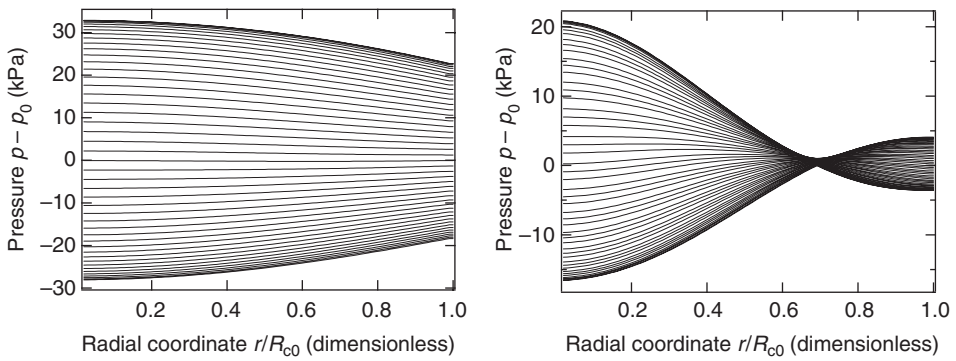


FIGURE 12.24 Pressure distributions of the liquid phase inside a bubble cloud. Left panel: $\Delta p = 10$ kPa, $f = 200$ kHz; right panel: $\Delta p = 10$ kPa, $f = 600$ kHz.

that the natural frequencies become lower when the damping effects are taken into account. In the 600 kHz case, there is one pressure node and the pressure at the center of the cloud is shifted almost π radians backward from that at the boundary of the cloud. This is the second resonance mode of a spherical bubble cloud (see Figure 12.22). As in the case of the first resonance mode, the frequency is almost the same as the second mode natural frequency (d’Agostino and Brennen, 1989).

12.2.3.4.2 High-Pressure-Amplitude Cases ($\Delta p = 75$ kPa, 100 kPa)

When the pressure amplitude becomes higher, the oscillations of the cloud show strong nonlinearity. Figure 12.25 shows the water pressure in the cloud under the same conditions as the surface plot. The range of the normalized time is from $4.05T$ to $4.30T$. In this case, the shock wave is generated inside the cloud by the process of wave focusing. The speed of sound in the bubbly flow strongly depends on the void fraction and is directly dependent on the pressure fluctuations. The harmonic pressure wave easily generates the shock wave inside the bubbly liquid. The shock wave in the bubbly liquid causes the collapse of the bubbles, so that high energy is concentrated near the center of the cloud. As a result, the normalized pressure becomes much higher when the pressure amplitude becomes significant to generate the shock wave. For example, in the case of 100 kPa pressure amplitudes, even when the frequency is much

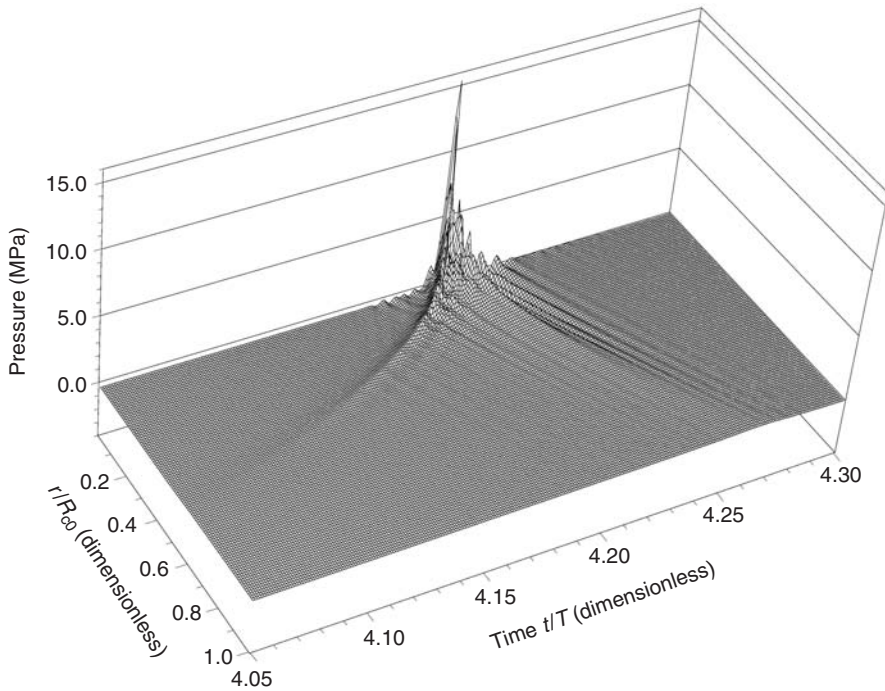


FIGURE 12.25 Surface plot of the liquid pressure inside a bubble cloud ($\Delta p = 100$ kPa, $f = 180$ kHz).

lower, the pressure wave can generate a shock and high pressures as observed for the 180 kHz case. Additionally, since a high pressure wave with a high frequency is generated when the bubbles near the center of the cloud collapse, precursors appear in front of the shock wave before the focusing.

The results indicate that the bubbles inside a bubble cloud violently collapse when the frequency of the irradiated ultrasound is the same or lower than the natural frequency of the cloud for a sufficiently large ultrasound pressure amplitude.

12.3 Droplet Breakup, Coalescence, and Wall Impact

C. Tropea and I.V. Roisman

The usual description of the spray transport involves the solution of the mass and the momentum balance equations for the liquid phase (droplets) and of the ambient gas flow as well as the forces associated with the droplet–gas interactions (drag forces). The details and various approaches to such modeling can be found in Chapter 13. The phenomena considered in the present chapter include the droplet breakup due to the interaction with the air-flow, collisions with another drop or with a wall. In [Figure 12.26](#), the spray atomization, transport, and wall impact are shown schematically, involving these phenomena. They lead to alterations in the distributions of the drop diameters and velocity in the spray. Accounting for such alterations significantly complicates the modeling of spray transport, considerably extends the numerical simulations and thus, in many numerical simulations the effect of the drop break-up and coalescence is assumed negligibly small and neglected. However, the drop fragmentation in the near-atomizer region determines the average drop diameter of the spray obtained and therefore cannot be neglected. The secondary breakup of drops can be caused by the interaction of a spray with a high-speed gas jet or by a shock wave. The effect of binary collisions becomes significant in the region of the interaction of two (or more) sprays, and the case of the propagation of very dense spray, the near-wall region (where the impacting spray interacts with the spray of the secondary droplets produced by spray–wall impact).

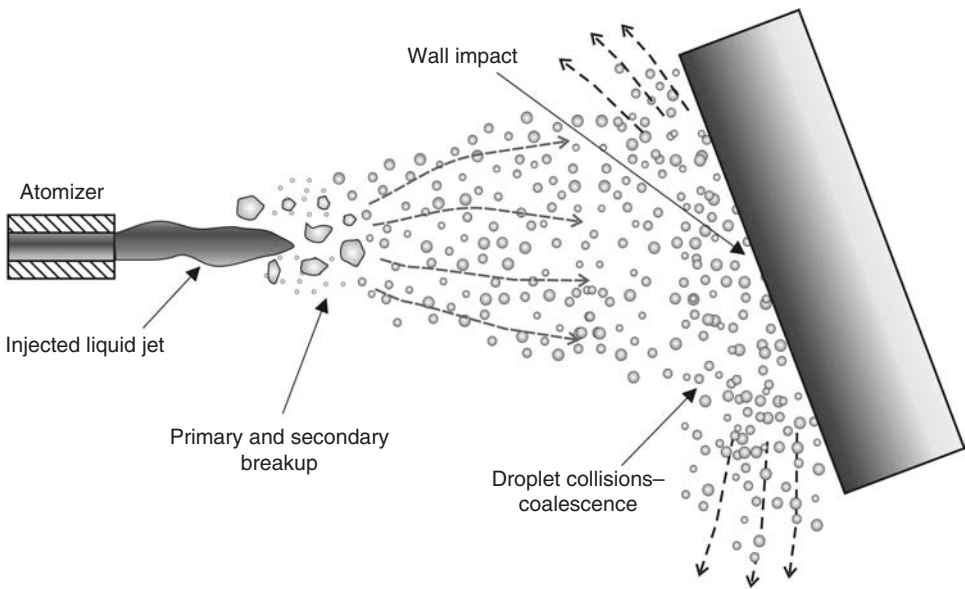


FIGURE 12.26 Sketch of spray atomization, transport and wall impact.

When a spray impacts onto a substrate, a part of the droplet volume deposits on it and forms a thin fluctuating liquid film. Another part of the spray volume rebounds and creates a flow of secondary droplets. One of the key elements in the creation of such secondary spray is the drop impact onto a wall, also described in the present chapter.

The common feature of the phenomena described here is the significant change of the drop shape due to the impact with another drop (binary drop collisions), its deformation and breakup by ambient air flow, or due to the impact onto a dry or wet substrate, as illustrated in Figure 12.27.

The main parameters determining the drop deformation and breakup are the Reynolds number $Re = DU/\nu$ and the Weber number $We = DU^2/\sigma$, where D is the drop diameter, U the characteristic velocity, ν the kinematic viscosity, and σ the surface tension. If both these numbers are large ($Re \gg 1$, $We \gg 1$), the droplet deformation is inertia-dominated. The drop deformation often leads to the creation of an expanded relatively thin free liquid sheet (lamella) bounded by a rim, formed due to capillary forces (see Figure 12.28a). In other cases, the drop deformation leads to the appearance of the finger-like jets ending with a droplet, as shown schematically in Figure 12.28b.

These forms appear due to capillary forces. The rim velocity differs from the velocity of the liquid in the lamella. The motion of the rim is determined by the capillary forces, the internal viscous stresses, the inertia of the liquid entering the rim from the lamella, and the aerodynamic drag force. The simplest case of the motion of the rim bounding a steady uniform liquid sheet was analyzed by Taylor (1959). In this case, the capillary force per unit length, 2σ , is balanced by the inertia of the liquid entering the rim, $\rho w_{\text{rim}}^2 \delta$. The relative rim velocity w_{rim} is expressed in the form:

$$w_{\text{rim}} = \sqrt{\frac{2\sigma}{\rho\delta}} \quad (12.64)$$

The analysis of the droplet appearing at the end of a free liquid jet (Figure 12.28b) is very similar. The momentum equation of this droplet appearing at the end of a steady jet of the diameter D_j expresses the balance of the inertia of the liquid entering the droplet from the jet, the capillary forces, and the pressure in the jet due to surface tension. The relative droplet velocity is

$$w_{\text{droplet}} = \sqrt{\frac{2\sigma}{\rho D_j}} \quad (12.65)$$

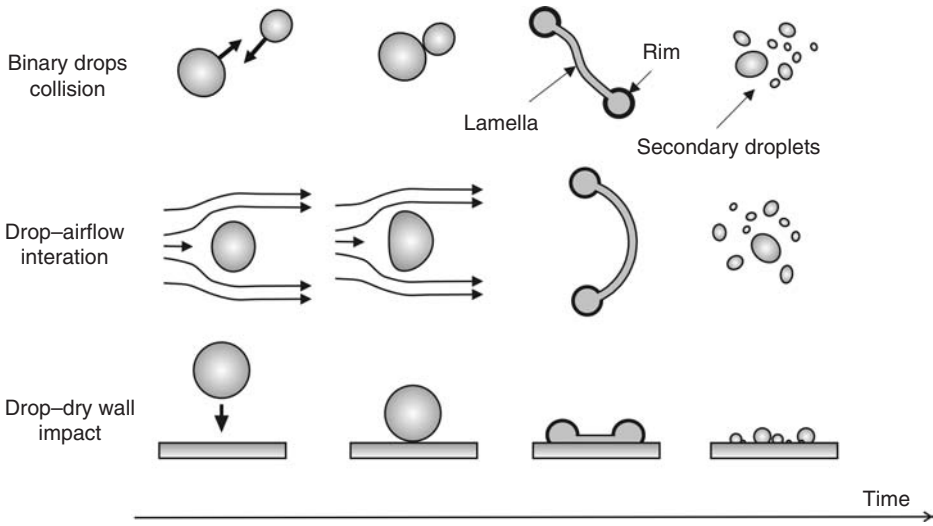


FIGURE 12.27 Successive stages of drop deformation and break up due to the binary drop collision, drop/airflow interaction and drop/wall impact.

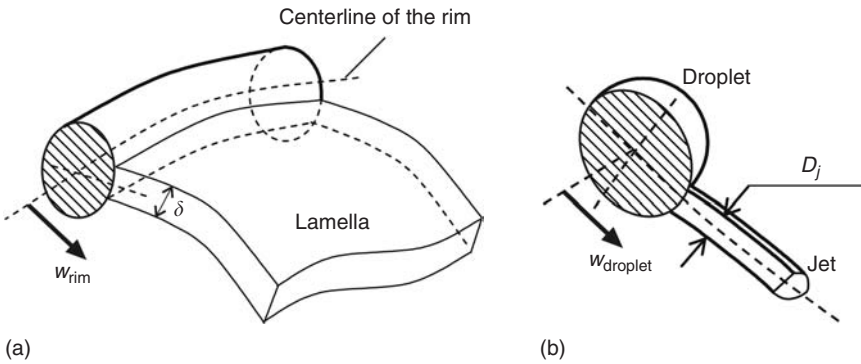


FIGURE 12.28 Capillary effects at the free boundary: (a) element of rim bounding a liquid sheet; (b) droplet appearing at the end of a liquid jet.

12.3.1 Droplet Breakup Mechanisms

The main subjects in the study of the drop breakup are usually the regimes of the breakup, the time of breakup, and the outcome: size, number and velocities of the secondary droplets. We distinguish here two main directions of the breakup study:

- aerodynamic breakup, important for the description of sprays, associated with the drop suddenly exposed to a high-speed gas flow or break-up by a shock wave propagating in the ambient gas. The velocity of the drop relative to the velocity of the ambient gas flow and corresponding pressure gradients at the drop surface are the main reasons for the breakup.
- the breakup in a viscous flow, with the application to the rheology of emulsions, when the drop deforms and breaks up mainly due to the shear stresses appearing in the ambient viscous liquid.

In addition, there are many specific cases of drop impact which will not be described in detail here, for example, the deformation and breakup involving non-Newtonian drops or flows (Ha and Leal, 2001) in an electric field (Ha and Yang, 1998), a turbulent fluid flow (Sevink and Park, 1973), and an acoustic field (Yarin et al., 2002).

12.3.1.1 Regimes of the Aerodynamic Drop Breakup

The typical dimensionless parameters used in the description of the aerodynamic breakup are the Reynolds number $Re_g = \rho_g w D / \mu_g$ and Weber number $We_g = \rho_g w^2 D / \sigma$ based on the properties of the ambient gas, as well as Ohnesorge number $Oh = \mu_l / \sqrt{\rho_l D \sigma}$, where w is the relative droplet–gas velocity. These parameters determine the degree of the drop deformation and the mode of the drop breakup.

The first attempt to classify the various regimes of drop break-up using the Weber number, We_g , and Ohnesorge number, Oh , was made by Hinze, (1955). A more detailed map of these regimes at various Ohnesorge numbers has since been created on the basis of extensive experimental studies on a drop breakup (Hinze, 1955; Hsiang and Faeth, 1992, 1995). Most of the observations show that the critical We_g numbers, corresponding to the regime thresholds, are almost independent of the Ohnesorge number if it is small ($Oh < 0.1$). An increase in the Weber number leads to an increase in drop deformation. At some critical Weber number the drop breaks up. Several main regimes of breakup shown schematically in Figure 12.29 can be observed:

Bag break-up, shown in Figure 12.29a, takes place in the range $12 < We_g < 15$ at $Oh < 0.1$. In this regime the lamella deforms and takes an expanding bag-like shape. At some time instant the lamella disintegrates. The rim then breaks up due to the Rayleigh capillary instability.

At higher relative velocities, $80 < We_g < 350$ at $Oh < 0.1$, the main drop deformation takes place in the thin boundary layer of the frontal surface of the drop. The flow in the liquid layer yields the *boundary layer stripping* (Hinze, 1955; Ranger and Nicholls, 1969; Delplanque and Siringano, 1994). The resulting thin liquid film then disintegrates in the airflow (Figure 12.29b). This mechanism is also called *shear breakup*. An alternative description of the drop breakup mechanism in this range of relative velocities, called *stretching/thinning breakup*, is given in Liu and Reitz (1997) and Lee and Reitz (2000). In these studies the main source of drop deformation is associated with the low-pressure region near the drop equator. The pressure gradient along the drop surface leads to the drop stretching in the plane normal to the direction of the airflow. The edges of the obtained lamella are thin because the inertial forces in the film significantly exceed capillary forces. Such a film is then deflected in the direction of the gas flow (Figure 12.29c)

If the relative velocity is so high such that the gas Weber number exceeds 350 ($We_g > 350$), the droplet deforms very quickly and takes the form of a wavy thin sheet. This sheet then breaks up into ligaments and secondary droplets: *catastrophic breakup* shown in Figure 12.29d (Hwang et al., 1996).

Note that the phenomenon of drop breakup cannot always be classified by the above mentioned regimes. Some studies are devoted to the investigation of *multimode regimes*, mainly in the range between the bag breakup and shear breakup. In Pilch and Erdman (1987) and Joseph et al. (1999) the bag-and-stamen breakup at $50 < We_g < 100$ were mentioned. The description and temporal parameters of bag–plume and plume–shear breakup regimes can be found in Dai and Faeth (2001).

The best fit for the threshold of breakup regimes and the degree of drop deformation by a shock wave based on the experimental data from Hsiang and Faeth (1995) for $Oh < 2 \times 10^{-4}$ is obtained in Schmehl (2003) in the form

$$We < 0.6(1 + 0.8Oh^{0.8} + 9 \times 10^{-5}Oh^{2.4}) \quad \text{deformation} < 5\%, \text{ no breakup, } Oh < 6 \times 10^2$$

$$We = 1.1(1 + 0.7Oh^{0.85} + 1.5 \times 10^{-4}Oh^{2.4}) \quad \text{deformation } 10\%, \text{ no breakup, } Oh < 6 \times 10^2$$

$$We = 2.3(1 + 0.75Oh^{0.8} + 2.5 \times 10^{-4}Oh^{2.4}) \quad \text{deformation } 20\%, \text{ no breakup, } Oh < 6 \times 10^2$$

$$3(1 + 15Oh^{1.2}) < We < 13(1 + 1.7Oh^{1.4}) \quad \text{drop oscillations, no breakup, } Oh < 3 \times 10^{-1}$$

$$13(1 + 1.7Oh^{1.4}) < We < 35(1 + 0.65Oh^{1.4}) \quad \text{bag breakup, } Oh < 4$$

$$35(1 + 0.65Oh^{1.4}) < We < 80(1 + 0.6Oh^{1.5}) \quad \text{multimode breakup, } Oh < 15$$

$$80(1 + 0.6Oh^{1.5}) < We \quad \text{shear breakup, } Oh < 6$$

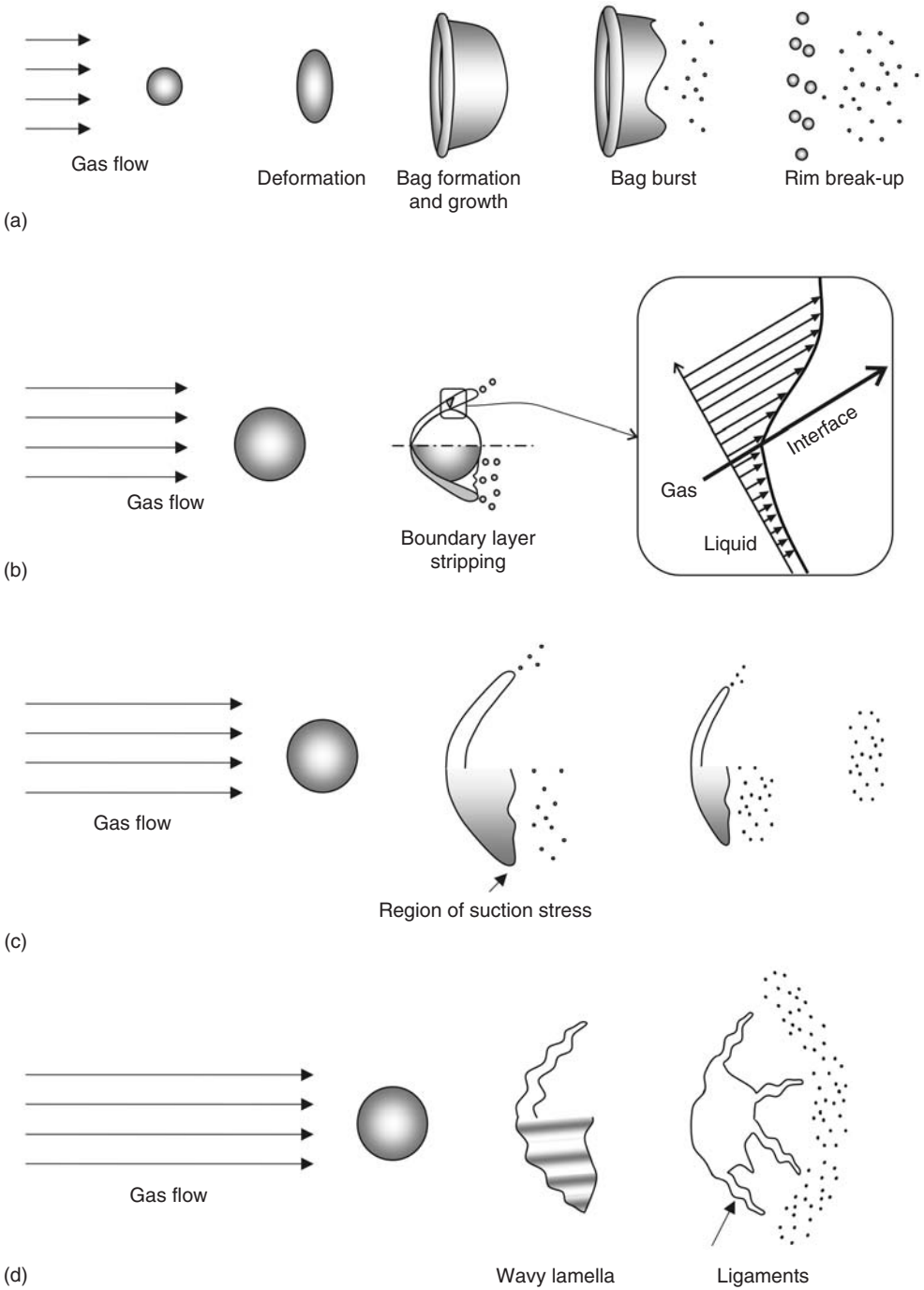


FIGURE 12.29 Mechanisms of aerodynamic breakup.

The increasing drop viscosity slows the rate of drop deformation; however, the maximum drop deformation is virtually not affected by the Ohnesorge number.

The axisymmetric shape of the drop deformed by a shock wave can be approximately described by two dimensions: its length L in the axial direction and its diameter D . The empirical expression for the degree

of the maximum drop deformation by a shock wave is obtained in Hsiang and Faeth (1995):

$$\left(\frac{D}{L}\right)_{\max} = (1 + 0.007We^{1/2})^3 \tag{12.66}$$

The temporal behavior of the drop during the breakup process is illustrated in Figure 12.30 using the characteristic shear breakup time defined in Ranger and Nicholls (1969):

$$t^* = \frac{D_0}{w_0} \sqrt{\frac{\rho_l}{\rho_g}} \tag{12.67}$$

where D_0 and w_0 are the initial drop diameter and the initial relative velocity to the gas. The gray area corresponds to the time intervals at which a drop breaks up and generates secondary droplets.

12.3.1.2 Aerodynamic Breakup Outcomes

The secondary droplets obtained by drop breakup are usually in a relatively wide range of diameters and velocities. The Sauter mean diameter, D_{32} , is one of the most convenient integral parameters characterizing the drop size. This parameter is modeled in Hsiang and Faeth (1992) as a function of the size of the viscous boundary layer appearing on the front surface of the drop. The resulting expression for small Ohnesorge number ($Oh < 0.1$) is

$$D_{32} = 6.2D_0Oh^{1/2}We_g^{-1/4} \tag{12.68}$$

In Schmehl (2003a) an alternative empirical correlation for the Sauter mean diameter (SMD) is proposed, fitting the collected experimental data more precisely:

$$D_{32} = 1.5D_0Oh^{0.2} \left(\frac{1 + 1.7Oh^{1.4}}{We_g}\right)^{0.25} \tag{12.69}$$

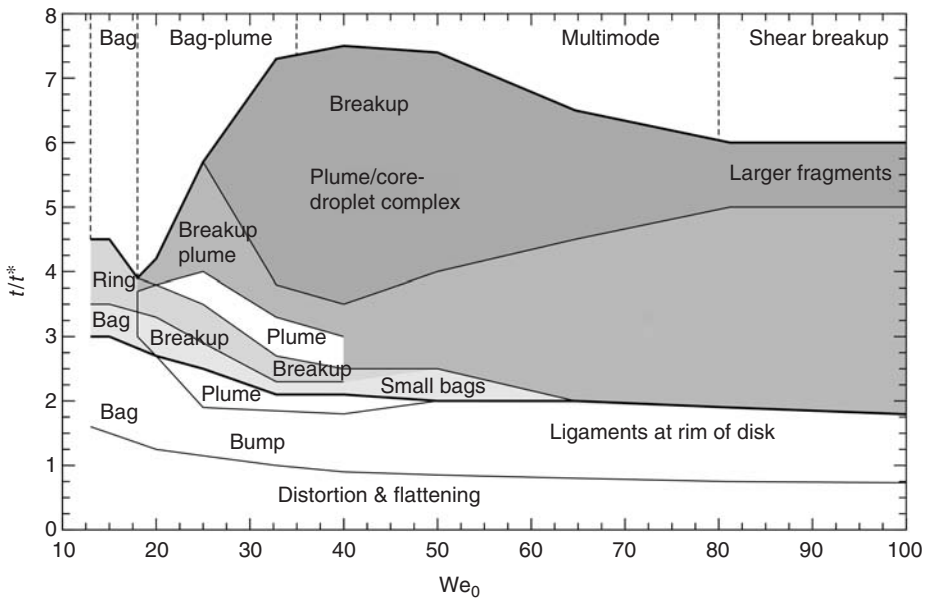


FIGURE 12.30 Stages of droplet deformation and break-up for various regimes of aerodynamic breakup ($Oh < 0.1$). (Adapted from Schmehl, R., *Proceedings of the International Conference on Liquid Atomization and Spray Systems ICLASS-2003*, July 13–18, 2003, Sorrento, Italy, 2003b. The experimental data are from Dai, Z., and Faeth, G.M., *Int. J. Multiphase Flow*, 27, 217, 2001; Krzeczowski, S.A., *Int. J. Multiphase Flow*, 6, 227, 1980; Wiezba, A., *Exp. Fluids*, 9, 1329, 1990.)

Hsiang and Faeth (1992) have found that the diameters of the droplets (excluding the size of the parent drop) can be described well using the universal root normal distribution function with the $D_{0.5}/D_{32} = 1.2$, where $D_{0.5}$ is the mass median diameter (MMD). The definitions of various mean diameters can be found in Lefebvre (1989).

The next parameter characterizing the breakup outcome is the velocity of the fragments. Their velocity changes during the breakup period due to the drag force applied from the ambient gas flow. The deceleration associated with this drag depends on the fragment's size, yielding a velocity-dependent distribution. The velocity distribution of fragments at the instant when the breakup process is completed is obtained in Hsiang and Faeth (1993) in the following form:

$$w_0/w = 1 + 2.7 \left(\sqrt{\frac{\rho_g}{\rho_l}} \frac{D_0}{D} \right)^{2/4} \tag{12.70}$$

In this empirical correlation, w and D are the relative velocity and the diameter of the fragments, and w_0 is the initial relative velocity of the drop.

12.3.1.3 Breakup in a Viscous Flow

The interest in the phenomenon of drop breakup in a viscous flow is derived from the problems of mixing, blending, dispersion, and the studies of rheology and formation of emulsions. A drop located in the viscous flow deforms, stretches, and then, if the velocity gradient reaches some critical value, breaks up. For a description of the dynamics of drop deformation and breakup in viscous flows see the reviews by Stone (1994) and Eggers (1997).

The governing parameters determining the deformation and breakup of drops in a viscous flow are the viscosity ratio $\lambda = \mu_l/\mu_g$, the density ratio $\beta = \rho_l/\rho_g$, the capillary and Reynolds numbers $Ca = G\mu_g D_0/\sigma$ and $Re = P_g G^2 D_0/\mu_g$, where G is the magnitude of the velocity-gradient tensor. However, the drop breakup depends not only on the instantaneous flow conditions, but also on their history (Bently and Leal, 1986; Grace, 1982). Quick changes in flow conditions enhance drop breakup.

Four mechanisms of drop breakup in a viscous flow are shown schematically in Figure 12.31, (Stone, 1994).

Capillary break-up (Tomotika, 1935; Mikami et al., 1975; Tjahjadi et al., 1992) takes place when the diameter of the thread-like drop is so small that it is broken by a growing capillary wave. The drop can also break near the middle of the thread (Barthes-Biesel and Acrivos, 1973). Such *necking breakup* leads to the formation of two similar droplets. *End pinching* (Grace, 1982; Taylor, 1934; Stone and Leal, 1989a,b; Stone et al., 1989) is the breakup of the thread-like (or finger-like) drop near the droplet at its end (see also Figure 12.31). The addition of surfactants to the fluid of a deforming, low-viscosity ratio drop ($\lambda < 0.1$) can lead to *tip streaming* (Ha and Yang, 1998; de Bruijn, 1993). Tip streaming was also observed in the experiments with the deformation of viscoelastic drops (Milliken and Leal, 1991).

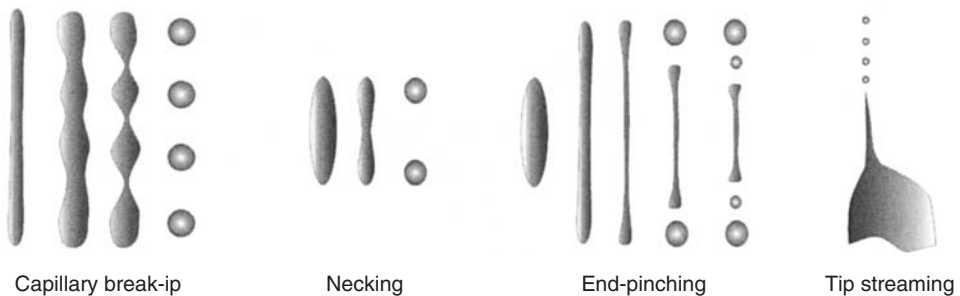


FIGURE 12.31 Modes of drop breakup in a viscous flow.

The shape of the drop deforms under the action of stresses generated by the outer flow. This deformation increases as the capillary number grows. The stable solution for the shape of the deformed drop in an extensional flow is obtained by Acrivos and Lo (1978) for inviscid drops

$$h(z) = \frac{D_0}{8Ca} \left[1 - \left(\frac{z}{10D_0Ca^2} \right) \right] \quad (12.71)$$

and the asymptotic value for the critical capillary number for the viscous drop is

$$Ca_{cr}\lambda^{1/6} = 0.148 \quad (12.72)$$

which is valid for the small viscosity ratio ($\lambda \ll 1$).

12.3.2 Binary Drop Collisions

A collision of two drops is shown schematically in Figure 12.32, where the main geometrical parameters of the collision are illustrated: the separation distance between the droplet centers χ and the collision angle $\psi = \arcsin[\chi/(R_1 + R_2)]$. The relative velocity is denoted as w . The main dimensionless parameters governing the binary drop collision phenomenon include the Weber number, $We = \rho_1 w^2 (R_1 + R_2) / \sigma$, the impact parameter $B = \chi / (R_1 + R_2)$ (see studies of Ashgriz and Poo [1990]; Jiang et al., [1992] and Qian and Law [1997]), the drop diameter ratio, $\Delta = R_1 / R_2 < 1$, and the Reynolds number.

The influence of the viscosity of the fluid on the binary collision in vacuum, particularly on the temporal evolution of the drop size, was investigated in Willis and Orme (2003). They found that a higher Reynolds number corresponded to higher characteristic times of drop deformation.

A detailed study of the collision of drops of the same diameter can be found in Qian and Law (1997). Several regimes of collision are observed in this work: coalescence, bouncing, stretching separation, and reflexive separation. These regimes are shown schematically in Figure 12.33.

At relatively high Weber numbers, when the phenomenon is inertia-dominated, the near head-on collision (regimes (c) and (d)) can be subdivided into several main stages, similar to the stages of the impact of a drop on a dry wall (see Section 12.3.3): initial drop deformation leading to the formation of a relatively thin expanding liquid film, bounded by a rim. This rim expands and then recedes. The kinetic energy of the drop accumulates in the rim at the instant when it merges. This kinetic energy leads to the creation of a nearly cylindrical jet bounded by two droplets. The liquid from the jet enters these two droplets. If the time of the jet breakup is smaller than the time of the merging of the droplets, the collision leads to separation; otherwise, it ends with coalescence.

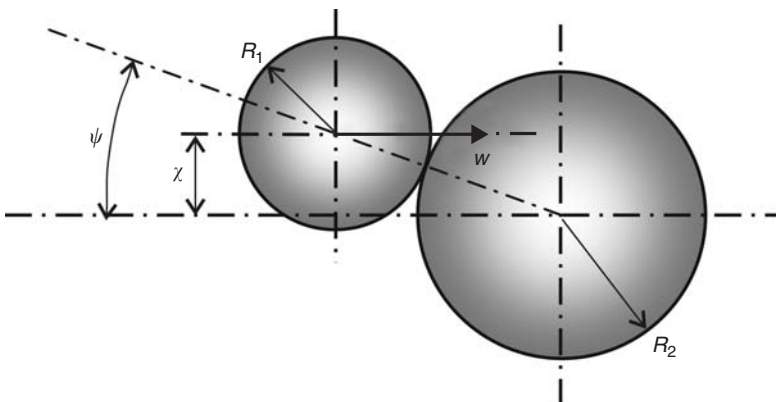


FIGURE 12.32 Sketch of a binary drop collision.

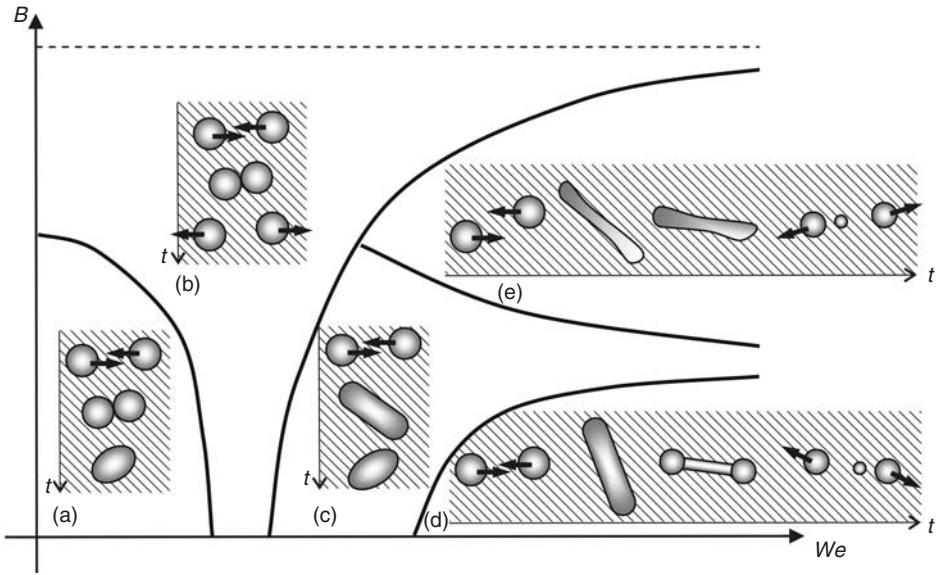


FIGURE 12.33 Regimes of hydrocarbon drops collisions: (a) coalescence; (b) bouncing; (c) coalescence; (d) reflexive separation; (e) stretching separation. (Adapted from Qian, J., and Law, C.K., *J. Fluid Mech.*, 331, 59, 1997.), $\Delta = 1$.

At relatively low values of the Weber number, the phenomenon is governed by the behavior of the film of the ambient liquid–gas in the gap between the approaching drops. It is known that the expression for the pressure in this film is singular if its thickness approaches zero. The drops will coalesce if the film drains to a thickness comparable with the characteristic distance associated with the van der Waals force (Chesters, 1991).

The stretching separation regime corresponds to the nonsymmetric collision of two drops at a high Weber number. Such an impact produces a stretching filament, which breaks up by “end pinching” (Brenn et al., 2001), (Eggers, 1993).

The regimes shown in Figure 12.33 do not reflect all the variations of the considered phenomena. For example, the collision of two drops of $\Delta = 1/4$ observed in Podvysotsky and Shraiber (1984) yields the penetration of the smaller drop into the larger, followed by the creation of a relatively long jet behind the bigger drop. This jet then breaks up into several secondary droplets.

Among the models describing the critical parameters that correspond to the separation–coalescence threshold are the models of Park (1970), based on the balance of the surface forces in the neighborhood of the contact of two drops and the forces associated with the angular momentum. In Brazier-Smith et al. (1972) the kinetic energy of rotation of the drop obtained by coalescence is accounted for. The energy balance of the colliding drops leads to the following expression for the critical impact factor:

$$B_{cr} = \left[\frac{24[1 + \Delta^2 - (1 + \Delta^3)^{2/3}](1 + \Delta^3)^{11/3}}{5We\Delta^5(1 + \Delta)^2} \right]^{1/2} \tag{12.73}$$

The criterion for the reflexive separation based on the energy balance of the system is obtained in Ashgriz and Poo (1990) in the form

$$We > 3 \frac{\Delta(1 + \Delta^3)^2}{\Delta^6 C_1 + C_2} [7(1 + \Delta^3)^{2/3} - 4(1 + \Delta^2)] \tag{12.74}$$

where the parameters $C_1 = 2(1 - C_3)^2(1 - C_3^2)^{1/2} - 1$ and $C_2 = 2(\Delta - C_3)^2(\Delta^2 - C_3^2)^{1/2} - \Delta^3$, with the parameter C_3 being $C_3 = B(1 + \Delta)/2$ and $\Delta < 1$. The above expression is obtained by a simplified approximation of the shape of the deformed drop by a disc.

The model for the critical Weber number of the stretching separation is

$$We = \frac{4(1 + \Delta^3)^2[3(1 + \Delta)(1 - B)(\Delta^3 C_4 + C_5)]^{1/2}}{\Delta^2[(1 + \Delta^3) - (1 - B^2)(C_4 + \Delta^3 C_5)]} \quad (12.75)$$

where

$$C_4 = \begin{cases} 1 - \frac{1}{4\Delta^3}(2\Delta - \tau)^2(\Delta + \tau) & \text{for } \tau > \Delta \\ \frac{\tau^2}{4\Delta^3(3\Delta - \tau)} & \text{for } \tau < \Delta \end{cases}, \quad C_5 = \begin{cases} 1 - \frac{1}{4}(2 - \tau)^2(1 + \tau) & \text{for } \tau > 1 \\ \frac{\tau^2}{4(3 - \tau)} & \text{for } \tau < 1 \end{cases}$$

with the parameter τ being $\tau = (1-B)(1 + \Delta)$.

Qian and Law (1997) have also considered the energy balance of two colliding drops of the same diameter. They have accounted for the energy loss during collision due to viscous dissipation. Their result yields the linear dependence of the critical Weber number that corresponds to the separation-coalescence threshold on the Ohnesorge number. Their result, best fitting the existing experimental data, is given in the form

$$We_{cr} = 30Oh + 15 \quad (12.76)$$

with the Ohnesorge number being defined as $Oh = 16\mu_1/\sqrt{\rho_1 R \sigma_1}$.

12.3.3 Drop-Wall Impact

Many processes involving drop and sprays also involve their impact onto a surface. Universal relations describing the outcome of drop-wall impact do not exist simply because of the large number of influencing parameters:

- Reynolds number and Weber number of incident drop
- Surface orientation (normal-inclined)
- Surface structure (rough-smooth) and chemical composition (hydrophobic-hydrophilic)
- Dry or wet surface, including the hydrodynamics of the liquid film in the case of a wet surface
- Surface temperature

Obviously, additional properties of the impinging drop may also be of importance, such as boiling point, heat of vaporization, or contact angle with the surface.

Understanding drop-wall impact represents a key technology for some processes, for example, ink jet printing or near net-shape manufacturing, where solidification must also be accounted for (Madejski, 1983; Poulidakos and Waldvogel, 1996; Liu and Orme, 2001). Very high-speed drop impacts can even lead to damage or erosion of the solid surfaces, like turbine blades or airplane surfaces. In such ultra-high-speed drop impacts, compressibility is one important factor, leading to the propagation of shock waves in the drop and in the target material (Lesser and Field, 1983; Korobkin, 1997). However, drop-wall impact is also an elemental part of spray-wall impact, which itself is an essential process in many technologies: spray cooling, spray painting, fuel injection, drop separators, etc. Whether spray impact can be treated as the superposition of many individual drop impacts depends on the spray density and on the hydrodynamics of the liquid film on the surface. This topic will not be addressed in the present article, but is discussed in Section 8.3.

In the following discussion, the phenomenon of drop impact has been divided into impact onto dry surfaces and onto liquid films. In the former case, the wettability of the surface may become important whereas in the latter case, the hydrodynamics of the liquid film must be considered. A good collection of papers dealing with various specific aspects influencing drop impact phenomena can be found in Rein, (2002).

12.3.3.1 Wetting of a Dry Surface: Static and Dynamic Contact Angles

The stationary shape of a drop on a dry solid surface depends on its volume, density and on the surface wettability property, described by a static (or equilibrium) contact angle θ_e , defined in Figure 12.34. In the case of a smooth, homogeneous, rigid surface, this angle depends on the surface (or interface) free energy of the solid–gas interface, σ_{sv} , the solid–liquid interface, σ_{sl} , and the liquid–gas interface, σ (surface tension). The equilibrium condition at the contact line leads to *Young’s relation*

$$\cos \theta_e = \frac{\sigma_{sv} - \sigma_{sl}}{\sigma} \tag{12.77}$$

The wetting of the substrate is total, $\theta_e = 0$, if the RHS of (12.77) is >1 . The surface is partially wettable if the absolute value of the RHS of (12.77) is < 1 , yielding a value of the equilibrium contact angle in the range $0 < \theta_e < \pi$. Within this range, hydrophobic ($\theta_e > \pi/2$) and hydrophilic ($\theta_e < \pi/2$) surfaces can also be distinguished.

When the liquid spreads on the substrate under the action of gravity and capillary forces (spontaneous spreading) or due to inertial forces (forced wetting), the position of the contact line moves and the apparent dynamic contact angle θ_d differs from the static one. The dynamic contact angle depends on the contact line velocity U_c if the capillary number $Ca = U_c \mu / \sigma$ is relatively small. This dependence is shown schematically in Figure 12.35. The sign of U_c is positive if the contact line moves toward the gas phase. Two distinct branches of the curve $\theta_d = \theta_d(U_c)$ are considered in relation to the direction of motion of the contact line: the advancing dynamic contact angle for $U_c > 0$ and receding contact angle for $U_c < 0$.

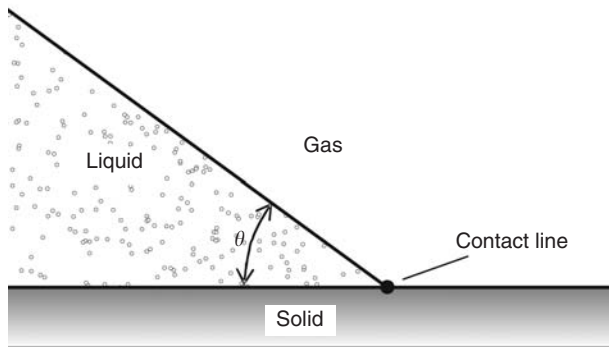


FIGURE 12.34 Sketch defining the contact angle and the contact (or triple) line.

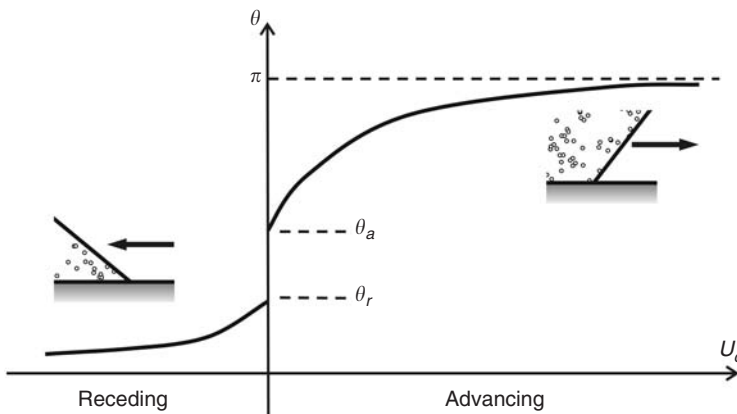


FIGURE 12.35 Hysteresis of the dynamic contact angle.

Next, the static advancing, θ_a , and static receding, θ_r , contact angles can be defined as two different limits of the dynamic contact angle as the velocity U_c approaches zero:

$$\theta_a = \lim_{U_c \rightarrow +0} \theta_d(U_c), \quad \theta_r = \lim_{U_c \rightarrow -0} \theta_d(U_c)$$

The hysteresis in the values of θ_a and θ_r is related to the microstructure of the surface (roughness, chemical nonhomogeneity) and the presence of impurities in the liquid and on the substrate. The contact angle of the liquid in the equilibrium state can thus vary in the range $\theta_r < \theta < \theta_a$.

The dynamic contact angle at $\theta_c \approx 0$ and $Ca \ll 1$ depends on the capillary number Ca only (Hoffman, 1975). An empirical correlation for the dynamic contact angle for such cases is obtained in Voinov (1976) and Tanner (1979) in the form

$$\theta_d \sim Ca^{1/3} \quad (12.78)$$

which is known as the *Hoffman–Voinov–Tanner law* (Kistler, 1993).

Generally, the dynamic contact angle may also depend on the hydrodynamics of the liquid behind the contact line. Two main approaches to the problem of dynamic contact angle are considered to date: the hydrodynamic approach (with the most general analysis in Cox (1986)) and the molecular-kinetic approach (initiated in Blake, 1968; Blake and Haynes, 1969). See the detailed reviews of the wettability phenomena and modelling in Kistler (1993) and Blake (1993). More recent work can be found in Blake et al. (1999).

Some biological or micro- and nanostructured surfaces are extremely hydrophobic. Barthlott and Neinhuis (1997) studied the morphology of lotus plant leaves, revealing a self-cleaning property through rain, fog or dew (Lotus effect). Considerable effort is presently being directed toward producing synthetic water-repellent surfaces with prescribed surface morphologies. Onda et al. (1996) produced a fractal alkylketene dimer (AKD), reaching an apparent contact angle in their experiments of 174°C, Bico et al. (1999) and Richard and Qu  r   (2000) have investigated a single drop impact onto such highly hydrophobic surfaces, observing that the drop can fully bounce after impact on such surfaces.

Spontaneous drop spreading is analysed in the theoretical works of Hocking and Rivers (1982), Dussan and Chow (1983), Pozdikidis (1990), and Reznik and Yarin (2002). The inertial effects in such low-speed drop impacts are small in comparison with the capillary forces and viscous drag. At higher impact speeds, inertia and viscous forces can no longer be neglected, and this situation is considered in the following section.

12.3.3.2 Drop Impact onto a Dry Substrate

The phenomenon of drop impact onto a dry substrate can be subdivided into several main phases, shown in Figure 12.36. The first phase is the initial drop deformation during which the drop shape transforms from a nearly spherical shape into a thin liquid film (lamella) expanding on the wall. The duration of this first phase is approximately $t_{\text{init}} \sim D_0/U_n$, where D_0 is the initial drop diameter and U_n is the normal component of the impact velocity. During the second phase of the drop impact, the spreading lamella is bounded by a rim, formed by capillary forces. The formation of this rim leads to the typical pizza-like shape of a spreading drop. The position of the rim determines the size and the shape of the wetted spot on the substrate. At some time instant $t = t_{\text{max}}$, the size of the wetted spot reaches a maximum. Then, if the substrate is partially hydrophobic, the drop begins to recede, leading to the third phase of drop impact. At some further time instant $t = t_{\text{merg}}$, the rim merges. If the kinetic energy of the rim at the time instant $t = t_{\text{merg}}$ is high enough, the rim-merging process can lead to the appearance of a finger-like central jet ejected from the surface.

If the Reynolds and the Weber numbers are high, the first phase of the initial deformation and the spreading of the drop are dominated by inertia. The evolution of the drop diameter during these two phases and the value of the maximum spread diameter are almost independent of the static contact angle (Rioboo et al., 2002). The receding of the drop is, in contrast, caused by the forces associated with the wettability.

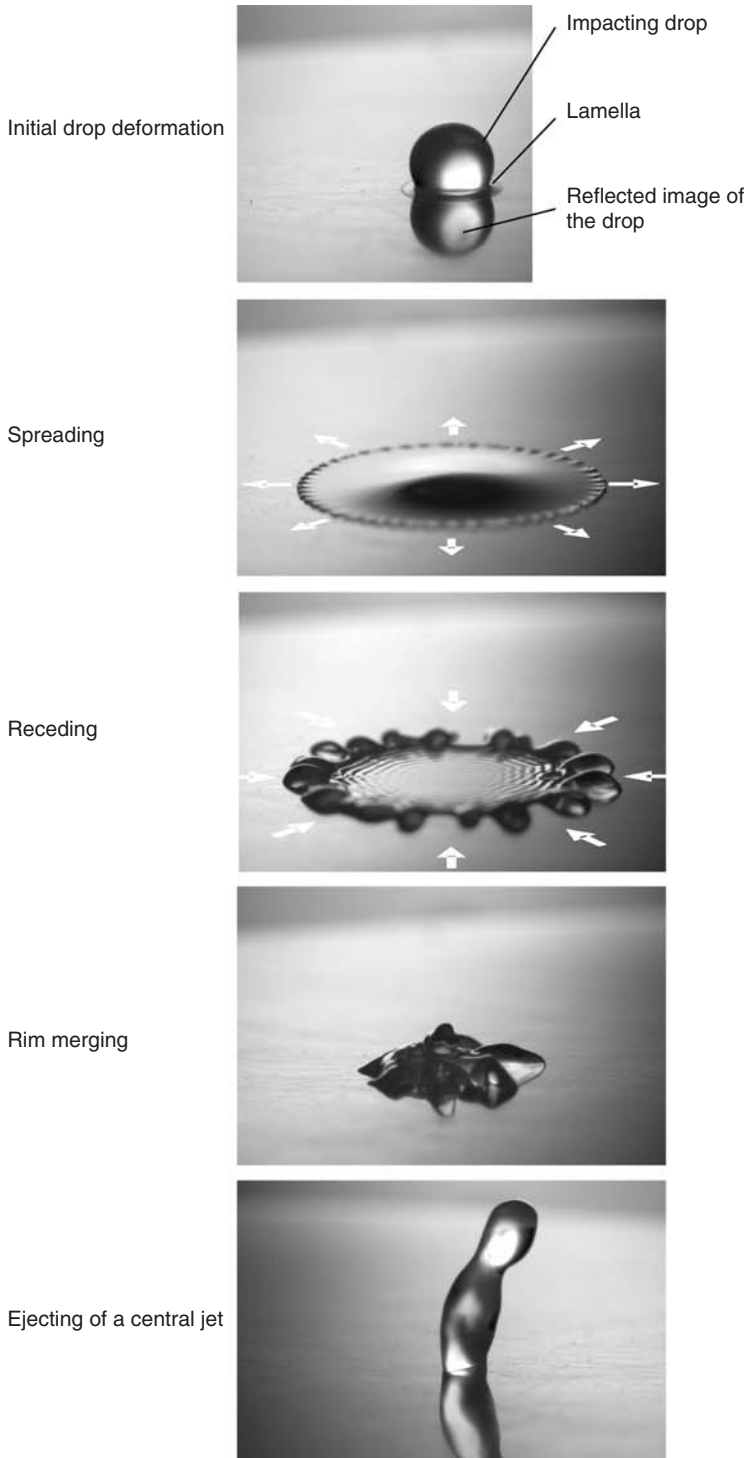


FIGURE 12.36 Stages of single drop impact onto a dry, partially wettable substrate. (Adapted from Rioboo, R., Marengo, M. and Tropea, C., *Exp. Fluids*, 33, 112, 2002.)

In each stage of impact, the drop can lose its stability and break up. The experimental studies of drop impact focus mainly on the determination of the various outcomes of the impact event (see Hartley and Brunskill, 1958; Levin and Hobbs, 1971; Stow and Stainer, 1977; Stow and Hadfield, 1981; Mao *et al.*, 1997; Range and Feuillebois, 1998). The influence of the surfactants added to the liquid on the evolution of the diameter of the spreading drop is studied in Mourougou-Candoni *et al.* (1999).

A number of different outcomes of drop impact are classified in Rioboo *et al.* (2001) (see Figure 12.37). A *prompt splash* occurs at high impact velocities on a rough surface during the first stage of initial drop deformation. A number of jets are formed in the region of the contact line as a result of its perturbation by the wall's roughness. These jets then break up into secondary droplets. The mechanism of *corona splash* after a drop impact onto a dry wall is not yet completely clear. It can be caused either by air entrainment into the contact line region or by the bending instability of a lamella spreading radially on the substrate. This type of splash is more typical for the high-speed drop impact onto a wetted wall. At some time instant this lamella (initially planar) begins to deform and to eject a nearly cylindrical, uprising crown-like sheet. A number of small jets then appear at the edge of this sheet, subsequently breaking up into secondary droplets. The drop can also break up during its receding phase. This *receding breakup* is caused by a disjoining of the contact line due to the local wall microstructure or chemical inhomogeneity. The *partial rebound* occurs when the duration of the central jet stretching is longer than the time required for its capillary breakup. Drop impact onto a highly hydrophobic surface can lead to a complete *rebound*. If the parameters of drop impact are below the splashing threshold it *deposits* on the surface without breakup.

An empirical relation for the splashing threshold is obtained in Mundo *et al.* (1998). The drop will not splash if

$$K = WeOh^{-0.4} < 657 \quad (12.79)$$

A recent study of drop impact onto inclined surfaces (Šikalo, 2003) indicates that this relation is also applicable if only the wall-normal component of velocity is used. Alternative but very similar relations for the splash limit on dry surfaces have been suggested by Marengo (1999) and Samenfink (1997)

The evolution of drop diameter can also be influenced by the addition of additives to the liquid, for example, surfactants.

12.3.3.3 Drop Impact onto a Wetted Wall

Numerous studies of drop impact onto a liquid film have led to similar data concerning the splash threshold, drop shape, crown propagation, fingering of the rim, etc. (Levin and Hobbs, 1971; Macklin and Metaxas, 1976; Cossali *et al.*, 1997; Cossali *et al.*, 2004).

Depending on the impact parameters and the film thickness, several impingement regimes have been determined. The collision can result in *sticking*, *rebound*, *deposition*, and *splash* (Stanton and Rutland, 1996) as shown in Figure 12.38. In Cossali *et al.* (1997) two types of splash were observed: *corona splash* (when the impact results in the creation of a crown-like sheet, which then breaks up) and *prompt splash* (when small secondary droplets are ejected from the region where the drop contacts the free surface of the film). Also the formation of a central finger-like jet was observed in the case of high-velocity impact into a deep pool or onto a relatively thick film (Ogüz and Prosperetti, 1990).

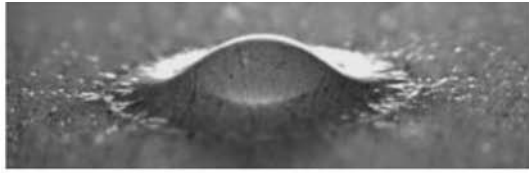
The stick regime occurs when the nearly spherical drop adheres to the film. The condition for the stick regime, $We < 5$ in Stanton and Rutland (1996), is based on the experimental results of Rodrigues and Mesler (1985), Walzel (1980), Jayaratne and Mason (1964).

The rebound regime occurs in the Weber number range $5 < We < 10$ (Rodrigues and Mesler, 1985). For a Weber number > 10 , the deposition of the impinging drop takes place when the parameters of the impact are below the splash threshold.

The splash threshold represents the conditions at which secondary droplets are first observed and takes a form similar to Eq. (12.79), with empirical modifications for the liquid film. (Samenfink, 1997; Mundo *et al.*, 1998; Cossali *et al.*, 1997; Wang and Chen, 2000).

Cossali *et al.* (1997) have obtained images of a splashing drop, showing the details of crown formation and jetting. The following empirical relation for the critical K number, depending on the dimensionless

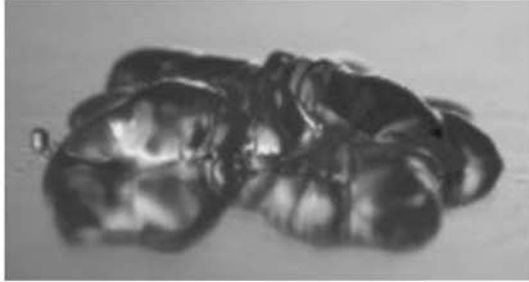
Prompt splash



Corona splash



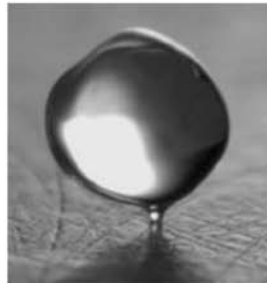
Receding break-up



Partial rebound



Rebound



Deposition

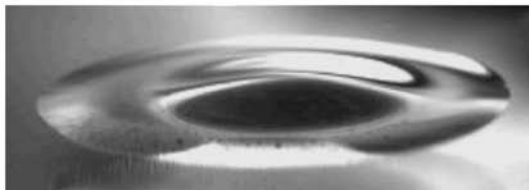


FIGURE 12.37 Classification of different outcomes of drop impact onto a dry substrate. The images are from Rioboo, R. et al., *Atomization Sprays*, 11, 155, 2001.

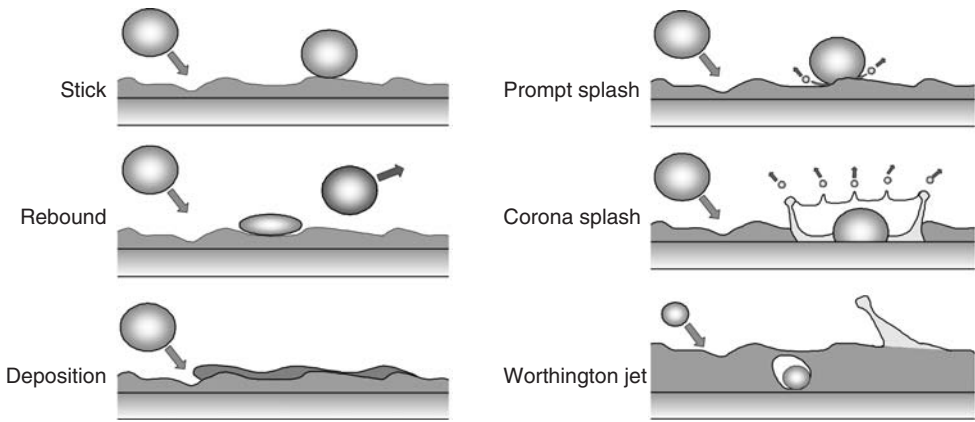


FIGURE 12.38 Single drop impact onto a wetted surface.

film thickness δ (scaled to the drop diameter), has been proposed:

$$K = 2100 + 5800\delta^{1.44} \quad \text{for } 0.1 < \delta < 1 \quad \text{and} \quad Oh > 7 \times 10^{-3} \quad (12.80)$$

Note that in spite of the fact that the K number is a parameter having “round” powers of We and Oh , it is completely empirical.

Oguz and Prosperetti (1990) have studied the impact of a single drop in a deep pool or relatively thick liquid film. The main subjects of this experimental, theoretical, and numerical study were the crater expansion in the liquid pool, bubble entrapment, and the creation of the central jet. The dominant factors influencing the phenomenon are the inertia of the liquid, capillary forces, and gravity. Bubble entrainment takes place in the range of parameters

$$41.3 Fr^{0.179} < We < 48.3 Fr^{0.247} \quad (12.81)$$

where $Fr = U^2/(gD_0)$ is the Froude number; and g the acceleration due to gravity. These upper and lower bounds are obtained by fitting the experimental data.

12.3.3.4 Theoretical Modeling of Drop Impact

The modeling of drop impact phenomena involves the description of an unsteady flow governed by inertia, capillary forces, and viscous drag. In the case of drop impact onto a dry wall, the forces associated with surface wettability are also important.

One parameter characterizing drop impact onto a dry wall is the maximum spread diameter. Most of the models are based on the energy balance of the drop (Collins et al., 1990; Chandra and Avedisian, 1991; Pasandideh-Fard et al., 1996; Fukai et al., 1995; Mao et al., 1997). In all of these approaches, the drop shape is assumed to be a disc at the instant when the drop diameter reaches its maximum value. Moreover, the total kinetic energy of the drop at this instant is assumed to vanish.

Another feature of drop impact is the instability of the lamella, leading to its breakup, which has been studied by Kim et al. (2000), and Fedorchenko and Chernov (1999).

In the study of the normal impact of a drop onto a dry, partially wettable wall (Roisman et al., 2002), the temporal evolution of the drop diameter — its spreading and receding — is determined by the motion of a torus-like rim, bounding a thin radially expanding film (lamella). The equations of motion of the film are obtained from its mass and momentum balance.

One important result of the studies of drop impact onto a stationary uniform liquid film is the temporal expansion of the radius R_{cr} of the crown. The dependence $R_{cr} \sim \sqrt{t}$ is obtained by Yarin and Weiss (1995), who describe the base of the crown as a kinematic discontinuity in the liquid film. In recent work (Trujillo and Lee, 2001), this theory is modified by taking into account the effect of the viscous forces.

In Roisman and Tropea (2002), the theory of the formation of the uprising sheet and its shape, valid for the general, nonaxisymmetric case, is developed. All of these models have been developed for the case of drop impact onto relatively thin films ($\delta < 0.5$).

12.4 Particle Interactions

Y. Tsuji and R.W. Lyczkowski

With respect to the particle–particle interactions in multiphase flow dynamics, two phenomena are identified. One is collision and the other is contact. From the viewpoint of physics, collision and contact do not differ much. Collision is merely contact with a short time duration. However, the approach of modeling is different for each. For collision or contact, two models are normally used: the hard particle model and the soft-particle model.

The hard particle model is easy to use but applicable only to the binary collision. The relation between the pre- and postcollision velocities is given explicitly using the coefficient of restitution and friction coefficient. When the particulate phase is dispersed, it is sufficient to consider only simple binary collisions and not multiple collisions.

In the soft particle model, the whole process of collision or contact is solved by the numerical integration of the equations of motion. The computation time is much longer using the soft particle model than in the hard particle model, but the applicability is wider for the soft particle model than the hard particle model.

Another important issue is the erosion associated with particle-wall contact. Particles impacting a wall can remove material, the amount depending on the impact velocity, the approach angle and the properties of the material.

12.4.1 Particle–Particle Collision

Y. Tsuji

In general, particle–particle collision is negligible in dilute gas–particle flows. While this is true in most cases, whether particle–particle collision should be considered or not depends not only on particle concentration, but also on the velocity fluctuation or relative velocity between individual particles. If all the particles move at the same velocity, particles do not collide no matter how high the concentration is. On the other hand, recent studies (Yamamoto et al., 2001) have shown that particle–particle collision should not be neglected at volume fractions greater than 10^{-4} . Dense and dilute flows are discussed in Section 1.2.6.

When particles collide, they lose kinetic energy due to the inelastic property of the particle material. The case of the two spheres shown in Figure 12.39 is considered here. Section 12.4.1.1 describes the hard sphere model and Section 12.4.1.2 describes the soft sphere model.

12.4.1.1 Hard Sphere Model

The hard sphere model is based on the impulsive force which is defined by the integral of the force acting on a particle versus time. If the particles are assumed to be rigid spheres, the impulsive equations are given as follows.

$$m_1(\mathbf{v}_1 - \mathbf{v}_1^{(0)}) = \mathbf{J} \tag{12.82}$$

$$m_2(\mathbf{v}_2 - \mathbf{v}_2^{(0)}) = -\mathbf{J} \tag{12.83}$$

$$I_1(\boldsymbol{\Omega}_1 - \boldsymbol{\Omega}_1^{(0)}) = a_1 \mathbf{n} \times \mathbf{J} \tag{12.84}$$

$$I_2(\boldsymbol{\Omega}_2 - \boldsymbol{\Omega}_2^{(0)}) = a_2 \mathbf{n} \times \mathbf{J} \tag{12.85}$$

where \mathbf{n} is the normal unit vector directed from particle 1 to particle 2 at the moment of contact and \mathbf{J} is the impulsive force exerted on particle 1, which acts on particle 2 as the reaction; subscripts 1 and 2 refer to the two particles. The superscript (0) signifies values before collision and I is the moment of inertia given by $I = (2/5)ma^2$. In the above equations, the particle mass m , size (radius = a), velocities before collision

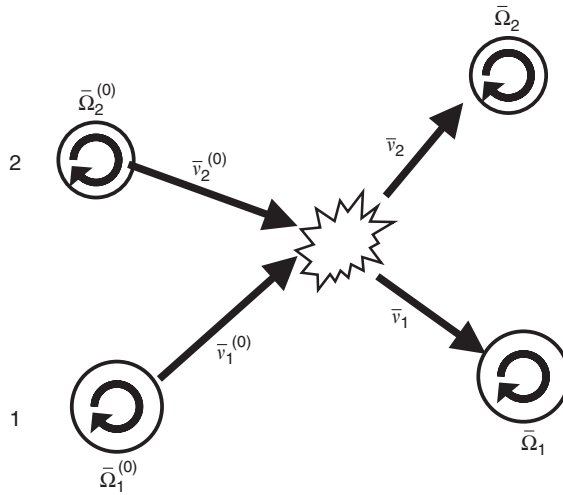


FIGURE 12.39 Particles colliding.

TABLE 12.4 Relation between Particle Velocities Before and After Collision

Condition	$\frac{\mathbf{n} \cdot \mathbf{G}^{(0)}}{ \mathbf{G}_{ct}^{(0)} } < \left(\frac{2}{7}\right) \frac{1}{f(1+e)}$	$\frac{\mathbf{n} \cdot \mathbf{G}^{(0)}}{ \mathbf{G}_{ct}^{(0)} } > \left(\frac{2}{7}\right) \frac{1}{f(1+e)}$
Translation velocity	$\mathbf{V}_1 = \mathbf{V}_1^{(0)} - (\mathbf{n} - f\mathbf{t})(\mathbf{n} \cdot \mathbf{G}^{(0)})(1+e) \frac{m_2}{m_1 + m_2}$ $\mathbf{V}_2 = \mathbf{V}_2^{(0)} + (\mathbf{n} - f\mathbf{t})(\mathbf{n} \cdot \mathbf{G}^{(0)})(1+e) \frac{m_1}{m_1 + m_2}$	$\mathbf{V}_1 = \mathbf{V}_1^{(0)} - \left\{ (1+e)(\mathbf{n} \cdot \mathbf{G}^{(0)})\mathbf{n} + \frac{2}{7} \mathbf{G}_{ct}^{(0)} \mathbf{t} \right\} \frac{m_2}{m_1 + m_2}$ $\mathbf{V}_2 = \mathbf{V}_2^{(0)} + \left\{ (1+e)(\mathbf{n} \cdot \mathbf{G}^{(0)})\mathbf{n} + \frac{2}{7} \mathbf{G}_{ct}^{(0)} \mathbf{t} \right\} \frac{m_1}{m_1 + m_2}$
Angular velocity	$\boldsymbol{\Omega}_1 = \boldsymbol{\Omega}_1^{(0)} + \left(\frac{5}{2a_1}\right) (\mathbf{n} \cdot \mathbf{G}^{(0)})(\mathbf{n} \times \mathbf{t}) f(1+e) \frac{m_2}{m_1 + m_2}$ $\boldsymbol{\Omega}_2 = \boldsymbol{\Omega}_2^{(0)} + \left(\frac{5}{2a_2}\right) (\mathbf{n} \cdot \mathbf{G}^{(0)})(\mathbf{n} \times \mathbf{t}) f(1+e) \frac{m_2}{m_1 + m_2}$	$\boldsymbol{\Omega}_1 = \boldsymbol{\Omega}_1^{(0)} - \frac{5}{7a_1} \mathbf{G}_{ct}^{(0)} (\mathbf{n} \times \mathbf{t}) \frac{m_2}{m_1 + m_2}$ $\boldsymbol{\Omega}_2 = \boldsymbol{\Omega}_2^{(0)} - \frac{5}{7a_2} \mathbf{G}_{ct}^{(0)} (\mathbf{n} \times \mathbf{t}) \frac{m_2}{m_1 + m_2}$

Note: e , coefficient of restitution; f , Coulomb's friction coefficient; $\mathbf{G}^{(0)} = \mathbf{v}_1^{(0)} - \mathbf{v}_2^{(0)}$ is the relative velocity of particle centers before collision; $\mathbf{G}_{ct}^{(0)} = \mathbf{G}^{(0)} + \alpha_1 \boldsymbol{\Omega}_1^{(0)} \times \mathbf{n} + \alpha_2 \boldsymbol{\Omega}_2^{(0)} \times \mathbf{n}$ is the relative velocity of the contact point before collision; $\mathbf{t} = \mathbf{G}_{ct}^{(0)} / |\mathbf{G}_{ct}^{(0)}|$ is the unit vector of the tangential direction.

$\mathbf{v}^{(0)}$, and positions before collision are given. The unknown variables are the impulsive force J and the post-collision velocities \mathbf{v} . The above equations can be solved analytically with some assumptions. The results are shown in Table 12.4. The derivation of the solutions is described in Crowe et al. (1997a).

12.4.1.2 Soft Sphere Model

12.4.1.2.1 Modeling

The basic concept of the soft sphere model is the same as the damping vibration shown in Figure 12.40. The motion of the body with mass m is given by the following differential equation:

$$m\ddot{x} + \eta\dot{x} + kx = 0 \tag{12.86}$$

where x is the distance from the equilibrium position of the mass, η the damping coefficient of the dash-pot, and k is the stiffness of the spring. In the above equation, the relationship between the force and

displacement is assumed to be linear. The kinetic energy is lost in the dashpot. The work by the dashpot is proportional to the velocity of the mass. There are three modes of motion depending on the parameters: underdamping, overdamping, and critical damping modes.

In the soft sphere model, the same mechanism is assumed for the particle–particle interaction. Figure 12.41 shows that particle i approaches particle j under the influence of inertia and external forces. Particle i at the moment of contact is shown by the dotted line, and the two particles contact at the point C . In the next moment, contact forces occur between the two particles. Actually, the particles should deform and the contact forces could be functions of deformation. In the soft sphere model, the two particles approaching with a relative velocity are made to overlap without changing their shapes. The overlap distance δ is made to correspond to the deformation of the particles. The larger the overlap distance, the larger is the contact force.

A model based on the damping vibration is convenient to express the contact force. Thus, a spring, a dash-pot, and other mechanical components are set between particle i and particle j as shown in Figure 12.42, where the figure (a) corresponds to the case of the normal force and (b) to the case of the tangential force. The coupler shown in Figure 12.42 connects the two particles when they are in contact but allows the particles to separate under the influence of repulsive forces. The tangential force is modeled by a spring and dash-pot in the same way as the normal force as shown in Figure 12.42b. If the tangential force exceeds the yield stress, the two particles slide under the application of a normal force and a friction force results. To express this friction force, a friction slider is set in Figure 12.42b. This model for contact forces was proposed by Cundall and Stack (1979). With the soft sphere model, not only can the relationship between pre- and post-collision velocities be obtained but also the forces acting on the spheres during contact.

With the hard sphere model, the post-collision velocities are given as functions of precollision velocities and other parameters such as the coefficient of restitution and the friction coefficient. The soft sphere model starts with the differential equations. Therefore, variations of momentum and displacement are obtained for arbitrary times as solutions of the differential equations.

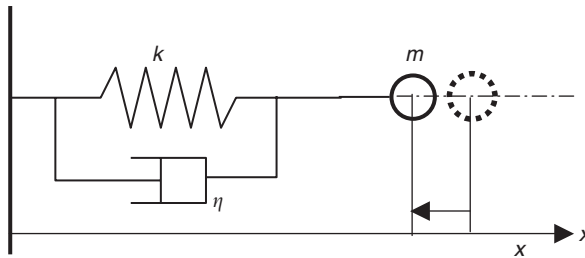


FIGURE 12.40 Damping vibration.

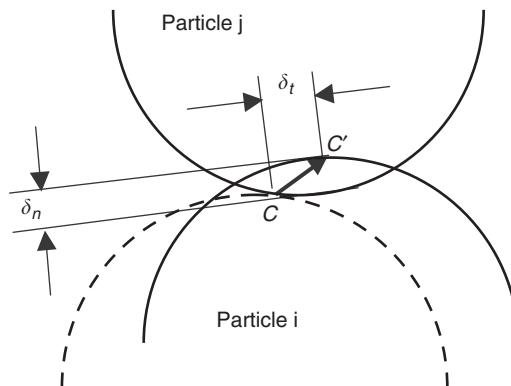


FIGURE 12.41 Two particles contacting.

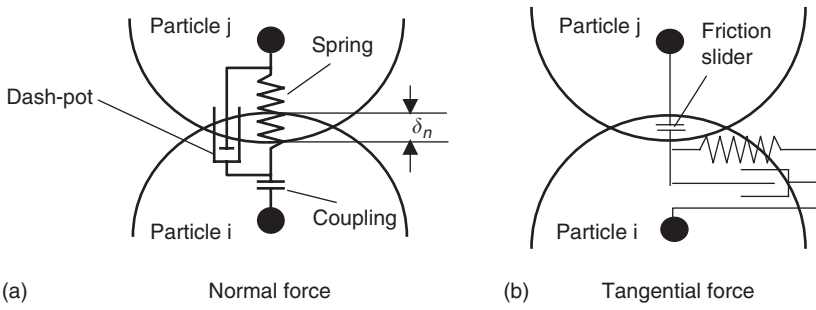


FIGURE 12.42 Soft sphere model.

The effects of these mechanical components on particle motion appear through the following parameters: stiffness K ; damping coefficient η ; and friction coefficient f .

The normal component of the contact force, F_{nij} , acting on particle i is given by the sum of the forces due to the spring and the dash-pot. If the particles are assumed to be two-dimensional disks, the effect of the spring is linear against the overlap distance, and the force F_{nij} is expressed by

$$F_{nij} = (-k_n \delta_n - \eta_{ij} \mathbf{G} \cdot \mathbf{n}) \mathbf{n} \tag{12.87}$$

where δ_n is the overlap distance (displacement of particle caused by the normal force), \mathbf{G} is the velocity vector of particle i relative to particle j , and ($\mathbf{G} = \mathbf{v}_i - \mathbf{v}_j$), and \mathbf{n} is the unit vector drawn from the center of particle i to that of particle j . According to Hertzian contact theory, the normal force varies to the $3/2$ power of the displacement in the case of three-dimensional spheres and, therefore, the force F_{nij} acting on particle i regarded as a sphere is expressed by

$$F_{nij} = (-k_n \delta_n^{3/2} - \eta_{ij} \mathbf{G} \cdot \mathbf{n}) \mathbf{n} \tag{12.88}$$

The tangential component of the contact force, F_{tij} is given by

$$F_{tij} = -k_t \delta_t - \eta_{ij} \mathbf{G}_{ct} \tag{12.89}$$

where k_t and η_{ij} are, respectively, the stiffness and damping coefficient in the tangential direction, and \mathbf{G}_{ct} is the slip velocity of the contact point, given by

$$\mathbf{G}_{ct} = \mathbf{G} - (\mathbf{G} \cdot \mathbf{n}) \mathbf{n} + a_i \boldsymbol{\Omega}_i \times \mathbf{n} + a_j \boldsymbol{\Omega}_j \times \mathbf{n} \tag{12.90}$$

where a_i , a_j are the radii of particle i and particle j , respectively.

Note that the tangential displacement δ_t is a vector and its direction is not equal to the slip velocity vector \mathbf{G}_{ct} in three-dimensional motion in general. If the following relation

$$|\mathbf{F}_{tij}| > f |\mathbf{F}_{nij}| \tag{12.91}$$

is satisfied, particle i slides and the tangential force is given by

$$\mathbf{F}_{tij} = -f |\mathbf{F}_{nij}| \mathbf{t} \tag{12.92}$$

instead of Eq. (12.89). Equation (12.92) is the Coulomb-type friction law. The friction coefficient f is measurable and regarded as a parameter, that can be given empirically. The vector \mathbf{t} in Eq. (12.92) is the unit vector defined by

$$\mathbf{t} = \frac{\mathbf{G}_{ct}}{|\mathbf{G}_{ct}|} \tag{12.93}$$

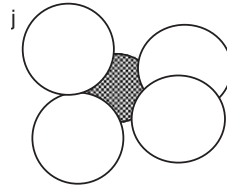


FIGURE 12.43 Particle with several contact forces.

In general, several particles are in contact with particle i at the same time as shown in Figure 12.43. Therefore, the total force and torque acting on particle i is obtained by taking the sum of the above forces with respect to j .

$$\mathbf{F}_i = \sum_j (\mathbf{F}_{nij} + \mathbf{F}_{tij}) \tag{12.94}$$

$$\mathbf{T}_i = \sum_j (a\mathbf{n} \times \mathbf{F}_{ij}) \tag{12.95}$$

12.4.1.2.2 Determination of Stiffness k , Damping Coefficient η , and Friction Coefficient f

The stiffness k_n can be given using the Hertzian contact theory when physical properties such as the Young’s modulus and Poisson ratio are known. The stiffness of a sphere is expressed as

$$k_n = \frac{4}{3} \left(\frac{1 - \sigma_i^2}{E_i} + \frac{1 - \sigma_j^2}{E_j} \right)^{-1} \left(\frac{a_i + a_j}{a_i a_j} \right)^{1/2} \tag{12.96}$$

where E and σ are Young’s modulus and Poisson ratio, respectively, and a is the particle radius; subscripts i and j denote particle i and particle j , respectively.

If particle i and j have the same radii and the same physical properties, the stiffness k_n simplifies to

$$k_n = \frac{\sqrt{2rE}}{3(1 - \sigma^2)} \tag{12.97}$$

The tangential stiffness k_t can be given using Mindlin’s theory as

$$k_t = 8 \left(\frac{1 - \sigma_i^2}{H_i} + \frac{1 - \sigma_j^2}{H_j} \right)^{-1} \left(\frac{a_i + a_j}{a_i a_j} \right)^{1/2} \delta_n^{1/2} \tag{12.98}$$

where H_i and H_j are the shear moduli of particle i and particle j , respectively. If both particles have the same properties, the tangential stiffness k_t also simplifies to

$$k_t = \frac{2\sqrt{2rH}}{(2 - \sigma^2)} \delta_n^{1/2} \tag{12.99}$$

where H is related to the Young’s modulus E and Poisson ratio σ , as follows:

$$H = \frac{E}{2(1 + \sigma)} \tag{12.100}$$

As shown above, the stiffness can be determined by material properties. This is the advantage of this model. Unfortunately, it is often difficult in practice to use the stiffness calculated by the Hertzian theory, because the time step Δt for numerical integration is so small that an excessive amount of computational time is needed. It is empirically known that the time step Δt should be $< 1/10$ of the natural oscillation period $2\pi\sqrt{m/k}$ of a mass–spring system. Therefore, in many cases, a small value of stiffness is assumed for the convenience of the calculation. In some cases, the results based on a stiffness much smaller than an actual value are

not so different from those based on the precise stiffness value. Fortunately, this is the case for fluid–particle multiphase flows, where fluid forces acting on particles make the difference in stiffness a minor effect.

12.4.1.2.3 Damping Coefficient

Cundall and Strack (1979) proposed the following expressions for the damping coefficients:

$$\eta_n = 2\sqrt{mk_n} \quad (12.101)$$

$$\eta_t = 2\sqrt{mk_t} \quad (12.102)$$

which were derived for the critical damping condition of a single degree-of-freedom system consisting of a mass, spring, and dash-pot. The reason for choosing the critical damping condition, as shown in Eqs. (12.101) and (12.102), is the requirement that bouncing motion after collision should be damped as soon as possible.

Another method for determining the damping coefficient is based on the idea that the damping coefficient should be related to the coefficient of restitution, which is regarded as a physical property of the particle material. Fortunately, the coefficient of restitution can be measured in a simple experiment.

If the relationship between spring force and displacement is linear, the solution of Eq. (12.86) can be used to relate the damping coefficient to the coefficient of restitution (Tsuji et al., 1993). Let us assume that x denotes the distance of the particle center from the wall and the particle collides with the wall at time $t = 0$ with the initial velocity $v = v_0$ and initial position of particle center $x = x_0$. The initial velocity is negative. The underdamping solutions are given as

$$\text{Position } x = \frac{v_0}{q} \sin(qt) \exp(-\gamma\omega t) + x_0 \quad (12.103)$$

$$\text{Velocity } \dot{x} = \frac{v_0}{q} \exp(-\gamma\omega t) q \cos(qt) - \gamma\omega \sin(qt) \quad (12.104)$$

where $\omega = \sqrt{k/m}$, $\gamma = \eta/(2\sqrt{mk})$, and $q = \omega\sqrt{1 - \gamma^2}$.

The particle position decreases, reaches the minimum value, and recovers to the initial position at $x = x_0$ at $t = \pi/q$ which is equal to half of the oscillation period. The particle velocity at $t = \pi/q$ is expressed as

$$v_1 = [\dot{x}]_{t = \pi/q} = -v_0 \exp\left(-\frac{\gamma\omega\pi}{q}\right) \quad (12.105)$$

The ratio of v_1 to v_0 corresponds to the coefficient of restitution e :

$$e = \exp\left(-\frac{\gamma\omega\pi}{q}\right) \quad (12.106)$$

From the above equations,

$$\eta = -\frac{2\ln e}{\sqrt{\pi^2 + \ln e}} \sqrt{mk} \quad (12.107)$$

Tsuji et al. (1992) showed that the damping coefficient η_n for a nonlinear spring is numerically related to the restitution coefficient. According to Tsuji et al. (1992) the damping coefficient η_n is expressed by

$$\eta_n = \alpha \sqrt{mk_n} \delta_n^{1/4} \quad (12.108)$$

where α is a constant related to the coefficient of restitution. The relationship between α and coefficient of restitution e is shown in [Figure 12.44](#). With respect to the damping coefficient η_t in the tangential direction, the same value as used for η_n is often used for η_t , but with no firm justification.

12.4.1.3 Cohesive Force

Interparticle forces due to the wetness of particle surfaces, electrostatic charges, and the van der Waals forces are known to cause the adhesion of a particle to a wall or to another particle.

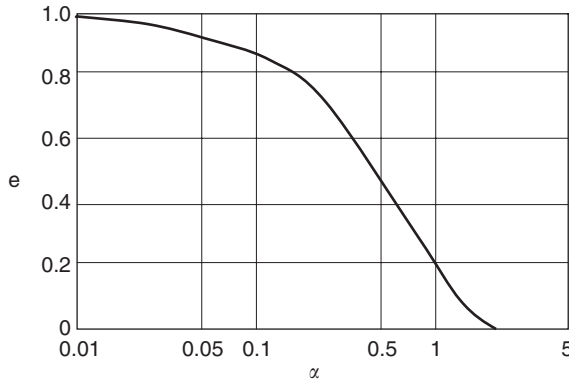


FIGURE 12.44 Relationship between α and coefficient of restitution e .

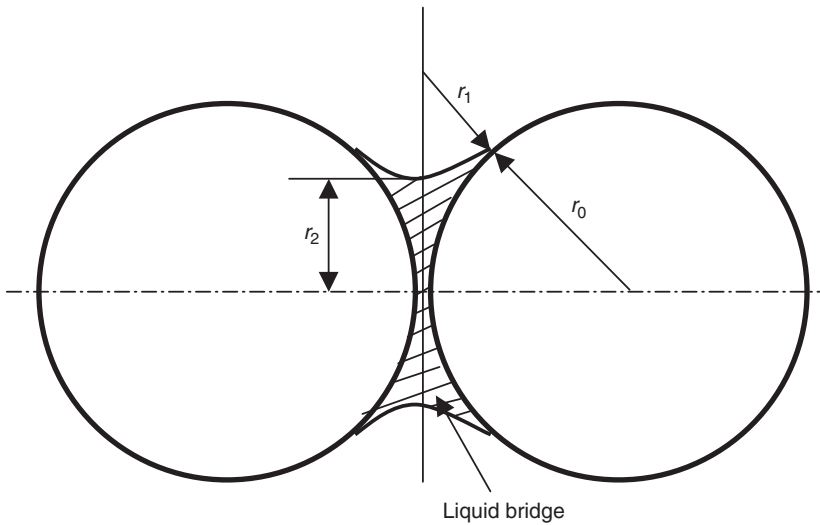


FIGURE 12.45 Liquid bridge between two spheres.

12.4.1.3.1 Force Due to a Liquid Bridge

As shown in Figure 12.45, a liquid bridge is formed between particles due to condensation under an environment of high humidity. The liquid surface is concave due to surface tension and the pressure is negative inside the bridge. The force acting on the particle is the sum of the force due to the negative pressure and the cohesive force due to capillarity.

The force due to the liquid bridge F_l is given as

$$F_l = \pi a_2^2 \sigma \left(\frac{1}{a_1} - \frac{1}{a_2} \right) + 2\pi a_2 \sigma \cos \theta \tag{12.109}$$

where σ is the surface tension (N/m) and θ the contact angle between the liquid and the particle surface. The contact angle θ can be assumed to be zero in the case of water. This equation is called the Laplace–Young equation.

12.4.1.3.2 Electrostatic Force

Particles in the gas are usually charged and an electrostatic force acts on the particles. Electrostatic force F_e between charged particles is given by the Coulomb formula

$$F_e = \frac{1}{4\pi\epsilon_0} \frac{q_1 q_2}{a^2} \quad (12.110)$$

where q_1 and q_2 are charges on the particles, ϵ_0 dielectric constant (F/m) in vacuum, and a is the distance between particle centers. If the signs of q_1 and q_2 are different, an attractive force acts on the two particles, and if not, the force is repulsive.

The cohesive force acting on the spherical particles in contact with each another is given by

$$F_E = \frac{\pi\sigma_1\sigma_2}{\epsilon_0} d^2 \quad (12.111)$$

where σ_1 and σ_2 are charge density (C/m²) of the two particles. The above equation is derived under the assumptions that the particles are charged uniformly and that charging can be regarded as concentrated at the particle centers. The effect of the particle size on the force is larger for the Coulomb cohesive force than for the van der Waals force.

12.4.1.3.3 van der Waals Forces

The van der Waals forces arise from molecular interaction between solid surfaces. This force becomes apparent when very smooth surfaces are brought into contact. To estimate the magnitude of van der Waals forces acting on solid bodies, the contribution of many molecules comprising the surfaces must be considered. Hamaker (1937) carried out calculations for various geometries. The force F between two infinite flat plates with separation z is expressed by

$$F = \frac{A}{6\pi z^3} \quad (12.112)$$

where F is the force per unit area and A is called the Hamaker constant. The force between the two spheres shown in Figure 12.46 is expressed by

$$F = \frac{Ad}{12z^2} \quad (12.113)$$

where z is the separation distance at the point of contact which is dependant on the roughness of the spheres and d is

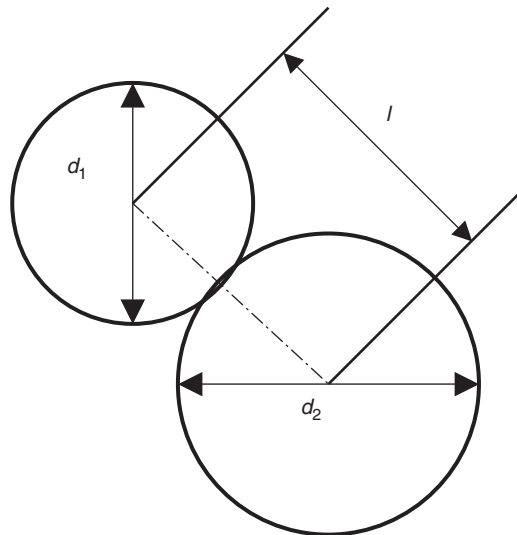


FIGURE 12.46 Two particles in contact.

TABLE 12.5 Hamaker Constant

Hamaker Constant Material	Hamaker Constant ($J \times 10^{20}$)
Water	4.38
Polystyrene	6.15 – 6.6
Al ₂ O ₃	15.5
Cu	28.4
Au	45.5

$$d = \frac{D_{p1}D_{p2}}{D_{p1} + D_{p2}} \tag{12.114}$$

The force between a sphere and a flat plate can be obtained by letting the diameter of one sphere be infinite, i.e., $d = D_p$ in Eq. (12.114). Table 12.5 shows examples of the Hamaker constant of various materials.

The Hamaker constant between different materials is given by

$$A_{12} = \sqrt{A_{11}A_{22}} \tag{12.115}$$

where A_{11} and A_{22} are the Hamaker constants of each material, respectively. The above relation is used for “dry” solids. If two solids are separated by a third material between them, the Hamaker constant is expressed by

$$A_{132} = (\sqrt{A_{11}} - \sqrt{A_{33}})(\sqrt{A_{22}} - \sqrt{A_{33}}) \tag{12.116}$$

where A_{33} is the Hamaker constant of the third material. The Hamaker constant A_{33} of air is very small and thus Eq. (12.116) is reduced to Eq. (12.115) in this case. Comparing Eqs. (12.115) and (12.116), it is found that the attractive force between two solids becomes smaller in water than in air. The above equation means that the sign of the van der Waals force between two solids can be negative, i.e., a repulsion force arises if A_{33} takes a value between A_{11} and A_{22} .

12.4.2 Particle–Wall Interaction

Y. Tsuji

The problem of particle–wall interaction is encountered when analyzing gas–particle flows contained within walls such as pipe flows, channel flows, and fluidized beds. The particle–wall interaction falls into two categories: hydrodynamic forces due to proximity of a wall and the purely mechanical interaction in the absence of a fluid. The Saffman lift force due to the velocity gradient near the wall is one example of hydrodynamic interaction. Another example is the fluid force acting on a particle approaching the wall in the normal direction. This interaction is observed when the case of two approaching particles is addressed. Assuming the diameter of one particle to be infinitely large, the particle–particle interaction is reduced to the particle–wall interaction. A hydrodynamic interaction of this type can prevent a particle from making contact with the wall. The postcollisional velocity of the particle is also affected by this interaction. This hydrodynamic interaction can be neglected if the particle inertia force is so large that collision takes place in a time that is small compared to the hydrodynamic relaxation time of the particle.

The treatment of the mechanical behavior associated with the particle–wall mechanical interaction depends on the inertia of the particle. When a massive particle collides with a wall, it rebounds but loses kinetic energy due to friction and inelasticity. For a very small particle approaching a wall, molecular forces become dominant compared with the inertia force. As a result, the particle is captured by the wall due to cohesion forces (Section 12.4.1.2), and neither rebounds from nor slides along the wall. Energy loss due to wall collision is considered in Section 12.4.2.1, where the analysis is based on a single spherical particle and a smooth wall. The energy loss at walls is readdressed in Section 12.4.2.2 where the case of a nonspherical particle impacting a rough wall is considered.

12.4.2.1 Momentum and Energy Exchange at Walls

Two models are used to deal with particle–wall and particle–particle collisions: the hard sphere model and the soft sphere model. The soft sphere model is based on the integrated forms of the equations of motion, namely, the impulsive equations. The particle velocities change continuously during the entire periods of pre-collision and post-collision, but the hard sphere model considers the momentum difference between periods. The difference in momentum between two instants of time is equal to the impulsive force acting on the particle during that time period:

$$m(\mathbf{v}^{(2)} - \mathbf{v}^{(1)}) = \mathbf{J} \quad (12.117)$$

where $\mathbf{v}^{(1)}$ and $\mathbf{v}^{(2)}$ are velocities at time 1 and time 2, respectively, and \mathbf{J} is the impulsive force acting on the particle during the period between the two times. The difference in angular momentum is expressed by

$$I(\Omega^{(2)} - \Omega^{(1)}) = -\mathbf{r} \times \mathbf{J} \quad (12.118)$$

where $\Omega^{(1)}$ and $\Omega^{(2)}$ are angular velocities at time 1 and time 2, respectively, and I is the moment of inertia of the particle. The impulsive force is defined by the integral of the force versus time when the force acts on the body. In general, Eqs. (12.117) and (12.118) are not sufficient to determine the relationship between the pre and postcollisional velocities. Auxiliary equations are necessary to close a set of equations. The auxiliary equations come from the concept of the coefficient of restitution and the friction coefficient.

In the soft sphere model, not only is the relationship between the pre and postcollisional velocities obtained, but the instantaneous motion during the whole collision process is obtained as well. In this section, the hard sphere model is explained while the soft sphere model is dealt with in Section 12.4.1.2.

Before proceeding to the analysis, it is necessary to define the coefficient of restitution e used in this section because the definition of e is somewhat arbitrary and there are few definitions available in the literature. Consider a particle colliding with a wall as shown in Figure 12.47. The symbol \mathbf{v} denotes the translation velocity. The velocity vector has two components: longitudinal component (x component) and the component normal to the wall (y component). The suffixes (0) and (2) denote the precollision velocity and postcollision velocities, respectively. The following definitions have been used in general:

$$e = \frac{|\mathbf{v}^{(2)}|}{|\mathbf{v}^{(0)}|} \quad (12.119)$$

$$e = \frac{v_y^{(2)}}{v_y^{(0)}} \quad (12.120)$$

$$e_x = v \frac{v_x^{(2)}}{v_x^{(0)}}, \quad e_y = v \frac{v_y^{(2)}}{v_y^{(0)}} \quad (12.121)$$

$$e = \frac{J'_y}{J_y} \quad (12.122)$$

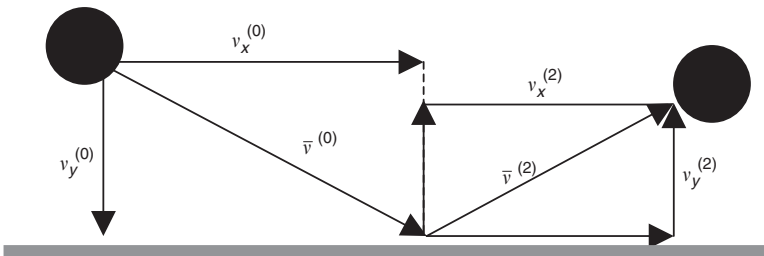


FIGURE 12.47 Particle colliding a wall.

where J_y and J'_y are the normal components of impulses acting on the particle during the collision period. The impulses J_y and J'_y are explained as shown in Figure 12.48. The process of collision is divided into two periods, one in which the material is compressed and the other in which the compression is released. J_y and J'_y are the y components of the impulsive force during the compression and recovery periods, respectively. Among the above four definitions, the second definition is used most widely. However, if this definition is adopted, the value of the coefficient for nonspherical particles depends on the location of the contact point between the particle and the wall. If the restitution coefficient is regarded as a property of the material, its value should not depend on the location of the contact point. From this point of view, a reasonable definition for the coefficient of restitution is given by Eq. (12.122). If the particle is a sphere, it is found that the impulse ratio J'_y/J_y is equal to the velocity ratio $v_y^{(2)}/v_y^{(0)}$.

Consider a three-dimensional collision of a spherical particle with a smooth flat wall, as shown in Figure 12.49. The velocities $v^{(0)}$ and $\Omega^{(0)}$ are the precollision translation and angular velocities, respectively. The corresponding post-collision velocities are expressed by $v^{(2)}$ and $\Omega^{(2)}$. The y -axis is normal to the wall and the x - and z -axis are in the plane of the wall. The subscripts x , y and z signify component directions. If the coefficient of restitution e and kinetic (sliding) friction f are known, the postcollision translation and angular velocities can be obtained by solving the impulsive equations. The results are shown in Table 12.6. In this table ϵ_x and ϵ_y are factors indicating the proportion of the velocity in each component direction, i.e., the direction cosines of the approaching velocity in the x - and z -plane. The factors ϵ_x and ϵ_y satisfy the relation

$$\epsilon_x^2 + \epsilon_z^2 = 1 \tag{12.123}$$

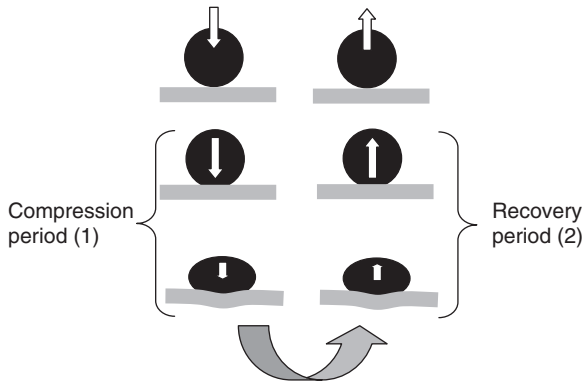


FIGURE 12.48 Compression and recovery periods in collision process.

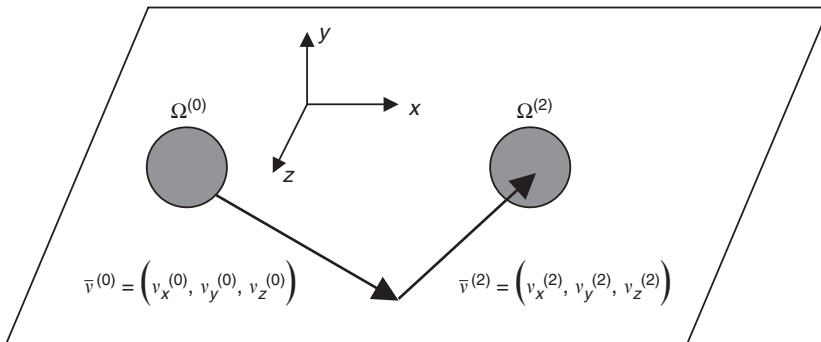


FIGURE 12.49 Three dimensional particle–wall collision.

TABLE 12.6 Relation Between Pre- and Post-Collisional Velocities

Condition	$\frac{v_y^{(0)}}{ \vec{v}^{(0)}} < -\frac{2}{7f(e+1)}$	$-\frac{2}{7f(e+1)} < \frac{v_y^{(0)}}{ \vec{v}^{(0)}} < 0$
Translation velocity	$v_x = \left(\frac{5}{7}\right)\left(v_x^{(0)} - \frac{2a}{5}\Omega_z^{(0)}\right)$ $v_y = -e v_y^{(0)}$ $v_z = \left(\frac{5}{7}\right)\left(v_z^{(0)} + \frac{2a}{5}\Omega_x^{(0)}\right)$	$v_x = v_x^{(0)} + \epsilon_x f(e+1)v_y^{(0)}$ $v_y = -e v_y^{(0)}$ $v_z = v_z^{(0)} + \epsilon_z f(e+1)v_y^{(0)}$
Angular velocity	$\Omega_x = \frac{v_z}{a}$ $\Omega_y = \Omega_y^{(0)}$ $\Omega_x = -\frac{v_x}{a}$	$\Omega_x = \Omega_x^{(0)} - \frac{5}{2a}\epsilon_z f(e+1)v_y^{(0)}$ $\Omega_y = \Omega_y^{(0)}$ $\Omega_z = \Omega_z^{(0)} + \frac{5}{2a}\epsilon_x f(e+1)v_y^{(0)}$

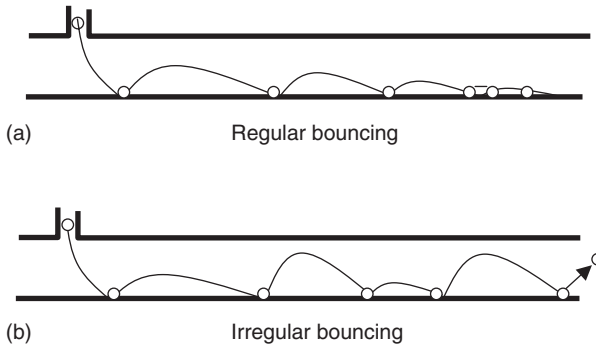


FIGURE 12.50 Regular and irregular bouncing.

In this analysis, Coulomb’s friction law is assumed for kinetic (sliding) friction

$$J_\tau = -f \cdot J_n \tag{12.124}$$

where J_τ and J_n are the tangential and normal components of the impulsive forces, respectively, and f is the friction coefficient. The derivation of the results is described in Crowe et al. (1997b).

12.4.2.2 Non-Spherical Particles: Rough Walls

When the coefficients of restitution e and dynamic friction f are given as physical properties of the particles, the postcollisional velocities can be expressed in terms of the precollisional velocities. The relation between these velocities for the case of a spherical particle and smooth wall is shown in Table 12.6. This relationship is useful for calculating particle trajectories in a field enclosed by walls. However, in some cases, the trajectory calculation in multiphase flows is not as straightforward as it might be. The coefficient of restitution e defined by Eq. (12.122) must be less than unity. If trajectory calculations were made for a long horizontal pipe or duct, particles repeatedly colliding with the wall would ultimately lose their vertical velocity component and slide along the wall as shown in Figure 12.50a. To avoid such an unrealistic result, the irregularity of collisions must be considered. If this irregularity is neglected, large particles cannot be suspended in the carrier fluid. Fluid dynamic forces, such as Magnus or shear lift forces, and fluid turbulence acting on the particles are sufficient to suspend small particles. However, the

mechanism responsible for suspending large particles in horizontal pipes is the irregular bouncing of the particles against the wall. In general, the irregularity is caused by particle shape (nonspherical particles) and/ roughness of the wall. In practice, both mechanisms are operative. Several models in regard to the irregular bouncing have been proposed. Those models are classified into two types: one in which the irregularity is attributed to the nonsphericity of the particle (Matsumoto and Saito, 1970a; Tsuji et al., 1989; 1991) and the other to wall roughness (Matsumoto and Saito, 1970b; Tsuji et al., 1987; Sommerfeld, and Zivkovis, 1992; Frank et al., 1993; Sommerfeld and Huber, 1999).

In the following paragraphs, first the nonspherical model and then the rough wall model are described. If the problem is two-dimensional, the treatment is relatively easy, because the cross-sectional shape of the particle is limited to a circle, ellipse, or an arbitrary shape. As shown in Figure 12.51, the distance between the particle center of gravity O and the contact point C depends on the incident attitude of the particle, which does not change in the case of a spherical particle. A set of values for r and θ shown in Figures 12.15b and c describe any particle shape. Impulsive equations are formed for a set of values for r and θ . In the numerical simulation, a pair of values for r and θ is chosen by random numbers. The post-collisional velocities are obtained from solutions of the impulsive equations.

It is difficult to deal, in a rigorous way, with the collision of an arbitrary three-dimensional, nonspherical particle having three components of translational and angular velocity. The complexity of the problem is reduced by using some assumptions. Examples of such assumptions are explained in Tsuji et al. (1991) and Crowe et al. (1997b).

The wall roughness model for irregular bouncing is shown in Figure 12.52. The choice of wall roughness is arbitrary. Several configurations could be considered, such as a wavy pattern, a combination of inclined planes, and so on. The calculation for a spherical particle bouncing on the rough wall is simpler than that for nonspherical particle on a flat wall if the pattern of roughness is specified, because the results shown in Table 12.6 can be used with some modifications. In the rough wall model, the point at which the particle collides with the wall is assumed to be on an inclined plane. Each inclined plane has its own coordinate system. The relationship between the coordinates, with and without an inclination angle, is easily described by using a matrix. Once particle velocities are transformed by the usual linear transformation technique into the coordinates corresponding to the inclined plane, the results shown in Table 12.6 can be used to obtain the post-collisional velocities. After this, the post-collisional velocities based on the coordinates on the

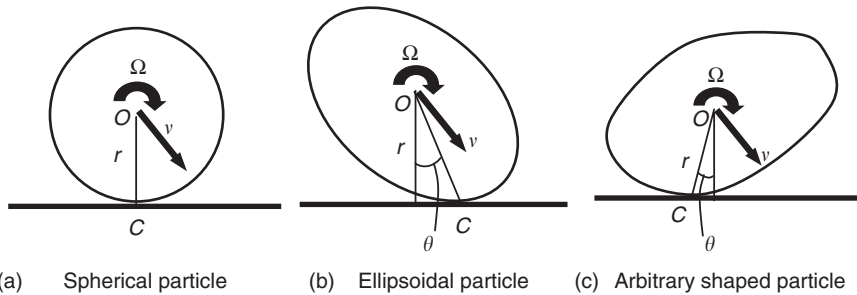


FIGURE 12.51 Contact point between particle and wall.

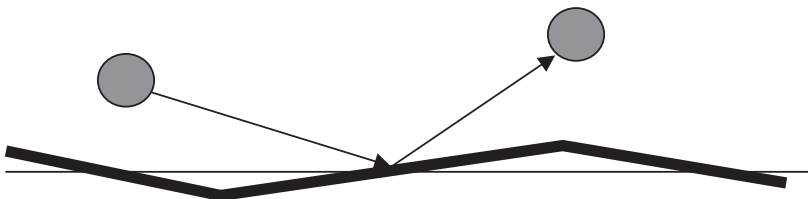


FIGURE 12.52 Particle collision with a rough wall.

inclined plane are retransformed into the original coordinate system. As with the nonspherical particle model, the rough wall models make it possible for the particles to move along with a bouncing motion in long, horizontal pipes or ducts.

Predicting the impact–rebound relations for particles with sharp edges, such as quartz particles, would be very difficult. Experiments (Tabakoff, 1982) with Quarta particles impacting on an aluminum surface show that for a given impact angle, there is a distribution of rebound angles. In this case, it is more pragmatic to use a Monte Carlo method with the measured distribution of rebound angles to model particle–surface impact.

12.4.3 Erosion*

R.W. Lyczkowski

A comprehensive literature review of erosion models is not attempted here. Engel (1978) has provided a good literature review up to 1978 and Sarkar (1980) has provided one up to 1980. The exhaustive review by Meng and Ludema (1995) found 182 equations for wear, and selected 28 for special study. A review done at the Morgantown Energy Technology Center (METC), now the National Energy Technology Laboratory (NETL), deals specifically with erosion in fluidized-bed combustors (FBCs), (Padyhe, 1985). Humphrey (1990) has reviewed the importance of various fundamental considerations relating to the motion of dilute suspensions of solids affected by the carrier fluid and a constraining surface. The summary of the models selected from the literature explains the criteria for their selection and points out their various shortcomings. The reasons leading to the more fundamental energy dissipation approach to modeling erosion are explained.

12.4.3.1 Single-particle Models

Single-particle erosion models treat the erosion process in terms of the interaction of a single particle with the eroding surface. Such models may be more appropriate for the case of erosion due to dilute solid suspensions, as in pneumatic conveying pipelines and elbows or in turbine blade cascades. In these cases, the particle–particle interactions are negligible, and the erosion process may be thought of as removal of surface material by the cumulative action of the individual particles. In this sense, these models are noncontinuum models.

12.4.3.1.1 Finnie's Ductile Erosion Model

According to Engel (1978), Finnie (1958) was the first to derive a single-particle erosive cutting model. Finnie (1960) discussed the assumptions of the model, quoted the results, and compared the results with experimental data. This model set the basic pattern and tone for all single-particle models, so it is discussed here in some detail. The major assumption is that a particle, approaching the eroding surface (or target) at angle α as measured from the surface (called the impingement angle), will remove material in much the same way as a machine tool would. The particle is assumed to be much harder than the surface and does not break up. The surface material is assumed to deform plastically during the cutting process; hence, the material is ductile. Ductile materials, such as aluminum or structural steel, can develop a relatively large tensile strength before they rupture.

The final expression for the volume of target material, W , removed and obtained by Finnie (1960) is as follows:

$$W = \begin{cases} c \frac{MV^2}{\Psi p K} \left[\sin(2\alpha) - \frac{6}{K} \sin^2(\alpha) \right], & \tan(\alpha) \leq \frac{K}{6} \\ c \frac{MV^2}{\Psi p K} \left[\frac{K \cos^2(\alpha)}{6} \right], & \tan(\alpha) > \frac{K}{6} \end{cases} \quad (12.125a)$$

$$(12.125b)$$

*Sections of this book chapter are corrected and condensed sections reprinted from *Progress in Energy and Combustion Science*, 28, Lyczkowski, R. W., and J. X. Bouillard, "State-of-the-Art Review of Erosion Modeling in Fluid/Solids Systems", 543-602, copyright 2002 with permission from Elsevier.

where M is the total mass of abrasive particles, V is the speed of the abrasive particles and, p is the eroding surface “flow stress.”

Finnie (1960) took $K = 2$, where K is the ratio of vertical to horizontal (frictional) force, and $\Psi = 1$, where Ψ is the ratio of the depth of contact to the depth of the cut. The constant c allows for the fact that many particles will not be as effective as the idealized model particle; Finnie arbitrarily took $c = 1/2$. To obtain the mass of eroded material removed, W is multiplied by ρ_t , the target density.

The erosion rate (or erosion velocity because it has dimensions of length/time), \dot{E} , is usually given as

$$\dot{E} = \dot{W}/A_t \tag{12.126a}$$

where \dot{W} is the volumetric rate of target material removal, and A_t is the average area of the target material. The erosion rate (or erosion velocity) of the target itself, \dot{E}_t , is given by

$$\dot{E}_t = -\dot{E} = -\dot{W}/A_t \tag{12.126b}$$

because the volumetric rate of change of the target itself is negative.

In order to apply the single-particle Finnie erosion model (or for that matter, any other single particle erosion model) to compute erosion rates for a continuum of solids, Eqs. (12.125a) and (12.125b) must be generalized. One way to do this is described below. Another way to do this is to use the kinetic theory of granular flow as described in Section 12.4.3.4.

First, the total particle mass, M , is replaced by the mass flux of solids, $\dot{m}_s = (1 - \epsilon)\rho_s v_s$, where $(1 - \epsilon) = \epsilon_s$ is the solids volume fraction, ρ_s is the particle density, and v_s is the magnitude of the velocity of the solids phase. The mass flux, \dot{m}_s , is assumed to be positive toward the eroding surface. The particle velocity, V , is replaced by v_s to obtain

$$\dot{E} = \begin{cases} C \frac{(1 - \epsilon)\rho_s v_s^3}{p} f(\alpha), & \dot{m}_s > 0 \\ 0, & \dot{m}_s < 0 \end{cases} \tag{12.127a}$$

where \dot{E} is the erosion rate (in m/sec) and $C = c/\Psi K$. The erosion rate is positive if the solids velocity vector points toward the eroding surface; otherwise, it is zero.

With $K = 2$, the angular dependency function $f(\alpha)$ is given by

$$f(\alpha) = \begin{cases} \sin(2\alpha) - 3\sin^2(\alpha), & \alpha \leq 18.43^\circ \\ \cos^2(\alpha)/3, & \alpha > 18.43^\circ \end{cases} \tag{12.127b}$$

$$\tag{12.127c}$$

Below 18.43° , the surface is cut until the particle leaves the surface; above 18.43° , cutting ceases before the particle leaves the surface. The transition angle 18.43° is close to the angle of maximum erosion, α_{\max} , given by Engel (1978) as

$$\alpha_{\max} = \frac{1}{2} \tan^{-1}(K/3) \tag{12.127d}$$

With $K = 2$, $\alpha_{\max} = 16.85^\circ$. Equation (12.127a) is in the same form as that used by Pourahmadi and Humphrey (1983) in their erosion modeling studies. They defined C as the fraction of particles cutting in an idealized manner, consistent with Finnie’s 1972 modification of his model. If one uses Finnie’s values of c , Ψ , and K , then $C = 1/8$.

Pourahmadi and Humphrey (1983) used the following expression for $f(\alpha)$:

$$f(\alpha) = \begin{cases} \sin(2\alpha) - 4 \sin^2(\alpha), & \alpha \leq 14.04^\circ \\ \cos^2(\alpha)/4, & \alpha > 14.04^\circ \end{cases} \tag{12.128a}$$

$$\tag{12.128b}$$

It may be that they used the original Finnie model with $K = 1.5$, in which case a value of $C = 1/6$ is obtained. Alternatively, they may have used Finnie's (1972) modified model, which accounted for particle inertia, with $K = 2$; in this case, $C = 1/8$. The value of C used by Pourahmadi and Humphrey (1983) is never mentioned, so either case is possible.

At 18.43° , Finnie's model ($K = 2, C = 1/8$) yields an erosion rate for ductile target materials given by

$$\dot{E}_{\text{FM}} = 0.075 \frac{\dot{m}_s v_s^2}{2p} \quad (12.129)$$

which is, in effect, the maximum value, \dot{E}_{FM} . Equation (12.129) predicts that only 7.5% of the particle's kinetic energy goes into erosion for a given hardness (or flow stress), p . The corresponding percentage for the Pourahmadi and Humphreys' expression ($C = 1/6$) is 7.8%. Using Eq. (12.129), Finnie (1960) analyzed some data taken for silicon carbide eroding SAE 1020 low carbon steel and found that the value of p exceeded the "true stress at fracture in a tension test" by a factor of almost 3. However, if Finnie's (1972) modification of his model (which accounts for particle inertia) is used together with his recommended values of c , Ψ , and K , then 5.9% of the particle's kinetic energy would go into erosion, instead of 7.5%.

Single-particle erosion models in general, and Finnie's erosion model in particular, cannot be used to calculate absolute erosion rates *a priori*. Finnie's erosion model can be used, together with estimates of target material flow stress (or hardness), to back out a value for parameter C to match the data. On the other hand, if a value for C is assumed, then the value of the flow stress or hardness appropriate for erosion is calculated from the data.

The angular dependence of the erosion rate predicted by using the original Finnie model and its first modifications is quite good up to 45° . Above 45° , the Finnie model underpredicts the erosion rate. At 90° , it predicts no erosion rate at all, whereas the analyzed data clearly indicate that this prediction is not correct. Further reworking of Finnie's theory did not resolve this problem (Finnie and McFadden, 1978). The Finnie model also predicts no erosion at 0° (scouring erosion). Shewmon and Sundararajan (1983) concluded from scanning electron microscope (SEM) examinations of erosion surfaces that the cutting tool analogy is not valid. They regarded the Finnie model to be of historical interest only and suggested other mechanisms for measuring the erosion rate, such as shear localization leading to lip formation and fracture.

12.4.3.1.2 Bitter's Combined Ductile and Brittle Erosion Model

The basic assumptions in Bitter's analysis are that deformation and cutting erosion occur simultaneously and that the two effects can be linearly superimposed (Bitter, 1963, 1963a). Thus, Bitter's work extends Finnie's model and corrects it by bringing in the concepts of a threshold erosion rate and energy dissipation. Physically, the impinging particle cannot erode the target material if its impacting velocity is smaller than a threshold velocity, V_{el} .

12.4.3.1.2.1 Brittle Erosion Model. In Bitter's model the brittle erosion rate is postulated to be equal to the energy dissipation of an elastic sphere deforming the planar target material surface elastically and plastically, divided by an energy (itself dependent on material properties) needed to remove material. This brittle erosion model is given by

$$W_b = \begin{cases} \frac{M[V \sin(\alpha) - V_{\text{el}}]^2}{2\varepsilon_b}, & V \sin(\alpha) > V_{\text{el}} \\ 0, & V \sin(\alpha) < V_{\text{el}} \end{cases} \quad (12.130a)$$

$$0, \quad V \sin(\alpha) < V_{\text{el}} \quad (12.130b)$$

where ε_b is the material-dependent deformation wear factor. The threshold velocity, V_{el} , is the velocity of collision at which the elastic limit of the eroding surface is just reached, given theoretically from the Hertz contact theory (Engel, 1978), by

$$V_{\text{el}} = 15.4 \sigma_y^{5/2} / (\rho_p^{1/2} E_r^2) \quad (12.131a)$$

where σ_y is the plastic load limit, ρ_p is the particle density, and E_r is the reduced Young's modulus of elasticity. The value of E_r is given by

$$E_r = \frac{1}{[(1 - \gamma_p^2)/(\pi E_p)] + [(1 - \gamma_t^2)/(\pi E_t)]} \equiv \frac{1}{(k_p + k_t)} \quad (12.131b)$$

where γ_p and γ_t are the Poisson's ratios, and E_p and E_t are the Young's moduli of elasticity, of the particle and target, respectively. The threshold velocity, V_{el} , which can be computed from Eq. (12.131a), can be determined from particle rebound data using the following relation (Bitter, 1963):

$$V_2 = (2V_1V_{el}^2)^{1/2} \quad (12.132)$$

where V_1 and V_2 are the velocities at the beginning (approach) and end (rebound) of collision, respectively.

12.4.3.1.2.2 Ductile Erosion Model. The portion of Bitter's model devoted to ductile erosion consists of the following:

$$Wd = \begin{cases} \frac{2MC'[V \sin(\alpha) - V_{el}]^2 V \cos(\alpha)}{[V \sin(\alpha)]^{1/2}} - \frac{C'[V \sin(\alpha) - V_{el}]^2}{[V \sin(\alpha)]^{1/2}} \phi, & \alpha \leq \alpha_0 \quad (12.133a) \\ \frac{M\{[V^2 \cos^2(\alpha)] - K_1[V \sin(\alpha) - V_{el}]^{3/2}\}}{2\phi} & \alpha > \alpha_0 \quad (12.133b) \end{cases}$$

where ϕ is the material-dependent cutting wear factor. The constants C' and K_1 are given by Neilson and Gilchrist (1968) as

$$C' = 0.288(\rho_p/\sigma_y)^{1/4}/\sigma_y \quad (12.134a)$$

and

$$K_1 = 8.036\sigma_y^2 E_r^{-2} (\sigma_y/\rho_p)^{1/4} \quad (12.134b)$$

The angle α_0 may be estimated from Finnie's model (Eq. [12.125]), or by equating Eqs. (12.133a) and (12.133b) and solving for α (Engel, 1978). The total erosion rate, W , is then given by the sum of W_b and W_d . The effect of K_1 is negligible in Eq. (12.133b) (where $\alpha > \alpha_0$) and can safely be dropped (Bitter, 1963a). If ϕ is associated with $3\Psi_p$ then (except for the factor c) Eq. (12.126b) ($\tan \alpha > K/6$) of Finnie's erosion model and Eq. (12.133b) ($\alpha > \alpha_0$) of Bitter's ductile erosion model are the same.

The interesting features of Bitter's model are that (1) for soft ductile materials, it produces wear curves similar to Finnie's, but with nonzero wear at 90°; and (2) for hard brittle materials, it produces wear curves that reach a maximum at 90°. The shapes of these curves are shown schematically in Figure 12.53.

Bitter's erosion model involves more material properties than Finnie's erosion model and includes those of the particle. However, Bitter's model still predicts zero wear at a zero impingement angle. In fact, the erosion rate is zero when $\alpha < \sin^{-1}(V_{el}/V)$, which is greater than zero. Bitter's model, like Finnie's, also assumes that the particles do not erode. The application of Bitter's model to the calculation of wear for a continuum of solids would be essentially the same as that for Finnie's model.

12.4.3.1.3 Neilson and Gilchrist's Combined Ductile and Brittle Erosion Model

Neilson and Gilchrist (1968) simplified Bitter's combined model by postulating a simplified ductile erosion model while retaining Bitter's brittle erosion model (Eqs. ([12.130]) and [12.131]). The result is

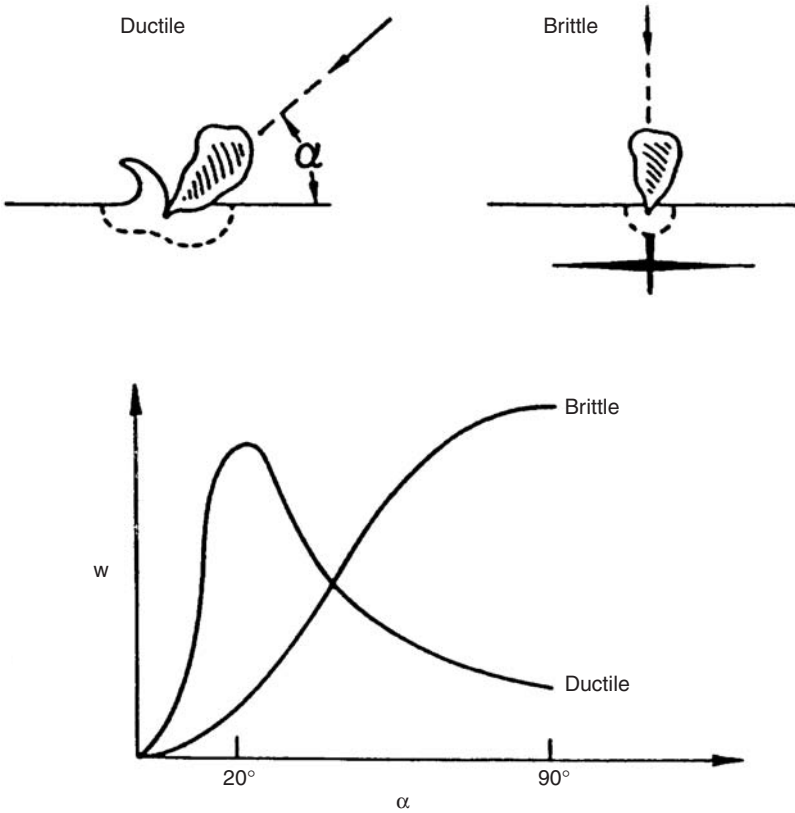


FIGURE 12.53 Erosion mechanisms show wear, W , tends as a function of impingement angle α .

given by

$$W = W_d + W_b = \begin{cases} \frac{M[V^2 \cos^2(\alpha) - V_p]^2}{2\phi} + \frac{M[V \sin(\alpha) - V_{el}]^2}{2\epsilon_b}, & \alpha \leq \alpha_0 \quad (12.135a) \\ \frac{M[V^2 \cos^2(\alpha)]}{2\phi} + \frac{M[V \sin(\alpha) - V_{el}]^2}{2\epsilon_b}, & \alpha > \alpha_0 \quad (12.135b) \end{cases}$$

with the proviso that $W_b = 0$ when $V \sin(\alpha) < V_{el}$.

In addition to a threshold velocity normal to the eroding surface, $V_n = V_{el}$, there is a threshold velocity parallel to the eroding surface, V_p , given by

$$V_p^2 = V^2 \cos^2(\alpha)[1 - \sin(\alpha)] \quad (12.136)$$

where n is an empirical constant and $\alpha_0 = \pi/2n$. Substitution of Eq. (12.136) into Eq. (12.135) results in

$$W = W_d + W_b = \frac{M[V^2 \cos^2(\alpha) \sin(n\alpha)]}{2\phi} + \frac{M[V \sin(\alpha) - V_{el}]^2}{2\epsilon_b}, \quad \alpha \leq \alpha_0 \quad (12.137)$$

Comparison of the first terms of Eqs. (12.137) and (12.135b) with Bitter's ductile erosion model (Eq. [12.133]) reveals the extent of Nielson and Gilchrist's simplifications. The first term of Eq. (12.135b) is the same as Bitter's ductile erosion model (Eq. [12.133b]) with $K_1 = 0$. The second terms of Eqs. (12.137) and (12.135b) are the same as Bitter's brittle erosion model, (Eq. [12.130a]).

12.4.3.1.4 Sheldon and Finnie’s 90° Brittle Erosion Model

Brittle materials, such as ceramics or glass, cannot deform plastically; instead, they crack and fracture when subjected to tensile stress. The angle of maximum erosion for brittle materials is near 90°. Sheldon and Finnie (1966) analyzed brittle erosion occurring at 90°. Their final result for spherical particles is given by

$$W = C_e R_p^\xi V^\eta \tag{12.138}$$

where

$$\xi = 3f/(f - 2), \tag{12.139a}$$

$$\eta = 2.4f/(f - 2), \tag{12.139b}$$

$$C_e = E_t^{0.8} \sigma_b^2 \tag{12.139c}$$

In the above relations, R_p is the particle radius, f is the coefficient of friction, and σ_b is the flexural strength. This model gives velocity exponents of 3.2, 2.72, and 2.66 for $f = 8, 16.9,$ and 20 (glass, graphite, and hardened steel), respectively.

12.4.3.2 Fluidized-Bed Models

Single-particle erosion models have been the subject of much more research than fluidized-bed erosion models. Only two fluidized-bed erosion models have been found in the literature; they are summarized in this section.

12.4.3.2.1 Soo’s Ductile and Brittle Erosion Models

Soo (1977) extended his treatment of heat transfer and charge transfer by impact to the treatment of material removal in the case of small deviations from elastic impact. Conceptually, Soo’s models resemble Bitter’s models in that the energy expended to remove material must exceed the yield stress in order for ductile or brittle failure to produce wear. Soo’s erosion models treat ductile wear and brittle wear separately.

12.4.3.2.1.1 Ductile Wear. Soo’s ductile wear model is expressed in terms of

$$\dot{E}_d = \cos(\alpha)[1 - K_d^* \sin(\alpha)^{-1/5}] \rho_p V^3 C_d f(1 + r^*)(2.94)(5/16) \eta_d / \epsilon_d \tag{12.140}$$

where V is the particle velocity, C_d a correction factor for nonsphericity (≈ 1), r^* the ratio of particle rebound to approach velocities, V_2/V_1 , ϵ_d the energy required to remove a unit volume of ductile material; and η_d the mechanical efficiency of impact ($\sim 10^{-4}$). (The ϵ_d obtained by Soo plays the same role as that of ϕ in Bitter’s ductile erosion model.) The dimensionless resistance parameter, K_d , is given by

$$K_d^* = 6\pi^2 \sigma_d (k_p k_t)^{1/2} / [2^{2/5} f C_d (1 + r^*)^{1/5} N_{IM}^{1/5}] \tag{12.141a}$$

where N_{IM} is the impact number given by

$$N_{IM} = (5\pi^2/2) \rho_p V^2 (k_p k_t)^{1/2} [(k_p k_t)^{1/2} + (k_t k_p)^{1/2}]^4 \tag{12.141b}$$

On the assumption that particle motion in a fluidized bed is random, Soo averages Eq. (12.140) over all directions and magnitudes to obtain

$$\dot{E}_{dFB} = (1 - 0.9586 \bar{K}_d^*) \bar{\rho}_p \bar{V}^3 \bar{C}_d \bar{f} (1 + \bar{r}^*)(2.94)(5/16) [2/(3\sqrt{\pi})] \eta_d \epsilon_d \tag{12.142}$$

where the overbar denotes averaging. This erosion rate given by Eq. (12.142) is no longer a function of impingement angle, α , and \bar{V}^2 (the intensity of random motion) replaces V^2 in the impaction number

(Eq. [12.141b]). Since particle motion in a fluidized bed is not completely random due to the presence of dead zones and jetting regions, for example, Eq. (12.140) may be preferred over Eq. (12.142).

12.4.3.2.1.2 Brittle Wear. Soo's brittle wear model is expressed in terms of

$$E_b = \sin(\alpha)[1 - K_b^* \sin(\alpha)^{-1/5}] \rho_p V^3 C_b (1 + r^*) (2.94)(5/16) \eta_b / \varepsilon_b \quad (12.143)$$

where C_b , ε_b , and η_b are the analogous terms for C_d , ε_d , and η_d in the ductile erosion model and K_b^* is given by

$$K_b^* = 6\pi^2 \sigma_b (k_p k_t)^{1/2} / [2^{2/5} C_b (1 + r^*)^{1/5} N_{IM}^{1/5}] \quad (12.144)$$

By averaging over all directions and magnitudes, as in the ductile erosion model, Soo obtains the following fluidized-bed brittle erosion model:

$$\dot{E}_{bFB} = (1 - 0.8981 \bar{K}_b^*) \rho_p \bar{V}^3 C_b (1 + \bar{r}^*) (2.94)(5/16) [2/(3\sqrt{\pi})] \eta_b \varepsilon_b \quad (12.145)$$

Clearly, Soo's erosion models resemble those that have been discussed previously. However, there are differences in the details of the exact angular dependence and the way in which the material properties enter.

Results from Soo's erosion models have not been compared with experimental data. Soo estimates that in the case of 700 μm dolomite particles eroding 316 stainless steel, $1 - K_d^* \approx 10^2$, $f \approx 0.1$, and $\eta_d C_d \approx 10^{-4}$. Assuming that $1 + \bar{r}^* \approx 1$, the ductile erosion estimated using Soo's model (Eq. [12.142]) is as follows:

$$E_{dFB} = 0.69 \times 10^{-7} \frac{\rho_p \bar{V}^3}{2\varepsilon_d} \quad (12.146)$$

This result is five orders of magnitude lower than \dot{E}_{FM} , the maximum erosion rate given by Finnie's model (Eq. [12.129]). Models of ductile erosion of tubes in FBCs are probably more appropriate than brittle erosion models. Soo's model can be used for a continuum of solids by replacing ρ_p with $(1 - \varepsilon)\rho_s$ and V^3 with v_s^3 .

The major shortcoming of all the models discussed thus far is that they incorporate the macroscopic or nominal fluid mechanical properties of particle velocity and impact angle, rather than local (or differential) properties. They also fail to account directly for particle fragmentation or attrition) and concentration of particles in the fluid stream. An exception is the model developed by Gansley and O'Brien (1990) which uses Davidson's bubble model (1961) in conjunction with the Finnie erosion model (1960). Finnie (1972) stated that no satisfactory explanation of concentration dependence existed, and that very little had been published concerning the effect of the carrier fluid itself. Humphrey (1990) addressed some of these problems in his review article where he also reviewed his group's research on coupling fluid mechanics and single-particle erosion models for dilute flows.

12.4.3.3 Power and Energy Dissipation Models

The origins and derivation of the power dissipation and energy dissipation erosion models are described in this section. We show that the conceptual bases for this approach can be traced back to empirical laws of size reduction, grinding, and comminution. We attempt to unify the concepts of ductile, brittle, abrasive, and impactation erosion. In effect we extend, in a rational manner, single-particle erosion models to continuum erosion models. The power dissipation model is shown to be a special case of what we call the energy dissipation model. The monolayer energy dissipation (MED) erosion model is described below.

12.4.3.3.1 Power Dissipation Erosion Model

Bitter (1963) postulated the concept that energy dissipation of the particles impinging on a surface gives rise to deformation wear. It was, however, the slurry erosion model of Ushimaru, Crowe, and Bernstein (1984), that provided us with the beginning point of the mechanistic monolayer energy dissipation (MED) and simplified closed-form MED (SCFMED) erosion models. Since the angle of approach of the particles eroding a slurry pipeline is essentially zero, none of the models described thus

far appeared to be useful. Therefore, a new model, termed the power dissipation model, was postulated by Ushimaru et al. (1984). No derivation was provided.

We trace the motivation and origins of this power dissipation erosion model in this section. The particle grinding (comminution) and abrasive erosion models provide the genesis of the so-called power energy dissipation erosion model. As early as 1885, Kick (1885) postulated that the energy, U , required to fracture particles in ball mills is directly proportional to the particle volume and independent of the number and size of the particles. This postulate, known as Kick's law, can be expressed as

$$U = K_1 V_p \tag{12.147}$$

where V_p is the volume of particles being ground in the ball mill and K_1 is a constant of proportionality having units of pressure (Walker and Shaw, 1954).

Rabinowicz's (1965) much later expression for two-body abrasive (sandpaper or scouring) erosion of a surface by particles is given as

$$\frac{V_t}{L} = kF/(3H) \tag{12.148}$$

where V_t is the volume of target removed, L is the distance traveled by the particle, F is the applied load (force), H is the hardness of the surface, and k is a dimensionless adjustable constant (sometimes called the abrasive wear coefficient) (Fiore et al., 1982) related to the average angularity of the abrasive particles. The equivalence of Eqs. (12.147) and (12.148) is easily seen by rewriting them in terms of V_p and V_t as

$$V_p = U/K_1 \tag{12.149a}$$

and

$$V_t = kFL/(3H). \tag{12.149b}$$

The factor of 3 in Eq. (12.149b) relates the yield strength, σ_b , to hardness, H , by $\sigma_y = 3H$. FL is an energy (force times distance). Comparison of Eqs. (12.149a) and (12.149b) reveals that FL is equivalent to U , K_1 is equivalent to $(3/k)H$, and V_t is equivalent to V_p . Thus, the two seemingly dissimilar processes of grinding of particles in ball mills and abrasive wear of a surface by particles are describable by the same relationship.

In their high-speed-photography slurry studies, Shook et al. (1983) observed that the particle motion was parallel to the pipe wall in the region of high concentration where the erosion rates were high. Hence, the simple Rabinowicz abrasion relationship holds. A heuristic generalization of this relationship is made in order to compute the volumetric loss-per-unit-time-per-unit area, \dot{E} caused by the flow of a slurry. Using Eq. (12.149b), \dot{E} is given by the following for a constant applied force, F :

$$\dot{E} = \dot{V}_t/A_t = kFL/(3A_tH) \tag{12.150a}$$

where \dot{V}_t plays the same role as \dot{W} in Eqs. (12.126a) and (12.126b) in the Finnie ductile erosion model described in Section 12.4.3.1. We replace the time rate of change of length, \dot{L} , by the velocity of the solids, v_s , and the applied load, F , by the force of the solids on the material surface, F_s , in Eq. (12.150a) to obtain

$$\dot{E} = \dot{V}_t/A_t = CF_s \cdot v_s/(A_tH) \tag{12.150b}$$

where C is a factor that includes $k/3$, to account for the fact that not all the volume, V_t , is removed (Fiore, et al., 1982). The force of the solids on the surface can be computed from

$$F_s = -(1 - \epsilon)\rho_s \frac{dv_s}{dt^s} V_f = -(1 - \epsilon)\rho_s \left[\frac{\partial v_s}{\partial t} + v_s \cdot \nabla v_s \right] V_f \tag{12.151}$$

where V_f is the volume of the fluid and d/dt^s is the total derivative following the solids velocity, \mathbf{v}_s . Combining Eqs. (12.150b) and (12.151), we obtain

$$\dot{E} = -C(1 - \varepsilon)\rho_s \frac{d\mathbf{v}_s}{dt^s} \cdot \mathbf{v}_s \left(\frac{V_f}{A_t} \right) / H \quad (12.152)$$

Equation (12.152) is the basic form of the “power dissipation” erosion model proposed in 1984 by Ushimaru et al. (1984). The factor C was not explicitly noted but was used, as will be discussed shortly. They used a “layer thickness” Δ , which can be associated with V_f/A_t . Defining the solids mass flux to be $\mathbf{q}_s = (1 - \varepsilon)\rho_s \mathbf{v}_s \Delta$, the power dissipation, P , was defined as

$$P = \frac{d\mathbf{v}_s}{dt^s} \cdot \mathbf{q}_s \quad (12.153)$$

Replacing the hardness, H , by a “specific energy,” E_{sp} , the erosion rate for the power dissipation model, E_{PD} , becomes

$$\dot{E}_{PD} = -CP/E_{sp} = -C \frac{d\mathbf{v}_s}{dt^s} \cdot \mathbf{q}_s / E_{sp} \quad (12.154)$$

\dot{E}_{PD} is positive, because the particles must decelerate in order for the force of the solids on the surface, \mathbf{F}_s , to be positive according to Eq. (12.151). The sign differs from that of Ushimaru et al. (1984) because they obviously considered their symbol, e , for the erosion rate to stand for $\dot{E}_t = -\dot{E}$, the erosion rate of the target itself (see Eq. [12.126b]).

Equation (12.152) states that the erosion rate is given by the total differential of the particle kinetic energy, multiplied by the mass flow of particles and divided by some material property resembling or related to hardness. Hence, we will write Eq. (12.152) symbolically as follows:

$$\dot{E}_{PD} = -\frac{C}{E_{sp}} \left(\frac{dKE_{sPD}}{dt} \right) \left(\frac{V_f}{A_t} \right) \quad (12.155)$$

where the rate of kinetic energy dissipation per unit volume of the solids (which for the sake of brevity we will call the energy dissipation rate) is defined as

$$\frac{dKE_{sPD}}{dt} = (1 - \varepsilon)\rho_s \mathbf{v}_s \left[\frac{\partial \mathbf{v}_s}{\partial t} + (\mathbf{v}_s \cdot \nabla \mathbf{v}_s) \right] = E_{PD} \quad (12.156)$$

The power dissipation erosion model has been derived heuristically in this section by generalizing the empirical abrasive erosion relationships. The more general energy dissipation model will be derived by more fundamental means in the next section, where the power dissipation model will be shown to be a special case.

Ushimaru et al. (1984) implemented the apparently fundamental power dissipation erosion model to analyze steady-state scouring erosion in a slurry jet pump and obtained reasonable comparisons with the data. They used a hydrodynamic code similar to that used by Sheldon et al. (1977).

Ushimaru et al. (1984) applied an empiricism that indicates that when the metal is removed with sandpaper, less than 10% of the grains in contact with the surface actually remove metal (Mulhearn and Samuels, 1962). The remaining particles cause only elastic deformation, which does not result in material wear. Hence, the factor C was taken to be 0.1. As discussed above, such factors are influenced by the hardness of the erodent relative to the eroding surface and the erosion mechanism, cutting tool (impaction), or sandpaper (abrasion).

We consider the results of Ushimaru et al. (1984) computations to be fortuitous since the kinetic energy dissipation *increased* through the slurry jet pump as the solids were accelerated. Had the solids decelerated, the kinetic energy dissipation would have *decreased*, and the erosion rate would have the wrong sign. Erosion can occur for both accelerating and decelerating solids flows and, therefore, the power dissipation model derived in this section and used by Ushimaru et al. (1984) cannot be considered to be sufficiently general irrespective of any possible confusion in sign convention. Humphrey (1990) discusses additional particle–surface interactions and related phenomena, which could enter into the factor C .

12.4.3.3.2 Energy Dissipation Models

It is necessary to extend the power dissipation erosion model to a two-phase continuum, consisting of both solids and fluid phases. The power dissipation model will be shown to be a special case of the more general energy dissipation model derived in this section.

The solids-phase momentum equation may be written in nonconservation law form as Bouillard et al. (1989)

$$\begin{aligned} & \rho_s(1 - \epsilon) \frac{\partial \mathbf{v}_s}{\partial t} + \rho_s(1 - \epsilon) \mathbf{v}_s \nabla \mathbf{v}_s \\ &= -(1 - \epsilon) \nabla P + \boldsymbol{\beta}(\mathbf{v}_g - \mathbf{v}_s) + G(\nabla \epsilon) + \rho_s(1 - \epsilon) \mathbf{g} + \nabla \cdot [(1 - \epsilon) \boldsymbol{\tau}_{sv}] \end{aligned} \quad (12.157)$$

where $\boldsymbol{\tau}_{sv}$ is the solids-phase shear stress tensor.

Following Bird et al. (1960) the equation of mechanical energy, extended to two-phase flow, is obtained by taking the scalar product of the solids velocity, \mathbf{v}_s , with Eq. (12.157) to obtain

$$\begin{aligned} & \rho_s(1 - \epsilon) \mathbf{v}_s \cdot \frac{\partial \mathbf{v}_s}{\partial t} + \rho_s(1 - \epsilon) \mathbf{v}_s \cdot (\mathbf{v}_s \cdot \nabla \mathbf{v}_s) \\ &= -(1 - \epsilon) \mathbf{v}_s \cdot \nabla P + \mathbf{v}_s \cdot \boldsymbol{\beta} \cdot (\mathbf{v}_g - \mathbf{v}_s) + \mathbf{v}_s \cdot G(\nabla \epsilon) + \rho_s(1 - \epsilon) \mathbf{v}_s \cdot \mathbf{g} + \mathbf{v}_s \cdot \nabla \cdot [(1 - \epsilon) \boldsymbol{\tau}_{sv}] \end{aligned} \quad (12.158)$$

Note that the sign convention of the viscous terms used is opposite to that of Bird, et al Lightfoot (1960). The last term in Eq. (12.158) may be split into two terms as:

$$\mathbf{v}_s \cdot [\nabla \cdot (\epsilon_s \boldsymbol{\tau}_{sv})] = \nabla \cdot [(\epsilon_s \boldsymbol{\tau}_{sv}) \cdot \mathbf{v}_s] - (\epsilon_s \boldsymbol{\tau}_{sv}) : \nabla \mathbf{v}_s \quad (12.159)$$

The first term on the RHS of Eq. (12.159) represents the rate of reversible work done by the solids viscous forces, while the second term represents the rate of irreversible conversion to internal energy and is shown to be always positive by (Bird et al., 1960). Substitution of Eq. (12.159) into Eq. (12.158) and solving for the rate of irreversible conversion to internal energy, E_{ED} , results in

$$\begin{aligned} E_{ED} &= -\frac{dKE_{ED}}{dt} = (\epsilon_s \boldsymbol{\tau}_{sv}) : \nabla \mathbf{v}_s \\ &= -\left\{ \epsilon_s \rho_s \mathbf{v}_s \cdot \frac{\partial \mathbf{v}_s}{\partial t} + \epsilon_s \rho_s \mathbf{v}_s \cdot \mathbf{v}_s \cdot \nabla \mathbf{v}_s + (\epsilon_s \mathbf{v}_s) \cdot \nabla P + \mathbf{v}_s \cdot \boldsymbol{\beta} \cdot (\mathbf{v}_s - \mathbf{v}_g) \right. \\ &\quad \left. - G(\epsilon_s) \mathbf{v}_s \cdot \nabla \epsilon - \epsilon_s \rho_s \mathbf{v}_s \cdot \mathbf{g} - \nabla \cdot [(\epsilon_s \boldsymbol{\tau}_{sv}) \cdot \mathbf{v}_s] \right\} \end{aligned} \quad (12.160)$$

where ϵ_s is $(1 - \epsilon)$.

Equation (12.160) is simply the portion of the solids-phase mechanical energy equation resulting in the rate of irreversible conversion to internal energy, a portion of which is available for energy transfer to the solid surface (i.e., the rate of kinetic energy dissipation per unit volume) to produce erosion. It is a direct extension of the well-accepted single-phase expression found in Bird et al. (1960).

Clearly, each term must be present, because each has a physical interpretation contributing to the energy dissipation. Equation (12.160) constitutes the rational extension of the kinetic energy dissipation rate for the power dissipation erosion model.

To see this, Eq. (12.160) is rewritten as

$$-E_{ED} = E_{PD} + \epsilon_s \mathbf{v}_s \cdot \nabla P + \mathbf{v}_s \cdot \boldsymbol{\beta} (\mathbf{v}_s - \mathbf{v}_g) - \mathbf{v}_s \cdot G(\epsilon) \nabla \epsilon - \epsilon_s \rho_s \mathbf{v}_s \cdot \mathbf{g} - \nabla \cdot [(\epsilon_s \boldsymbol{\tau}_{sv}) \cdot \mathbf{v}_s] \quad (12.161)$$

where E_{PD} is the rate of kinetic energy dissipation per unit volume for the power dissipation erosion model given by Eq. (12.156). Equation (12.161) also shows that the sign for the power dissipation rate used by Ushimaru et al. (1984) appears to be incorrect.

From Eq. (12.160), it is clear that the terms representing the irreversible rate of internal energy conversion, $(\epsilon \vec{\tau}_{sv}) : \nabla v_s$, are equivalent to all of the seven terms in the braces. The MED model was therefore refined by Bouillard et al. (1989). These energy dissipation rate models, which are programmed into the EROSION/MOD1 computer program (Lyczkowski et al., 1994), are given by

$$U_{ED} = (\text{the terms in braces}) \text{ in Eq. (12.160)} = E_{ED} d_p \tag{12.162a}$$

$$U_{EDv} = [(\epsilon_s \vec{\tau}_{sv}) : \nabla v_s] d_p = E_{EDv} d_p \tag{12.162b}$$

$$U_{EDvCF} = [(\epsilon_s \vec{\tau}_{sv}) : \nabla v_s + \vec{\beta}_B v_s^2 / 2] d_p = E_{EDvCF} d_p \tag{12.162c}$$

and

$$U_{EDvREL} = [(\epsilon_s \vec{\tau}_{sv}) : \nabla v_s + \epsilon_s \vec{\beta}_B (v_f - v_s)^2] d_p = E_{EDvREL} d_p \tag{12.162d}$$

The particle diameter, d_p , was argued by Bouillard et al. (1989) to arise from the observation that most of the energy dissipation occurs in a monolayer of particles in the vicinity of the eroding surface as shown in Figure 12.54. Hence the ratio V_f/A_p , which arises in the power dissipation model, becomes $V_f/A_t = d_p$. The erosion rates for the MED erosion model are given by:

$$\dot{E}_{ED} = C U_{ED} / E_{sp} \tag{12.163a}$$

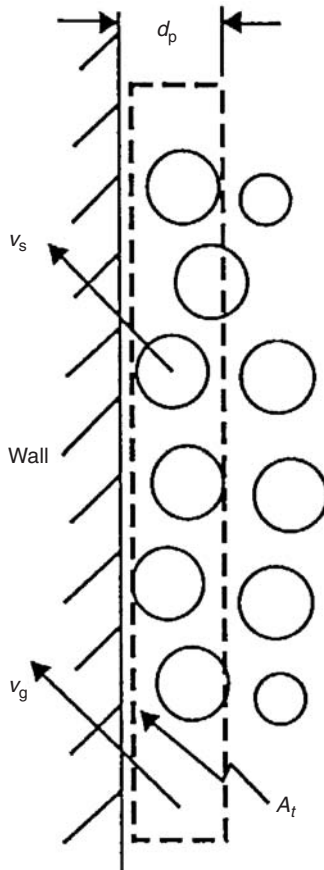


FIGURE 12.54 Conceptual picture of the MED erosion model.

$$\dot{E}_{EDv} = CU_{EDv}/E_{sp} \tag{12.163b}$$

$$\dot{E}_{EDvCF} = CU_{EDvCF}/E_{sp} \tag{12.163c}$$

and

$$\dot{E}_{EDvREL} = CU_{EDvREL}/E_{sp} \tag{12.163d}$$

Equations (12.163a–12.163d) may be written succinctly as

$$\dot{E}_{ED\alpha} = CU_{ED\alpha}/E_{sp} = CE_{ED\alpha}d_p/E_{sp} \tag{12.164}$$

where $U_{ED\alpha}$ and $\dot{E}_{ED\alpha}$ are given by Eqs. (12.162a)–(12.162d) and Eqs. (12.163a)–(12.163d) respectively with $\alpha = 1, v, vCF, \text{ and } vREL$, respectively. Details of the derivation of Eqs. (12.163b)–(12.163d) are given by Bouillard and Lyczkowski (1991). E_{sp} is the specific energy, which is a material property related to hardness or flow stress, p . Some typical values of hardnesses are given by Wood and Woodford (1980) and Ushimaru et al. (1984), who claim that $E_{sp} \approx 2 \times p$.

The MED erosion models given by Eqs. (12.163a)–(12.163d) can be interpreted as an extension of the power dissipation erosion model given by Eq. (12.155) with $V_f/A_t = d_p$. We chose $E_{sp} = p$. Bouillard and Lyczkowski (1991) showed that the factor C is in fact related to the target–particle coefficient of restitution, e , given by

$$V_{s1}^2 - V_{s2}^2 = (1 - e^2)V_{s1}^2 \tag{12.165}$$

where V_{s1} and V_{s2} are the approach and rebound solids velocities, respectively, by

$$C = 1 - e^2. \tag{12.166}$$

Typically, $e^2 \approx 0.9$ (Savage, 1982), which fortuitously agrees with the value used in the power dissipation erosion model by Ushimaru et al. (1984), which was based on the data of Mulhern and Samuels (1962). This is the default value used in the EROSION/MOD1 computer code (Lyczkowski et al., 1994b). Therefore, the definitive form of the MED erosion model becomes

$$\boxed{\dot{E}_{ED\alpha} = (1 - e^2)U_{ED\alpha}/p = (1 - e^2)E_{ED\alpha}d_p/p} \tag{12.167}$$

These MED erosion models are based on the premise that the mechanical energy of the solids is irreversibly dissipated in the neighborhood of stationary surfaces by three competitive mechanisms: (1) heat transfer between the fluid-and-solids phase, between the fluid phase and stationary surfaces, and between the solids phase and stationary surfaces; (2) erosion of stationary surfaces; and (3) attrition of solids. Thus, the rate of energy dissipated during erosion represents only a fraction of the total energy dissipation (which is related to the total entropy production).

The presently recommended MED erosion model, which is essentially the one derived by Bouillard et al. (1989), as refined by Bouillard and Lyczkowski (1991), is Eq. (12.167) with $U_{ED\alpha}$ given by Eq. (12.163c) and is written as

$$\boxed{\dot{E}_{MED} = (1 - e^2)[(\epsilon_s \boldsymbol{\tau}_{sv}) : \nabla \mathbf{v}_s + \beta_B \mathbf{v}_s \cdot \mathbf{v}_s / 2]d_p/p = \dot{E}_{EDvCF}} \tag{12.168}$$

In their cold fluidized-bed erosion experiments, Wood and Woodford (1979) found that the erosion rate increased with increasing particle diameter. For example, they obtained erosion rates of 0.036, 0.48, and 1.16 mm/1000 h for aluminum tubes for 100, 930, and 1900 μm silica sand; these values suggest a very nearly linear dependence. Basically, linear dependence was found for all the other materials tested. Therefore, the choice of the particle size dependence in the MED erosion models given by Eqs. (12.167) and (12.168) appears justified.

12.4.3.3.3 Simplified Closed-Form MED (SCFMED) Erosion Model

Bouillard and Lyczkowski (1991) developed a simplified mechanistic monolayer energy dissipation (MED) erosion model using a variational principle that placed the closed-form MED erosion model derived by Bouillard et al. (1989) on a firm foundation. A modification of that model is presented here to assist the practicing engineer to quickly estimate erosion rates (see Section 12.4.3.6).

The erosion rate from the simplified quasi one-dimensional MED erosion model, \dot{E}_{EDCF} , may be written in the form, modified for Hydrodynamic Model B (Bouillard et al., 1989; Bouillard and Lyczkowski, 1991) as

$$\dot{E}_{\text{EDCF}} = \dot{E}_o \frac{(1 - \varepsilon)(\varepsilon - \varepsilon_{\text{gd}})}{\varepsilon^2} + K \frac{(\varepsilon - \varepsilon_{\text{gd}})}{\varepsilon^2} (U - \varepsilon V_s) \quad (12.169)$$

where U is the superficial gas velocity, V_s is the solids-phase velocity, and ε is the void fraction. The erosion rate group, \dot{E}_o , is given by

$$\dot{E}_o = (1 - e^2) \frac{75 \mu_g g x_d}{(\phi_s d_p E_{\text{sp}})} \quad (12.170)$$

and

$$K = (1 - e^2) \frac{0.875 g x_d \rho_g}{E_{\text{sp}}} \quad (12.171)$$

The units of \dot{E}_o are in terms of velocity, commonly expressed in mm/1000 h or $\mu\text{m}/100$ h. K is dimensionless, e is the particle-surface restitution coefficient, which is the ratio of particle rebound velocity, V_{p2} to particle approach velocity V_{p1} and x_d is a characteristic acceleration distance of the order of the heat exchanger tube spacing in FBCs. The rest of the symbols are defined in Nomenclature.

Experimental evidence presented by Zhu (1988) strongly supports the additional approximation that the solids velocity V_s in the vicinity of tubes is close to the superficial gas velocity, U . With the approximation $V_s = U$, Eq. (12.169) may be written in the strikingly simple dimensionless form as

$$\dot{E}_{\text{EDCF}}/\dot{E}_o = f(\varepsilon)(1 + 0.01167Re) \quad (12.172)$$

where the fluidization Reynolds number $Re = (\phi_s d_p) \rho_g U / \mu_g$ and

$$f(\varepsilon) = \frac{(1 - \varepsilon)(\varepsilon - \varepsilon_{\text{gd}})}{\varepsilon^2} \quad (12.173)$$

12.4.3.4 Kinetic Theory Models

The kinetic theory of granular flow erosion model developed by Ding and Lyczkowski (1992) offers an alternative approach to extending single particle erosion models. A summary of the approach applied to the Finnie erosion model is given in this section.

The Finnie erosion model given by Eqs. (12.125a) and (12.125b) is written as a function of the particle's instantaneous speed in the vicinity of an eroding surface, c_w , angle of attack, α , and mass $M = \pi d_p^3 \rho_p / 3$ as

$$W = B_F M c_w^2 f(\alpha), \quad (12.174)$$

where

$$B_F = \frac{1}{8P_H} \quad (12.175)$$

where P_H is the Vickers hardness or flow stress, and $f(\alpha)$ is given by Eqs. (12.127b) and (12.127c).

Finnie's single-particle erosion model is combined with the kinetic theory of granular flow (Ding and Gidaspo, 1990), to obtain an expression for erosion due to repeated impacts on the eroding surfaces. The erosion rate, \dot{E} , of a solid surface caused by repeated impacts with the surface can be obtained by calculating the number of particles within a range c to $c + dc$ per unit volume and unit time times the erosion

caused by a single particle impact. Thus, the erosion rate caused by repeated impacts given by Eq. (12.174) is integrated over all impact velocities in the range of $(-\infty, +\infty)$ to obtain

$$\dot{E} = \int_{c_w \cdot n > 0} (c_w \cdot n) B_F M c_w^2 f(\alpha) f_w(r, c, t) dc_w, \tag{12.176}$$

where the single-particle velocity distribution function in the vicinity of the eroding surface, f_w , is assumed to be Maxwellian, (Gidaspow, 1994).

Carrying out the integration of Eq. (12.176), the result is

$$\dot{E} = 2\varepsilon_s \rho_p B_F \left[\frac{(2T)^{3/2}}{\sqrt{\pi}} F_1(\theta_c) + \frac{v_w^2}{2} \sqrt{\frac{2T}{\pi}} F_1(\theta_c) + \frac{3}{2} v_w T F_2(\theta) \right], \tag{12.177a}$$

where

$$F_1(\theta_c) = \frac{\pi}{8} - \frac{\theta_c}{4} + \frac{1}{12} \sin^4(\theta_c) + \frac{1}{16} \sin^4(\theta_c) - \frac{3}{4} \cos^4(\theta_c) - 0.1 \tag{12.177b}$$

and

$$F_2(\theta_c) = -\frac{2}{5} + \frac{1}{15} \sin^5(\theta_c) - \frac{2}{5} \cos(\theta_c) \sin^4(\theta_c) + \frac{2}{15} (\cos(\theta_c) \sin^2(\theta_c) + 2 \cos(\theta_c)) + \frac{3}{5} \cos^2(\theta_c) \sin^3(\theta_c) + \frac{2}{5} \sin^3(\theta_c) = 0.06 \tag{12.177c}$$

Details of the integration process are given in Ding and Lyczkowski (1992). This approach is similar to that used by Soo (1977) to obtain the fluidized-bed erosion models described in Section 12.4.3.2.

Rogers (1995) developed a similar model using Finnie’s (1958) single-particle erosion model and the kinetic theory of granular flow. That model is more involved and requires a certain amount of iteration between the erosion calculations and the experimental data to determine adjustable parameters that minimize the difference. The kinetic theory model given by Eq. (12.177a) requires only the knowledge of the granular temperature and some measure of target hardness.

The input to the kinetic theory erosion model given by Eq. (12.177a) may be the computed granular temperature (Ding and Lyczkowski, 1990) or experimental data, such as the one obtained by Cody et al. (1996) using a nonintrusive vibration probe. They obtained the granular temperature data as a function of fluidizing velocity for glass spheres ranging in diameter from 595 to 63 μm encompassing Geldart type-B (and nearly D) and the transition to Geldart type-A particles. Such data can be used as a check on the consistency between erosion measurements and granular temperature measurements.

The number of particles, P_w , colliding with a wall having an area A in a time interval dt can be estimated as

$$P_w = \int (c_w \cdot n) f_w(r_w, C_w, t) dc_w dA dt \tag{12.178}$$

Then the number of collisions per unit area per unit time is obtained from

$$N_{pw} = \int_{c_w \cdot n > 0} \frac{P_w}{dA dt} = \int_{c_w \cdot n > 0} (c_w \cdot n) f_w(r, c, t) dc_w = \frac{6\varepsilon_s}{\pi d_p^3} \sqrt{\frac{T}{2\pi}} \tag{12.179}$$

12.4.3.5 Lagrangian Particle and Discrete Element Models

12.4.3.5.1 Lagrangian Models

Tabakoff (1982, 1991) and co-workers at the University of Cincinnati, Hussain and Tabakoff (1974), and Grant and Tabakoff (1975) have been engaged in turbine blade erosion and particulate flow research since 1971. It is their hope that the incorporation of erosion into the engine design as a parameter could lead to the production of an erosion-tolerant engine. They have developed a steady-state computer program capable of describing three-dimensional particle trajectories through turboaxial or radially rotating turbomachinery. Tabakoff (1991) has reviewed this work up to 1990; the same year Humphrey (1990) reviewed the subject of erosion in turbomachinery and related phenomena.

The experimental data on the coefficient of restitution (the ratio of rebound to approach velocities) and the ratio of rebound to impingement angle are obtained experimentally by the group using high-speed photography or laser doppler anemometry and are expressed in terms of impingement angle. In the computer model first developed by Hussain and Tabakoff (1974), these ratios are used to account for momentum loss of the particles caused by collision with the turbine blades or channel walls in the Lagrangian trajectory calculations.

The major force on the particles is given by a drag expression similar to the one used in the FLU-FIX/MOD2 computer code (Lyczkowski, et.al., 1994a). The added mass, Basset, and Bagnold forces on the particles are neglected. The compressible, nonviscous, steady-state gas-phase momentum equations are assumed to be unaffected by the particles. This implies low particle loadings, an assumption that allows the use of existing single-phase computer codes for turbomachinery. The three-dimensional Eulerian gas flow and Lagrangian particle trajectory equations are solved on a square grid with the coordinates fixed on the rotating blade (one row of blades is solved at a time).

This same group has also simulated erosion with a Monte Carlo technique (Grant and Tabakoff, 1975). The erosion model, used to compute the erosion rates, also incorporates the particle rebound data; it is given by a semiempirical equation that relates the mass of material removed (in mg) to the mass of particles (g), as follows:

$$S = K_1 f(\alpha) V^2 \cos^2(\alpha) (1 - R_T^2) + K_3 (V \sin^4(\alpha)) \quad (12.180)$$

where

$$R_T = 1 - 0.0016V \sin(\alpha) \quad (12.181a)$$

and

$$f(\alpha) = \begin{cases} 1 + K_{12} \sin[(90/\alpha_0)\alpha], & 0 < \alpha < 2\alpha_0 \\ 1, & \alpha > 2\alpha_0 \end{cases} \quad (12.181b)$$

$$(12.181c)$$

in which α_0 is the angle corresponding to maximum erosion. The parameters α_0 , K_1 , K_{12} , and K_3 are material-dependent empirical constants. Comparison of Eq. (12.180) with Eqs. (12.135a) and (12.135b) shows that this model is a variant of the Neilson and Gilchrist combined ductile and brittle erosion model. The approach speed V and impact angle α are computed from the particle trajectory computer program.

Sheldon et al. (1977) developed a numerical method to predict erosion on a horizontal, round tube wall. It is known as particle-source-in-cell (PSI-Cell), (Crowe et al., 1977), in which the particles are treated as sources of mass, momentum, and energy in the gas phase. The momentum equations for the incompressible, two-dimensional viscous Eulerian gas phase include a momentum sink term due to particle drag and, thus, would appear to be an improvement over Tabakoff's equation; however, the model does not contain the void fraction as a variable. Hence, the assumption of low particle loadings is again implicit, and the approach is similar to the "dusty gas" model of Rudinger and Chang (1964). The Eulerian gas flow equations and Lagrangian particle trajectory equations are solved iteratively, using an extension of the TEACH program developed at Imperial College, London (Gosman and Pun, 1974). A two-parameter turbulence model and heat transfer, are included in the PSI-Cell technique) but it appears that they were not used in this erosion prediction.

The particle trajectory calculations use empirical rebound angle and coefficient of restitution data in a manner similar to that of Hussain and Tabakoff (1974). The erosion model is very simple and is given by

$$\left(\frac{\text{mass removed}}{\text{mass abrasive}} \right) \approx f(\alpha) V^{2.35} \quad (12.182)$$

where $f(\alpha)$ is given by an experimental curve. The exponent on the particle velocity is taken from the Sheldon and Finnie 90° brittle erosion model (Sheldon and Finnie, 1966). The erosion curve for $f(\alpha)$ was determined for impingement angles as low as 4° by using hardened steel shot (Ro45) of 270 μm average diameter striking 6061-T6 aluminum alloy, a ductile material. The rebound data were obtained from

multiple flash exposures of 3.175 mm ball bearings striking the same aluminum alloy. Erosion data taken by blasting the steel shot through a horizontal tube 4.95 mm in diameter and 30.5 cm long, made of the same aluminum alloy, were in reasonable agreement, considering that the majority of particles were incident at less than 5° (probably deduced from the trajectory computations), which corresponds to almost pure abrasion (scouring). Whether a coefficient of proportionality was introduced into Eq. (12.182) is uncertain.

12.4.3.5.2 Discrete Element Models

An alternative to extending single-particle erosion models using the hydrodynamic models contained in the FLUFIX/MOD2 computer code (Lyczkowski et al., 1994a) and kinetic theory of granular flow models contained in the IFAP computer code (Ding and Gidaspow, 1990; Ding and Lyczkowski, 1992) is to use the instantaneous time-dependent particle velocities computed by the discrete element method (DEM) (Rong et al., 1999; Rong and Horio 2001). Tsuji et al. (1993) refer to this method as the discrete particle simulation. Tsuji (2000) summarized Japanese activities on discrete particle simulation. Rong et al. (1999) reviewed the DEM literature and applied the technique to describe particle motion and erosion in fluidized beds containing an immersed single tube as well as tube arrays. However, they failed to refer to the work of Walton and collaborators (see e.g., Walton and Braun, 1994), who use basically the same approach as DEM and refer to the technique as particle dynamics. The DEM calculations were performed in two dimensions using a stair case approximation to the round tubes and treated the particles as circles. Walton and Braun generally use spherical particles in three dimensions. Their application is to test the assumptions made in the kinetic theory of granular flow.

The numerical results from the DEM for particle and bubble patterns computed by Rong et al. (1999) agreed qualitatively, and more quantitative computations such as bubble frequency (2 to 3 Hz), bed expansion, bubble velocity (~ 0.7 m/sec), and particle impact velocity bracketed data were taken at atmospheric conditions pressure. The effect of moderate pressure (1.2 MPa) increased the computed bubble frequency from 4 to 8 Hz as well as the particle impact velocity; however, no comparisons were made with these data.

The energy calculated by the DEM was used with the Finnie erosion model; however, no comparisons were made with data. Using a hardness of 6×10^8 kgf/m² (600 kgf/mm² or $\sim 6,000$ MPa) that corresponds roughly to hardened steel (see Wood and Woodford, 1980; Ushimaru et al., 1984), Rong and Horio (2001) computed erosion rates of the order of 10 μ m/ 1000 h (0.01 mm/100 h), which are in rough agreement with rates predicted by Lyczkowski and Bouillard (2002).

The shortcoming of the DEM is that it uses a system of dashpots and springs, which may render it unsuitable for truly predictive calculations. An alternative is DNS of fluidized particles pioneered by Joseph (2001). This method requires no adjustable parameters and appears to be truly predictive if the number of particles can be made sufficiently large. Videos of their simulations are available at http://www.aem.umn.edu/Solid-Liquid_Flows/

12.4.3.6 Sample Calculations and Data Comparisons

The SCFMED erosion model given by Eq. (12.172) was used to predict erosion rates quickly by using data that are easily obtained experimentally, such as bed expansion. *In lieu* of actual data, the time-averaged bed expansion was obtained from the detailed hydrodynamic computations performed by Bouillard and Lyczkowski (1991) for a few (three-) tube approximation of the International Energy Agency (IEA) Grimethorpe tube bank “C1” configuration (Parkinson et al., 1986), over the U/U_{mf} range from 1.0 to 2.7 for 500 μ m diameter glass beads having a density $\rho_s = 2.44 \times 10^3$ kg/m³. The reader is referred to Bouillard and Lyczkowski (1991) for further details of the calculations.

The fluidized-bed void fraction is obtained as a function of the time-averaged fluidized-bed height, H , from the following solids overall mass conservation equation:

$$\varepsilon = 1 - (H_{mf}\varepsilon_{smf}/H) \quad (12.183)$$

where $\varepsilon_{smf} = (1 - \varepsilon_{mf})$ is the solids volume fraction at minimum fluidization and $H_{mf} = 44.2$ cm is the bed height at minimum fluidization. The rest of the parameters used to evaluate Eq. (12.172) at 25°C and 1.01 kPa are given by $\mu_g = 1.82 \times 10^{-5}$ Pa sec, $\rho_g = 1.83$ kg/m³, $E_{sp} = 294$ MPa, $d_p = 0.05$ cm, $x_d = 55$ mm, $e^2 = 0.9$, $\phi_s = 1.0$, and $\varepsilon_{gd} = 0.4$.

E_{sp} corresponds to the hardness of pure aluminum (30 kgf/mm², 294 MPa) and x_d is the minimum horizontal spacing between tubes (89 – 33.7 mm = 55.3 mm) for Grimethorpe tube bank “C1” Parkinson et al. (1986). The results of the calculations are listed in Table 12.7 and are plotted in Figure 12.55, where they are compared with the full MED erosion model results. As can be seen, the agreement is excellent. The results of the full MED and SCFMED erosion calculations are compared in Figure 12.55 with the data of Wood and Woodford (1980), Parkinson et al. (1985, 1986), Zhu et al. (1990), and Foster Wheeler (Podolski et al., 1991) taken under similar operating conditions. As can be seen, the agreement is excellent. Also shown is the sensitivity of the results to a threefold increase in the apparent hardness of aluminum due to surface oxidation. (90 kgf/mm², 882 MPa). In spite of the diverse sources of the data, such agreement with the simplified MED erosion model is remarkable. The simplified MED erosion model, Eqs. (12.169)–(12.173) takes a few minutes to compute on a pocket calculator vs. a month on a mainframe computer using the FLUFIX/MOD2 (Lyczkowski et al., 1994a) and EROSION/MOD1 (Lyczkowski et al., 1994b) computer programs.

If the physical input parameters of the SCFMED erosion model are missing, they must be estimated by (1) reviewing available databases for each parameter; (2) estimating the range of uncertainties, e.g., tube hardness; and (3) identifying contradictions from different estimation procedures. Lyczkowski and Bouillard (1986) used the SCFMED erosion model to develop a mechanistic erosion scaling procedure.

TABLE 12.7 Metal Wastage Predictions from SCFMED Erosion Model

U/U_{mf}	U , (cm/sec)	H , (cm)	ϵ	$f(\epsilon)$	Re	\dot{E}_{EDCF}/\dot{E}_o
1.0	0.209	44.2	0.40	0	10.5	0
1.12	0.234	46	0.42	0.066	11.7	0.075
1.7	0.355	50	0.47	0.168	17.8	0.203
2.3	0.481	55	0.52	0.213	24.2	0.273
2.7	0.564	59	0.55	0.223	28.4	0.296

$\dot{E}_o = 1.8 \text{ mm}/1000 \text{ h}$.

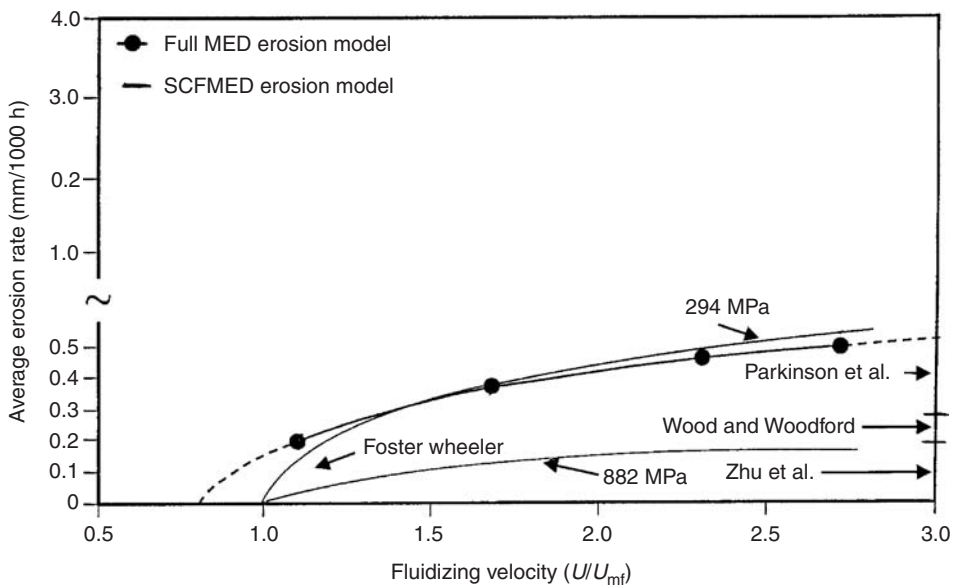


FIGURE 12.55 Comparison of closed-form MED and SCFMED erosion models with available data for aluminum tubes. Data source key: Parkinson et al. (1985, 1986); Wood and Woodford (1980); Zhu et al. (1990); and Foster Wheeler From Podolski et al. (1991).

A more complete description of the material in this section may be found in Lyczkowski and Bouillard (2002a, 2003), which also includes a review of the work of Chalmers University which extended the MED erosion model.

12.5 Particle and Droplet Dispersion in Turbulent Flows

T.R. Troutt

12.5.1 Introduction

Droplet and particle dispersion in turbulence is important in many engineering applications. The mixing of droplets in liquid-fueled combustion systems is dependent on turbulent dispersion. The degree of mixing establishes the local fuel-to-air ratio, which affects the combustion efficiency and pollution generation. One important parameter which influences the dispersion is the droplet-fluid time ratio or the Stokes number. The objective of this section is to review the current state of understanding of particles and droplets in turbulent structures. This review will primarily involve dilute two-phase turbulent flows.

Dilute models for particle-fluid turbulence interaction with heavy particles may be based on one or two-way coupling. With one-way coupled models it is assumed that the particle phase has a negligible effect on the fluid-phase turbulence, whereas two-way coupled models include particulate effects on the fluid-phase turbulence. A map proposed for coupling interactions projected onto volume fraction-particle Reynolds number space is shown in Figure 12.56. For low particle volume fractions and particle Reynolds numbers, it is expected that one-way coupling dominates. However, as the particle Reynolds number is increased and the particles begin to generate wakes, fluid-phase turbulence will be produced requiring two-way coupled models. An increase in the particle volume fraction will also lead to two-way coupling, since the bulk

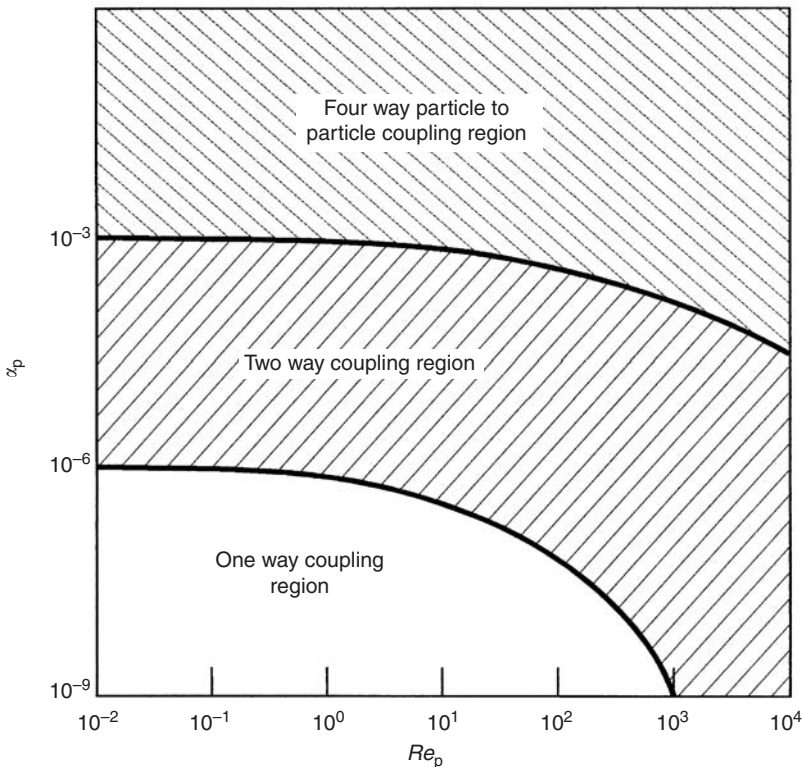


FIGURE 12.56 Two-phase coupling regions for particle-fluid turbulence interaction.

density of the particles will become significant. When particle volume fractions exceed 10^{-3} , the possibility of four-way coupling occurs in which particle–particle interactions are significant (Crowe et al., 1996). This region is associated with dense-phase flows.

12.5.2 Time Scales

To implement the Lagrangian approach on particulate dispersion in a two-phase flow, a particle motion equation is required. For dilute two-phase flow environments with low particle Reynolds numbers, Maxey and Riley (1983) derived a complex integral-differential equation involving six different forces. However, if the material density of the particulate phase is much greater than the density of the fluid phase (heavy particle situation) and body forces are neglected, then the well-known Stokes drag force term is assumed to become the dominate force on the particles. (Crowe et al., 1998)

The Stokes drag term can be associated with a time scale of the particle motion called the particle response time, τ_p , introduced in Section 1.2. If the particle motion equation is nondimensionalized with a characteristic fluid velocity, U , and length scale, ℓ , then the motion equation for heavy particles becomes

$$\frac{d\mathbf{v}}{dt} = \frac{f}{Stk}(\mathbf{v} - \mathbf{u})$$

where \mathbf{v} is the particle velocity, \mathbf{u} the fluid velocity, and Stk the Stokes number defined as $Stk = (\tau_v/\tau_f)$, with τ_f being the fluid time scale. The factor f is the ratio of drag to Stokes drag.

For particle dispersion in turbulent flows, the choice of the appropriate fluid time scale to use in the Stokes number ratio introduces some ambiguity into the formulation. Since turbulent flows exhibit a range of time scales from the integral τ_l to the Kolmogorov τ_k and since the ratio of the two time scales, τ_k/τ_l , varies with the turbulence Reynolds number as $Re_\tau^{-1/2}$, a wide variation of possible Stokes number exist. In addition, the integral time scale may be associated with either Lagrangian or Eulerian viewpoints. Detailed descriptions of various turbulent time scales can be found in Tennekes and Lunley (1972).

12.5.3 Particle Dispersion in Turbulent Shear Flows

During the past 15 years, considerable experimental and numerical research has been conducted concerning particle dispersion in turbulent shear flows. This research has been spurred on by the development of new physical models for the particle dispersion process and the application of new experimental techniques and more powerful computational tools.

The physical model development has emphasized the role that organized vortex structures produced in turbulent flows might have in the particle dispersion process. Organized vortex structures have been recognized for several decades as a significant component of free turbulent shear flows (Ho and Huerre, 1984).

The role that organized vortex structures might play in the particle dispersion process has been investigated both experimentally and numerically by several research groups. Most of the early efforts in this area have concentrated on free shear flows with low particle concentrations and small particle Reynolds numbers (i.e., one-way coupling situations).

The experimental efforts in these two-phase flows have involved flow visualization techniques, laser anemometry techniques and more recently particle image velocimetry (PIV) techniques. A review on standard PIV techniques is available in Liu and Adrian (1993). Information concerning advanced scanning PIV techniques for obtaining three-dimensional flow information can be found in Kiger (1998). Several informative reviews concerning the results of these experimental investigations are available in Crowe et al. (1993, 1995) and Eaton and Fessler (1994). In essence, several important findings obtained from these free shear flow investigations have been reported:

1. Large-scale vortex structures are important controlling mechanisms for the particle dispersion process.
2. Particle dispersion levels tend to maximize at intermediate, $0(1)$ – $0(10)$, values of Stokes numbers.
3. Intermediate value Stokes number particles tend to concentrate preferentially near the outer boundaries of large-scale vortex structures.

The tendency of intermediate value Stokes number particles to accumulate around the outer boundaries of the organized vortex structures is most apparent in turbulent plane wake experiments. Figure 12.57 from Yang et al. (2000) shows instantaneous particle concentration maps for two nominal Stokes numbers obtained using PIV techniques from a plane wake experiment. The flow time scale for computing the Stokes number is based on the initial wake width and the free-stream velocity. These experimental results clearly illustrate the striking differences that changes in Stokes number can have on the turbulent particle dispersion process.

Extensive numerical studies have been made to examine the particle dispersion process in free shear flows. These numerical studies have employed various approaches including discrete vortex models, direct numerical simulations, and large eddy simulations. Initially, most of these numerical studies concentrated on one-way particle coupling situations with two-dimensional flow fields in order to clarify and simplify the interpretation of the results. The results of these initial numerical efforts strongly supported and extended the experimental efforts.

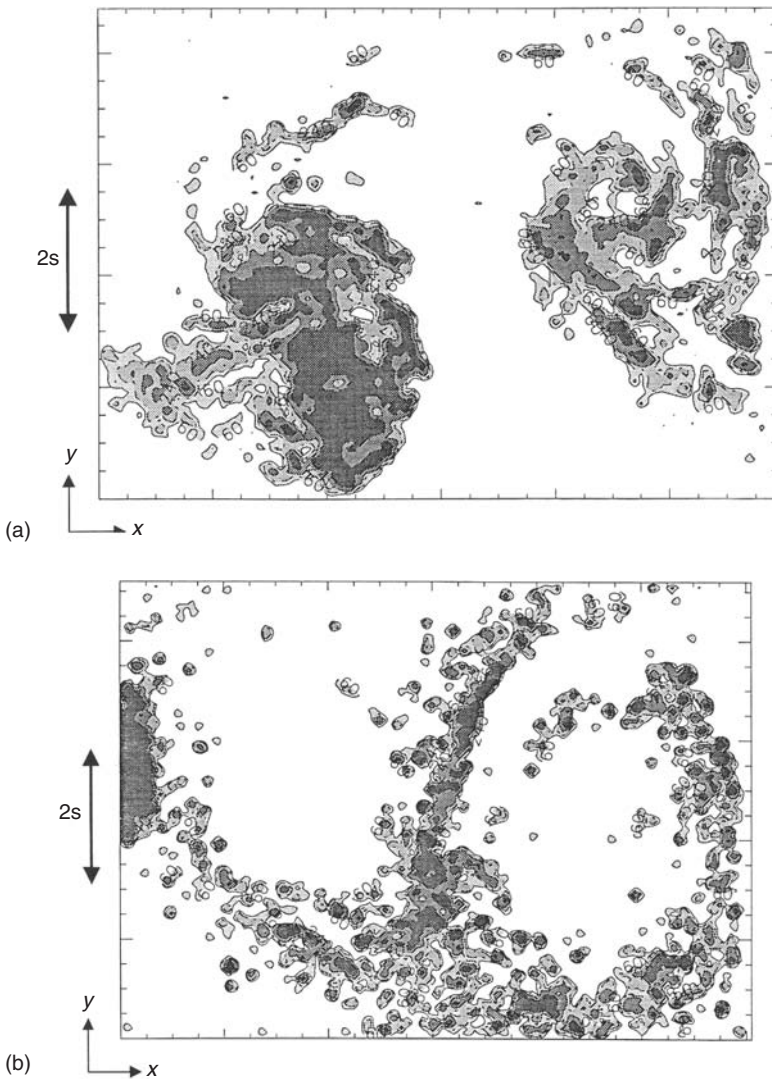


FIGURE 12.57 (a) Instantaneous number density map of 10 μm particles, $Stk = 0.15$; (b) Instantaneous number density map of 30 μm particles, $Stk = 1.4$. The initial wake width is $2s$.

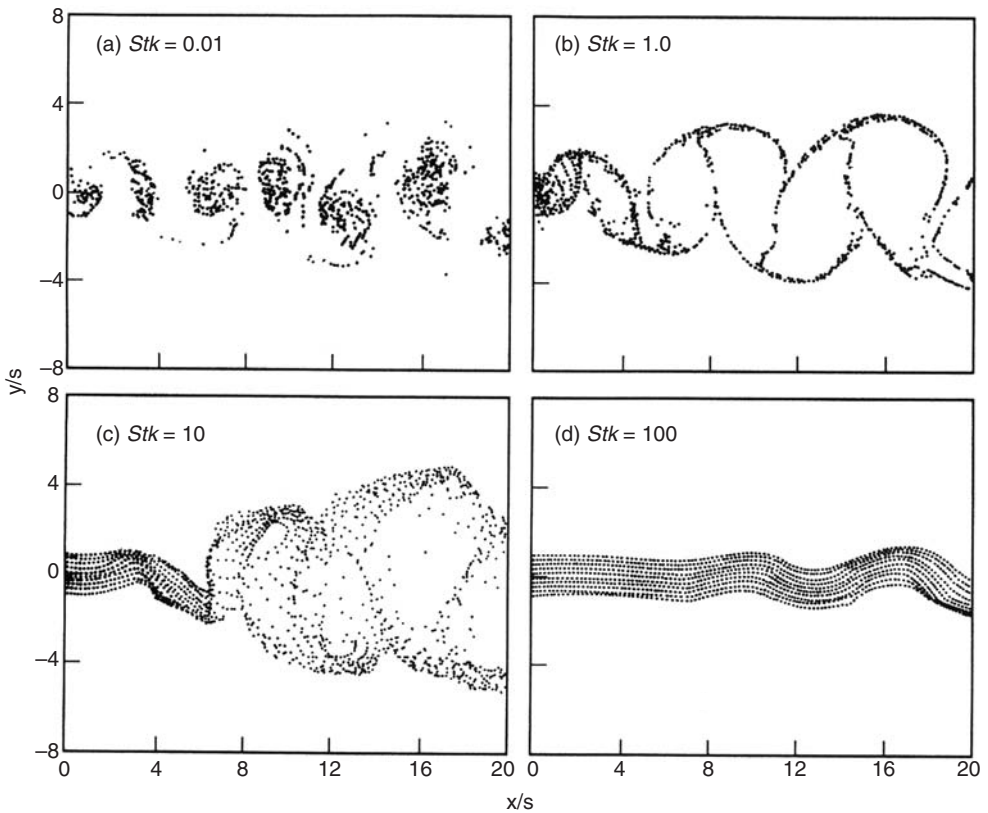


FIGURE 12.58 Instantaneous particle dispersion patterns from numerical simulation of the plane wake: (a) $Stk = 0.01$; (b) $Stk = 1.10$; (c) $Stk = 10$; (d) $Stk = 100$. (Tang et al., 1992)

Figure 12.58 shows an example result from a plane flow simulation over a wide range of particle Stokes numbers. The high degree of order exhibited by the Stokes number unity result indicates that turbulent flows may actually be antimixing agents under specific flow situations. An extensive review discussing the application and results from two-phase numerical studies involving primarily one-way coupling can be found in Crowe et al. (1996).

Although direct experimental confirmation of numerical predictions is difficult to obtain, recently, Yang et al. (2000) have reported some quantitative experimental results of one-way coupling predictions in a plane wake that agree closely with previous numerical studies.

In recent years, the two-phase free shear flow numerical efforts have begun to focus on three-dimensional simulations of particle dispersion in free shear flows (Ling et al., 1998) and on the development of models and simulation techniques involving two-way coupling environments (Crowe 2000; Ling et al., 2000, 2001).

Some relatively recent experimental and numerical two-phase flow studies have also been carried out in confined shear flows. The earliest direct numerical simulation work on wall-bounded two-phase flow involved studies of aerosol deposition in a turbulent channel by McLaughlin et al. (1989) and Brooke et al. (1992). Their results indicated that particles tended to accumulate in streak flow patterns within the viscous sublayer.

Experimental work by Fessler et al. (1994) on particles in turbulent channel flow indicated that preferentially concentrated particle distributions were observed on the centerline for particles with Stokes numbers of order unity based on the Kolmogorov time scale. Later, numerical studies by Rouson and Eaton (2001) concerning a particle laden turbulent channel flow, although at a lower Reynolds number, indicated that the observed particle distributions near the centerline were probably initially produced by

the streak-like particle patterns found in the viscous sublayer and propelled to the centerline by large-scale turbulent mixing.

12.5.4 Body Force Effects on Particle Dispersion

The turbulent dispersion of heavy particles under the influence of body forces was initially investigated during the mid-20th century by researchers interested in atmospheric pollution problems. The equation of motion to be applied in this situation for small Reynolds number particles can be given as

$$\frac{d\mathbf{v}}{dt} = \frac{f}{Stk}(\mathbf{u} - \mathbf{v}) + \frac{\hat{\mathbf{g}}}{Fr}$$

where $\hat{\mathbf{g}}$ is a unit vector in the direction of the body force or gravitational acceleration and $Fr = U^2/gL$ with g being the magnitude of the body force or gravitational acceleration. The nondimensional gravity term is here related to a reciprocal Froude number. Therefore, small particle dispersion in dilute two-phase turbulent flows involving a gravitational body force can be viewed as a function of particle Stokes number, particle Reynolds number, Froude number, and flow Reynolds number.

An additional quantity for evaluating the significance of gravity or body force in this type of particle dispersion process is the terminal velocity, $V_t = g\tau_v/f$. If this velocity is high, compared with typical turbulent or mean flow velocities, then gravitational or body force effects may dominate the dispersion process. If the terminal velocity is of comparable magnitude to flow velocities then time-scale ratios involving particle residence times in turbulent vortices and Lagrangian vortex time scales become essential for developing qualitative understanding of the gravitational or body force affected dispersion process.

Owing to the complexity of this problem and the rather limited understanding of the nature of the atmospheric flow, time-averaged isotropic turbulent flow models were initially used for analyzing the dispersion process. A review covering earlier work on this type of problem can be found in Stock (1996).

In more recent times, direct numerical simulation studies involving isotropic and shear flow turbulent particle dispersion with body forces have been carried out by Squires and Eaton (1991a–1991c), Wang and Maxey (1993), and by Raju and Mieberg (1995). These studies have more explicitly illustrated the combination of effects in these situations.

A large eddy simulation (LES) of suspended particles in a homogeneous two-phase turbulent flow was initially carried out by Deutsch and Simonin (1991). Recent examples involving the use of LES for two-phase flow analysis can be found in Wang and Squires (1996), Armenio et al. (1999), and Yuu et al. (2001).

The initial applied problem of pollutant dispersion in environmental flows with complex terrain or complicated weather patterns is still at an incomplete level of understanding. Sophisticated numerical simulation tools such as two-phase LES combined with powerful computational hardware will be needed to develop this area further.

12.5.5 Two-Way Coupling Effects on Particle Dispersion

During the past 10 years, considerable attention has been turned to the effects of coupling, between the particle phase and the fluid carrier phase. In the case of dilute two-phase flows, these effects are typically referred to as two-way coupling. Since the turn of the millennium, these efforts have intensified to a point where this area has become one of the centers of activity within the two-phase community. This activity mostly focuses on modeling and simulation areas; however, a few interesting experimental studies have also been reported. A recent review of the two-way coupled model developed by Crowe (2000) highlights some potential pitfalls and inaccuracies that can arise if temporal and spatial-averaging procedures are not carried out in a consistent manner.

A consistent averaging approach for two-phase flow modeling has been developed by Crowe and Gilland (1998). This approach produces a two-phase turbulent energy equation with specific new terms for the generation of turbulence by particles and a term for the transfer of kinetic energy from the particles to the carrier phase. Physical models for evaluating the importance of these terms are presently being developed.

At present, there is no general consensus regarding the effect of particles on the turbulent flow. The particle effect on the turbulence level will probably be a function of particle diameter, particle Reynolds number, particle concentration level and the characteristic scales of the turbulent flow. Several on-going studies have been involved with numerical and experimental investigations of two-way coupling effects.

A compilation of previous experimental results by Gore and Crowe (1989) indicated that relatively large particles tend to increase the turbulence intensity levels while relatively small particles tend to have little effect on the turbulence levels or slightly decrease the levels of turbulence. This finding is obviously consistent with the fact that large particles tend to move at high particle Reynolds numbers thereby producing turbulent wakes that consequently increase overall turbulence levels. Whereas small particles at high loading levels may tend to increase effective viscosity levels through an Einstein-Batchelor type mechanism (Batchelor, 1967).

Although the reported Gore and Crowe trend seemed to be consistent with generally accepted physical understanding of particle flow modification effects, one of its basic tenets, namely that small particles tend to attenuate turbulence, was brought into question by Elghobashi and Truesdell (1993). In that study, involving a numerical simulation of homogeneous turbulence and dispersed solid particles, results were produced that showed that turbulence intensity levels might actually increase for small particles at low Reynolds numbers thus contradicting the Gore and Crowe proposal. More recent numerical studies of small particles carried out using similar techniques involving higher resolution and more particles by Ferrante and Elghobashi (2003), however appear to contradict the initial reported contradiction thus bringing the simulation results into general agreement with the original proposal by Gore and Crowe.

A perspective on this issue of turbulence modification by particles can be obtained from a recently presented energy equation derivation by Crowe (2001) and applied to a one-dimensional wall constrained two-phase flow situation. The resulting turbulence energy equation is given as

$$\frac{d}{dt}(mk) = NC_D(U - V)^2 + \tau_w UL - m\varepsilon$$

where the first term on the RHS gives the particle drag effect on the flow, the second term involves the shear stress at the constraining wall boundary and the third term represents the dissipation in two-phase flow. If the dissipation term is moved to the LHS of the equation, then the effect of particle drag on the turbulent flow can be clearly delineated.

$$\frac{d}{dt}(mk) + m\varepsilon = NC_D(U - V)^2 + \tau UL$$

This result shows that particle drag effects will increase the level of turbulence energy, or increase the dissipation rate, or increase both, or increase one more than it decreases the other.

This finding is consistent with both the previous experimental results and numerical simulations. At high Reynolds number, the primary effect of the particles is probably to increase the turbulence energy levels. At low Reynolds number, the primary effect of the particles is probably to increase the dissipation rate and therefore to slightly decrease turbulence energy levels. At intermediate Reynolds number, both effects are increased creating an approximately nullifying effect on the resulting turbulence energy levels. Obviously, a better understanding of the detailed flow fields generated by the particles is a necessary requirement for progress in this area.

12.6 Turbulence Modulation by Particles

J.K. Eaton

12.6.1 Introduction

This section addresses modification of the carrier-phase turbulence in dispersed multiphase flows. Specifically, high Reynolds number flows with relatively dilute loadings of small particles or droplets in a

turbulent gas or liquid flow are considered. In such cases, there is an equivalent single-phase flow in which the turbulence is produced by mean shear or other mechanisms unrelated to the presence of a second phase. To first order, we may think of the dispersed multiphase flow as a turbulent single-phase flow (the carrier phase) contaminated by a set of widely spaced, small particles. For the present discussion, we use the generic term “particles” to refer to any second phase distributed in small discrete masses.

For very light loadings of particles or very light responsive particles, the turbulence is unchanged by the contaminant phase. The motions of particles may be computed assuming that they do not have any global effect on the turbulence, and the turbulence may be represented by any model that works for an equivalent single-phase flow. This is the case of one-way coupling. However, in many disperse flows, the presence of the particles changes the carrier-phase turbulence significantly. In order to compute the particle motions, heat, and mass transfer, chemical reaction rates, particle-agglomeration, etc., we must first understand and model how the carrier-phase turbulence is modified. This is the case of two-way coupling.

The turbulence properties of the carrier phase can be characterized in terms of various statistical quantities such as turbulent kinetic energy, Reynolds stresses, spectra, or two-point correlations. The term turbulence modulation means that one or more of the statistical properties of the carrier phase turbulence is changed by the presence of particles. Most frequently, one refers to changes in the carrier-phase turbulent kinetic energy, which may be either attenuated or augmented. Turbulence attenuation commonly occurs in gas flows laden with solid particles or liquid droplets, while augmentation is fairly common in liquid flows carrying either particles or bubbles. However, the turbulent kinetic energy changes do not fully describe the changes to the turbulence. For example, in some cases, particles may distort the turbulence energy spectrum substantially, while causing only small changes to the turbulent kinetic energy. In other cases, particles may locally distort turbulent eddies.

An important question is: Why is turbulence modulation an important phenomenon that we need to understand? The most obvious answer is that turbulence modulation is sometimes so large that it completely changes the character of the turbulence and the behavior of engineering devices. [Figure 12.59](#) shows turbulent kinetic energy data from the centerplane of a fully developed turbulent channel flow laden with either 150 μm glass or 70 μm copper particles. At the heaviest mass loading ratio of 0.4, the copper particles reduce the turbulence kinetic energy by a factor of more than 7. Note that this loading corresponds to a volume fraction of only 5.5×10^{-5} and a mean particle separation distance of >20 particle diameters. This is clearly a very dilute flow, but the particles have a dominant effect on the turbulence behavior. Such reductions in the turbulence levels can have major effects on the overall multiphase flow behavior. One effect is that particle dispersion by turbulence is likely to be much lower than a simple one-way coupling model would predict. One would expect that mixing and chemical reaction rates also would be affected when turbulence levels are reduced to such a degree. An example in which this could be very important is fast fluidized beds, where chemical reaction and the turbulence transport properties are critical.

Turbulence augmentation may also have substantial effects, especially in low turbulence flows. The addition of small-scale turbulence induced by turbulent particle wakes can cause large increases in energy and species transport in nominally laminar flows. Even small-scale turbulence is much more effective than molecular diffusion, so again turbulence modulation may lead to substantial changes in the performance of multiphase systems.

The degree of turbulence modulation can vary from very small to quite large. Gore and Crowe (1991) reviewed experimental data for the restricted case of particle-laden pipe and jet flows. The percentage change in the streamwise turbulence intensity varied from -90 to $+350\%$ over the range of particle and flow parameters examined. While many cases showed substantial modulation, a large fraction of the experiments showed only small changes. The only consistent trend that emerged from the data review was that small particles attenuate turbulence, while large particles augment turbulence. They found that the critical particle diameter separating attenuation from augmentation was approximately one tenth of the scale of the most energetic eddies.

The qualitative rule of thumb developed by Gore and Crowe generally holds, but it does not allow prediction of the degree by which the turbulence will be changed. No general theory or data correlation has emerged that allows reliable prediction of the level or character of turbulence modulation for an

arbitrary dispersed multiphase flow. There are several reasons for the lack of progress in this area. First is the difficulty in measuring the carrier-phase turbulence in the presence of a substantial number of particles. Second is the fact that several different mechanisms may produce turbulence modulation as discussed in the next section. In some flows, two or more of these mechanisms may be active and counteract each other. If the counteracting mechanisms are not recognized, the results may be confusing. Finally, there is the huge parameter space involved. An incompressible, single-phase flow is typically defined by only the geometry and the Reynolds number. The addition of a second phase adds many more parameters, even if the second phase consists of monodisperse round spheres. In such a case, additional dimensionless parameters that arise are the particle Stokes number $Stk = \tau_p / \tau_t$, where τ_p is the particle aerodynamic time constant and τ_t is a time scale of the turbulence, the particle diameter normalized by a turbulence length scale d/l_t , and the particle Reynolds number $U_{rel}d/\nu$. Of course, even more parameters are important if the particles are polydisperse, nonspherical, or if they themselves are fluid (droplets or bubbles).

The following subsections provide a general discussion of the mechanisms by which particles can change the carrier-phase turbulence and give a brief overview of methods used to explore turbulence modulation. This is followed by a survey of experimental and computational observations of turbulence modulation for several types of dispersed flows. These observations provide some general guidance for estimating the likely level of turbulence modulation in a given flow. However, the survey also points out the wide variability in the degree of modulation among seemingly very similar flows.

12.6.2 Mechanisms of Turbulence Modification

The exact mechanisms of turbulence modulation are not very well understood, and the available theories often cannot predict the level or even sign of the change in turbulent kinetic energy. Nevertheless, there are some basic mechanisms of particle-turbulence interaction that we know play a role in turbulence modulation. All the known mechanisms require that the particles be large enough that they cannot follow the flow, so that there is a substantial instantaneous relative velocity between a particle and the carrier fluid.

One route to turbulence modulation by particles is through the carrier-phase mean velocity. If the mean carrier-phase velocity field is changed by the addition of particles, then the mean strain field and the turbulence production rate will also be changed. For example, if a concentrated stream of high-velocity particles is introduced into a gas flow, a local jet will be formed in the carrier flow due to the drag of the particles applied to the gas. The turbulence production in the jet shear layers is likely to increase the turbulent kinetic energy. This mechanism of turbulence modulation will not be considered in detail here. Presumably, the effects of carrier mean flow distortions on the carrier turbulence can be predicted by single-phase turbulence models, and calculation of carrier-phase mean flow distortions by inhomogeneous particle flows is straightforward. However, when considering turbulence modulation experiments, we must be aware that this mechanism may be affecting the results. This is frequently the case in liquid–solid flows.

A mechanism for turbulence augmentation when particles are relatively large is unsteady particle wakes. In a uniform stream, the wake of a sphere is asymmetric for Reynolds number > 210 and unsteady for Reynolds numbers > 270 (Bagchi and Balachandar, 2002). When there is a mean velocity difference between the particles and the carrier fluid due to gravity or acceleration of the carrier phase, energy is transferred from the particles to small-scale, carrier-phase velocity fluctuations. In most dispersed gas–solid flows, the particle volume fraction is very small and the particle wakes occupy only a small fraction of the flow volume, so the unsteady wake effect creates only minor changes in the turbulence. However, the unsteady wakes are a significant source of turbulence augmentation in some liquid–solid flows, where the particle volume fraction is not small and the particle Reynolds number is in the vortex-shedding regime.

A related mechanism is the superposition of many randomly positioned laminar or “laminar-like” wakes as investigated by Parthasarathy and Faeth (1990) and Chen and Faeth (2001). They investigated turbulence modulation in the absence of shear production, so all the observed turbulence was produced

by particle wakes. Chen and Faeth (2001) developed a dimensional correlation that relates the turbulence level to the mean dissipation of energy due to the relative motion of the particles and fluid. For typical multiphase flows, carrier-phase shear production of turbulence dominates, and laminar wakes are relatively unimportant in setting the level of turbulent kinetic energy. However, the superposed effect of the wakes is apparent in several experiments where turbulence spectra are measured. It is common to see a turnup in the spectra at a large wave number, which is apparently related to the particle wakes (cf., Rogers and Eaton, 1991).

The mechanism, believed by most to cause turbulence attenuation is the so-called extra dissipation of turbulence by particles. A particle that cannot respond to the turbulent velocity fluctuations exerts a force on the fluid that opposes the relative motion. When the particles are heavy (i.e., have large Stokes numbers), the relative motion is produced mostly by the carrier-phase fluctuations. The cloud of dispersed particles produces a nonuniform force field that instantaneously opposes the carrier-phase velocity fluctuations, thereby extracting energy from the turbulence. Some of the energy taken from the carrier-phase turbulence is transferred to fluctuating kinetic energy of the particles. However, most goes into producing local flow distortions around each particle. For small particles, the length scales of the flow distortions are small and the corresponding velocity gradients are large, so the local flow distortions are dissipated rapidly by viscosity. Therefore, we see that the particles act as a short circuit of the regular turbulence energy cascade. Energy can be absorbed from the carrier-phase turbulence at any frequency that is too high for the particles to follow. That energy is passed directly to scales comparable to the particle diameter, and is dissipated.

Preferential concentration of particles into specific turbulence structures and preferential sweeping of particles into downflow zones offer two other possible mechanisms of turbulence modulation. Preferential concentration occurs when particles with particle time constants comparable to eddy time scales are swept out of vortex cores and concentrated in convergence zones (Squires and Eaton, 1991). A simplified analysis by Eaton and Fessler (1994) showed that particles apply an angular impulse opposing the vortex rotation as they are spun out of a simple vortex. For Stokes numbers near unity, the ratio of the angular impulse to the initial angular momentum of the vortex is $1.3\phi/Stk$, where ϕ is the mass loading ratio. This would act to suppress vortices with time scales near the particle time constant.

Preferential concentration in a gravitational field results in preferential sweeping of particles into downflow zones, and a higher than expected average settling velocity (Maxey, 1987). Numerical simulations by Ferrante and Elghobashi (2003) indicate that preferential sweeping at moderate mass loading creates substantial anisotropy in the turbulence and slows the decay of isotropic turbulence. It is important to note that at high Reynolds numbers, the turbulence has a wide range of time and length scales. Preferential concentration may occur in a narrow range of scales depending on the particle size range. Therefore, it is likely that eddies in a certain size range would be effected most by the particle forces.

The mechanisms discussed in the previous two paragraphs treat the particles as a cloud that produces a nonuniform but continuous force-field applied to the carrier-phase flow. However, in most cases where turbulence modulation is significant, the particles are too large and too widely spaced to be considered as applying a continuous force field onto the turbulence. An examination of the channel flow case illustrated in [Figure 12.59](#) is instructive. The experiments were performed in air, with a channel half-width of 20 mm and a Reynolds number of 13,800 based on the half-height and the bulk velocity. The particles had a typical Reynolds number based on the relative velocity of about 20. The Kolmogorov length scale and the Taylor microscale at the channel centerplane were approximately 170 and 3000 μm , respectively, and the viscous length scale was 31 μm . The particle diameter of 150 μm was comparable to the smaller scales of the turbulence, and the average particle spacing of 2100 μm (at 40% mass loading) means that each eddy in the energy-containing range would only contain a few particles at the most. Although these values are specific to a single experiment, they are quite characteristic of experiments where strong attenuation is observed.

At the typical particle Reynolds number, the region of significant flow distortion extends several particle diameters from the particle surface, especially in the particle wake. We expect that the particles produce significant local distortion of the small-scale motions. Moreover, the fact that the average particle spacing is so large means that the force applied is not continuous. This is likely to produce a significant

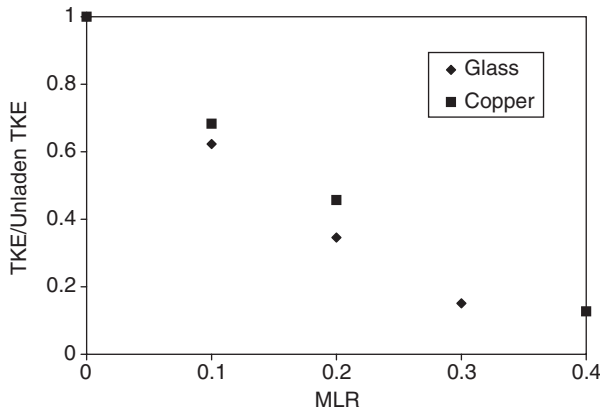


FIGURE 12.59 Attenuation of turbulent kinetic energy as a function of mass loading ratio on the centerplane of fully developed channel flow for 150 μm diameter glass and 70 μm diameter copper beads. (From Paris, T. and Eaton, J.K., Report TSD-137, Department of Mechanical Engineering, Stanford University, 2001. With permission.)

distortion of the energy-containing eddies and could lead to a higher turbulent dissipation rate. Furthermore, the fact that the particle diameter is comparable to the Kolmogorov scale indicates that the particles experience significant velocity gradients rather than the locally uniform flow assumed in most models. This means that the particles experience forces transverse to the relative velocity (cf. Bagchi and Balachandar, 2002). We group these effects of relatively large particle diameter and spacing under the heading “eddy distortion.” It will be shown in the following two sections that these effects are not accounted for in existing two-way coupling models.

12.6.3 Analytical Approaches

A common approach to modeling the effects of particles on turbulence is to treat the particles as applying a continuous force field onto the fluid phase where the force is the reaction force to the particle drag (cf. Chen and Wood, 1985; Berlemont et al., 1990; Rogers and Eaton, 1991). Following the development of Rogers and Eaton, the modified Navier–Stokes equations are

$$u_{i,t} + u_j u_{ij} = -\frac{1}{\rho_f} p_{,i} + \nu u_{i,jj} - \frac{1}{\rho_f} F_i$$

where indicial notation is used and commas imply derivatives. F_i is the force per unit volume applied by the particles onto the fluid. Assuming a linear drag law and neglecting forces other than drag, we get

$$F_i = \frac{c}{\tau_p} (u_i - v_i)$$

where c is the local particle mass concentration, u_i the fluid velocity, and v_i the particle velocity. Next, the Reynolds decomposition is applied, the mean flow component is subtracted, and the fluctuating component is squared and averaged to obtain the turbulent kinetic energy transport equation. Rogers and Eaton assumed homogeneous flow so that transport and diffusion terms could be neglected. Further, assuming constant fluid density and constant particle time constant yields

$$\frac{D}{Dt} \frac{q^2}{2} = P - \varepsilon - \frac{1}{\rho_f \tau_p} [C(\overline{u_i' u_i'} - \overline{u_i' v_i'}) + (U_i + V_i) \overline{c' u_i'} + (\overline{c' u_i' u_i'} - \overline{c' u_i' v_i'})]$$

Here the production term P and the dissipation term ε are identical to the single-phase terms. It is commonly assumed that the second and third terms in the brackets are negligible further simplifying the equation. The term $(C/\rho_f \tau_p)(\overline{u_i' u_i'} - \overline{u_i' v_i'})$ is commonly called the extra dissipation due to particles.

There are several deficiencies in the proceeding analysis. One obvious problem is the assumption that the force applied onto the fluid is linearly proportional to the fluid/particle velocity difference. Most cases in which turbulence attenuation is significant involve particle Reynolds numbers greater than unity. Furthermore, the instantaneous force on a particle is affected by the local straining field. When the particle diameter is comparable to or larger than the Kolmogorov scale, the flow around the particle is highly nonuniform. The force applied by the particle on the fluid is almost never aligned with the instantaneous velocity difference, and the root mean square force magnitude is probably larger than would be estimated by assuming locally uniform flow around the particles.

A second major deficiency is that the analysis assumes that energy transferred to the particle is eliminated from consideration. However, when a force is applied to a particle, that particle accelerates and creates local flow distortion. The assumption is that these fluid motions are at very small scale and are quickly dissipated by viscosity. However, we again note that the particles are often larger than the smallest scales of turbulence. In this case, it is more appropriate to assume the particle-turbulence interaction as transferring energy between different scales of velocity fluctuation.

Crowe et al. (1997) pointed out that the interphase forces do not occur at a point and that the analysis must be carried out over small control volumes possibly incorporating multiple particles. Crowe (2000) developed a model for turbulence modulation applying the volume averaging approach to the mechanical energy equation. The problem with this approach is again that in practical situations, the particles usually have scales comparable with some turbulence scales. If an averaging volume is chosen such that it incorporates at least one interparticle spacing, then we must also consider that some of the turbulence is averaged. A model must account for the effects of this turbulence, which is not resolved by the averaged equation set.

Of course, all analytical models of turbulence have aspects, which cannot be strictly justified on theoretical grounds. The appropriate question is, do these models offer predictive capability over some useful range of turbulence and particle parameters? Unfortunately, the answer in the present case is no. The extra dissipation due to particles terms above and the model presented in Crowe (2000) both show increasing attenuation of turbulence with decreasing particle time constant. Many of the experiments discussed below show the opposite trend. Particles with time constants comparable to the Kolmogorov time scale have not been observed to cause significant attenuation, while larger particles at similar loading cause strong attenuation. Crowe's model captures the fact that very large particles cause turbulence augmentation.

12.6.4 Methods for Studying Turbulence Modulation

Scientific study of turbulence modulation is a relatively recent endeavor because it requires the use of advanced optically based instrumentation or powerful supercomputers to make significant advances. Here we give a very brief overview of the methods used to provide the data on carrier-phase turbulence modulation.

The challenge for laboratory experiments is to measure the turbulence properties of the carrier phase in the presence of a large number of particles. Almost all measurements are made with laser-based instrumentation due to problems of probe interference and probe damage when hot wire or other invasive measurement techniques are used. Laser Doppler anemometry (LDA) has been used extensively since the work of Lee and Durst (1982). The challenge in LDA is to discriminate between signals coming from carrier-phase tracer particles and the generally stronger signals coming from the dispersed particles comprising the second phase. When the dispersed-phase particles are relatively large and monodisperse, the discrimination can be done based on the signal pedestal amplitude (cf. Kulick et al., 1994). Since the mean velocity and turbulence levels may differ significantly between the two phases, crosstalk in which particle-phase signals are interpreted as arising from tracer particles must be carefully monitored to insure reliable turbulence measurements. A more robust but more difficult and expensive technique is phase Doppler anemometry (PDA) in which the particle size and velocity are measured simultaneously (Bachalo and Houser, 1984). This technique can give poor results for nonspherical particles, but generally works well for phase separation if there is a significant difference between the tracer size and the smallest dispersed particles.

Particle image velocimetry (PIV) has been used extensively for multiphase flow research in recent years. As with LDA, the challenge is to measure the fluid phase using tracer particles that are generally significantly smaller than the larger particles comprising the second phase. Imaging the small particles in the presence of strong light scattering from the particulate phase is difficult, and image artifacts caused by out-of-focus particles can result in interphase crosstalk. Khalitov and Longmire (2002) provide a review of different techniques for two-phase PIV measurements. For gas–solid flows, the tracer particles generally are much smaller than the particulate phase. Imaging parameters are chosen so the tracers appear dim and cover only 1 or 2 pixels, while the large particle images are saturated and cover multiple pixels (Sakakibara et al., 1996). Various multistep image processing techniques (cf. Khalitov and Longmire, 2002; Kiger and Pan, 2000; Paris and Eaton, 1999) are used to reduce the noise and crosstalk. Generally, these techniques are effective for volume fractions below about 0.01%. In liquid–solid flows or bubbly flows, the tracer particles can contain fluorescent dye allowing separation of the phase images using color. Measurements at high solids concentration are possible in liquid using refractive index matching (Cui and Adrian, 1997).

There are also considerable difficulties in using numerical solutions of the Navier–Stokes equations to explore turbulence modulation effects. A typical turbulent particle-laden flow contains an extremely large range of length scales ranging from the boundary layer on individual particles to the largest eddies having scales comparable to the flow geometry. For high Reynolds number flow containing a large number of particles, direct solution of the Navier–Stokes equations including a correct specification of the boundary conditions on each particle and resolution of all scales of the flow would require more computer resources than will be available for some time. Therefore, approximate models are required to represent either the particle-scale motions or the energy containing turbulent scales. Squires and Eaton (1990) and Elghobashi and Truesdell (1993) adapted single-phase direct numerical simulation codes for isotropic flows by using simple drag laws to compute the force applied onto each particle by the flow, and applying the reaction force back onto the fluid as a variable body force. The method which has come to be called the “point-force coupling scheme” applies the force only to the grid points immediately surrounding the particles resulting in an intermittent body force field. The method is not valid unless the particles are significantly smaller than both the turbulence Kolmogorov scale and the grid spacing. However, as discussed above, most flows in which there is substantial turbulence modulation violate these conditions. While the point-force coupling scheme has been applied widely, it has not been tested rigorously against experimental data. Simonin and Squires (2003) assert that the point-force coupling method accounts for the direct modification of large scales, but not for turbulence production by particle wakes. Maxey and co-workers (cf. Lonholt et al., 2002) developed an approximate force-coupling scheme that distributes the force applied by a particle with a Gaussian distribution and includes both monopole and dipole contributions. This scheme has been validated for low Reynolds number flows with a small number of particles, but it has not been tested for turbulence modulation cases.

Recently, researchers have begun to address particle-turbulence interaction using simulations that fully resolve the flow around a single particle in a small region of turbulent flow. Bagchi and Balachandar (2003) used a large spherical coordinates grid to examine the forces on a particle in turbulent flow for particle Reynolds numbers of the order of 100 and particle diameters of 1.5 to 10 times the Kolmogorov scale. These simulations used frozen turbulence advected past the particle, so they could not assess the effects of the particle on the turbulence. Burton and Eaton (2002, 2003) used an overset grid code to compute the evolution of decaying homogeneous turbulence with a single embedded particle. These two studies are the beginning of a new approach to provide detailed information that can be used to develop advanced force coupling models.

12.6.5 Observations of Turbulence Modulation

Experiments on turbulence modulation in gas-particle flows show a consistent trend that small particles attenuate turbulence, while large particles augment it. Gore and Crowe (1991) and Crowe (2000) collected data from several experiments in pipe and channel flows and showed that turbulence is attenuated when

the particle diameter is less than about 1/10 of a characteristic turbulence length scale and is augmented for larger particles. Unfortunately, this finding is not sufficient, since the degree of turbulence modulation varies widely between experiments depending on the flow parameters. In this section, we examine the turbulence modulation results from a cross-section of experiments and numerical simulations in an effort to discern other trends that could help to predict turbulence modulation in previously unexplored flows. No effort is made to provide a comprehensive review. Rather, a few specific flow types were chosen based on the existence of multiple experiments or simulations over a similar parameter range.

12.6.5.1 Homogeneous Gas–Solid Flows

The flow regime most commonly explored using numerical simulations is homogeneous gas-phase turbulence with dilute loadings of solid particles. The reader is reminded that these simulations require assumptions that are not strictly valid, and the codes may yield incorrect results. All of the numerical studies have been confined to the small particle regime in which turbulence attenuation is expected, and the Taylor microscale Reynolds number is quite small, ranging from 20 to 94 in the cases discussed below.

Stationary (forced) isotropic turbulence was examined by Squires and Eaton (1990) and Boivin et al. (1998) for particle mass loading ratios ranging from 0.1 to 1.0 and Stokes numbers based on the Kolmogorov scale (Stk_k) ranging from 1.3 to 11.4. Both the studies indicated substantial turbulence attenuation, with the degree of attenuation increasing with increasing mass loading. The maximum reduction in the turbulent kinetic energy (TKE) was 56%. Squires and Eaton found essentially no effect of varying Stk_k from about 1.4 to 4.7, while Boivin et al. found that the attenuation increased monotonically as the Stk_k increased from 1.3 to 11.4 at a mass loading ratio of 0.2. The opposite trend was observed when the mass loading ratio was increased to 1.0. One consistent finding of these studies and several others discussed below is that the turbulence spectra are distorted, showing attenuation at low frequency and augmentation at higher frequency.

Decaying isotropic turbulence analogous to grid turbulence was simulated by Elghobashi and Truesdell (1993), Druzhinin and Elghobashi (1999), Ferrante and Elghobashi (2003), and Sundaram and Collins (1999). It is difficult to discern any consistent trends from these results. Sundaram and Collins varied the particle diameter and the Stokes number maintaining a constant mass loading ratio of 0.14. They found that the attenuation increased as the Stokes number increased from 1.6 to 6.4. Ferrante and Elghobashi observed a similar trend for Stk_k ranging from 0.1 to 5. The overall attenuation levels in the latter case were quite small with a maximum reduction in kinetic energy of 30% at a mass loading ratio of 1.0.

Most of the computations discussed above focused on cases without gravity. However, Druzhinin and Elghobashi, and Ferrante and Elghobashi each ran a case including a body force in the particle equation of motion. In both cases, very substantial turbulence augmentation was observed, even though the particles were quite small ($d_p/l_e < 0.01$). This contradicts the great body of experimental evidence (cf. Gore and Crowe, 1991).

An attempt was made to determine trends in the degree of turbulence modification as a function of various parameters. Turbulence modification was found to increase with increasing mass loading. Figure 12.60 shows a plot of the turbulent kinetic energy (TKE) normalized by the unladen TKE for cases which had Stk_k near 5. Turbulence attenuation was always small ($< 22\%$) for mass loadings less than or equal to 20%. Substantial changes to the turbulence were only found for relatively large loadings.

Figure 12.61 shows the turbulence attenuation plotted against Stk_k for cases in which the mass loading ratio is approximately unity. For the cases of decaying isotropic turbulence, the Stokes number changes with time. A representative value midway through the decay was chosen for the purposes of this plot. There is an evidence of a trend of increasing turbulence attenuation with increasing Stk_k . However, the Squires and Eaton and Boivin et al. cases for Stk_k near 1 break with the trend. The differences between these cases and the case of Ferrante and Elghobashi are quite large, even though the flow and particle parameters are quite similar. This may be due to differences in the implementation of force coupling scheme in the simulation or in the initial conditions for the velocity field. A similar trend of increasing attenuation with increasing Stokes number was seen for cases which had mass loading near 0.2. However, at such a relatively light loading, the attenuation was always small at all Stokes numbers.

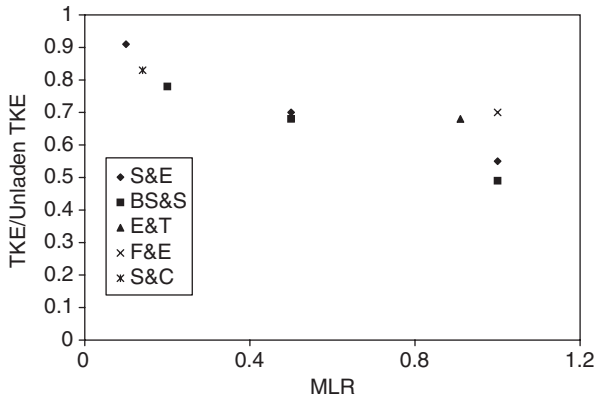


FIGURE 12.60 Attenuation of turbulent kinetic energy in simulated isotropic turbulence for cases with Stk_k near 5. (From Squires, K.D. and Eaton, J.K., *Phys. Fluids A*, 2, 1191–1203, 1990; Boivin, M. et al., *J. Fluid. Mech.*, 375, 235–263, 1998; Elghobashi, S. and Truesdell, G.C., *Phys. Fluids A*, 5, 1790–1801, 1993; Ferrante, A. and Elghobashi, S., *Phys. Fluids*, 15, 315–329, 2003; Sundaram, S. and Collins, L.R., *J. Fluid. Mech.*, 379, 105–143, 1999. With permission.)

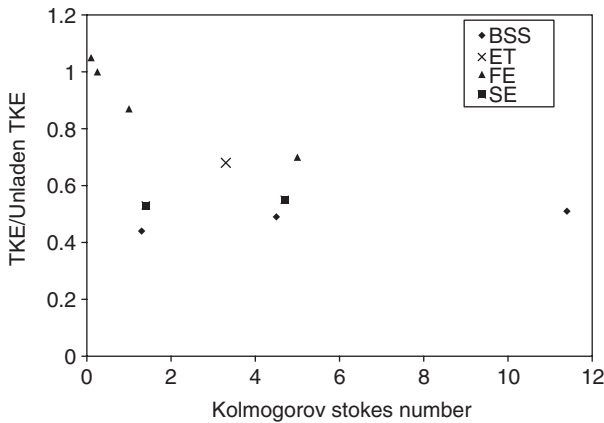


FIGURE 12.61 Attenuation of turbulent kinetic energy in isotropic turbulence for MLR near 1 as a function of Stk_k . (From Boivin, M. et al., *J. Fluid. Mech.*, 375, 235–263, 1998; Elghobashi, S. and Truesdell, G.C., *Phys. Fluids A*, 5, 1790–1801, 1993; Ferrante, A. and Elghobashi, S., *Phys. Fluids*, 15, 315–329, 2003; Squires, K.D. and Eaton, J.K., *Phys. Fluids A*, 2, 1191–1203, 1990. With permission.)

Only a few experiments have been reported on the behavior of particle-laden homogeneous turbulence. Schreck and Kleis (1993) examined grid turbulence in a downflow water channel laden with relatively large solid particles ($d_p/l_k = 5$). Volume concentrations were as large as 1.5%. Reductions in the TKE of 20% were observed for the heaviest particles at the largest concentration. Geiss et al. (2001) examined grid turbulence in a downflow wind tunnel. The flow carried a 35% (by wt) loading of 110- μ m-diameter glass particles. This short paper gives few details on the experiment, but kinetic energy reductions of up to 44% were observed at the most downstream station. Note that this reduction is comparable with the reductions observed in some of the simulations at substantially higher mass loading. Based on this experiment and some of the wall-bounded flow measurements reported below, there is an indication that the simulation techniques under-predict turbulence attenuation.

12.6.5.2 Wall-Bounded Gas–Solid Flows

The strongest effects of turbulence modification have been observed in wall-bounded flows including pipe flows, channel flows, and boundary layers. Much of the original experimental work on turbulence

modulation was done in pipe flows with notable contributions from Lee and Durst (1982), Tsuji and Morikawa (1982), and Tsuji et al. (1984). More recently, considerable effort has been focused on fully developed turbulent channel flows and flat plate boundary layers. Kulick et al. (1994), Paris and Eaton (2001), and Kussin and Sommerfeld (2002) all examined fully developed air channel flows at similar Reynolds numbers. Each experiment covered a reasonably broad range of particle parameters lending new insight into turbulence modulation.

Kulick et al. (1994) conducted experiments in a long vertical downflow air channel flow at a Reynolds number of 13,800 based on the channel half-width and the bulk velocity. Special care was taken to insure very uniform particle loading, and as a result, the mean gas-phase velocity profile was the same at all particle mass loading ratios. Experiments were conducted with 50- and 90- μm -diameter glass beads and 70 μm copper beads. The Stokes numbers based on the centerline Kolmogorov time scale were 9, 23, and 50 for the three particle classes. Gas-phase measurements were made using LDA with submicron tracer particles that were easily discriminated from the larger dispersed particles. Turbulence modification was small ($< 10\%$) for particles with $Stk = 9$, substantial for $Stk = 23$, and very large for $Stk = 50$. Figure 12.62 reproduced from Kulick and Eaton shows the streamwise turbulence intensity profiles for copper beads at various mass loading ratios. The turbulence is attenuated across the entire profile, with the largest attenuation near the centerline.

Paris and Eaton (2001) conducted experiments in the same channel flow facility using phase-discriminated PIV to verify the earlier LDA results for copper beads. They also conducted separate experiments by using 150 μm glass beads, which had almost the same aerodynamic time constant as the copper. By virtue of their larger diameter, the particle Reynolds numbers were over two times greater for the glass ($Re_p = 19$ vs. 8). The centerline results, shown in Figure 12.59, showed similar attenuation levels as observed by Kulick for the copper, and also showed consistently that the higher Reynolds number glass particles produced larger attenuation. Note that the data plotted in Figure 12.59 incorporate fluctuating velocity measurements in the streamwise and spanwise directions.

Kussin and Sommerfeld (2002) and Lain et al. (2002) made measurements in a horizontal channel flow for a variety of particle sizes. The half-height Reynolds number was 21,000 and smooth- and rough-wall cases were examined. Measurements were made by using a phase-Doppler anemometer. Unfortunately, the particle size distribution was wide and the flow tracers were large (nominally 4 μm in diameter), so

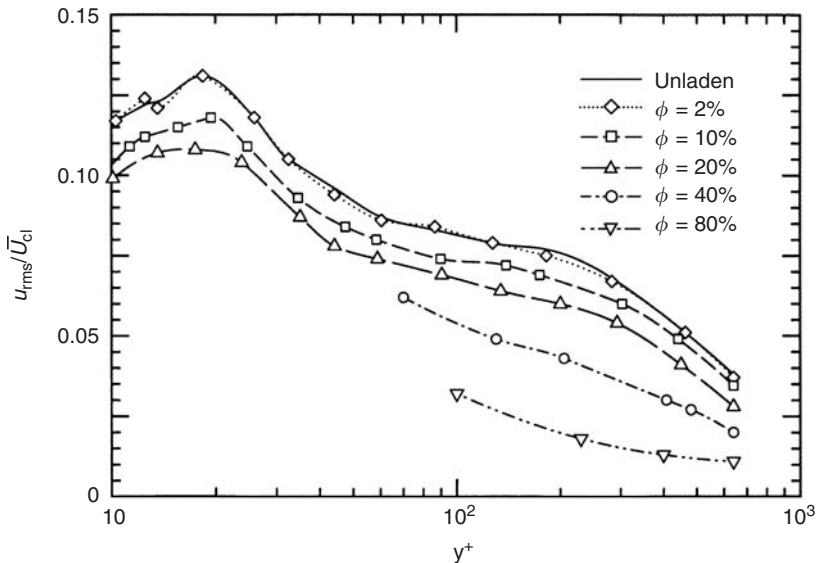


FIGURE 12.62 Streamwise turbulence intensity in fully developed channel flow laden with 70 μm copper beads. (From Kulick et al., *J. Fluid. Mech.*, 277, 285–309, 1994. With permission.)

the gas-phase turbulence measurements were contaminated by particle-phase measurements. As a result, the turbulence measurements are quite noisy. Nevertheless, because both the particle size and mass loading ratio were varied over wide ranges, trends were easily observed. Figure 12.63 shows the streamwise turbulence intensity data for the Kussin and Sommerfeld's rough-wall cases. The data have been averaged across the channel to reduce noise, normalized by the average value from all cases at zero loading, and squared for comparison with the TKE data presented in other plots. The data are presented for 60, 100, and 195 μm glass beads, which have Stokes numbers of 35, 120, and 350 and Reynolds numbers of 7, 23, and 72, respectively. Here the Stokes number is based on the estimated centerline Kolmogorov time scale to allow comparison to the homogeneous turbulence cases discussed above. All three particle sizes produce substantial attenuation with the degree of attenuation decreasing with increasing particle size. Also shown in Figure 12.63, for comparison, are the Paris and Eaton data for the channel centerplane. The copper and glass beads used by Paris and Eaton had Stokes numbers of 47 and 49, respectively. The attenuation was larger for these cases, but note that the largest attenuation in channel flows normally occurs at the centerplane. It is interesting to note that the 60 μm particles, which produced the largest attenuation in the Kussin and Sommerfeld's experiments, have Stokes numbers similar to the 150 μm glass beads that produced the strongest attenuation in the Paris and Eaton experiments.

Kussin and Sommerfeld also presented measurements with 0.6- and 1-mm-diameter glass beads with mass loadings ratios up to 2.0. These cases showed significant turbulence augmentation near the channel centerplane and moderate attenuation near the walls. They concluded that this was a particle Reynolds number effect since the relative velocity between the gas and particles was smaller near the walls than in the channel center region. The particle Reynolds numbers at the centerplane were approximately 350 and 500 for the 0.6 and 1 mm beads, respectively. This indicates that unsteady particle wakes probably played a role in the turbulence augmentation.

The channel flow experiments discussed here along with several other wall-bounded flow experiments give a fairly consistent picture. Very small particles with $Stk \leq 10$ do not cause significant changes to the turbulence. As the particle size increases, the particles cannot follow the turbulent fluctuations and turbulence attenuation increases rapidly. Attenuation reaches a maximum around $Stk = 50$. The attenuation can be very large for particles in this size range. As particle size increases further, the effects of superimposed laminar wakes or unsteady wakes begin to have an effect, decreasing the overall level of turbulence attenuation, and eventually causing substantial augmentation.

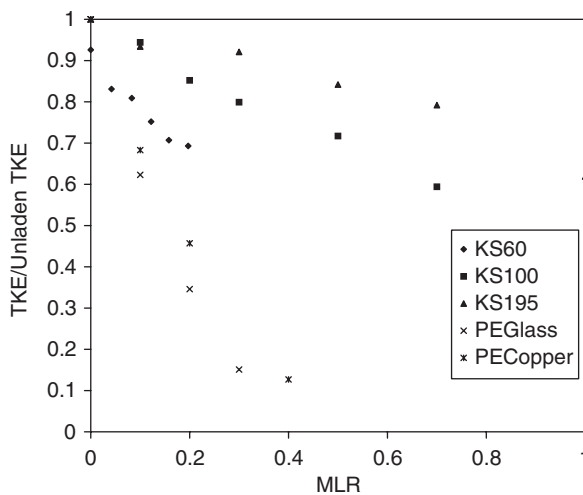


FIGURE 12.63 Streamwise normal stress (from Kussin, J. and Sommerfeld, M., *Exp. Fluids*, 33, 143–159, 2002; with permission) averaged across the channel and centerplane TKE (from Paris, T. and Eaton, J.K., Report TSD-137, Department of Mechanical Engineering, Stanford University, 2001. With permission).

12.6.5.3 Free Shear Flows

Particle and droplet-laden jets, mixing layers, and separated flows have a wide range of applications, so the fluid-phase turbulence behavior has been studied in a number of such flows. The flow geometries and particle parameters vary widely from experiment to experiment, so it has not been possible to extract trends as was done in the previous two sections. Here we just discuss a few of the important experimental results to show the types of behaviors that have been observed.

A number of studies, including Shuen et al. (1985), Mostafa et al. (1989) and Longmire and Eaton (1990), have examined round jets discharging downward into quiescent air. Shuen et al. examined the far field of a jet discharging from a pipe for a range of particle sizes and mass loading ratios up to 66%. They observed changes in the turbulent stresses of less than 10%. Mostafa et al. examined the near field of a similar jet at mass loading ratios of 0.2 and 1.0. Detailed comparisons to the unladen turbulence measurements were not presented, but the authors noted a reduction of 40% in the TKE on the jet centerline for a mass loading of 1.0. It is important to note that the jet was supplied from a turbulent pipe flow. Although the jet exit plane was not documented, it is likely that the turbulence level in the plane was substantially lower for the particle-laden case than for the single-phase flow.

Free shear flows are subject to the Kelvin–Helmholtz instability that produces large roller vortices. An important issue to understand is how the particles might affect these vortices. A simplified analysis by Yang et al. (1990) showed that particles slow the development of roller vortices. On the other hand, Longmire and Eaton (1990) found little effect of particles on the near-field development of roller vortices for mass loading ratios up to 0.8. This finding is corroborated by research in backward-facing step flows, which have been studied by Maeda et al. (1982), Hishida and Maeda (1991), Hardalupus et al. (1992), and Fessler and Eaton (1999). All these experiments were conducted in the small particle regime. Some experiments observed almost no change to the turbulence while the others showed either small attenuation or augmentation of the turbulence. Overall, the particle effects on the turbulence are much smaller than in wall-bounded flows probably because the extra dissipation due to particles is overwhelmed by the strong shear production in free shear flows.

12.6.5.4 Liquid–Solid Flows

Another important class of multiphase flows is liquid–solid flows in which solid particles are dispersed in a turbulent liquid flow. We consider here only flows with relatively low volume fraction analogous to the gas–solid flows discussed above. At high particle volume fraction, the interaction among the particles is more important than the particle-turbulence interaction. The liquid–solid material density ratio is usually between 1 and 5, so the mass loading ratio is very small for dilute volume fractions. Another consequence of the near-unity density ratio is that the particle Stokes number is small, unless the particles are quite large. The only cases for which turbulence modulation is observed are thus flows in which the particles are large relative to the turbulence scales.

There are several recent experiments on particle-laden water channel flows, where detailed measurements have been acquired by using laser-based techniques. Kiger and Pan (2002) studied a 40 mm-wide water channel operated at a Reynolds number of 12,000 and laden with 195- μm -diameter glass beads at a mass loading ratio of 0.0006. Relatively small (8 to 10%) increases in the turbulence intensity were observed across the channel.

Suzuki et al. used a 40 mm wide, vertical water channel at a very low Reynolds number ($Re_h = 2900$). The flow was laden with 400 μm ceramic particles at a mass loading ratio of 0.0012. The particle diameter in this case was about two times the Kolmogorov scale near the wall and the particle Reynolds number was of the order of 30. The turbulence was almost unchanged near the wall. However, u'^2 , increased by more than a factor of 4 near the channel center region.

Sato et al. (2000) examined a similar channel at the same Reynolds number using 190 μm ($Re_p = 10$) or 400 μm ($Re_p = 50$) glass beads. The 190 μm particles were smaller than the centerline Kolmogorov scale, while the 400 μm particles were larger. The mass loading ratio was about 0.0004 for the 190 μm particles, and 0.00033 and 0.00086 for the 400 μm particles. Using the relatively large volume fraction, measurements were only possible near the channel centerline. The smaller particles produced relatively

small increases in the kinetic energy, while the large particles increased the TKE by roughly a factor of 4. Doubling the mass loading for the 400 μm particles had a relatively small effect.

The indication from these liquid–solid experiments is that particles cause very large turbulence augmentation in this regime. It should be noted, however, that in the vertical channels, the particles changed the mean velocity profile significantly, which may have led to increases in the TKE. Overall, based on the recent channel experiments and older pipe flow data, it seems safe to conclude for liquid–solid cases that particles significantly smaller than the Kolmogorov scale produce relatively small changes in the turbulence while larger particles can produce very substantial augmentation. The lack of any effect by the smaller particles is probably due to the fact that small particles have very small Stokes numbers in liquid–solid flows.

12.6.6 Summary

We have seen that dispersed particles in the dilute regime can cause very large changes in the turbulence levels in typical shear flows. In gas flows, very small particles do not affect the flow, but particles with sizes of the order of the Kolmogorov scale can cause very significant attenuation. The attenuation appears to reach a maximum for Stk_k near 50 and particle Reynolds number of the order of 10. As particle size increases, the effect of particle wakes plays an increasing role first decreasing the turbulence attenuation and eventually causing large turbulence augmentation. Turbulence modulation is much weaker in flows such as free shear flows where strong shear production dominates.

In liquid flows laden with solid particles, turbulence attenuation is rarely observed. Because of the small solid–liquid material density ratio, small particles have very low Stokes numbers and thus have little effect on the flow. Particles that are large enough to have significant slip velocity relative to the flow are large relative to relevant turbulent length scales. In this case, the superposed wakes of the particles act to increase the turbulence substantially.

While numerous models for turbulence modulation have been proposed, none of them are capable of accurately predicting the degree of turbulence modulation for arbitrary flow and particle parameters. Further research is needed to understand proper modeling of the particle–fluid interaction in order to fully capture the competing effects of several turbulence modulation mechanisms.

The author received invaluable assistance from graduate students Wontae Hwang, Ryan Rogers, Tomohiko Tanaka, and Ern Soo Lee in preparing this chapter.

12.7 Combustion

F. Mashayek

12.7.1 Introduction

Two-phase flows involving a carrier gas laden with a dispersed phase composed of a large number of solid particles or liquid drops occur in many natural and technological applications. One of the most important applications involves the endothermic chemical reaction of the dispersed phase, as a fuel, with the carrier gas, as an oxidizer. For example, the engines that propel missiles, jets, and many other devices must rely heavily on combustion in a two-phase environment. Within the combustion chamber the liquid fuel, which is first atomized into small drops, undergoes evaporation and reaction with the oxidizer gas. To enhance the rate of mixing and reaction, these systems are designed to operate in the presence of turbulence. Furthermore, chemical reaction triggers the formation of high-gradient regions in the flow and thus serves as a source for generation and amplification of instabilities which lead to turbulence. As a result, turbulence cannot be ignored in majority of the situations involving chemically reacting flows. The presence of turbulence significantly adds to the complexity of such flows and to the challenges encountered in their physical understanding, theoretical description, and practical prediction. These challenges are primarily a consequence of the numerous degrees of freedom associated with a turbulent flow, which

itself has remained as one of the main unsolved problems in science and engineering. The addition of fuel drops, with the associated phenomena of evaporation and chemical reaction, further introduces new sets of variables, often accompanied by large variations in scales.

The topic of combustion, let alone in the presence of a second phase, is too broad to be covered in one section. Furthermore, if the solid phase is carbonaceous, both heterogeneous and homogeneous oxidation occurs. A thorough description of heterogeneous or homogeneous combustion requires basic knowledge in thermodynamics, fluid mechanics, heat transfer, chemical reaction, two-phase transport, etc. Owing to space limitation, in this section, we deal only with drop evaporation and combustion and refer to the review articles by Annamalai and Ryan (1993), Annamalai et al. (1994), and references therein for a detailed discussion of solid-particle combustion. We also restrict our discussion to subcritical conditions and refer to a recent review by Bellan (2000) for supercritical fluid behavior and modeling. As argued above, the presence of turbulence cannot be overlooked in a majority of practical situations. Turbulence effects will be discussed very briefly here and the reader is referred to several other chapters, in this handbook, which are entirely devoted to interactions of the dispersed-phase with turbulence. Nevertheless, regardless of the role of turbulence, the dispersed-phase processes could become “interactive” when the distance between the drops is comparable to a few times the drop radius. In this situation, evaporation and combustion of one drop may significantly be affected by the presence of other drops.

The next section provides a brief overview of single-phase or gaseous combustion. This overview assists the reader, with no or little knowledge of combustion to follow the main discussions on two-phase combustion. The discussion of drop evaporation and combustion is presented first for an isolated drop. Although in an actual spray, isolated drop burning is somewhat unlikely, the study of isolated drops serves as an important first step toward understanding the physical phenomena and the underlying mechanisms for evaporation and combustion. It should be emphasized that the theoretical study of isolated drops involves several simplifying assumptions, the validity of which may be arguable in real sprays, in particular near the injector where the spray is dense. For example, the isolated drop combustion model results predict increasing temperature as the size is reduced, which is contrary to the industrial experience. Therefore, the interactions among the drops must be considered. This is the subject of the second part of this discussion, where a group of drops is considered. From a modeling and theoretical point of view, it is noted that the models for group combustion often use the isolated drop results as their starting point, hence another reason for discussing isolated drops. Finally, we conclude with a general discussion of practical spray modeling. This discussion is of a general nature and addresses various available modeling strategies very briefly. Appropriate references are provided for the interested readers and a combination of models that may be most viable with the existing computational resources is recommended.

12.7.2 Overview of Single-Phase (Gaseous) Combustion

Liquid-fuel combustion systems lead to a chemical reaction between the fuel vapor and the oxidizer gas, thus forming a single-phase, or homogeneous (typically gaseous), combustion process. Therefore, as a necessary prelude to two-phase combustion, in this section we provide a brief overview of the gaseous combustion. Gaseous combustion can be described through continuum transport equations for mass fractions of various species that are participating in the chemical reaction. For a system of n chemically reacting species, the mass balance for the mass fraction Y_i of species i yields

$$\rho \frac{\partial Y_i}{\partial t} + \rho \mathbf{u} \cdot \nabla Y_i = -\nabla \cdot \mathbf{j}_i + \omega_i, \quad i = 1, 2, \dots, n \quad (12.184)$$

where \mathbf{j}_i and ω_i denote the diffusive flux and the chemical source term, respectively. The molecular transport processes that cause the diffusive flux can be quite complicated (Willams, 1985). For turbulent flows, which occur in many practical applications, this term can be simplified by considering a binary flux approximation, $\mathbf{j}_i = -\rho D_i \nabla Y_i$, where D_i is the binary diffusion coefficient, or mass diffusivity, of species i with respect to an abundant species. While this approximation provides a convenient form for describing the governing transport equations in turbulent flows, it should not be used in laminar flame calculations (Peters, 2000).

For a total number of r reactions

$$\sum_{i=1}^n v'_{ik} X_i \Leftrightarrow \sum_{i=1}^n v''_{ik} X_i, \quad k = 1, 2, \dots, r \quad (12.185)$$

that may be considered in the calculation, the chemical source term ω_i in Eq. (12.184) is described as

$$\omega_i = W_i \sum_{k=1}^r (v''_{ik} - v'_{ik}) w_k \quad (12.186)$$

where $\sum_{i=1}^n \omega_i = 0$, and for inert, nonreacting species $\omega_i = 0$. In Eq. (12.185), v'_{ik} and v''_{ik} are the stoichiometric coefficients on the reactants and products sides, respectively, for the i th species in the k th reaction, and X_i represents the chemical formula for species i . In Eq. (12.186), W_i is the molecular weight of species i and w_k is the rate of reaction k in a mechanism containing r chemical reactions

$$w_k = k_{fk} \prod_{i=1}^n \left(\frac{\rho Y_i}{W_i} \right)^{v'_{ik}} - k_{bk} \prod_{i=1}^n \left(\frac{\rho Y_i}{W_i} \right)^{v''_{ik}} \quad (12.187)$$

Here k_{fk} and k_{bk} are the rate coefficients of the forward and backward reactions, respectively, and are in general temperature-dependent. They may also depend on pressure in some cases.

To simplify the analysis, a "global" reaction mechanism may be considered. For overall reaction of the fuel F and oxygen O_2 , yielding the products P, the global reaction mechanism can be described as



For this single-step reaction, the reaction rate is written as

$$\omega = A \left(\frac{\rho Y_F}{W_F} \right)^{n_f} \left(\frac{\rho Y_{O_2}}{W_{O_2}} \right)^{n_{O_2}} \exp\left(-\frac{E}{RT}\right) \quad (12.189)$$

where A is the preexponential factor and E the activation energy. The exponential expression $A \exp(-E/RT)$ is known as the Arrhenius form and is widely used to describe the temperature dependency of the reaction rate. The exponents n_f and n_{O_2} relate to "reaction order." According to Eq. (12.189), overall the reaction is of the order $n_f + n_{O_2}$. For global reactions, n_f and n_{O_2} are not necessarily integers and are found by curve-fitting experimental data. In general, a particular global expression in the form of Eq. (12.189) holds only over a limited range of temperatures and pressures, and may depend on the details of the apparatus used to define the rate parameters (Turns, 1996).

In addition to species transport equation (12.184), the overall continuity, momentum, and energy equations of the mixture are needed to describe the gaseous combustion system fully. The continuity and momentum equations are similar to those in nonreacting flows; the energy equation is modified to account for combustion effects. The latter can be derived from the first law of thermodynamics as (Peters, 2000),

$$\rho \frac{\partial h}{\partial t} + \rho \mathbf{u} \cdot \nabla h = \frac{\partial p}{\partial t} + \mathbf{u} \cdot \nabla p - \nabla \cdot \mathbf{j}_q + q_R \quad (12.190)$$

where the frictional heating has been neglected as it has a small contribution for low-speed flows. The last term, q_R , is due to radiation and must be retained in furnace combustion. Here, the enthalpy h of the mixture is defined in terms of the enthalpies h_i of species i

$$h = \sum_{i=1}^n Y_i h_i \quad (12.191)$$

Assuming ideal gas, h_i only depends on temperature T

$$h_i = h_{\text{ref},i} + \int_{T_{\text{ref}}}^T c_{\text{pg},i}(T) dT \quad (12.192)$$

where $c_{pg,i}$ is the constant-pressure specific heat of species i and T is in Kelvin. Reference enthalpy $h_{ref,i}$ includes the chemical bond energy and is generally taken to be zero for H_2 , O_2 , N_2 , and solid carbon. The reference enthalpy of combustion products such as CO_2 and H_2O are negative and are tabulated (Burcat, 1984). The specific heat of the mixture is also defined in terms of specific heats of various species

$$c_{pg} = \sum_{i=1}^n Y_i c_{pg,i} \tag{12.193}$$

The heat flux j_q in Eq. (12.190) includes the effect of enthalpy transport by the diffusive fluxes j_j

$$j_q = -k\nabla T + \sum_{i=1}^n h_i j_i \tag{12.194}$$

To conclude, the system of continuity, momentum, energy, and species conservation equations is augmented by the equation of state for ideal gas.

12.7.3 Isolated Drop

Evaporation and combustion of a single drop are among the fundamental processes in liquid-fuel combustion and have been studied extensively, since the pioneering works of Spalding (1953) and Godsave (1953). The analysis for a general case involving all important processes such as internal circulation, drop deformation, (Haywood et al., 1994a, 1994b; Mashayek, 2001), turbulence (Sornek et. al., 2000; Wu et al., 2001), and gravity (Gogos et al., 2003) effects is quite complicated. Under special circumstances, simplifying assumptions can be made to derive an analytical solution. This solution is very useful in providing insights into the physics of drop evaporation and combustion, and has produced reasonable predictions in real applications. In this section, we briefly review the derivation of the analytical solution and its underlying physical assumptions.

12.7.3.1 Evaporation

Consider an isolated drop evaporating in a quiescent and infinitely large medium and assume that the evaporation is quasi-steady, i.e., at any instant of time, the process can be described as if it were in steady state. The drop temperature is uniform, typically at the saturation temperature $T_s < T_b$, where T_b is the boiling point of the fuel at the given pressure. Without the loss of generality, in the following we assume that the drop is at its boiling temperature. The drop preheat period does not significantly contribute to the overall combustion process and can be neglected. Also, in order to find an analytical solution, all thermophysical properties are assumed constant (Turns, 1996).

With these assumptions, the gas-phase mass conservation for a spherically symmetric drop at quasi-steady state reads

$$\dot{m} = \rho v 4\pi r^2 = \text{constant} \tag{12.195}$$

A relationship for the temperature variation in the gas can be found by considering the gas-phase energy conservation, which states a balance between the conduction and convection heat transfer

$$4\pi k_g \frac{d}{dr} \left(r^2 \frac{dT}{dr} \right) = \dot{m} c_{pg} \frac{dT}{dr} \tag{12.196}$$

Here T is the gas temperature and g refers to the gas properties. For a unitary Lewis number ($Le = k_g / \rho c_{pg} D$), by defining $\xi = c_{pg} / 4\pi k_g = 1/4\pi \rho D$, the following problem can be stated for the gas-phase temperature:

$$\frac{d}{dr} \left(r^2 \frac{dT}{dr} \right) = \xi \dot{m} \frac{dT}{dr} \tag{12.197}$$

with boundary conditions $T(r = a) = T_b$ and $T(r \rightarrow \infty) = T_\infty$, where a is the drop radius. The solution of this equation for constant \dot{m} yields

$$T(r) = \frac{(T_\infty - T_b)\exp(-\xi\dot{m}/r) - T_\infty\exp(-\xi\dot{m}/a) + T_b}{1 - \exp(-\xi\dot{m}/a)} \quad (12.198)$$

which indicates a steep temperature gradient near the surface of the drop. This temperature gradient determines the heat conducted into the drop, which will be consumed entirely for evaporation since the drop is at its boiling point. Therefore, writing the energy balance at the drop–gas interface gives

$$4\pi k_g a^2 \left. \frac{dT}{dr} \right|_a = \dot{m} h_{fg} \quad (12.199)$$

Differentiating Eq. (12.198) and substituting into Eq. (12.199) the mass flow rate of the vapor

$$\dot{m} = \frac{4\pi k_g a}{c_{pg}} \ln(1 + B_c) \quad (12.200)$$

is obtained, where

$$B_c = \frac{c_{pg}(T_\infty - T_b)}{h_{fg}} \quad (12.201)$$

is the transfer number, also known as the Spalding number. With the relation for mass in terms of drop diameter and density, a more common form of Eq. (12.200) is the so-called d^2 law written as

$$d^2(t) = d_0^2 - Kt, \quad K = \frac{8k_g}{\rho_l c_{pg}} \ln(1 + B_c) \quad (12.202)$$

where d is the drop diameter with an initial value of d_0 and subscript l refers to liquid properties.

To account for the temperature dependency of thermophysical properties, following the approach of Law and Williams (1972) for burning drops, c_{pg} and k_g are evaluated at the temperature $\bar{T} = (T_b + T_\infty)/2$

$$c_{pg} = c_{pF}(\bar{T}), \quad k_g = 0.4k_{F}(\bar{T}) + 0.6k_{\infty}(\bar{T}) \quad (12.203)$$

where F refers to fuel vapor. Other approximations are suggested in Hubbard et al. (1975).

Adopting a similar set of assumptions as in the above analysis, Mashayek (2001) investigated the effect of a deformation in the surface of a drop on its rate of evaporation by conducting finite element simulations of the gas surrounding the drop. The drop was assumed to be at its boiling temperature and the gas properties were considered constant for a quasi-steady analysis. The surface of the drop was deformed using spherical harmonics

$$h(\phi) = R_n[1 + \varepsilon_n P_n(\cos \phi)] \quad (12.204)$$

where $P_n(\cos \phi)$ is the Legendre polynomial of degree n , ε_n the amplitude of disturbance (with respect to the spherical shape), and R_n a correction factor introduced to keep the volume of the drop the same as the amplitude is changed. All lengths were normalized with the radius of the unperturbed (spherical) drop. Figure 12.64 shows the computational domain and the coordinate system used. The angle ϕ is measured from the axis of symmetry toward the equator of the drop.

Figure 12.65 shows the deviation parameter ψ as a function of ϕ for $n = 2$ at various amplitudes. Here, ψ indicates the difference between the evaporation rates of the deformed drop and the spherical drop as normalized by the evaporation rate of the spherical drop. The results indicate that the evaporation rate is larger near the axis of symmetry and lower near the equator, and the deviation from the evaporation rate

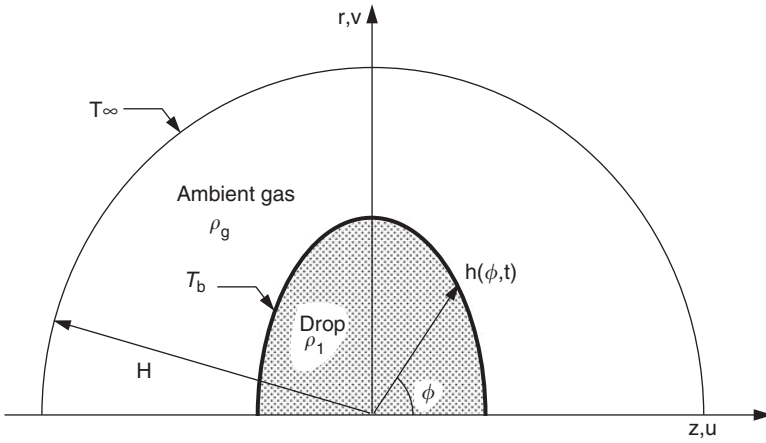


FIGURE 12.64 Coordinate system and solution domain used in computations of a deformed drop (Mashayek, 2001).

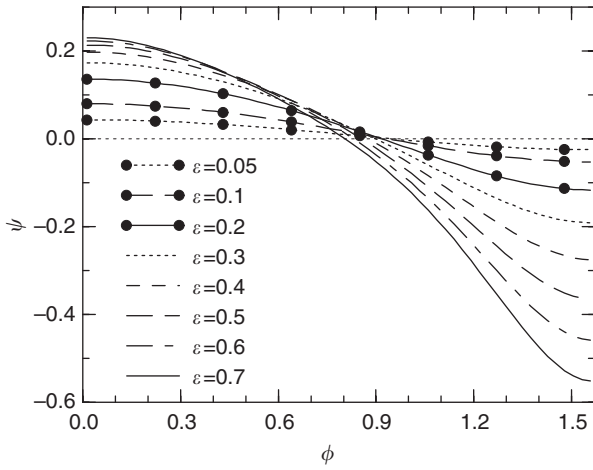


FIGURE 12.65 Variations of the normalized mass flux with angle ϕ at various amplitudes for a drop deformed with second spherical mode $n = 2$ (Mashayek, 2001).

of a spherical drop increases with the increase in the amplitude. Based on the results of the simulations, the following model was presented for calculating the evaporation rate of a deformed drop:

$$\chi = \left[F_n \left(K - \frac{2}{\varrho} \right) + \frac{2}{\varrho} \right] \beta \tag{12.205}$$

where K and ϱ are the surface curvature and the nondimensional radius of the equivalent spherical drop, respectively. Also,

$$\chi = \left[\frac{\rho_1 \sigma}{r_0} \right]^{(-1/2)} \dot{m} \tag{12.206}$$

is the normalized evaporation rate and

$$\beta = \frac{1}{2} (\rho_1 r_0 \sigma)^{(-1/2)} \left(\frac{k_g}{C_{pg}} \right) \ln(1 + B_e) \tag{12.207}$$

where r_0 and σ are the initial radius of the unperturbed drop and the surface tension coefficient, respectively. The function F_n depends on the mode of the surface disturbance and is defined as

$$F_n = \frac{3n + 2}{2[n(n + 1) + 2]} \quad (12.208)$$

Equation (12.205) is valid for surface amplitudes up to 10% of the initial drop radius and has been tested for $0.1 \leq B_e \leq 2$ and for surface deformation up to $n = 8$. It is noted that Eq. (12.205) reduces to Eq. (12.200) for a spherical drop for which the surface curvature $K = 2/\rho$.

12.7.3.2 Combustion

The analysis of a burning drop is understandably more complicated, but an analytical solution can be found for a simplified case. The diffusion flame requires that fuel and oxidizer react in stoichiometric proportions at the spherical flame that forms around the drop at a radius r_f . The reaction is assumed to be infinitely fast and the flame is represented by an infinitesimally thin sheet. A single-component fuel is considered with zero solubility for gases and there is phase equilibrium at the drop surface.

The analysis is also based on a unitary Lewis number, which represents the relative importance of the thermal conductive transfer and transport by mass diffusion. For $Le > 1$, the mass diffusion transports thermal energy in the direction of increasing concentration. The role of the nonunitary Lewis number has been examined quantitatively in Chiu (2000) by using a canonical theory of drop.

Figure 12.66 illustrates the two main regions formed inside and outside the flame. In the first region, between the drop surface and the flame, the fuel vapor concentration decreases monotonically with the radius, whereas the products concentration shows the opposite variation. Since the products do not dissolve in the liquid, they do not move and remain stagnant in this region. At the flame, the products concentration reaches the maximum (unity) and the fuel concentration is zero. In the region outside the flame, the products concentration decreases monotonically with an increase in radius. The oxidizer concentration decreases from its free-stream value of $Y_{Ox,\infty}$ at distances far away from the flame to zero at the flame.

Based on the physical model illustrated in Figure 12.66, the analysis is conducted to determine five parameters: fuel mass flow rate \dot{m}_F , fuel mass fraction at the drop surface Y_{Fs} , drop surface temperature T_s , flame temperature T_f , and flame radius r_f . The final results can be summarized as follows (Turns, 1996):

$$T_f = \frac{q_{i-1} + h_{fg}}{c_{pg}(Y_{Ox,\infty} + \nu)} [\nu B_c - Y_{Ox,\infty}] + T_s \quad (12.209)$$

$$r_f = a \frac{\ln(1 + B_c)}{\ln[(\nu + Y_{Ox,\infty})/\nu]} \quad (12.210)$$

$$Y_{Fs} = \frac{B_c - Y_{Ox,\infty}/\nu}{1 + B_c} \quad (12.211)$$

$$\dot{m}_F = \frac{4\pi k_g a}{c_{pg}} \ln(1 + B_c) \quad (12.212)$$

where

$$B_c = \frac{Y_{Ox,\infty} \Delta h_c / \nu + c_{pg}(T_\infty - T_s)}{q_{i-1} + h_{fg}} \quad (12.213)$$

with Δh_c denoting the lower heating value. One may rewrite Eq. (12.212) as

$$\dot{m}_F = \frac{2Sh\pi k_g a}{c_{pg}} \ln(1 + B_c) \quad (12.214)$$

using the Sherwood number $Sh = h_m d / \rho D$ with h_m denoting the mass transfer coefficient.

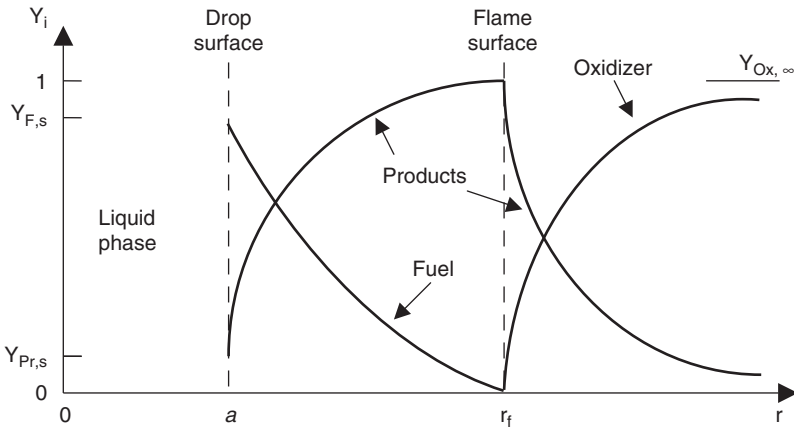


FIGURE 12.66 Species profiles in spherical drop burning without convection effects.

In this form, convective effects can also be included by empirically modifying Sh . For a spherical drop in a quiescent atmosphere, $Sh = 2$ and empirical correlations are found in literature for cases with convective effects. It is also noted that Eq. (12.212) can be expressed in form of the d^2 law in Eq. (12.202) with B_c replacing B_v .

In Eqs. (12.209) and (12.213), q_{i-l} is the rate of heat conducted into the interior of the drop per unit mass flow rate of vapor. The expression for q_{i-l} depends on the model used for drop heatup. If the drop rapidly heats up then one can assume negligible thermal inertia and $q_{i-l} = 0$. The other easily tractable model is the so-called “onion-skin” model for which $q_{i-l} = c_{pl}(T_s - T_0)$, where T_0 is the drop initial temperature.

Equations (12.209)–(12.213) can be evaluated for assumed T_s value. For a saturated drop surface, one may alternately use the Clausius–Clapeyron relation to derive an expression for T_s in terms of the gas pressure P

$$T_s = \frac{-B_c}{\ln \left[\frac{-Y_{F,s} P W_{Pr}}{A(Y_{F,s} W_F - Y_{F,s} W_{Pr} - W_F)} \right]} \quad (12.215)$$

where subscript Pr refers to products. Equation (12.215) can be used in conjunction with an iterative approach to determine T_s along with the other unknowns. The effects of temperature dependency of the properties can be approximated by following the suggestions in Law and Williams (1972):

$$c_{pg} = c_{pF}(\bar{T}), \quad k_g = 0.4k_F(\bar{T}) + 0.6k_{Ox}(\bar{T}), \quad \rho_l = \rho_l(T_s) \quad (12.216)$$

where $\bar{T} = (T_s + T_f)/2$.

The assumption of quasi-steadiness is convenient for arriving at a closed analytical solution. However, this assumption could break down as a consequence of unsteady diffusion, drop heating, fuel vapor accumulation, compositional change of multicomponent drops, natural and forced convection, and finite-rate chemical kinetics (Chiu, 2000). The effect of this assumption was investigated by Law et al. (1980) for both evaporating and burning drops. The quasi-steadiness assumption implies that the total mass of vapor between the flame and the drop surface remains constant. However, when a drop is suddenly placed in an environment for which the vapor mass fraction is less than the saturation vapor mass fraction, the drop starts to evaporate and the mass of the vapor gradually increases. During these initial times, there is not much fuel vapor available for burning. For a lower flow rate of fuel into the flame, a lower supply of O_2 is required, thus the flame stands closer to the drop surface. As more fuel vapor is produced compared to fuel consumption, fuel vapor accumulates, the flame is pushed away from surface,

and the burning rate gradually increases due to larger flame surface area for consumption. At larger times, the drop radius is small, vapor production is low, and hence consumption exceeds supply and as such flame is pushed back toward the surface. This behavior was captured by the analysis in Law et al. (1980) as demonstrated in Figure 12.67, for three different values of $Y_{O_2, \infty}/v$. It is observed that for small $Y_{O_2, \infty}/v$, the flame may not reach a steady location and instead continue to expand outward. The results in Law et al., (1980) also provided the rate of variation of d^2/d_0^2 and indicated that the d^2 law is adequate in predicting the evaporation rate and the instantaneous drop size. This suggests that, despite the variations in flame surface location, the quasi-steady analysis may provide reasonable predictions for the drop burning rate, which is of primary concern in theoretical description of combustion systems.

In the presence of a convective flow, the flame surface could significantly deviate from a spherical shape. Chiu and Huang (1996) formalized the concept of the multistate for a drop, which refers to the existence of more than a single state under a given relative Reynolds number (see below) and ambient temperature. Three distinctive flame shapes were recognized, namely, *envelope* flame, *wake* flame, and *boundary layer* flame. The last flame is stabilized in the boundary layer of the liquid sphere. According to Chiu and Huang, there are five distinct regions of Reynolds number bands in which the following multistates are possible: (1) one-state envelope flame; (2) two-state envelope flame vaporization; (3) three-state envelope flame-wake flame vaporization; (4) two-state wake flame vaporization; and (5) one-state vaporization. This multistate behavior also depends on temperature that affects the transfer number and the Damköhler number Da . The Damköhler number is a measure of the relative importance of the flow time scale and combustion time scale. For an infinitely fast reaction $Da \rightarrow \infty$.

The effects of convection can be considered in the calculations by introducing a Nusselt number, Nu , into Eq. (12.212) as

$$\dot{m}_F = \frac{2\pi k_g a Nu}{c_{pg}} \ln(1 + B_c) \quad (12.217)$$

The following empirical relations have been suggested for Nu as a function of relative Reynolds number, $Re_r = v_r d \rho_g / \mu_g$, where v_r represents the relative velocity between the drop and the surrounding gas:

Ranz and Marshall (1952):

$$Nu = 2 + 0.572 Re_r^{1/2} Pr^{1/3}, \quad 1 < Re_r < 2000 \quad (12.218)$$

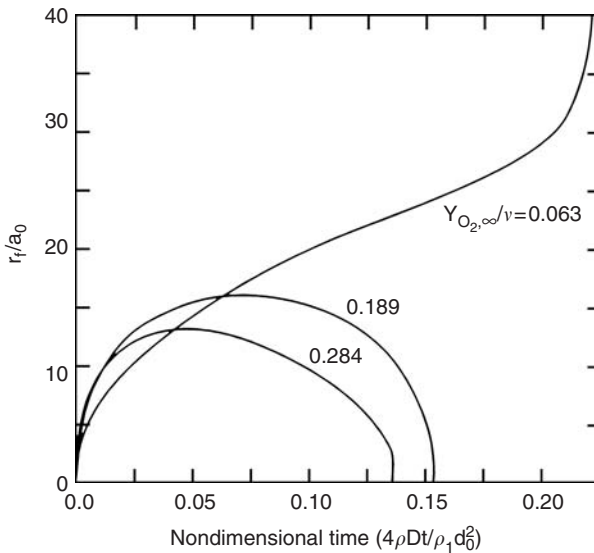


FIGURE 12.67 Temporal variations of the normalized flame radius for a heptane drop burning in the standard atmosphere (Law et al., 1980).

Clift et al. (1978):

$$Nu = \begin{cases} 1 + (1 + Re_r)^{1/3}, & Re_r < 1 \\ 1 + (1 + Re_r)^{1/3} Re_r^{0.077}, & Re_r \geq 1 \end{cases} \quad (12.219)$$

Faeth (1977):

$$Nu = 2 + \frac{0.555 Re_r^{1/2} Pr^{1/3}}{[1 + 1.23/(Re_r Pr^{4/3})]^{1/2}} \quad (12.220)$$

where Pr is the Prandtl number. It is noted that for all these relations $Nu = 2$ in the absence of convection and Eq. (12.217) reduces to Eq. (12.212).

12.7.4 Groups of Drops

The analysis of a single drop is instructive for a basic understanding of evaporation and combustion processes; however, in real applications of liquid fuel sprays, large number of drops are present. In these situations, the interactions between neighboring drops become important for high drop number density (Umemura, 1994). These interactions are discussed in this section.

12.7.4.1 Interactive Evaporation

As the distance between two evaporating drops decreases, the drops compete for heat. Furthermore, the vapor concentration increases, while the temperature decreases. This combination results in a saturation condition in the spacing between the drops. A criterion for interactive evaporation of two drops is given in Annamalai and Ryan (1992) by considering the temperature profiles (Eq. [12.198]) around each drop. Based on this criterion, interaction between two drops becomes significant at a distance where the difference between the drop wet bulb temperature (taken as the drop surface temperature boundary condition) and the local temperature is 90% of the difference between the drop wet bulb temperature and the ambient temperature. This situation occurs at $r = 10a$; therefore, two evaporating drops begin to interact when the interdrop spacing l is such that $l < 20a$.

Theoretical studies often consider a group of drops confined in a spherical region with radius R_c . The analysis is conducted by considering different time scales, including the individual drop heating time and the time for penetration of heat from outside to the core of the group of drops (Annamalai and Ryan, 1992). Another important phenomena is the Stefan flow, which is due to the blowing of vapor from the drops and may drag the drops outwardly in dense sprays (Umemura, 1994). Nevertheless, most studies have neglected the effect of the Stefan flow and, as a result, predict higher evaporation rates. This is also true for an isolated drop, *i.e.*, a higher evaporation rate is predicted for an isolated drop when Stefan effects are neglected. However, the ratio of the evaporation rates, termed as the “correction factor” η remains the same with or without Stefan effects. The correction factor is defined as the ratio of the vapor mass flow rate \dot{m}_s of a single drop in the group to the vapor mass flow rate \dot{m}_{iso} of an isolated drop

$$\eta = \dot{m}_s / \dot{m}_{iso} \quad (12.221)$$

The group evaporation usually results in $\eta < 1$.

In situations like spray combustion, the group of drops is suddenly exposed to a hot ambient gas. In these situations, the drops at the center of the group evaporate rather quickly and create a saturation condition in the spacing between the drops. This case can be analyzed as a confined volume problem with adiabatic condition with respect to the outside gas. A detailed discussion of various studies on group evaporation is presented in Annamalai and Ryan (1992); here we provide a brief summary of the final results from some of these studies.

Zung (1967) presented a 'cellular model' in which the inner drops evaporated in an adiabatic impermeable cell. For the drops in the outer cell, it was assumed that only one half of the drop (shaded area in Figure 12.68) participated in evaporation and the other half did not evaporate. When the outside layer evaporated, the next layer was considered. Zung's analysis did not consider the energy balance equation and predicted that, for a fixed cloud radius, the cloud evaporation time reduces proportional to the drop radius regardless of the heat transfer from the ambient gas. Improved results were later presented by Tishkoff (1979) by considering a 'bubble model' as shown in the inset of Figure 12.68. The spherical shell with radius b , considered around the drop with radius a , was permeable and elastic. Mass, energy, and species conservation equations were solved and unsteady drop heating was allowed with a quasi-steady analysis for the gas phase. Saturation was reached for small b/a , whereas for large b/a the drop fully evaporated. The transition from partial to full evaporation was dependent on temperature and pressure of the gas. The ratio b/a increased with the decrease in the initial gas temperature and pressure. Similar studies were also conducted by Bellan and Cuffel (1983), Bellan and Harstad (1987), and Bellan and Harstad (1988), who also included turbulence effects.

The above studies were conducted by concentrating on the details of flow around individual drops within a cell, bubble, etc. A different class of studies has been reported in the literature that provides solutions for the global behavior of a cloud of drops by considering continuum transport equations for the entire cloud. These macroscopic equations are derived by averaging over a volume containing the drops of interest and are similar to equations for the gas, but with source terms due to drop evaporation (and combustion in case of a reacting system). For example, for quasi-steady evaporation of a cloud of monosized

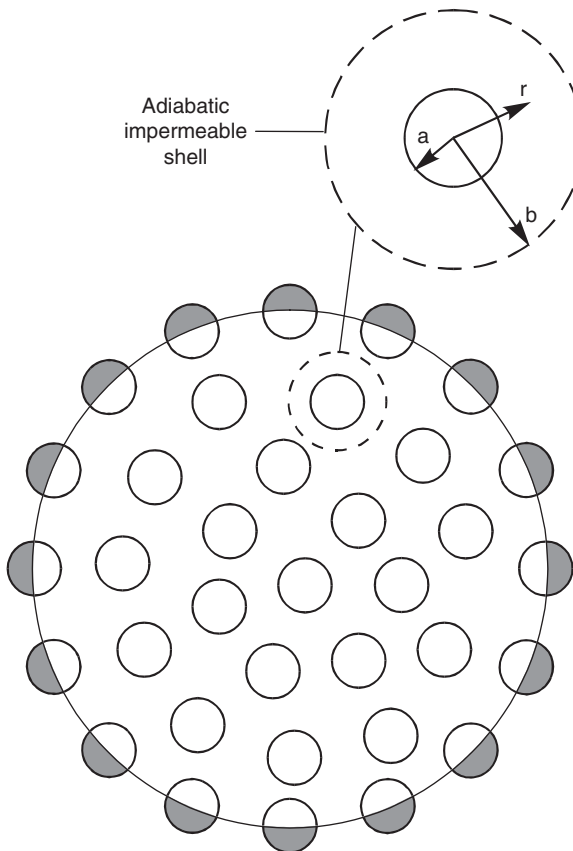


FIGURE 12.68 Illustration of cell model for group combustion (Annamalai and Ryan, 1992).

drops, when the Stefan flow is neglected the continuum equation for the average vapor mass fraction, $Y(r)$, in a spherical coordinate is described as (Annamalai and Ryan, 1992)

$$\frac{1}{r^2} \frac{d}{dr} \left(\rho D r^2 \frac{dY}{dr} \right) = \begin{cases} -\dot{m}''' & \text{for } r < R_c \\ 0 & \text{for } r > R_c \end{cases} \quad (12.222)$$

The volumetric source term \dot{m}''' is due to evaporation of drops and is obtained by averaging over all the drops present in the volume of interest. The appropriate boundary conditions for this problem are

$$Y(r) = Y_\infty, \quad r \rightarrow \infty \quad (12.223)$$

$$dY/dr = 0, \quad r = 0 \quad (12.224)$$

The solution of Eq. (12.222) with boundary conditions Eqs. (12.223) and (12.224) for a monosized and uniform cloud yields the average correction factor as

$$\eta = \frac{3}{G} \left[1 - \frac{\tanh\{G^{(1/2)}\}}{G^{(1/2)}} \right] \quad (12.225)$$

Here G is the group evaporation number:

$$G = 2Sh\pi n a R_c^2 \quad (12.226)$$

where n is the number density of the drops. It should be noted that the definition of G depends on the geometry and spray distribution parameters in the cloud. Various forms used by researchers are summarized in Table 3 of Annamalai and Ryan (1992).

Annamalai (1985) considered Stefan flow in the quasi-steady analysis of a cloud of drops and showed that

$$\dot{m}_c = \dot{m}_{c,SE} \left[1 - \frac{\tanh\{G^{(1/2)}\}}{G^{(1/2)}} \right] \quad (12.227)$$

where \dot{m}_c is the cloud evaporation rate for a monosized and uniform ($n = \text{constant}$) cloud and

$$\dot{m}_{c,SE} = \begin{cases} 4\pi\rho D \ln(1 + B_e)nR_c & \text{(Stefan flow included)} \\ 4\pi\rho D B_e nR_c & \text{(Stefan flow neglected)} \end{cases}$$

The average evaporation rate per drop is

$$\dot{m}_{s,c} = \frac{\dot{m}_c}{\frac{4}{3}\pi R_c^3} \quad (12.228)$$

which yields

$$\eta = \frac{\dot{m}_{s,c}}{\dot{m}_{iso}} = \frac{3}{G} \left[1 - \frac{\tanh\{G^{(1/2)}\}}{G^{(1/2)}} \right] \quad (12.229)$$

for a monosized and uniform cloud. It is interesting to note that Eq. (12.229) with Stefan flow included is the same as Eq. (12.225), which was obtained by neglecting Stefan flow.

The G number can be used as an indicator for the denseness of a spray. Evaluation of Eq. (12.229) shows $\eta \approx 0.9$ and 0.1 for $G = 0.1$ and 100 , respectively. Therefore, for practical purposes, clouds having $G < 0.1$ may be considered dilute enough such that drops can be treated as isolated. Clouds with $G > 100$ should be considered as dense. For very small G values, approaching zero, every drop in the cloud is surrounded

by the gas at T_∞ , whereas for very large values of G , approaching infinity, every drop in the interior of the cloud is at the same temperature. In the latter case, the vapor mass fraction in the spacing between the drops corresponds to the saturated condition and only drops near the outer region of the cloud evaporate. In this case, the cloud is said to evaporate in the “sheath” evaporation mode. It should also be noted that, in a real spray situation, drops move around with the flow and drop-drop collisions are likely for dense clouds. In this situation, the analysis here may not be applicable.

The effects of size distribution was also considered in Annamalai (1985) by assuming a monotonic distribution for the number density n and drop radius a in the form

$$\frac{na}{(na)_{R_c}} = \left[\frac{r}{R_c} \right]^{-q} \quad (12.230)$$

where $(na)_{R_c}$ is the reference quantity at $r = R_c$. For $q = 0$, Eq. (12.230) yields the uniform distribution considered above. The correction factor for this case is given as

$$\eta = \left[1 + \frac{G_1}{3 - q} + \frac{G_1^{(1/2)}}{3 - q} \frac{I_{(5-2q)/(2-q)}[2G_1^{(1/2)/(2-q)}]}{I_{(3-q)/(2-q)}[2G_1^{(1/2)/(2-q)}]} \right]^{-1} \quad (12.231)$$

with G_1 defined as

$$G_1 = (1 - q)^{(1/3)}G \quad (12.232)$$

for fixed size, varying number density, and

$$G_1 = (1 - q/3)G \quad (12.233)$$

for fixed number density, varying size. In Eq. (12.231), $I_{(5-2q)/(2-q)}$ represents the modified Bessel function of the order $(5-2q)/(2-q)$.

12.7.4.2 Interactive Combustion

The analysis in previous sections for an isolated drop assumes that a spherical flame is formed at a radius r_f around the drop. This assumption may be valid as long as there is no other drop in the vicinity of the first drop. When the distance l between two drops is decreased there is an opportunity for two flames to interact. This interaction is intensified by the fact that the two drops must also compete for oxygen in order to continue their combustion. This intuitive conclusion can also be drawn from Eq. (12.210), for the flame radius, in which $Y_{O_x, \infty}$ appears in the denominator. With the decrease in $Y_{O_x, \infty}$, the denominator becomes smaller and the flame radius increases. As the distance between the two drops is further decreased, their flames merge and a common flame is formed around the two drops. According to Williams (1985), a simple criterion for the interaction of two burning drops can be stated as $l < 2r_f$.

Similar interactions occur for a system consisting of a large number of drops, forming a group of drops. In this case, several different “modes” of group combustion can be identified. A large body of literature is devoted to group combustion studies; however, it appears that the studies by Chiu and co-workers (Suzuki and Chiu, 1971; Chiu and Liu, 1977; Chiu et al., 1982) have been more widely recognized. In order to characterize various combustion modes, Suzuki and Chiu (1971) and Chiu et al. (1982) used the group-combustion number:

$$G = 3[1 + 0.276Re_r^{(1/2)}Sc^{(1/3)}]LeN^{(2/3)}(d/l) \quad (12.234)$$

where Sc is the Schmidt number and N the total number of drops in the group. This nondimensional number represents the ratio of the heat transfer in the gas phase and the heat transfer between two phases accounting for the convective effect.

The G number has been used to differentiate between weak and strong drop interactions. According to Chiu et al. (1982), four modes of group combustion are identified as shown in Figure 12.69. For low values

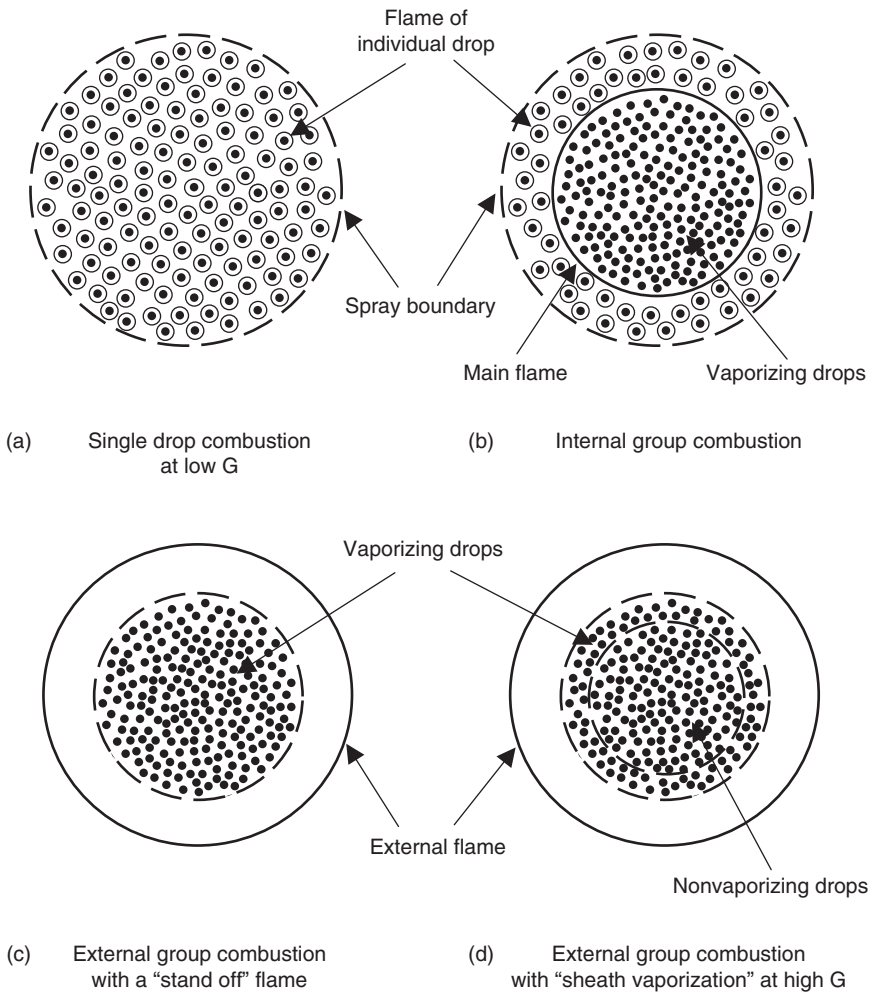


FIGURE 12.69 Four group combustion modes of a drop cloud according to Chiu et al. (1982).

of G , the drops are widely separated and individual drop combustion is dominant (Figure 12.69(a)). As G is increased, the spacing between the drops decreases and the flames from various drops combine. For moderate increases in G , the main flame is located somewhere within the cloud of drops (Figure 12.69(b)). Between this main flame and the external boundary of the cloud, single drop burning is observed. Further increase in G pushes the flame outside the cloud boundary and forms a "stand off" flame (Figure 12.69(c)). In this case, all the drops are vaporizing as combustion takes place at the flame. Finally, for very large values of G , while the standoff flame forms outside the cloud, the drops in the core of the flame are saturated and do not evaporate. In this sheath evaporation case, evaporation occurs only for the drops located near the edge of the cloud (Figure 12.69(d)). As these boundary drops fully evaporate, the evaporation front shrinks toward the center of the cloud and the drops in the core begin to evaporate.

The above group combustion modes can be applied to spray combustion as shown in Figure 12.70 (Chiu and Croke, 1981). Due to cold temperatures and high drop number density in the spray near the nozzle, the ignition of the spray takes place at a distance from the nozzle exit. Once the spray is ignited, an external flame forms, while the core of the spray consists of evaporating drops. Further downstream, the spacing between the drops increases and the flame penetrates into the spray, thus forming multiple group combustion. At the end, combustion continues by consuming the unburnt gaseous fuel.

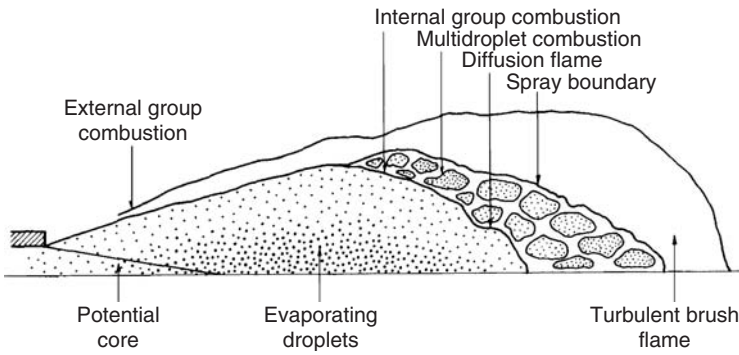


FIGURE 12.70 Schematic of liquid-fuel spray group combustion (Chiu and Croke, 1981).

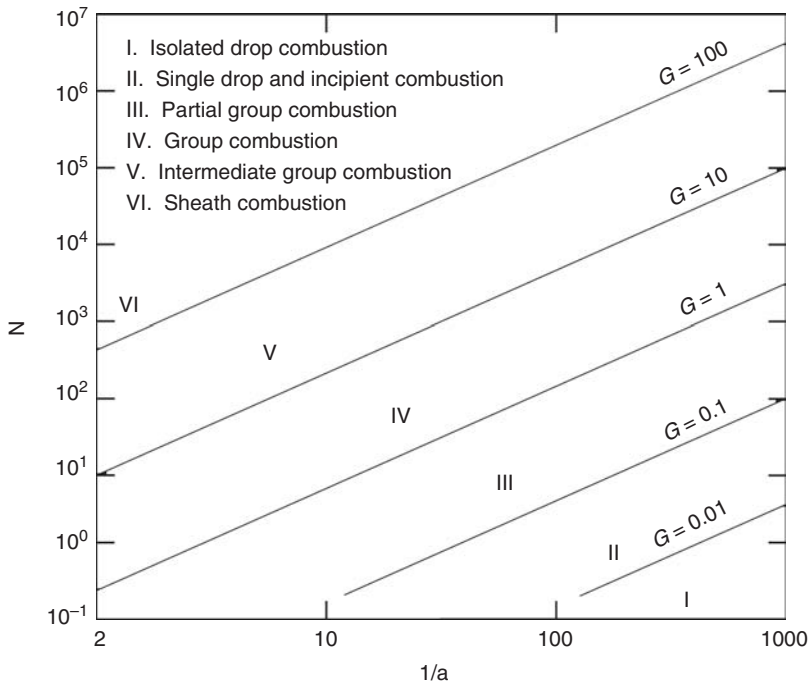


FIGURE 12.71 Group combustion number as a function of nondimensional spacing l/a and the total number of drops (Annamalai and Ryan, 1992).

Annamalai and Ryan (1992) presented a modified form of the spray classification of Chiu and co-workers by considering six modes of combustion as seen in Figure 12.71. This figure maps these various modes on a plot of the total number of drops in the cloud vs. the ratio of the drop spacing to drop diameter l/a for various values of G in Eq. (12.226). Region (I) corresponds to isolated drop combustion for $G < 0.01$, whereas region (II) involves isolated to incipient group combustion for $0.01 < G < 0.1$. The incipient combustion is when the flame radii of the center drops in the cloud just touch each other. Regions (III), (IV), and (V) for $0.1 < G < 1$, $1 < G < 10$, and $10 < G < 100$ are termed as partial group combustion, group combustion, and intermediate group combustion, respectively. In partial group combustion, while there is a group flame for the inner drops, the outer drops burn with individual flames, but still allow O_2 to penetrate into the flame located within the cloud. Finally, for $G > 100$, combustion is in

the sheath mode, where the temperature at the cloud surface is at the wet bulb temperature of the drops and the cloud behaves as an equivalent single drop of radius R_c . Any convective effects will move the lines in Figure 12.71 downward, and this movement will be greater at smaller interdrop spacing.

The model of Chiu and co-workers and their G parameter have been extensively assessed by experimentalists in spray combustion (Chen and Gomez, 1997; Wark et al., 2000). Wark et al. (2000) examined the variation of G in their experiment of an acoustically forced jet. The forcing resulted in the formation of organized structures consisting of core and wings as seen in Figure 12.72. A phase Doppler interferometry was used to obtain drop statistics for calculation of the group-combustion number. It was not possible to generate experimentally the exact conditions to evaluate G using Eq. (12.234). Therefore, several assumptions were made, including the neglect of the convective effects and unity Lewis number. The expression of G used by Wark et al. (2000), after applying the simplified assumptions, was

$$G = 2\pi n d (R_c)^2 \tag{12.235}$$

which is the same as Eq. (12.226) when $Sh = 2$ is used in the absence of convective effects. The drop number density n was obtained directly from the measurements. The mean drop diameter from the measurements was used as a representative diameter for use in Eq. (12.235), although the drop size distribution was not uniform. The assessment of G was very sensitive to the choice of R_c as witnessed from Eq. (12.235). An appropriate value was chosen for R_c , depending on whether the core or the wing region was considered. In the core region, the radius of the drop-laden portion of the jet was considered as a reasonable choice.

Wark et al. (2000) calculated the axial variation of G as shown in Figure 12.73. The results suggested that close to the nozzle, the jet was burning in external sheath mode and then changed to internal group burning after $z/D \approx 2$, where D and z represent the jet diameter and the axial distance, respectively. After the third structure, the value of G dropped significantly, corresponding to individual drop burning. From the comparison of Figure 12.72 and Figure 12.73, it was not unreasonable to expect external sheath burning

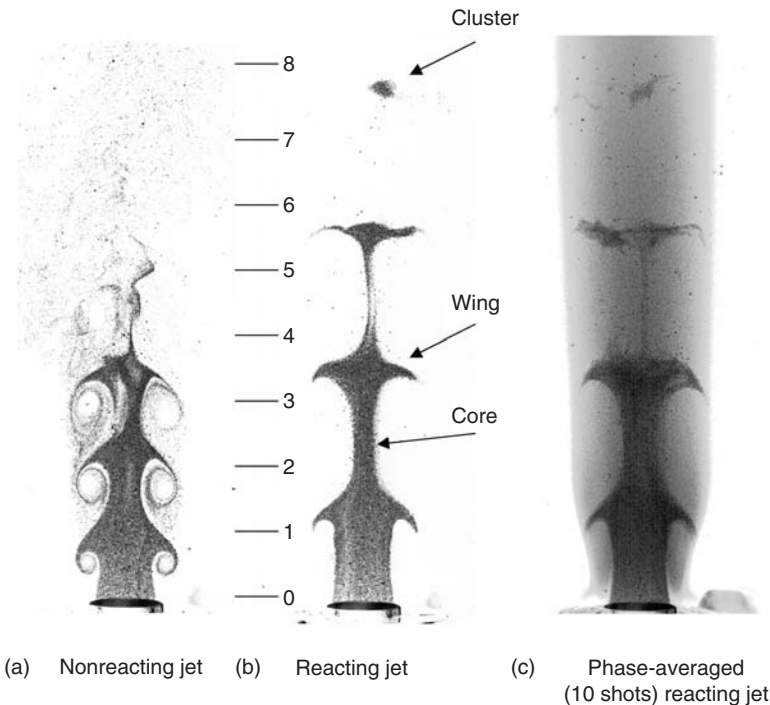


FIGURE 12.72 Phase-locked images of the drop-laden jet considered in the study of Wark et al. (2000).

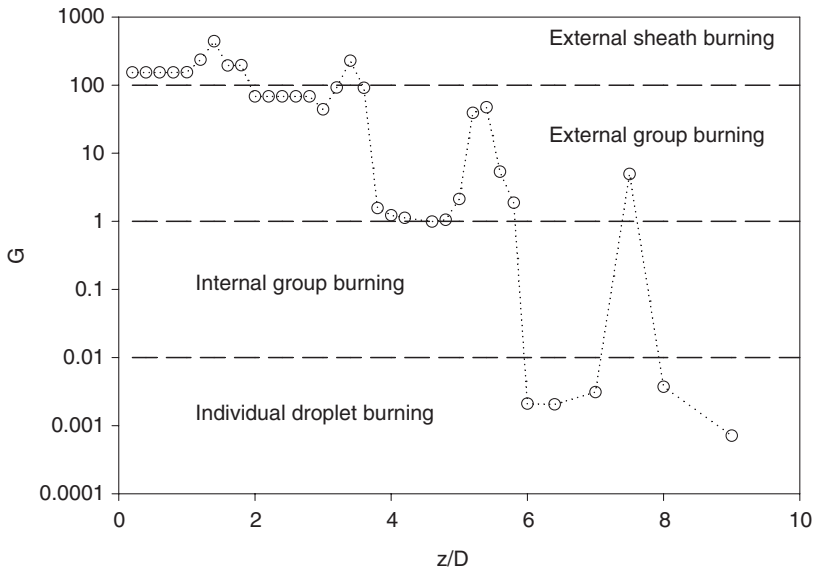


FIGURE 12.73 Phase-locked (0°) axial development of the group combustion behaviour of drops (Wark et al., 2000).

early in the flame. However, Wark et al. (2000) questioned whether individual drop burning occurred between the third and fourth structures, as predicted by the calculation of G . This was in agreement with previous experiments (e.g., McCreath and Chigier, 1973), which did not show any signs of single drop burning in the spray.

Annamalai (1985) provided similar relations to those in Eqs. (12.227), (12.229), and (12.231) for quasi-steady combustion of a cloud of drops. These relations were provided for both monosized uniform cloud and a cloud with the product of size and number density of the drops given as Eq. (12.230). These results gave correction factors, which can be used for the calculation of the cloud burning rate in terms of the burning rate of an isolated drop.

12.7.5 Spray Modeling

The theoretical approaches discussed in previous sections are very useful for developing a fundamental understanding of the physical processes involved in two-phase combustion. However, as emphasized in the introduction, the practical situations encountered in spray combustion often involve turbulence whose effect cannot be fully described by these theories. See Li (1997) for a review of spray combustion in laminar stagnation flows. A thorough description of spray combustion requires modeling of turbulence interactions with drops and its effect on chemical reaction. More specifically, modeling is required for three interactive processes, namely, turbulence, combustion, and drop dispersion.

The modeling of turbulence effects on drop dispersion is extensively discussed in various chapters of this handbook. The different modeling approaches for particle/drop-laden turbulent flows were recently reviewed by Mashayek and Pandya (2003) and were categorized into two main groups as Eulerian–Lagrangian and Eulerian–Eulerian. In both approaches, the carrier gas is considered as a continuum phase and is solved in the Eulerian frame. In the first approach, the drops are treated in the Lagrangian frame, which is more natural. In the second approach, Eulerian (macroscopic) equations are derived for drops using a variety of methods. (Drew, 1983; Jackson, 1997; Zhang and Prosperetti, 1994; Pandya and Mashayek, 2003). This Eulerian–Eulerian approach has received some success, particularly as a theoretical basis for revealing different physical phenomena (Elperin et al., 1996; Pandya and Mashayek, 2002). Nevertheless, it appears that most of the practical treatments of sprays have been

based on the Eulerian–Lagrangian approach. Therefore, in this section, we focus our attention exclusively on the Lagrangian approach.

The level of modeling for turbulence varies depending on the nature of the problem and the computational resources available. To this end, the most common Lagrangian approaches may be divided into three groups: direct numerical simulation (DNS), large-eddy simulation (LES), and stochastic simulation. In all these methods, the flow is seeded or injected by a large number of drops, which are followed individually in the Lagrangian frame using the equations described in Section 1.4 of this handbook. In DNS, no modeling is performed for turbulence and all the various time and length scales are resolved exactly by considering small time step and grid sizes. However, for situations involving a large number of drops, it is not possible to resolve the details of the flow in and around each drop. Therefore, physical models are introduced for describing heat, mass, and momentum transfer between the two phases, as elaborated in this section and also reviewed in Section 1.4 of this handbook. DNS requires significant computational resources and its application has been limited to simple geometries and low Reynolds numbers. (Mashayek, 2000; Reveillon and Vervisch, 2000). A remedy to the limitations of DNS would be via LES, where the small scales of the flow are filtered and simulations are conducted for the large scales only. This, however, requires modeling at the so-called subgrid level and has produced some challenges in the past (Lesieur and Métais, 1996; Meneveau and Katz, 2000). The trade-off is a relaxation in the required computational time as compared to DNS. The application of LES to particle-laden flows is still at its early stages and there are several remaining issues that need to be addressed. These include the effect of the (filtered) subgrid-scale fluctuations on the particles and vice versa (Sankaran and Menon, 2002).

The most practical method of choice for simulation of spray combustion has been via stochastic modeling. These models are derived by using various methods, including those based on time-series analysis (Box and Jenkins, 1976; Gao and Mashayek 2004) and the Langevin equation (Pozorski and Minier, 1998). In stochastic simulation, the carrier gas is simulated using various single-point turbulence models, primarily based on Reynolds average Navier–Stokes (RANS) modeling approach. The RANS models provide mean values along with second-order moment statistics of the carrier gas properties such as velocity, temperature, and species concentration. The role of the stochastic model is to provide fluctuating values for carrier-gas properties for each drop in the system. These fluctuating quantities are required in order to capture the effects of turbulence on the drops. Stochastic models can be derived systematically to include important turbulence properties such as spatial and temporal correlations either implicitly or explicitly. From the implementation point of view, the eddy interaction (EI) models offer many simplifications and have been extensively used for modeling of spray combustion (Gosman and Ioannides, 1981). In EI models, a drop is allowed to interact with the same eddy until it crosses the eddy or for the lifetime of the eddy, whichever is shorter. The turbulence intensity of the eddy is sampled randomly based on the second-order moments calculated by RANS.

The other important aspect in theoretical description of spray combustion is the interaction between turbulence and chemical reaction. Turbulence significantly affects chemical reaction by a substantial increase in the rate of mixing of various species, while chemical reaction and its heat release tend to generate high-gradient regions of temperature and density, thus enhancing the flow instability and turbulence. Turbulence modeling for combustion has been the subject of an overwhelming number of studies within the past four decades and is not reviewed in this section in detail. A number of different methods have emerged from these studies with varying levels of success (Peter, 2000; Pope, 1985; Givi, 1989). Nevertheless, the issue of turbulence modeling for combustion still appears far from being fully resolved and is even more complicated by the fact that chemistry mechanisms are not yet well understood. These mechanisms could involve hundreds of steps and are not tractable in the presence of turbulence with the existing computational resources. Many efforts are being devoted to reduce the number of steps, which can be simulated for turbulent flows. Turbulence modeling for combustion has been recently reviewed by Peters (2000). Among the more popular models are the laminar flamelet models, (Williams, 1975; Bray and Peters, 1994), the probability density function (pdf)-based models (Pope, 1985; Givi, 2003), the eddy-breakup models (Spalding; 1971), and the eddy dissipation models (Magnussen and Hjertager, 1977), which provide different levels of accuracy and complexity. The pdf models are based either on an

assumed pdf shape or a modeled transport equation for the pdf of velocity, temperature, and species concentration in time and space. The solution of the full pdf transport equation is computationally intensive and is mostly done via Monte Carlo methods.

The mass loading of the dispersed phase in a spray is usually high, such that the presence of the drops can significantly affect the properties of the carrier gas via exchange of mass, momentum, and energy. This phenomena, referred to as “two-way coupling,” must be considered in describing various transport equations for the carrier phase. Since the drops are followed in a Lagrangian frame, and the carrier gas is simulated in the Eulerian frame, a numerical model is devised to express Eulerian source-sink terms in the carrier-phase equations in terms of the individual drop effects. In most of the practical applications, the drops are treated as point sources within a given computational cell. The effects of each drop are distributed over the nodes of the cell, with some weights inversely proportional to the distance of the drop from various nodes. This approach is known as particle-source in cell (PSI-Cell) method (Crowe et al., 1977). The approximations involved in this approach, has prompted some researchers to seek more accurate methods (see e.g. Maxey et al., 1997); however, due to its simplicity of implementation, PSI-cell has remained as a method of choice for simulation of turbulent sprays. If the number of drops within a cell is large, interaction among the drops must also be considered.

The task of combining various combustion models with two-phase models and turbulence models is understandably much more challenging and many different combinations can be offered. A reasonably accurate and yet computationally feasible combination would be via stochastic modeling for the dispersed phase along with the flamelet approach for combustion. The simulation of turbulence, once dominated by RANS models, is now also being conducted via LES models. By offering advantages in highly transient flows, LES is growing as a viable replacement for RANS in the future. Nevertheless, with the current computational resources, RANS still remains as the primary method of choice for large-scale, high-velocity combustors and boilers.

Nomenclature

Latin

a	Radius
A	Hamaker constant
B	Impact factor
B_e	Transfer number
c_1	Speed of sound in liquid
c_p	Specific heat at constant pressure
Ca	Capillary number
C_D	Drag coefficient
C_L	Lift coefficient
D	Diffusion coefficient
D_j	Jet diameter
e	Specific energy, coefficient of restitution
E	Young's modulus, activation energy
\dot{E}	Erosion rate
E_M	Mechanical potential energy
f_p	Pulsation frequency
Fr	Froude number
F	Force vector
g	Acceleration due to gravity
G	Relative velocity vector
h	Enthalpy

h_{fg}	Latent heat of evaporation
H	Total head, hardness
H_{sv}	Net positive suction head
I	Moment of inertia
j_i	Diffusive flux
J	Impulsive force
k	Ratio of specific heats, Boltzmann's constant, spring constant, turbulence energy
k_g	Conductive heat transfer coefficient
K_G	Gas constant
L	Latent heat
m	Molecular unit mass, mass
m_G	Gas mass
M	Mass of abrasive particles
\dot{M}_v	Mass flux due to phase change
n	Number density
\mathbf{n}	Normal unit vector
N_s	Specific speed
Nu	Nusselt number
Oh	Ohnesorge number
p	Pressure, erosion surface flow stress
q	Charge
q_R	Radiation heat transfer
Q	Volumetric flow rate
r	Radius
\Re	Gas constant
R_b	Rayleigh-Plesset bubble radius
R_c	Bubble cloud initial radius
Re	Reynolds number
St	Strouhal number
t	Time
t_c	Collapse time
T	Temperature
u	Impact speed
\mathbf{u}, \mathbf{v}	Velocity vector
v_s	Solids velocity
W	Volume of target material
W_i	Molecular weight of species "i"
We	Weber number
Y_i	Mass fraction of species "i"

Greek Symbols

α	Accommodation coefficient, angle of impingement
β	Bubble number density
Γ	Circulation
δ_n	Overlap distance
ε	Volume fraction, dissipation rate
ε_o	Dielectric constant
λ	Viscosity ratio
μ	Viscosity
ρ	Density

σ	Surface tension, cavitation number, Poisson ratio, charge density
σ_b	Flexural strength
σ_y	Plastic load limit
σ_T	Thoma number
τ	Individual bubble volume
ω_i	Chemical source term for species "i"
ω_n	Natural frequency
Ω	Rotational speed
$\mathbf{\Omega}$	Rotational velocity vector

Subscripts

b	Bubble
cr	Critical
g	Gas
e	Equilibrium state
i	Species "i"
iso	Isolated
l	liquid
m	maximum, mixture
n	noncondensable gas
r	Reduced
s	Solids
w	Wall
∞	Ambient conditions

References

- Acrivos, A. and Lo, T.S., Deformation and breakup of a single slender drop in an extensional flow, *J. Fluid Mech.*, 86, 641, 1978.
- Annamalai, K. and Ryan, W., Interactive processes in gasification and combustion. Part I: Liquid drop arrays and clouds, *Prog. Energy Combust. Sci.*, 18, 221–295, 1992.
- Annamalai, K. and Ryan, W., Interactive processes in gasification and combustion Part II: Isolated carbon, coal and porous char particles, *Prog. Energy Combust. Sci.*, 19, 383–446, 1993.
- Annamalai, K., *Evaporation and Combustion of a Cloud of Drops*, ASME, HTD Vol. 45, 1985, pp. 27–35.
- Annamalai, K., Ryan, W., and Dhanapalan, S., Interactive processes in gasification and combustion. Part III: Coal/char particle arrays, streams and clouds, *Prog. Energy Combust. Sci.*, 20, 487–618, 1994.
- Arakeri, V.H. and Acosta, A.J., Viscous effects in the inception of cavitation on axisymmetric bodies, *ASME J. Fluids Eng.*, 95, 519, 1973.
- Armenio, V., Piomelli, U., and Fiorotto, V., Effect of the subgrid scales on particle motion, *Phys. Fluids*, 11, 3030–3042, 1999.
- Arndt, R.E.A. and Keller, A.P., Water quality effects on cavitation inception in a trailing vortex, *ASME J. Fluids Eng.*, 114, 430, 1992.
- Arndt, R.E.A., Cavitation in vortical flows, *Annu. Rev. Fluid Mech.*, 34, 143, 2002.
- Ashgriz, N. and Poo, J.Y., Coalescence and separation in binary collision of liquid drops, *J. Fluid Mech.*, 221, 183, 1990.
- Bachalo, W.D. and Houser, M.J., Phase Doppler Spray Analyzer for Simultaneous Measurements of Drop Size and Velocity Distributions, *Optical Eng.*, 23, 583–590, 1984.
- Badock, C., Wirth, R., Fath, A., and Leipertz, A., Investigation of cavitation in real size diesel injection nozzles, *Int. J. Heat Fluid Flow*, 20(5), 538, 1999.

- Bagchi, P. and Balachandar, S., Effect of turbulence on the drag and lift of a particle, *Phys. Fluids*, 15, 3496–3513, 2003.
- Bagchi, P. and Balachandar, S., Shear vs. vortex-induced lift on a rigid sphere at moderate Re ., *J. Fluid Mech.*, 473, 379–388, 2002.
- Bailey, M.R., Khokhlova, V.A., Sapozhnikov, O.A., Kargl, S.G., and Crum, L.A., Physical mechanisms of the therapeutic effects of ultrasound (Review), *Acoust. Phys.*, 49, 369, 2003.
- Barthes-Biesel, D. and Acrivos, A., Deformation and burst of a liquid drop freely suspended in a shear field, *J. Fluid Mech.*, 61, 1, 1973.
- Barthlot, W. and Neinhuis, C., Purity of the sacred lotus, or escape from contamination in biological surfaces, *Planta*, 202, 1, 1997.
- Batchelor, G.K., *An Introduction to Fluid Dynamics*, Cambridge University Press, Cambridge, 1967, pp. 250–253.
- Beckett, M.A. and Hua, I., Impact of ultrasonic frequency on aqueous sonoluminescence and sonochemistry, *J. Phys. Chem. A*, 105, 3796, 2001.
- Bellan, J. and Cuffel, R., A theory of non-dilute spray evaporation based upon multiple drop interactions, *Combust. Flame*, 51, 55–67, 1983.
- Bellan, J. and Harstad, K., Analysis of the convective evaporation of nonlinear cluster of drops, *Int. J. Heat Mass Transfer*, 30, 125–136, 1987.
- Bellan, J. and Harstad, K., Turbulence effects during evaporation of drops in clusters, *Int. J. Heat Mass Transfer*, 31, 1655–1668, 1988.
- Bellan, J., Supercritical (and subcritical) fluid behavior and modelling: Drops, streams, shear and mixing layers, jets and sprays, *Prog. Energy Combust. Sci.*, 26, 329–366, 2000.
- Bently, B.J. and Leal, L.G., An experimental investigation of drop deformation and breakup in steady, two-dimensional linear flows, *J. Fluid Mech.*, 167, 241, 1986.
- Berlemont, A., Desjonqueres, P., and Gousebet, G., Particle Lagrangian simulation in turbulent flows, *Int. J. Multiphase Flow*, 16, 19–34, 1990.
- Bico, J., Marzolin, C., and Quéré, D., Pearl drops, *Europhys. Lett.*, 47, 220, 1999.
- Biesheuvel, A. and van Wijngaarden, L., Two phase flow equations for a dilute dispersion of gas bubbles in liquid, *J. Fluid Mech.*, 148, 301–318, 1984.
- Bird, R.B., Stewart, W.E., and Lightfoot, E.N., *Transport Phenomena*, 3rd ed., Wiley, New York, 1960.
- Birkhoff, G., Note on Taylor instability, *Q. Appl. Math.*, 12, 306–309, 1954.
- Bitter, J.G.A., A study of erosion phenomena, Part I, *Wear*, 6, 5, 1963.
- Bitter, J.G.A., A study of erosion phenomena, Part II, *Wear*, 8, 161, 1963a.
- Blake, F.G., The Onset of Cavitation in Liquids, Tech. Memo, No. 12, Acoustics Res. Lab., Harvard Univ., 1949.
- Blake, J.R. and Gibson, D.C., Cavitation bubbles near boundaries, *Annu. Rev. Fluid Mech.*, 19, 99, 1987.
- Blake, T.D. and Haynes, J.M., Kinetics of liquid-liquid displacement, *J. Coll. Interface Sci.*, 30, 421, 1969.
- Blake, T.D., Bracke, M., and Shikhmurzaev, Y.D., Experimental evidence of nonlocal hydrodynamic influence on the dynamic contact angle, *Phys. Fluids*, 11, 1995, 1999.
- Blake, T.D., Dynamic contact angles and wetting kinetics, in *Wettability*, Berg, J.C., Ed. Surfactant Science Series, Marcel Dekker, New York, 1993.
- Blake, T.D., The contact angle and two-phase flow, Ph.D. thesis, University of Bristol, U.K., 1968.
- Boivin, M., Simonin, O., and Squires, K.D., Direct numerical simulation of turbulence modulation by particles in isotropic turbulence, *J. Fluid Mech.*, 375, 235–263, 1998.
- Borotnikova, M.I. and Soloukin, R.I., A calculation of the pulsations of gas bubbles in an incompressible liquid subject to a periodically varying pressure, *Sov. Phys. Acoust.*, 10, 28–32, 1964.
- Bouillard, J.X., and Lyczkowski, R.W., On the Erosion of Heat Exchanger Tube Banks in Fluidized Beds, *Powder Technol.*, 68, 37, 1991.
- Bouillard, J.X., Lyczkowski, R.W., Folga, S., Gidaspow, D., and Berry, G.F., Hydrodynamics of Erosion of Heat Exchanger Tubes in Fluidized-Bed Combustors, *Canadian J. Chem. Eng.*, 67, 218, April 1989.

- Box, G.E.P. and Jenkins, G.M., *Time Series Analysis*, Holden-Day, Oakland, CA, 1976.
- Bray, K.N.C. and Peters, N., Laminar flamelets in turbulent flames, in *Turbulent Reacting Flows*, Libby, P.A. and Williams, F.A., Eds., Academic Press, London, 1994, pp. 63–113.
- Brazier-Smith, P.R., Jennings, S.G., and Latham, J., The interaction of falling water drops: coalescence, *Proc. Roy. Soc. Lond. A*, 326, 393, 1972.
- Brenn, G., Valkovska, D., and Danov, K.D., The formation of satellite droplets by unstable binary drop collisions, *Phys. Fluids*, 13, 2463, 2001.
- Brennen, C.E., Fission of collapsing cavitation bubbles, *J. Fluid Mech.*, 472, 153–166, 2002.
- Brennen, C.E., *Cavitation and Bubble Dynamics*, Oxford University Press, Oxford, 1995.
- Brennen, C.E., Cavitation in biological and engineering contexts, *Proceedings of the 5th International Symposium on Cavitation*, Osaka, Japan, 2003.
- Brooke, J.W., Kontomaris, K., Hanratty, T.J., and McLaughlin, J.B., Turbulent deposition and trapping of aerosols at a wall, *Phys. Fluids A*, 4, 825–834, 1992.
- Brujan, E.A., Keen, G.S., Vogel, A., and Blake, J.R., The final stage of the collapse of a cavitation bubble close to a rigid boundary, *Phys. Fluids*, 14, 85, 2002.
- Burcat, A., Thermophysical data for combustion calculations, in Gardiner, W.C., Ed., *Combustion Chemistry*, Springer-Verlag, New York, NY, 1994, pp. 455–504.
- Burton, T.M. and Eaton, J.K., Fully Resolved Simulations of Particle-Turbulence Interaction, Report TSD-151, Department of Mechanical Engineering, Stanford University, 2003.
- Burton, T.M. and Eaton, J.K., Analysis of a fractional-step method on overset grids, *J. Computat. Phys.*, 177, 336–364, 2002.
- Carey, V.P., *Liquid-Vapor Phase-Change Phenomena: An Introduction to the Thermophysics of Vaporization and Condensation Processes in Heat Transfer Equipment*, Hemisphere, Washington, DC, 1992.
- Carlson, B., Avoiding cavitation in control valves, *ASHRAE J.*, 43, 58, 2001.
- Ceccio, S.L. and Brennen, C.E., Observations of the dynamics and acoustics of travelling bubble cavitation, *J. Fluid Mech.*, 233, 633, 1991.
- Ceccio, S.L., Gowing, S., and Gindroz, B., Comparison of CSM bubble detection methods, *ASME Fluids Eng. Div. FED-226*, 43, 1991.
- Chahine, G.L. and Duraiswami, R., Dynamical interactions in a multi-bubble cloud, *ASME J. Fluids Eng.*, 114, 680–686, 1992.
- Chahine, G.L. and Kalumuck, K.M., Development of a near real-time instrument for nuclei measurement: the ABS Acoustic Bubble Spectrometer®, *Proceedings of the 4th ASME-JSME Joint Fluids Engineering Conference*, Honolulu, Hawaii, 2003.
- Chandra, S. and Avedisian, C.T., On the collision of a droplet with a solid surface, *Proc. R. Soc. London A*, 432, 13, 1991.
- Chapman, R.B. and Plesset, M.S., Thermal effects in the free oscillation of gas bubbles, *ASME J. Basic Eng.*, 93, 373–376, 1971.
- Chen, C.P. and Wood, P.E., A turbulence closure model for dilute gas-particle flows, *Canadian J. Chem. Eng.*, 63, 349–360, 1985.
- Chen, G. and Gomez, A., Dilute laminar spray diffusion flames near the transition from group combustion to individual droplet burning, *Combust. and Flame*, 110, 392–404, 1997.
- Chen, J.-H. and Faeth, G.M., Continuous-phase properties of homogeneous particle-laden turbulent flows, *AIAA J.*, 39, 180–183, 2001.
- Chesters, A.K., The modeling of coalescence processes in fluid liquid dispersions – A review of current understanding, *Trans. Inst. Chem. Eng.*, 69, 259, 1991.
- Chiu, H.H. and Croke, E.J., Group Combustion of Liquid Fuel Sprays, Technical Report 81–2, University of Illinois at Chicago, Energy Technology Lab, 1981.
- Chiu, H.H. and Huang, J.S., Multiple-state phenomena and hysteresis of a combusting isolated droplet, *Atomiz. Sprays*, 6, 1–26, 1996.
- Chiu, H.H., Advances and challenges in droplet and spray combustion. I. toward a unified theory of droplet aerothermochemistry, *Prog. Energy Combust. Sci.*, 26, 381–416, 2000.

- Chiu, H.H. and Liu, T.M., Group combustion of liquid droplets, *Combust. Sci. and Tech.*, 17, 127–142, 1977.
- Chiu, H.H., Kim, H.Y., and Croke, E.J., Internal group combustion of liquid droplets, in *Proceedings of 19th Symposium (International) on Combustion*, The Combustion Institute, Pittsburgh, PA, 1982, pp. 971–980.
- Clift, R., Grace, J.R., and Weber, M.E., *Bubbles, Drops, and Particles*, Academic Press, New York, NY, 1978.
- Cody, G. D., Goldfarb, D.J., Storch, G.V., Jr., and Norris, A.N., Particle Granular Temperature in Gas Fluidized Beds, *Powder Technol.*, 87, 211, 1996.
- Coleman, A.J., Kodama, T., Choi, M.J., Adams, T., and Saunders, J.E., Cavitation threshold of human tissue exposed to 0.2-MHz pulsed ultrasound: preliminary measurements based on a study of clinical lithotripsy, *Ultrasound Med. Biol.*, 21, 405, 1995.
- Collings, E.W., Markworth, J.K., McCoy, J.K., and Saunders, J.H., Splat-quench solidification of freely falling liquid-metal drops by impact on a planar substrate, *J. Mater. Sci.*, 25, 3677, 1990.
- Cossali, G.E., Coghe, A., and Marengo, M., The impact of a single drop on a wetted surface, *Exp. Fluids*, 22, 463, 1997.
- Cossali, G.E., Marengo, M., Coghe, A., and Zhdanov, S., The role of time in single splash on thin film, *Exp. Fluids*, 36, 888, 2004.
- Cox, R.G., The dynamics of the spreading of liquids on a solid surface. Part 1. Viscous flow, *J. Fluid Mech.*, 168, 169, 1986.
- Crowe, C.T., On models for turbulence modulation in fluid-particle flows, *Int. J. Multiphase Flow*, 26, 719–727, 2000.
- Crowe, C.T., Carrier phase turbulence in dispersed phase flows, Key note Address *International Conference on Multiphase Flows*, New Orleans, 2001.
- Crowe, C.T. and Gillandt, I., Turbulence modulation of fluid-particle flows, A basic approach, *3rd International Conference on Multiphase Flows*, Lyon France, June 8–12, 1998.
- Crowe, C.T., Chung, J.N., and Troutt, T.R., Particle dispersion by organized turbulent structures, *Particulate Two-Phase Flow*, Roco, M.C., Ed., Chap. 18, 1993, pp. 626–669.
- Crowe, C.T., Sharma, M.P., and Stock, D.E., The particle-source-in cell (PSI-cell) model for gas-droplet flows, *J. Fluids Eng.*, 99, 325–332, 1977.
- Crowe, C.T., On models for turbulence modulation in fluid-particle flows, *Int. J. Multiphase Flow*, 20S, 169–209, 2000.
- Crowe, C.T., Sharma, M.P., and Stock, D.E., The Particle-Source in cell (PSI-Cell) model for Gas-Droplet flows, *J. Fluids Eng.*, 6, 325–332, 1977.
- Crowe, C.T., Summerfeld, M., and Tsuji, Y., *Multiphase Flows with Droplets and Particles*, CRC Press, Boca Raton, FL, 1998, pp. 12–22.
- Crowe, C.T., Troutt, T.R., and Chung, J.N., Numerical models for two-phase turbulent flows, *Ann. Rev. Fluid Mech.*, 28, 11–43, 1996.
- Crowe, C.T., Troutt, T.R., and Chung, J.N., Particle Interactions with Vortices, Green, S.I., Ed., Chap. XIX, 1995, pp. 829–858.
- Cui, M.M. and Adrian, R.J., Refractive index matching and marking methods for highly concentrated solid-liquid flows, *Exp. Fluids*, 22, 261–264, 1997.
- Cundall, P. A. and Strack, O.D., A discrete numerical model for granular assemblies, *Geotechnique*, 29, 47, 1979.
- d’Agostino, L. and Brennen, C., Linearized dynamics of spherical bubble clouds, *J. Fluid Mech.*, 199, 155–176, 1989.
- d’Agostino, L. and Acosta, A.J., Cavitation susceptibility meter with optical cavitation monitoring. Part Two. Experimental apparatus and results, *ASME J. Fluids Eng.*, 113, 270, 1991.
- Dai, Z. and Faeth, G.M., Temporal properties of secondary drop breakup in the multimode breakup regime, *Int. J. Multiphase Flow*, 27, 217, 2001.
- Davidson, J.F., Symposium on fluidization – discussion, *Trans. Inst. Chem. Engineers*, 39, 230, 1961.
- de Bruijn, R.A., Tip streaming of drops in simple shear flows., *Chem. Eng. Sci.*, 48, 277, 1993.

- Delplanque, J.-P. and Siringano, W.A., Boundary layer stripping effects on droplet transcritical convecting vaporization, *Atomization Sprays*, 4, 325, 1994.
- Deutsch, E. and Simonin, O., Large eddy simulation applied to the modeling of particulate transport in turbulent two-phase flows, 8th *Symposium on Turbulence Shear Flows*, Technical University Munich, 1991, pp.10.1.1–10.1.6.
- Ding, J. and D. Gidaspow, A Bubbling Model Using Kinetic Theory of Granular Flow, *AICHE J.*, 36 (4), 523, 1990.
- Ding, J. and R.W. Lyczkowski, Three-Dimensional Kinetic Theory Modeling of Hydrodynamics and Erosion in Fluidized Beds, *Powder Technology*, 73, 127, 1992.
- Drew, D.A., Mathematical modeling of two-phase flow, *Annu. Rev. Fluid Mech.*, 15, 261–291, 1983.
- Druzhinin, O.A. and Elghobashi, S., On the decay rate of isotropic turbulence laden with microparticles, *Phys. Fluids* 11, 602–610, 1999.
- Druzhinin, O.A., The influence of particle inertia on the two-way coupling and modification of isotropic turbulence by microparticles, *Phys. Fluids*, 13, 3738–3755, 2001.
- Dussan, E.B.V. and Chow, R.T., On the ability of drops or bubbles to stick to nonhorizontal surfaces or solids, *J. Fluid Mech.*, 137, 1, 1983.
- Eaton, J.K. and Fessler J.R., Preferential concentration of particles by turbulence, *Int. J. Multiphase Flow*, 26, 719–727, 1994.
- Eaton, J.K. and Fessler, J.R., Preferential concentration of particles by turbulence, *Int. J. Multiphase Flow*, 20, 169–209, 1994.
- Eggers, J., Nonlinear dynamics and breakup of free-surface flows, *Rev. Mod. Phys.*, 69, 865, 1997.
- Eggers, J., Universal pinching of three dimensional axisymmetric free-surface flow, *Phys. Rev. Lett.*, 71, 3458, 1993.
- Eisfeld, F., Investigation of the Penetration, the Spreading, and the Atomization of a Diesel Injection Jet using High Speed Cinematography, *Proc. SPIE Int. Soc. Opt. Eng.*, 4948, 182, 2002.
- Elghobashi, S.E. and Truesdell, G.C., On the two-way interaction between homogeneous turbulence and dispersed solid particles I: turbulence modification, *Phys. Fluids A*, 5, 1790–1796, 1993.
- Elperin, T., Kleeorin, N., and Rogachevskii, I., Turbulent thermal diffusion of small inertial particles, *Phys. Rev. Lett.*, 76, 224–227, 1996.
- Engel, P.A., *Impact Wear of Materials*, Elsevier Scientific Publishing Co., Amsterdam, 1978.
- Esche, R., Untersuchung der schwingungskavitation in Flüssigkeiten, *Acustica*, 2, AB208-AB218, 1952.
- Faeth, G.M., Current status of droplet and liquid combustion, *Prog. Energy Combust. Sci.*, 3, 191–224, 1977.
- Fedorchenko, A.I. and Chernov, A.A., Formation of fingers at the front of an axially symmetric film of liquid upon the impact of a drop with a solid surface, *Dokl. Phys.*, 44, 570, 1999.
- Ferrante, A. and Elghobashi, S., On the physical mechanism of two-way coupling in particle-laden isotropic turbulence, *Phys. Fluids*, 15, 315–329, 2003.
- Ferrel, G.W. and Crum, L.A., A novel cavitation probe design and some preliminary measurements of its application to megasonic cleaning, *J. Acoust. Soc. Am.*, 112, 1196, 2002.
- Fessler, J.R. and Eaton, J.K., Turbulence modification by particles in a backward-facing step flow, *J. Fluid Mech.*, 394, 97–117, 1999.
- Fessler, J.R., Kulick, J.D., and Eaton, J.K., Preferential concentration of heavy particles in a turbulent channel flow, *Phys. Fluids*, 6, 3742–3749, 1994.
- Finnie, I. and McFadden, D.H., On the velocity dependence of ductile metals by solid particles at low angles of incidence, *Wear*, 48, 181, 1978.
- Finnie, I., Erosion of Surfaces by Solid Particles, *Wear*, 3, 87, 1960.
- Finnie, I., Some Observations on the Erosion of Ductile Metals, *Wear*, 19, 81, 1972.
- Finnie, I., The Mechanism of Erosion of Ductile Metals, in *Proceeding of the Third National Congress on Applied Mechanics*, American Society of Mechanical Engineers, 1958, p. 527.
- Fiore, N.F., Anthony, N.C., and Kosel, T.H., Abrasion in Multi phase Alloys, in *Proceedings of the Corrosion-Erosion-Wear of Materials in Emerging Fossil Energy Systems*, Berkeley, CA, Jan. 17-19, 1982, Levy, A.V., Ed., National Association of Corrosion Engineers, Houston, 1982, p. 266.

- Flynn, H.G., *Physics of Acoustic Cavitation in Liquids*, Physical Acoustics, 1B. Academic Press, New York, 1964.
- Franc, J.P., Avellan, F., Belhadji, B., Billard, J.Y., Briançon-Marjollet, L., Fréchou, D., Fruman, D.H., Karimi, A., Kueny, J.L., and Michel, J.M., *La Cavitation. Mécanismes Physiques et Aspects Industriels*, Presses Universitaires de Grenoble, Grenoble, 1995.
- Frank, Th., Schade, K.P., and Petrak, D., Numerical simulation and experimental investigation of a gas-solid two-phase flow in a horizontal channel, *Int. J. Multiphase Flow*, 19, 187, 1993.
- Frenkel, J., *Kinetic Theory of Liquids*. Oxford University Press, New York, 1946.
- Fujikawa, S. and Akamatsu, T., Effect of the non-equilibrium condensation of vapour on the pressure wave produced by the collapse of a bubble in a liquid, *J. Fluid Mech.*, 97, 481–512, 1980.
- Fukai, J., Shiiba, Y., Yamamoto, T., Miyatake, O., Poulidakos, D., Megaridis, C.M., and Zhao, Z., Wetting effects on the spreading of a liquid droplet colliding with a flat surface: Experiment and modelling, *Phys. Fluids*, 7, 236, 1995.
- Gansley, R.R. and O'Brien, T.J., A Model for Bubble-Induced Erosion in Fluidized-Bed Combustors and Comparison with Experiment, *Wear*, 137 107, 1990.
- Gao, Z. and Mashayek, F., Stochastic model for non-isothermal droplet-laden turbulent flows, *AIAA J.*, 42, 255–260, 2004.
- Geiss, S., Sadika, A., Maltsev, A., Dreizler, A., and Janicka, J., Investigations of turbulence modulation in turbulent particle laden flows, *Z. Agnew Math. Mech.*, 81, S527–S528, 2001.
- George, D.L., Iyer, C.O., and Ceccio, S.L., Measurement of the bubbly flow beneath partial attached cavities using electrical impedance probes, *ASME J. Fluids Eng.*, 122, 151, 2000.
- Gidaspow, D., *Multiphase Flow and Fluidization, Continuum and Kinetic Theory Descriptions*, Academic Press, San Diego, CA, 1994.
- Gindroz, B. and Billet, M.L., Influence of the nuclei on the cavitation inception for different types of cavitation on ship propellers, *ASME Fluids Eng. Div. FED-177*, 1, 1993.
- Givi, P., Model free simulations of turbulent reactive flows, *Prog. Energy Combust. Sci.*, 15, 1–107, 1989.
- Givi, P., Subgrid scale modeling in turbulent combustion: A review, *AIAA Paper 2003–5081*, 2003.
- Godsave, G.A.E., Studies of the combustion of drops in a fuel spray, In *Proceedings of 4th Symposium (International) on Combustion*, The Combustion Institute, Baltimore, MD, 1953, pp. 818–830.
- Gogos, G., Soh, S., and Pope, D.N., Effects of gravity and ambient pressure on liquid fuel droplet evaporation, *Int. J. Heat Mass Transfer*, 46, 283–296, 2003.
- Goldsmith, W., The state of head injury biomechanics: past, present and future: Part 1, *Crit. Rev. Biomed. Eng.*, 29, 441, 2001.
- Gore, R.A. and Crowe, C.T., Effect of particle size on modulating turbulence intensity, *Int. J. Multiphase Flow*, 15, 279–285, 1989.
- Gore, R.A. and Crowe, C.T., Modulation of turbulence by a dispersed phase, *ASME J. Fluids Eng.*, 113, 304–307, 1991.
- Gosman, A.D. and Ioannides, E., Aspects of computer simulation of liquid-fueled combustors, *AIAA Paper 81-0323*, 1981.
- Gosman, A.D. and Pun, W.M., Calculation of Recirculating Flows (lecture notes), Report HTS/74/2, Imperial College, London, 1974.
- Grace, H.P., Dispersion phenomena in high viscosity immiscible fluid systems and application of static mixers as dispersion devices in such systems, *Chem. Eng. Commun.*, 14, 225, 1982.
- Grant, G. and Tabakoff, W., Erosion Predictions in Turbomachinery Resulting from Environmental Solid Particles, *J. Aircraft*, 12, 642, May 1975.
- Ha, J.-W. and Leal, L.G., An experimental study of drop deformation and breakup in extensional flow at high capillary number, *Phys. Fluids*, 13, 1568, 2001.
- Ha, J.-W. and Yang, S.-M., Effect of nonionic surfactant on the deformation and breakup of a drop in an electric field, *J. Colloid Interface Sci.*, 206, 195, 1998.
- Hamaker, H. C., The London–Van der Waals' attraction between spheroid particles, *Physica*, 4, 1058, 1937.
- Hammitt, F.G., *Cavitation and Multiphase Flow Phenomena*, McGraw-Hill, New York, 1980.

- Hao, Y. and Prosperetti, A., The effect of viscosity on the spherical stability of oscillating gas bubbles, *Phys. Fluids*, 11, 1309–1317, 1999.
- Hardalupus, Y., Taylor, A.M.K.P., and Whitelaw, J.H., Particle dispersion in a vertical round sudden expansion flow, *Proc. Royal Soc. London A* 341, 411–442, 1992.
- Hartley, G.S. and Brunskill, R.T., Reflection of water drop from surfaces, in *Surface phenomena in chemistry and biology*, Vol. 57, Pergamon Press, Oxford, 1958, pp. 214–223.
- Hatamiya, S. and Tanaka, H., A study on the mechanism of dropwise condensation, *Trans. Jpn. Soc. Mech. Eng.* (in Japanese), B-52, 2214, 1986.
- Haywood, R.J., Rensizbulut, M., and Raithby, G.D., Numerical solution of deforming evaporating droplets at intermediate Reynolds numbers, *Num. Heat Transfer*, 26, 253–272, 1994a.
- Haywood, R.J., Rensizbulut, M., and Raithby, G.D., Transient deformation and evaporation of droplets at intermediate Reynolds numbers, *Int. J. Heat Mass Transfer*, 37, 1401–1409, 1994b.
- Hilgenfeldt, S., Grossmann, S., and Lohse, D., A simple explanation of light emission in sonoluminescence, *Nature*, 398, 402, 1999.
- Hinze, J.O., Fundamentals of the hydrodynamic mechanism of splitting in dispersion processes, *AICHE J.*, 1, 289, 1955.
- Hishida, K. and Maeda, M., *Turbulence Characteristics of Particle-laden Flow Behind a Rearward Facing Step*, ASME FED Vol. 121, 207–212, 1991.
- Ho, C.M. and Huerre, P., Perturbed free shear layers, *Ann. Rev. Fluid Mech.*, 16, 365–424, 1984.
- Hocking, L.M. and Rivers, A.D., The spreading of a drop by capillary action, *J. Fluid Mech.*, 121, 425, 1982.
- Hoffman, R.L., A study of the advancing interface. 1. Interface shape in liquid–gas systems, *J. Coll. Interface Sci.*, 50, 228, 1975.
- Holzfuß, J., Rugeberg, M., and Billo, A., Shock wave emissions of a sonoluminescing bubble, *Phys. Rev. Lett.*, 81, 5434, 1998.
- Hsiang, L.-P. and Faeth, G.M., Drop deformation and breakup due to shock wave and steady disturbances, *Int. J. Multiphase Flow*, 21, 545, 1995.
- Hsiang, L.-P. and Faeth, G.M., Drop properties after secondary breakup, *Int. J. Multiphase Flow*, 19, 721, 1993.
- Hsiang, L.-P. and Faeth, G.M., Near-limit drop deformation and secondary breakup, *Int. J. Multiphase Flow*, 18, 635, 1992.
- Hsieh, D.-Y. and Plesset, M.S., Theory of rectified diffusion of mass into gas bubbles, *J. Acoust. Soc. Am.*, 33, 206, 1961.
- Hsieh, D.-Y., Some analytical aspects of bubble dynamics, *J. Basic Eng.*, 87, 991–1005, 1965.
- Hubbard, G.L., Denny, V.E., and Mills, A.F., Droplet evaporation: Effects of transients and variable properties, *Int. J. Heat Mass Transfer*, 18, 1003–1008, 1975.
- Humphrey, J.A.C., Fundamentals of Fluid Motion in Erosion by Solid Particle Impact, *Int. J. Heat Fluid Flow*, 11, 170, 1990.
- Hussain, M.F. and Tabakoff, W., Computation and Plotting of Solid Particulate Flow in Rotating Cascades, *Comput. Fluids*, 2, 1974.
- Hwang, S., Liu, S., and Reitz, R. D., Breakup mechanisms and drag coefficients of high speed vaporizing drops, *Atomization Sprays*, 6, 353, 1996.
- Jackson, R., Locally averaged equations of motion for a mixture of identical spherical particles and a Newtonian fluid, *Chem. Eng. Sci.*, 52, 2457–2469, 1997.
- Jayarathne, O.W. and Mason, B.J., The coalescence and bouncing of water drops at an air/water interface, *Proc. Roy. Soc. London A*, 280, 545, 1964.
- Jiang, Y.J., Umemura, A., and Law, C.K., An experimental investigation on the collision behaviour of hydrocarbon droplets, *J. Fluid Mech.*, 234, 171, 1992.
- Johnston, D.N., Edge, K.A., and Vaughan, N.D., Experimental Investigation of Flow and Force Characteristics of Hydraulic Poppet and Disc Valves, *Proc. Inst. Mech. Eng., A: Power Process Eng.*, 205, 161, 1991.

- Joseph, D.D., Lift Correlations From Direct Numerical Simulation of Solid–Liquid Flow, Paper 385 presented at *ICMF-2001, 4th International Conference on Multiphase Flow*, May 27–June 1, 2001.
- Joseph, D.D., Belanger, J., and Beavers, G.S., Breakup of a liquid drop suddenly exposed to a high-speed airstream, *Int. J. Multiphase Flow*, 25, 1263, 1999.
- Jozsa, I., Sebestyen, G., and Kiss, J., 1994, Regulating valve cavitation in the power station, *ASME, Fluids Eng. Div. FED*, 194, 89.
- Kamath, V. and Prosperetti, A., Numerical investigation methods in gas-bubble dynamics, *J. Acoust. Soc. Am.*, 85, 1538–1548, 1989.
- Kameda, M. and Matsumoto, Y., Nonlinear oscillation of a spherical gas bubble in acoustic fields, *J. Acoust. Soc. Am.*, 106, 3156–3166, 1999.
- Kameda, M. and Matsumoto, Y., Shock waves in a liquid containing small gas bubbles. *Phys. Fluids*, 8, 322–335, 1996.
- Kameda, M., Shimauro, N., Higashino, F., and Matsumoto, Y., Shock waves in a uniform bubbly flow, *Phys. Fluids*, 10, 2661–2668, 1998.
- Keller, J.B. and Kolodner, I.I., Damping of underwater explosion bubble oscillation, *J. Appl. Phys.*, 27, 1152–1161, 1956.
- Khalitov, D.A. and Longmire, E.K., Simultaneous two-phase PIV by two-parameter phase discrimination, *Exp. Fluids*, 32, 252–268, 2002.
- Kick, F., *Dar Gesetz der proportionalen Widerstande und seine Anwendung*, Leipzig, Germany, 1885.
- Kiger, K.T. and Pan, C., PIV technique for the simultaneous measurement of dilute two-phase flows, *J. Fluids Eng.*, 122, 811–818, 2000.
- Kiger, K.T. and Pan, C., Suspension and turbulence modification effects of solid particulates on a horizontal turbulent channel flow, *J. Turbulence*, 3, 2002.
- Kiger, K.T., Scanning PIV technique to resolve dispersed two-phase flow, *Third International Conference on Multiphase Flow*, ICMF 1-98 Lyon France, June 8–12, 1998.
- Kim, H.-Y., Feng, Z.C., and Chun, J.-H., Instability of a liquid jet emerging from a droplet upon collision with a solid surface, *Phys. Fluids*, 12, 531, 2000.
- Kistler, S.F., Hydrodynamics of wetting, in *Wettability*, Berg, J.C., Ed., *Surfactant Science Series*, Marcel Dekker, New York, 1993.
- Knapp, R. T., Daily, J. W., and Hammitt, F. G., *Cavitation*, McGraw-Hill, New York, 1970.
- Koch, G.W., Sillett, S.C., Jennings, G.M., and Davis, S.D., The limits to tree height, *Lett. Nat.*, 428, 851, 2004.
- Korobkin, A., Analytic theory of liquid-solid impact, *Phil. Trans. R. Soc. Lond. A*, 355, 507, 1997.
- Krzczkowski, S.A., Measurements of liquid droplet disintegration mechanisms, *Int. J. Multiphase Flow*, 6, 227, 1980.
- Kuhn de Chizelle, Y., Ceccio, S.L., and Brennen, C.E., Observations and scaling of travelling bubble cavitation, *J. Fluid Mech.*, 293, 99, 1995.
- Kulick, J.D., Fessler, J.R., and Eaton, J.K., Particle response and turbulence modification in fully developed channel flow, *J. Fluid Mech.*, 277, 285–309, 1994.
- Kussin, J. and Sommerfeld, M., Experimental studies on particle behavior and turbulence modification in horizontal channel flow with different wall roughness, *Exp. Fluids*, 33, 143–159, 2002.
- Laberteaux, K.R. and Ceccio, S.L., Partial cavity flows. Part 1. Cavities forming on models without spanwise variation, *J. Fluid Mech.*, 431, 1, 2001a.
- Laberteaux, K.R. and Ceccio, S.L., Partial cavity flows. Part 2. Cavities forming on test objects with spanwise variation, *J. Fluid Mech.*, 431, 43, 2001b.
- Lain, S., Sommerfeld, M., and Kussin, J., Experimental studies and modeling of four-way coupling in particle-laden channel flow, *Int. J. Heat Fluid Flow*, 23, 647–656, 2002.
- Lauterborn, W., Acoustic Turbulence, *Front. Phys. Acoust.*, S.I.F.-XC III, 124–144, 1989.
- Lauterborn, W., Numerical investigation of nonlinear oscillations of gas bubbles in liquids, *J. Acoust. Soc. Am.*, 59, 283–293, 1976.
- Lauterborn, W., On the bifurcation structure of bubble oscillators, 11th ISNA, 71–80, 1987.

- Law, C.K. and Williams, F.A., Kinetics and convection in the combustion of alkane droplets, *Combust. Flame*, 19, 393–406, 1972.
- Law, C.K., Chung, S.H., and Srinivasan, N., Gas phase quasi-steadiness and fuel vapor accumulation effects on droplet burning, *Combust. Flame*, 38, 173–198, 1980.
- Lee, C.H. and Reitz, R.D., An experimental study of the effect of gas density on the distortion and breakup mechanism of drops in high speed gas stream, *Int. J. Multiphase Flow*, 26, 229, 2000.
- Lee, S.L. and Durst, F., On the motion of particles in turbulent duct flows, *Int. J. Multiphase Flow*, 8, 125–146, 1982.
- Lefebvre, H., *Atomization and Sprays*, Hemisphere Publishing Corporation, Washington, DC, 1989.
- Leger, A.T. and Ceccio, S.L., Examination of the flow near the leading edge of attached cavitation. Part 1. Detachment of two-dimensional and axisymmetric cavities, *J. Fluid Mech.*, 376, 61, 1998.
- Leighton, T.G., *The Acoustic Bubble*, Academic Press, London, 1994.
- Lesieur, M. and Métais, O., New trends in large-eddy simulations of turbulence, *Annu. Rev. Fluid Mech.*, 28, 45–82, 1996.
- Lesser, M. and Field, J., The impact of compressible liquids, *Annu. Rev. Fluid Mech.*, 15, 97, 1983.
- Levin, Z. and Hobbs, P.V., Splashing of water drops on solid and wetted surfaces: hydrodynamics and charge separation, *Phil. Trans. R. Soc. London A*, 269, 555, 1971.
- Li, C.-Y. and Ceccio, S.L., Interaction of single traveling bubbles with the boundary layer and attached cavitation, *J. Fluid Mech.*, 322, 329, 1996.
- Li, S.C., Spray stagnation flames, *Prog. Energy Combust. Sci.*, 23, 303–347, 1997.
- Lifka, J., Ondruschka, B., and Hofmann, J., The use of ultrasound for the degradation of pollutants in water: a quasonolysis — a review, *Eng. Life Sci.*, 3, 2003.
- Lindau, O. and Lauterborn, W., Cinematographic observation of the collapse and rebound of a laser-produced cavitation bubble near a wall, *J. Fluid Mech.*, 479, 327–348, 2003.
- Ling, W., Chung, J.N., and Crowe, C.T., Direct numerical simulation of the two-way coupled interaction between particles and mixing layer, *Proc. R. Soc. London A*, 456, 2931–2955, 2000.
- Ling, W., Chung, J.N., and Crowe, C.T., Direct numerical simulation of a two-way thermally coupled droplet-laden mixing layer, *J. Fluid Mech.*, 437, 45–68, 2001.
- Ling, W., Chung, J.N., Troutt, T.R., and Crowe, C.T., Direct numerical simulation of a three-dimensional mixing layer with particle dispersion, *J. Fluid Mech.*, 358, 61–85, 1998.
- Liu, Q. and Orme, M., On precision droplet-based net-form manufacturing technology, *Proc.-Inst. Mech. Eng. B, J. Eng. Manufacture*, 215, 1333, 2001.
- Liu, Z. and Reitz, R.D., An analysis of the distortion and breakup mechanisms of high speed liquid drops, *Int. J. Multiphase Flow*, 4, 631, 1997.
- Liu, Z.C. and Adrian, R., Simultaneous imaging of the velocity fields of two phases, in *Particulate Two-Phase Flow*, Roco, M.C., Ed., Butterworth-Heinemann, London, pp. 33–57, 1993.
- Longmire, E.K. and Eaton, J.K., Structure of a particle-laden round jet, *J. Fluid Mech.*, 236, 217–257, 1992.
- Lonholt, S., Stenum, B., and Maxey, M.R., Experimental verification of the force coupling method for particulate flows, *Int. J. Multiphase Flow*, 28, 225–246, 2002.
- Lyczkowski, R.W. and Bouillard, J.X., Scaling and Guidelines for Erosion in Fluidized Beds, *Powder Technol.*, 125, 217, 2002.
- Lyczkowski, R.W. and Bouillard, J.X., Corrigendum to “State-of-the-Art Review of Erosion Modeling in Fluid/Solids Systems” [*Prog. Energy Combust. Sci.* 28 (2002) 543–602], *Prog. Energy Combust. Sci.* 29(1), 85, 2003.
- Lyczkowski, R.W. and Bouillard, J.X., State-of-the-Art Review of Erosion Modeling in Fluid/Solids Systems, *Prog. Energy Combust. Sci.*, 28, 543, 2002a.
- Lyczkowski, R.W., Bouillard, J.X., and Folga, S.M., Users Manual for FLUFIX/MOD2: A Computer Program for Fluid-Solids Hydrodynamics, Argonne National Laboratory Sponsor Report, Argonne, IL, April 1992. Reprinted by USDOE METC as DOE/MC/24193-3491/NTIS No. DE94000033), available from NTIS, Springfield, VA, 1994a.

- Lyczkowski, R.W., Bouillard, J.X., Chang, S.L., and Folga, S.M., User's Manual for EROSION/MOD1: A Computer Program for Fluid Solids Erosion, Argonne National Laboratory Sponsor Report, Argonne, IL, April 1992. Reprinted by USDOE METC as DOE/MC/24193-3500/NTIS No. 94000032), available from NTIS, Springfield, VA, 1994b.
- Macklin, W.C. and Metaxas, G.J., Splashing of drops on liquid layers, *J. Appl. Phys.*, 47, 3963, 1976.
- Madejski, J., Droplets on impact with a solid surface, *Int. J. Heat Mass Transfer*, 26, 1095, 1983.
- Madge, B.A. and Jensen, J.N., Disinfection of wastewater using a 20-kHz ultrasound unit, *Water Environ. Res.*, 74, 159, 2002.
- Maeda, M., Hishida, K., & Furutani, T., Optical measurements of local gas and particle velocity in an upward flowing dilute gas–solids suspension, *Proceedings of the Polyphase Flow and Transport Technology*, Century 2-ETC, San Francisco, 1980, pp. 211–216.
- Magnussen, B.F. and Hjertager, B.H., On mathematical models of turbulent combustion with special emphasis on soot formation and combustion. In *Proceedings of 16th Symposium (International) on Combustion*, The Combustion Institute, Pittsburgh, PA, 1977, pp. 719–729.
- Mao, T., Kuhn, D.C.S., and Tran, H., Spread and rebound of liquid droplets upon impact on flat surfaces, *AIChE J.*, 43, 2169, 1997.
- Marengo, M., Tropea, C., Aufprall von Tropfen auf Flüssigkeitsfilme, Final report for project Tr 194/10, Deutsche Forschungsgemeinschaft, Technische Universität Darmstadt, Darmstadt, 1999.
- Mashayek, F. and Pandya, R.V.R., Analytical description of particle/droplet-laden turbulent flows, *Progress Energy Combust. Sci.*, 29, 329–378, 2003.
- Mashayek, F., Dynamics of evaporating drops. Part I: Formulation and evaporation model, *Int. J. Heat Mass Transfer*, 44, 1517–1526, 2001.
- Mashayek, F., Numerical investigation of reacting droplets in homogeneous shear turbulence, *J. Fluid Mech.*, 405, 1–36, 2000.
- Matsumoto, S. and Saito, S., Monte Carlo simulation of horizontal pneumatic conveying based on the rough wall model, *J. Chem. Eng. Japan*, 3, 223, 1970b.
- Matsumoto, S. and Saito, S., On the mechanism of suspensions in horizontal pneumatic conveying: Monte Carlo simulation based on the irregular bouncing model, *J. Chem. Eng. Japan*, 3, 83, 1970a.
- Matsumoto, Y. and Aoki, M., Growth and collapse of cavitation bubbles, *Bull. JSME* 27, 1352–1357, 1984.
- Matsumoto, Y. and Beylich, A.E., Influence of homogeneous condensation inside a small gas bubble on its pressure response, *J. Fluids Eng. Eng. ASME*, 107-2, 281–286, 1985.
- Matsumoto, Y. and Takemura, F., Influence of internal phenomena on gas bubble motion (Effects of thermal diffusion, phase change on the gas-liquid interface and mass diffusion between vapor and non-condensable gas in the collapsing phase), *JSME Int. J.*, B-37, 288–296, 1994.
- Matsumoto, Y. and Watanabe, M., Nonlinear oscillation of gas bubble with internal phenomena, *JSME Int. J. II-32*, 157–162, 1989.
- Matula, T.J., Hallaj, I., Cleveland, R.O., Crum, L.A., Moss, W.C., and Roy, R.A., The acoustic emissions from single-bubble sonoluminescence, *J. Acoust. Soc. Am.*, 103, 1377, 1998.
- Maxey, M.R. and Riley, J.J., Equation of motion for a small rigid sphere, *Phys. Fluids*, 26, 883–889, 1983.
- Maxey, M.R., Patel, B.K., Chang, E.J., and Wang, L.P., Simulations of dispersed turbulent multiphase flow, *Fluid Dyn. Res.*, 20, 143–156, 1997.
- Maxey, M.R., The gravitational settling of aerosol particles in homogeneous turbulence and random flow fields, *J. Fluid Mech.*, 174, 441–465, 1987.
- McCormick, B.W., On cavitation produced by a vortex trailing from a lifting surface, *J. Basic Eng.*, 84, 369, 1962.
- McCreath, C.G. and Chigier, N.A., Liquid spray burning in the wake of a stabilizer disk. In *Proceedings of 14th Symposium (International) on Combustion*, The Combustion Institute, 1973, pp. 1355–1363.
- McLaughlin, J.B., Aerosol particle deposition in numerically simulated channel flow, *Phys. Fluids A*, 1, 1211–1224, 1989.
- Meneveau, C. and Katz, J., Scale-invariance and turbulence models for large-eddy simulation, *Annu. Rev. Fluid Mech.*, 32, pp. 1–32, 2000.

- Meng, H. C. and Ludema, K.C., Wear Models and Predictive Equations: Their Form and Content, *Wear*, 181–183, 443, 1995.
- Mikami, T., Cox, R.G., and Mason, S.G., Breakup of extending liquid threads, *Int. J. Multiphase Flow*, 2, 113, 1975.
- Milliken, W.J. and Leal, L.G., Deformation and breakup of viscoelastic drops in planar extensional flows, *J. Non-Newtonian Fluid Mech.*, 40, 355, 1991.
- Mostafa, A.A., Mongia, H.C., McDonell, V.G., and Samuelsen, G.S., Evolution of particle-laden jet flows: a theoretical and experimental study, *AIAA J.* 27, 167–183, 1989.
- Mourougou-Candoni, N., Prunet-Foch, B., Legay, F., and Vignes-Adler, M., Retraction phenomena of surfactant solution drops upon impact on a solid substrate of low surface energy, *Langmuir*, 15, 6563, 1999.
- Mulhearn, T.O. and Samuels, L.E., The Abrasion of Metals: A Model of the Process, *Wear*, 5, 478, 1962.
- Mundo, C., Sommerfeld, M., and Tropea, C., On the modelling of liquid sprays impinging on surfaces, *Atomiz. Sprays*, 8, 625–652, 1998.
- Neilson, J.H. and Gilchrist, A., Erosion by a Stream of Solid Particles, *Wear*, 11, 111, 1968.
- Neppiras, E.A. and Noltingk, B.E., Cavitation produced by ultrasonics: theoretical conditions for the onset of cavitation, *Proc. Phys. Soc. London*, 64B, 1032–1038, 1951.
- Neppiras, E.A., Subharmonic and other low-frequency emission from bubbles in sound-irradiated liquids, *J. Acoust. Soc. Am.*, 46, 587–601, 1969.
- Niemczewski, B., Estimation of the suitability of selected organic solvents for ultrasonic cleaning, *Ultrasonics Sonochem.*, 6, 149, 1999.
- Nigmatulin, R.I., Khabeev, N.S., and Nagiev, F.B., Heat and mass transfer of vapours–gas bubbles in a liquid, *Int. J. Heat Mass Transfer*, 24, 1033–1044, 1981.
- Noltingk, B.E. and Neppiras, E.A., Cavitation produced by ultrasonics, *Proc. Phys. Soc., London*, 63B, 674–685, 1950.
- Oğuz, H.N. and Prosperetti, A., Bubble entrainment by the impact of drops on liquid surfaces, *J. Fluid Mech.*, 219, 143, 1990.
- Omta, R., Oscillation of a cloud of bubbles of small and not so small amplitude, *J. Acoust. Soc. Am.*, 82, 1018–1033, 1987.
- Onda, T., Shibuichi, S., Satoh, N., and Tsujii, K., Super-water-repellent fractal surfaces, *Langmuir*, 12, 2125, 1996.
- Padhye, A.R., Literature Review of Fundamental Erosion/Abrasion Models as Applicable to Wear of Fluidized Bed Internals, Topical Report, EG&G WASC, Inc., Morgantown, W.V., December 1985.
- Pandya, R.V.R. and Mashayek, F., Turbulent thermal diffusion and barodiffusion of passive scalar and dispersed phase of particles in turbulent flows, *Phys. Rev. Lett.*, 88, 044501–1–044501–4, 2002.
- Pandya, R.V.R. and Mashayek, F., Non-isothermal dispersed phase of particles in turbulent flow, *J. Fluid Mech.*, 475, 205–245, 2003.
- Paris, A.D. and Eaton, J.K., Measuring velocity gradients in a particle-laden channel flow, *Proceedings of the Third International Workshop on Particle Image Velocimetry, PIV99*, Santa Barbara, 1999, pp. 513–518.
- Paris, T. and Eaton, J.K., *Turbulence Attenuation in a Particle-Laden Channel Flow*, Report TSD-137, Department of Mechanical Engineering, Stanford University, 2001.
- Park, R.W., *Behaviour of Water Drops Colliding in Humid Nitrogen*, Ph.D. thesis, University of Wisconsin, WI, U.S.A., 1970.
- Parkinson, M.J., Jury, A.W., Napier, B.A., Kempton, T.J., and Holder, J.C., Cold Model Erosion Studies in Support of Pressurized Fluidized Bed Combustion, Electric Power Research Institute Final Report for Project 1337-2, April 1986.
- Parkinson, M.J., Napier, B.A., Jury, A.W., and Kempton, T.J., Cold Model Studies of PFBC Tube Erosion, in *Proceedings of the 8th International Conference on Fluidized-Bed Combustion*, Vol. II, National Technical Information Service, DOE/METC-85/6021, Springfield, VA, 1985, p. 730.
- Parthasarathy, R.N. and Faeth, G.M., Turbulence modulation in homogeneous dilute particle-laden flows, *J. Fluid Mech.*, 220, 485–514, 1990.

- Pasandideh-Fard, M., Qiao, Y.M., Chandra, S., and Mostaghimi, J., Capillary effects during droplet impact on a solid surface, *Phys. Fluids*, 8, 650, 1996.
- Pecha, R. and Gompf, B., Microimplosions: cavitation collapse and shock wave emission on a nanosecond time scale, *Phys. Rev. Lett.*, 84, 1328, 2000.
- Peters, N., *Turbulent Combustion*, Cambridge University Press, Cambridge, UK, 2000.
- Philipp, A. and Lauterborn, W., Cavitation erosion by single laser-produced bubbles, *J. Fluid Mech.*, 361, 75, 1998.
- Pilch, M. and Erdman, C., Use of break-up time data and velocity history data to predict the maximum size of stable fragments for acceleration induced break-up of a liquid drop, *Int. J. Multiphase Flow*, 13, 741, 1987.
- Plesset, M.S. and Mitchell, T.P., On the stability of the spherical shape of a vapor cavity in a liquid, *Q. Appl. Math.*, 13, 419–430, 1956.
- Plesset, M.S., The dynamics of cavitation bubbles, *ASME J. Appl. Mech.*, 16, 228–231, 1949.
- Podolski, W.F., Lyczkowski, R.W., Montrone, E., Drennen, J., Ai, Y.H. and Chao, B.T., A Study of Parameters Influencing Metal Wastage in Fluidized Bed Combustors, in *Proceedings of the 11th (1991) International Conference on Fluidized Bed Combustion*, Vol.2, Anthony, E.J., Ed., American Society of Mechanical Engineers, 1991, p. 609.
- Podvysotsky, A.M. and Shraiber, A.A., Coalescence and break-up of drops in two-phase flows, *Int. J. Multiphase Flow*, 10, 195, 1984.
- Pope, S.B., PDF methods for turbulent reactive flows, *Prog. Energy Combust. Sci.*, 11, 119–192, 1985.
- Porteiro, J.L.F., Weber, S.T., and Rahman, M.M., Experimental study of flow induced noise in counterbalance valves, *ASME Aerospace Division (AD)*, 53, 2, *Proceedings of the 4th International Symposium on Fluid-Structure Interactions, Aeroelasticity, Flow-Induced Vibration and Noise*, 1997, p. 557.
- Poulidakos, D. and Waldvogel, J., Heat transfer and Fluid dynamics in the process of spray deposition, *Adv. Heat Transfer*, 28, 1, 1996.
- Pourahmadi, F. and Humphrey, J.A.C., Modeling Solid-Fluid Turbulent Flows with Application to Predicting Erosion Wear, *Physico Chem. Hydrodyn.*, 4, 191, 1983.
- Pozdikidis, C., The deformation of a liquid drop moving normal to a plane wall, *J. Fluid Mech.*, 215, 331, 1990.
- Pozorski, J. and Minier, J., On the Lagrangian turbulent dispersion models based on the Langevin equation, *Int. J. Multiphase Flow*, 24, 913–945, 1998.
- Preston, A., Colonius, T., and Brennen C. E., Reduced-order modeling of diffusive effects on the dynamics of bubbles, *Proceedings of 5th International Symposium on Cavitation*, GS-2-013, 2003.
- Prosperetti, A., Crum, L.A., and Commander, K.W., Nonlinear bubble dynamics, *J. Acoust. Soc. Am.*, 83, 502–514, 1988.
- Prosperetti, A., The thermal behaviour of oscillating gas bubbles, *J. Fluid Mech.*, 222, 587–616, 1991.
- Putterman, S.J. and Weninger, K.R., Sonoluminescence: How bubbles turn sound into light, *Annu. Rev. Fluid Mech.*, 32, 445, 2000.
- Qian, J. and Law, C.K., Regimes of coalescence and separation in droplet collision, *J. Fluid Mech.*, 331, 59, 1997.
- Rabinowicz, E., *Friction and Wear of Materials*, Wiley, New York, 1965.
- Raja, N. and Meiburg, E., The accumulation and dispersion of heavy particles in forced two-dimensional mixing layers. Part2: The effect of gravity, *Phys. Fluids*, 7, 1241–1264, 1995.
- Ran, B. and Katz, J., Pressure fluctuations and their effect on cavitation inception within water jets, *ASME Fluids Eng. Div. FED*, 177, 31, 1993.
- Range, K. and Feuillebois, F., Influence of surface roughness on liquid drop impact, *J. Colloid Interface Sci.*, 203, 16, 1998.
- Ranger, A.A. and Nicholls, J.A., The aerodynamic shattering of liquid drops, *AIAA J.*, 7, 285, 1969.
- Ranz, W.E. and Marshall, W.R., Evaporation from drops, *Chem. Eng. Prog.*, 48, 141–173, 1952.
- Rayleigh, Lord, On the pressure developed in a liquid during the collapse of a spherical cavity, *Phil. Mag.*, 34, 94–98, 1917.

- Rein, M. Ed., *Drop-Surface Interactions*, Springer, Wien, 2002.
- Reveillon, J. and Vervisch, L., Spray vaporization in nonpremixed turbulent combustion modeling: A single droplet model, *Combust. Flame*, 121, 75–90, 2000.
- Reznik, S.N. and Yarin, A.L., Spreading of a viscous drop due to gravity and capillarity on a horizontal or an inclined dry wall, *Phys. Fluids*, 14, 118, 2002.
- Richard, D. and Quéré, D., Bouncing water drops, *Europhys. Lett.* 50, 769, 2000.
- Riesz, P., Kondo, T., and Krishna, C.M., Sonochemistry of volatile and nonvolatile solutes in aqueous solutions. E.p.r. and spin trapping studies, *Ultrasonics*, 28, 295, 1990.
- Rioboo, R., Marengo, M., and Tropea, C., Time evolution of liquid drop impact onto solid, dry surfaces, *Exp. Fluids*, 33, 112, 2002.
- Rioboo, R., Marengo, M., and Tropea, C., Outcomes from a drop impact on solid surfaces, *Atomization Sprays*, 11, 155, 2001.
- Rodrigues, F. and Mesler, R., Some drops don't splash, *J. Colloid Interface Sci.* 106, 347, 1985.
- Rogers, C.B. and Eaton, J.K., The effect of small particles on fluid turbulence in a flat-plate, turbulent boundary layer in air, *Phys. Fluids*, A 3, 928–937, 1991.
- Rogers, W. A., The Prediction of Wear in Fluidized Beds, *Trans. ASME J. Pressure Vessel Technol.*, 117, 142, 1995.
- Roisman, I.V. and Tropea, C., Impact of a drop onto a wetted wall: description of crown formation and propagation, *J. Fluid Mech.*, 472, 373, 2002.
- Roisman, I.V., Rioboo, R., and Tropea, C., Normal impact of a liquid drop on a dry surface: model for spreading and receding, *Proc. Royal. Soc. London A*, 458, 1411, 2002.
- Rong, D. and Horio, M., Behavior of Particles and Bubbles Around Immersed Tubes In a Fluidized Bed at High Temperature and Pressure: A DEM Simulation, *Int. J. Multiphase Flow*, 27, 89, 2001.
- Rong, D. Mikami, T., and Horio, M., Particle and Bubble Movements Around Tubes Immersed in Fluidized Beds-A Numerical Study, *Chem. Eng. Sci.*, 54, 5737, 1999.
- Rouson, D.W.I. and Eaton, J.K., On the preferential concentration of particles in turbulent channel flow, *J. Fluid Mech.*, 428, 149–169, 2001.
- Rudinger, G. and Chang, A., Analysis of Non-steady Two-Phase Flow, *Phys. Fluids*, 7, 1747, 1964.
- Sakakibara, J., Wicker, R.B., and Eaton, J.K., Measurements of the particle-fluid velocity correlation and the extra dissipation in a round jet, *Int. J. Multiphase Flow*, 22, 863–881, 1996.
- Samenfink, W., *Grundlegende Untersuchung zur Tropfeninteraktion mit schubspannungsgetriebenen Wandfilmen*, Ph.D. thesis, Universität Karlsruhe, Karlsruhe, Germany, 1997.
- Sankaran, V. and Menon, S., LES of spray combustion in swirling flows, *J. Turbulence*, 3, 011, 2002.
- Sarkar, A.D., *Friction Wear*, Academic Press, New York, 1980.
- Sato, Y., Fukuichi, U., and Hishida, K., Effect of inter-particle spacing on turbulence modulation by Lagrangian PIV, *Int. J. Heat and Fluid Flow*, 21, 554–561, 2000.
- Savage, S.B., *Granular Flow at High Shear Rates*, Academic Press, New York, 1982, pp. 339–357.
- Schmehl, R., Modeling droplet breakup in complex two-phase flows, *Proceedings of the International Conference on Liquid Atomization and Spray Systems ICLASS-2003*, July 13–18, 2003, Sorrento, Italy, 2003b.
- Schmehl, R., *Tropfendeformation und Nachzerfall bei der technischen Gemischaufbereitung*, Dissertation, University of Karlsruhe, Karlsruhe, Germany, 2003a.
- Schreck, S. and Kleis, S.J., Modification of grid-generated turbulence by solid particles, *J. Fluid Mech.* 249, 665–688, 1993.
- Sevik, M. and Park, S.H., The splitting of drops and bubbles by turbulent fluid flow, *J. Fluid Eng.*, 53, 1973.
- Sheldon, G.L. and Finnie, I., The Mechanism of Material Removal in the Erosive Cutting of Brittle Materials, *Trans. ASME, Series 13, J. Eng. Ind.*, 88, 393, 1966.
- Sheldon, G.L., Maji, J., and Crowe, C.T., Erosion of a Tube by Gas Particle Flow, *Trans. ASME, Ser. H, J. Eng. Mater. Technol.*, 99, 138, 1977.
- Shewmon, P. and Sundararajan, G., The Erosion of Metals, *Annu. Rev. Mater. Sci.*, 13, 303, 1983.
- Shimada, M., Matsumoto, Y., and Kobayashi, T., Influence of the nuclei size distribution on the collapsing behavior of the cloud cavitation. *JSME Int., Ser. B*, 43, 380–385, 2000.

- Shook, C.A., Ghosh, S.R., and Pilling, F.E., Wall Erosion in Slurry Couette Flow, in *Liquid-Solid Flows and Erosion Wear in Industrial Equipment*, Roco, M.C., Ed., American Society of Mechanical Engineers, New York, 63, 1983, p. 63.
- Shuen, J.-S., Solomon, A.S.P., Zhang, Q.-F., and Faeth, G.M., Structure of particle-laden jets: measurements and predictions, *AIAA J.* 23, 396–404, 1985.
- Šikalo, Š., *Analysis of droplet impact onto horizontal and inclined surfaces*, Ph.D. thesis, Technische Universität Darmstadt, Darmstadt, Germany, 2003.
- Simonin, O. and Squires, K.D., On two way coupling in gas–solid turbulent flows, *Proceedings of ASME, FEDSM03*, Honolulu, 2003.
- Sommerfeld, M. and Huber, N., Experimental analysis and modelling of particle-wall collisions, *Int. J. Multiphase Flow*, 25, 1457, 1999.
- Sommerfeld, M. and Zivkovis, G., Recent advances in the numerical simulation of pneumatic conveying through pipe systems, *Comput. Methods Appl. Sci.*, 1992, 201.
- Soo, S.L., A Note on Moving Dust Particles, *Powder Technol.*, 17, 259, 1977.
- Sornek, R. J., Dobashi, R., and Hirano, T., Effect of turbulence on vaporization, mixing, and combustion of liquid-fuel sprays, *Combust. Flame*, 120, 479–491, 2000.
- Soyama, H. and Asahara, M., Improvement of the corrosion resistance of carbon steel surface by a cavitating jet, *J. Mater. Sci. Lett.*, 18, 1953, 1999.
- Spalding, D.B., Mixing and chemical reaction in steady confined turbulent flames. In *Proceedings of 13th Symposium (International) on Combustion*, The Combustion Institute, Pittsburgh, PA, 1971, pp. 649–657.
- Spalding, D.B., The combustion of liquid fuels. In *Proceedings of 4th Symposium (International) on Combustion*, The Combustion Institute, Baltimore, MD, 1953, pp. 847–864.
- Squires, K.D. and Eaton J.K. Preferential concentration of particles by turbulence, *Phys. Fluids A*, 3, 1169–1178, 1991.
- Squires, K.D. and Eaton J.K., Particle response and turbulence modulation in isotropic turbulence, *Phys. Fluids A*, 2, 1191–1203, 1990.
- Squires, K.D. and Eaton, J.K., Lagrangian and Eulerian statistics obtained from direct numerical simulation of homogeneous turbulence, *Phys. Fluids A*, 3, 130–143, 1991a.
- Squires, K.D. and Eaton, J.K., Measurements of particle dispersion obtained from direct numerical simulation of isotropic turbulence, *J. Fluid Mech.*, 226, 1–35, 1991c.
- Squires, K.D. and Eaton, J.K., Preferential concentration of particles by turbulence. *Phys. Fluids A*, 3, 1169–1178, 1991b.
- Stanton, D.W. and Rutland, C.J., *Modeling Fuel Film Formation and Wall Interaction in Diesel Engines*, SAE Technical Papers Series 960628, 1996.
- Stock, D.E., Freeman scholar lecture: Particle dispersion in gases, *J. Fluids Eng.*, 118, 4–17, 1996.
- Stone, H.A. and Leal, L.G., Relaxation and breakup of an initially extended drop in an otherwise quiescent fluid, *J. Fluid Mech.*, 198, 399, 1989a.
- Stone, H.A. and Leal, L.G., The influence of initial deformation on drop breakup in subcritical time-dependent flows at low Reynolds numbers, *J. Fluid Mech.*, 206, 223, 1989b.
- Stone, H.A., Bentley, B.J., and Leal, L.G., An experimental study of transient effects in the breakup of viscous drops, *J. Fluid Mech.*, 173, 131, 1989.
- Stone, H.A., Dynamics of drop deformation and breakup in viscous fluids, *Annu. Rev. Fluid Mech.*, 26, 65, 1994.
- Storey, B.D. and Szeri, A.J., A reduced model of cavitation physics for use in sonochemistry, *Proc. R. Soc. Lond. A*, 457, 1685–1700, 2001.
- Stow, C.D. and Hadfield, M.G., An experimental investigation of fluid flow resulting from the impact of a water drop with an unyielding dry surface. *Proc. R. Soc. London A*, 373, 419, 1981.
- Stow, C.D. and Stainer, R.D., The physical products of a splashing water drop, *J. Met. Soc. Japan*, 55, 518, 1977.

- Sundaram, S. and Collins, L.R., A numerical study of the modulation of isotropic turbulence by suspended particles, *J. Fluid Mech.*, 379, 105–143, 1999.
- Suslick, K.S., Sonoluminescence and Sonochemistry, *Proceedings of the IEEE Ultrasonics Symposium*, 1, 523, 1997.
- Suzuki, T. and Chiu, H.H., Multi-droplet combustion of liquid propellants, in *Proceedings of 9th Symposium (International) on Combustion*, The Combustion Institute, Pittsburgh, PA, 1971, pp. 145–154.
- Suzuki, Y., Ikenoya, M., and Kasagi, N., Simultaneous measurement of fluid and dispersed phases in a particle-laden turbulent channel flow with the aid of 3-D PTV, *Exp. Fluids*, 29S, S185–S193, 2002.
- Tabakoff, W., Effect of Environmental Particles on a Radial Compressor, in *Proceedings of the Corrosion-Erosion-Wear of Materials at Elevated Temperatures*, Berkeley, CA, January 31–February 2, 1990, Levy, A.V., Ed., National Association of Corrosion Engineers, Houston, TX, June, 1991, pp. 26–1.
- Tabakoff, W., Erosion Behavior of Materials in Multiphase Flow, in *Proceedings of the Corrosion-Erosion-Wear of Materials in Emerging Fossil Energy Systems*, Berkeley, CA, Jan. 17-19, 1982, Levy, A. V., Ed., National Association Of Corrosion Engineers, Houston, 1982, p. 642.
- Tabakoff, W., Performance deterioration on turbomachinery with the presence of particles, Particulate Laden Flows in Turbomachinery, *AIAA/ASME Joint Fluids, Plasma, Thermodynamics and Heat Transfer Conference*, 3, 1982, p.3.
- Takemura, F. and Matsumoto, Y., Influence of internal phenomena on gas bubble motion (Effects of transport phenomena and mist formation inside bubble in the expanding phase). *JSME Int. J.*, B-37, 736–745, 1994.
- Tang, L., Wen, F., Crowe, C.T., Chung, J.N., and Troutt, T.R., Self-organizing particle dispersion mechanism in a plane wake, *Phy. Fluyids*, 4, 10, 1992, 2244–2251.
- Tanner, L.H., The spreading of silicone oil drops on solid surfaces, *J. Phys. D: Appl. Phys.*, 12, 1473, 1979.
- Taylor, G.I., The dynamics of thin sheets of fluid II. Waves on fluid sheets, *Proc. R. Soc. Lond. A*, 263, 296, 1959.
- Taylor, G.I., The formation of emulsions in definable fields of flow, *Proc. R. Soc. London A*, 146, 501, 1934.
- Tennekes, H. and Lumley, J.L., *A First Course in Turbulence*, MIT Press, Cambridge, MA, 1972.
- Tishkoff, J., A model for the effect of droplet interaction on vaporization, *Int. J. Heat Mass Transfer*, 22, 1407–1415, 1979.
- Tjahjadi, M., Stone, H.A., and Ottino, J.M., Satellite and subsatellite formation in capillary breakup, *J. Fluid Mech.*, 243, 297, 1992.
- Toegel, R. and Gompf, B., Does water vapor prevent upscaling sonoluminescence? *Phys. Rev. Lett.*, 85, 3165–3168, 2000.
- Tomita, Y. and Shima, A., High-speed photographic observations of laser-induced cavitation bubbles in water, *Acustica*, 71, 161, 1990
- Tomita, Y. and Shima, A., The effects of heat transfer on the behavior of a bubble and the impulse pressure in a viscous compressible liquid, *Z. Angew. Math. Mech.*, 59, 297, 1979.
- Tomita, Y. and Shima, A., High-speed photographic observations of laser-induced cavitation bubbles in water, *Acustica*, 71, 161–171, 1990.
- Tomotika, S., On the stability of a cylindrical thread of a viscous liquid surrounded by another viscous fluid, *Proc. R. Soc. London A*, 150, 322, 1935.
- Tran, B., Seo, J., Hall, T.L., Fowlkes, J.B., and Cain, C.A., Microbubble-enhanced cavitation for noninvasive ultrasound surgery, *IEEE Transactions Ultrasonics, Ferroelectrics, Frequency Control*, 50, 1296, 2003.
- Trujillo, M.F. and Lee, C.F., Modeling crown formation due to the splashing of a droplet, *Phys. Fluids*, 13, 2503, 2001.
- Tsuji, Y., Kawaguchi, T., and Tanaka, T., Discrete particle simulation of two-dimensional fluidized bed, *Powder Technol.*, 77, 79, 1993.
- Tsuji, Y. and Morikawa, Y., LDV measurements of an air-solid two-phase flow in a horizontal pipe, *J. Fluid Mech.*, 120, 385–409, 1982.
- Tsuji, Y., Activities in Discrete Particle Simulation in Japan, *Powder Technol.*, 113, 278, 2000.

- Tsuji, Y., Morikawa, Y., and Shiomi, H., LDV measurements of an air-solid two-phase flow in a vertical pipe, *J. Fluid Mech.*, 139, 417–434, 1984.
- Tsuji, Y., Morikawa, Y., Tanaka, T., Nakatsukasa, N., and Nakatani, M., Numerical simulation of gas–solid two-phase flow in a two-dimensional horizontal channel, *Int. J. Multiphase Flow*, 13, 671, 1987.
- Tsuji, Y., Shen, N.-Y., and Morikawa, Y., Lagrangian simulation of dilute gas-solid flows in a horizontal pipe, *Adv. Powder Technol.*, 2, 63, 1991.
- Tsuji, Y., Shen, N.-Y., and Morikawa, Y., Numerical Simulation of Gas-Solid Flows. I (Particle-to-Wall Collision), *Technological Reports of Osaka University*, 39, 1989, p. 233.
- Tsuji, Y., Tanaka, T., and Ishida, T., Lagrangian Numerical Simulation of Plug Flow of Cohesionless Particles in a Horizontal Pipe, *Powder Technol.*, 71, 239, 1992.
- Turns, S.R., *An Introduction to Combustion: Concepts and Applications*, McGraw-Hill, New York, Inc, 1996.
- Umemura, A., Interactive droplet vaporization and combustion: Approach from asymptotics, *Prog. Energy Combust. Sci.*, 20, 325–372, 1994.
- Ushimaru, K., Crowe, C.T., and Bernstein, S., *Design and Applications of the Novel Slurry Jet Pump*, Report EI84-108, Energy International, Inc., October 1984.
- Vakil, N. and Everbach, E.C., Transient acoustic cavitation in gallstone fragmentation: a study of gallstones fragmented *in vivo*, *Ultrasound Med. Biol.*, 19, 331, 1993.
- Versluis, M., Schmitz, B., von der Heydt, A., and Lohse, D., How snapping shrimp snap: through cavitating bubbles, *Science*, 289, 2114, 2000.
- Vogel, A., Hentschel, W., Holzfuss, J., and Luterborn, W., Cavitation bubble dynamics and acoustic transient generation in ocular surgery with pulsed Neodymium:YAG lasers, *Ophthalmology*, 93, 1259, 1986.
- Voinov, O.V., Hydrodynamics of wetting, (English translation), *Fluid Dyn.*, 11, 714, 1976.
- Wade, R.B. and Acosta, A.J., Experimental observation on the flow past a plano-convex hydrofoil, *ASME J. Basic Eng.*, 88, 273, 1966.
- Walker, D.R. and Shaw, M.C., A Physical Explanation of the Empirical Laws of Comminution, *AIME Mining Eng. Trans.*, 6, 313, 1954.
- Walton, O. and Braun, R.L., Simulation of Rotary-Drum and Repose Tests for Frictional Spheres and Rigid Sphere Clusters, in *DOE/NSF Workshop on Flow of Particulates on Fluids, Sept. 29-Oct. 1, 1993, Proceedings*, available from NTIS, U.S. Dept. Commerce, Springfield, VA, 1994, 131–148.
- Walzel, P., Zeteilgrenze beim Tropfenprall, *Chem. Ing. Tech.*, 5, 338, 1980.
- Wang, A.B. and Chen, C.C., Splashing impact of a single drop onto very thin liquid films, *Phys. Fluids*, 12, 2155, 2000.
- Wang, L.P. and Maxey, M.R., Settling velocity and concentration distribution of heavy particles in homogeneous turbulence, *J. Fluid Mech.*, 256, 27–68, 1993.
- Wang, W. and Squires, K.D., Large eddy simulation of particle deposition in a vertical turbulent channel flow, *Int. J. Multiphase Flow*, 22, 667–683, 1996.
- Wark, C., Eickmann, K., and Richards, C., The structure of an acoustically forced, reacting two-phase jet, *Combust. Flame*, 120, 539–548, 2000.
- Wiezba, A., Deformation and breakup of liquid drops in a gas stream at nearly critical Weber number, *Exp. Fluids*, 9, 1329, 1990.
- Williams, F.A., *Combustion Theory*, 2nd ed., The Benjamin/Cummings Publishing Company, Menlo Park, CA, 1985.
- Williams, F.A., Recent advances in theoretical description of turbulent diffusion flames, In Murthy, S. N.B., Ed., *Turbulence in Mixing Operations*, Plenum Press, New York, NY, 1975, pp 189–208.
- Willis, K. and Orme, M., Binary droplet collisions in a vacuum environment: an experimental investigation of the role of viscosity, *Exp. Fluids*, 34, 28, 2003.
- Wood, R.T. and Woodford, D.A., Tube Erosion in Fluidized Beds, Paper No. 42, *Proceedings of the 5th International Conference on Erosion by Liquid and Solid Impact*, Cambridge, England, September 1979.
- Wood, R.T., and Woodford, D.A., *Tube Erosion in Fluidized Beds*, General Electric Co. Report 11/ET-FUC79, U.S. Energy Research and Development Administration Report 81-12, December 1980.

- Wu, J.-S., Liu, Y.-J., and Sheen, H.-J., Effects of ambient turbulence and fuel properties on the evaporation rate of single droplets, *Int. J. Heat Mass Transfer*, 44, 4593–4603, 2001.
- Yamamoto, Y., Potthoff, M., Tanaka, T., Kajishima, T., and Tsuji, Y., Large-eddy simulation of turbulent gas–particle flow in a vertical channel: effect of considering inter-particle collisions, *J. Fluid Mech.*, 442, 303, 2001.
- Yang, Y., Crowe, C.T., Chung, J.N., and Troutt, T.R., Experiments on particle dispersion in a plane wake flow, *Int. J. Multiphase Flow*, 26, 1583–1607, 2000.
- Yarin, A.L. and Weiss, D.A., Impact of drops on solid surfaces: self-similar capillary waves, and splashing as a new type of kinematic discontinuity, *J. Fluid Mech.*, 283, 141, 1995.
- Yarin, A.L., Weiss, D.A., Brenn, G., and Rensink, D., Acoustically levitated drops: drop oscillation and break-up driven by ultrasound modulation, *Int. J. Multiphase Flow*, 28, 887, 2002.
- Young, F.R., *Cavitation*, McGraw-Hill, London, 1989.
- Yuan, W. and Schnerr, G.H., Numerical simulation of two-phase flow in injection nozzles: Interaction of cavitation and external jet formation, *ASME J. Fluids Eng.*, 125, 963, 2003.
- Yuu, S., Ueno, T., and Umekage T., Numerical simulation of the high Reynolds number slit nozzle gas-particle jet using subgrid-scale coupling large eddy simulation, *Chem. Eng. Sci.*, 56, 4293, 2001.
- Zhang, D.Z. and Prosperetti, A., Averaged equations for inviscid disperse two-phase flow, *J. Fluid Mech.*, 267, 185–219, 1994.
- Zhou, Y.-K., He, J.-G., and Hammitt, F.G., Cavitation erosion of diesel engine wet cylinder liners, *Wear*, 76, 321, 1982.
- Zhu, J., Tube Erosion In Fluidized Beds, PhD. Thesis, Department of Chemical Engineering, The University of British Columbia, May 1988.
- Zhu, J., Grace, R., and Lim, C.J., Tube Wear in Gas Fluidized Beds-I. Experimental Findings, *Chem. Eng. Sci.*, 45(4), 1003, 1990.
- Zung, J.T., Evaporation rate and lifetime of clouds and sprays in air — the cellular model, *J. Chem. Phys.*, 46, 2064–2070, 1967.